The Synthesis and Characterisation of Novel Ruthenium (II) Polypyridyl Complexes for use in Cellular Imaging

A thesis submitted to Dublin City University for the award of MSc.

By

Zoe Joseph Stack, B.Sc. (Hons)

School of Chemical Sciences,

Dublin City University,

Glasnevin,

Dublin 9.

August 2013

Supervisors: Prof. Tia Keyes / Prof. Robert Forster

Declaration

I hereby certify that this material, which I now submit for assessment on the programme of study leading to the award of MSc. is entirely my own work, that I have exercised reasonable care to ensure that the work is original, and does not to the best of my knowledge breach any law of copyright, and has not been taken from the work of others save and to the extent that such work has been cited and acknowledged within the text of my work.

Signed: 

ID No.: 59100907

Date: 22/08/2013

Table of contents

Chapter 2: Experimental

Chapter 3: Synthesis and Characterisation of ruthenium complexes suitable for bioconjugation

Abstract

Ruthenium polypyridyl complexes have been under extensive investigation for many years across a range of optical applications, from solar energy conversion to sensing due to their unique photophysical properties including intense polarised luminescence, large Stokes shifts, red emission wavelengths, and good photostability. These properties, along with the sensitivity of their luminenscene to molecular oxygen make them potentially invaluable probes for cellular imaging.

This thesis describes the study of cell uptake and luminescence and resonance Raman imaging of a novel Ru(II) polypeptide conjugate and attempts to attach an internal oxygen and pH insensitive reference to a related luminescent ruthenium complex to create a self-referenced probe.

Chapter 1 overviews the photophysics of ruthenium polypyridyl complexes and discusses current state of the art in their application to cellular imaging. In particular, we discuss how conjugation of these complexes to biomolecules has lead to more targeted and improved applications in medical diagnostics, photodynamic therapy and cellular imaging. Chapter 2 describes the experimental methodology used in this thesis.

Chapter 3 described the synthesis and photophysical characterisation of two novel ruthenium probes, $[Ru\ (NO_2phen)_2\ picCOOH]^{2+}$ and $[Ru\ (NO_2phen)_2\ picNH_2]^{2+}$, where NO_2phen is 5-nitro-1,10-phenanthraline and the pic ligands are 2-(4-Carboxylphenyl)imidazo [4,5-f]1,10-phenanthroline and 2-(4-Aminophenyl)imidazo[4,5-f]1,10-phenanthroline respectively. Both the carboxyl and amino functionalised nitrophenanthroline complexes behave very similarly and may be characterised by comparable absorbance, emission, Raman profiles and similar pH dependence. These complexes exhibited a Stokes' shift of over 150 nm as well as having long lived emission lifetime (over 400 ns) which make them potential candidates for cell imaging. In the latter part of this chapter attempts to conjugate these complexes to a reference probe are described. The ultimate goal of attaching both to a cell penetrating peptide and an internal reference proved unsuccessful despite numerous different attempts, and this

chapter concludes with a discussion of a different synthetic approach which may ultimately lead to the target complex.

Chapter 4 described the ability of a novel ruthenium – peptide conjugate to transport passively and irreversibly across the cellular membrane of mammalian SP2 and CHO cells. Using confocal microscopy, by comparison, the parent complex was found not to transport across the cell membrane, confirming it is the peptide which is behaving as a cargo carrier in this instance. Resonance Raman mapping was used to investigate the presence of the complex within both cell types, by analysing individual cells. The most intense Raman signals, corresponding to the greatest concentration of dye, were observed in the center of each cell. The localization of the dye within SP2 cells was not confirmed via co-localization studies, but it was found to localize in the endoplasmatic reticulum of CHO cells.

List of Acronyms

ACN – acetonitrile

Arg – Arginine

Arg_8 – octaarginine

BODIPY– borondipyrromethene

Bpy – 2,2'-bipyridyl

CHO – Chinese Hamster Ovary

CPP – Cell Penetrating Peptide

CT – Charge Transfer

DAPI – 4′,6-diamidino-2-phenylindole dihydrochloride

$DiOC_6$ – 3,3'-dihexyloxacarbocyanine iodide

DMSO – dimethylsulfoxide

Dpp – 4,7-diphenyl-1,10-phenanthroline

dppz – dipyridophenazine

EDC – ethyl(dimethylaminopropyl) carbodiimide

FLIM – Fluorescence lifetime imaging microscopy

FRET – Förster resonance energy transfer

HeLa – Cell line of human cervical carcinoma cells

HOMO– Highest Occupied Molecular Orbital

IC – Internal Conversion

ILCT – Inter Ligand Charge Transfer

ISC – Inter-System Crossing

LC – Ligand Centered

LUMO – Lowest Unoccupied Molecular Orbital

MLCT – Metal to Ligand Charge Transfer

NH_2phen – 5-amino-1,10-phenanthraline

NHS – N-Hydroxysulfosuccinimide

NMR – Nuclear Magnetic Resonance

NO_2phen – 5-nitro-1,10-phenanthraline

PBS – Phosphate buffer solution

Peg – Polyethylene Glycol

Phen – 1,10-phenanthraline

SP2 – Mouse myeloma cell line

TCSPC– Time Correlated Single Photon Counting

Acknowledgements

I would firstly like to express my gratitude to Prof. Tia Keyes for all her support and guidance throughout my thesis. I would also like to thank Prof. Robert Forster for offering advice and support.

This thesis could not have been undertaken without the input of Dr Damian Plazuk, who provided me with a ruthenium – peptide conjugate in great quantity which formed a major part of my work.

I would also like to thank everyone who assisted me with the synthetic side of my project, in particular the advice of Aaron Martin, Ciarán Dolan, Stephen Finn and Kellie Adamson.

The NBIPI staff provided vital support throughout my studies, in particular the technical input and training of Rob Woolley, Chuck Blackledge, Tibebe Lemma, Una Prendergast and Róisín Moriarty.

The staff within the School of Chemical Sciences in DCU: Ambrose, John, Vinny, Veronica, Mary, Catherine, Julie and Brendan, were also a massive help to me throughout my time in DCU.

I would like to thank Dr Elena Lestini for being a great help to me when I initially came to DCU and also Lorraine Blackmore for running numerous mass spec samples for me.

A special thanks to Mick Burke and finally Joan Kelly.

Chapter 1

1. Introduction

1.1 Ruthenium (II) Polypyridyl Complexes

1.1.1 Introduction to Molecular Photophysics

1.1.2 Quantum Yield (Φ) and Lifetime (τ)

1.1.3 Photophysics of Ruthenium (II) Polypyridyl Complexes

1.1.4 Ruthenium complexes with pH Sensitive Ancillary Ligands

1.2 Polypeptides as Transmembrane Transporters

1.2.1 Cell Penetrating Peptides

1.3 Metal Complexes as Bioanalytical Probes

1.3.1 Use of ruthenium complexes in cellular imaging

1.3.2 Ruthenium conjugated polypeptides in cellular imaging

1.3.3 Ruthenium conjugated polypeptides in Raman Mapping

1.3.4 Mechanism of cellular uptake of ruthenium dyes

1.4 Ruthenium complexes as intracellular sensors

1.4.1 ruthenium complexes as pH and O_2 sensors

1.4.2 BODIPY complexes as biological probes

1.1 Ruthenium (II) Polypyridyl Complexes

1.1.1 Introduction to Molecular Photophysics

Luminescence is the emission of light from a molecule as it deactivates from an electronically excited state. This process is typically instigated following the absorption of a photon which leads to the promotion of a ground state electron to a higher – lying orbital. The excited molecule is generally not a stable species and will seek to relax to ground state through radiative or non – radiative pathways or by undergoing a chemical transformation. Figure 1.1 shows the typical deactivation pathways available to an excited state molecule.

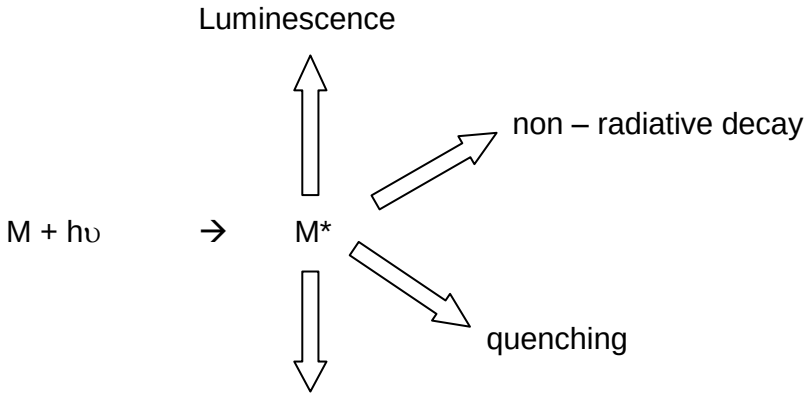

Figure 1.1 Typical excited state deactivation pathways

Figure 1.2 shows a Jablonski diagram which illustrates the competing photophysical processes by which the molecule may lose its excess energy in returning back to its original ground state energy level. When a molecule absorbs a photon of light, a fluorophore is promoted from its ground state to a higher vibronic level.

Depending on the nature of the excited state, radiative decay (luminescence) occurs as either fluorescence or phosphorescence; other non radiative processes are also possible. All are described below.

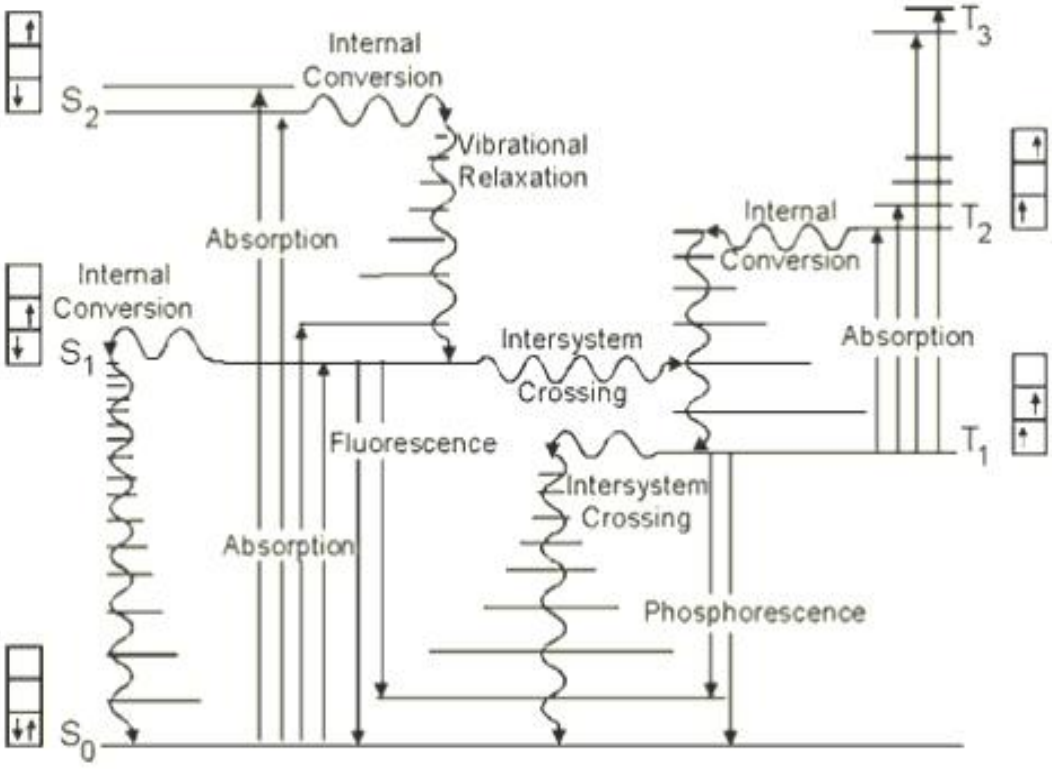

Figure 1.2: Jablonski diagram illustrating the radiative and non-radiative processes involved in the absorption and resultant relaxation of a molecule following excitation by a photon of light energy [1]

Fluorescence: Emission of a photon from one electronic state to a state of the same multiplicity. Figure 1.2 shows this process in solution typically occurs from the first singlet excited state to the ground state (i.e.. $S_1 \rightarrow S_0$). The excited molecule rapidly relaxes to the lowest vibrational state of S_1. The lifetime of this emission is usually very short, of the order of 10^{-8} s. Fluorescence generally occurs from a thermally equilibrated excited state, that is, the lowest energy vibrational state of S_1. The excited electron is paired to the second electron in the ground state orbital by opposite spin. This rapid return to the ground state is spin – allowed.

Phosphorescence: Emission of a photon as the electron moves between states of different multiplicity (e.g. $T_1 \rightarrow S_0$) is known as phosphorescence. The electron in the excited state has parallel spin to the ground state ($\uparrow\uparrow$) or ($\downarrow\downarrow$) and is spin forbidden however phosphorescence can be promoted in the presence of heavy atoms by spin orbit coupling. These forbidden transitions give slow emission decay rates (10^{-3} to 10^{-1}s), i.e. several orders of magnitude smaller than those for fluorescence.[2] As shown in the Jablonski diagram (Figure 1.12) and stated in Hund's rule: a singlet state (e.g. S_1) will be of higher energy than a triplet state (e.g. T_1) in the same configuration. Phosphorescence will occur at lower energy and therefore longer wavelength than fluorescence from a given molecule.

Internal Conversion: The non – radiative transition between electronic states of the same multiplicity ($S_2 \rightarrow S_1$) is known as internal conversion. This is an isoenergetic crossover between vibronic states which is followed by rapid vibrational relaxation to the lowest vibrational level of S_1. This process generally occurs on a 10^{-12} scale, hence typically occurs prior to emission as fluorescence lifetimes are of the order of 10^{-8} s.

Intersystem Crossing: The non – radiative, isoenergetic transition between vibronic states of different multiplicity ($S_1 \rightarrow T_1$) is known as intersystem crossing (ISC). This transition can occur from any singlet state and leads, following vibrational relaxation, to population of the lowest excited triplet state (T_1). This spin forbidden process is promoted in the presence of heavy atoms by spin orbit coupling.

1.1.2 Quantum Yield (Φ) and Lifetime (τ)

The fluorescence lifetime and quantum yield are two key characteristics of a fluorophore.[2] Quantum yield (ϕ_f) is defined as the number of photons emitted relative to the number of photons absorbed. The lifetime is important, as it determines the time available for the fluorophore to interact with or diffuse in its environment, and hence the information available from its emission. It is defined as the time taken for the luminescence intensity to decay, following excitation to $1/e^{th}$ of its initial intensity. These parameters can be measured and used to provide insight into the relaxation processes of a molecule arising from its return to the ground state and can be determined by the emissive rate of the fluorophore (Γ) and its rate of non – radiative decay to the ground state (k_{nr}). The fluorescent quantum yield as shown in equation 1.1 reflects the fraction of fluorophores that decay through emission:

$$\phi_f = \frac{k_r}{k_r + k_{nr}} \qquad \text{eqn 1.1}$$

If the rate of non-radiative relaxation (k_{nr}) is faster than that of luminescence (k_r), the quantum yield will be small and vice versa. Luminescent quantum yields can be close to unity if the radiationless decay rate is much smaller than the rate of radiative decay, that is $k_{nr} < \Gamma$. However due to vibrational/thermal losses, the energy yield of fluorescence is always less than unity. The luminescent quantum yield is a key parameter in calculating quenching rate constants, energy transfer rates and radiative and non-radiative decay rate constants.[3] The excited state lifetime of a fluorophore (τ) is defined as the average time the molecule spends in the excited state prior to relaxation to the ground state. Shown in equation 1.2 is the fluorescence lifetime of a molecule.

$$\tau = \frac{1}{k_r + k_{nr}} \qquad \text{eqn 1.2}$$

Fluorescence emission is a random process and few molecules emit their photons at precisely $t = \tau$, the difference between the natural and measured lifetime

Emission lifetimes and emission quantum yields provide a convenient means of measuring the unimolecular phototransitions expected to occur in a molecule including internal conversion (IC), intersystem crossing (ISC), fluorescence (F) or phosphorescence (P). Shown in equation 1.3 is the steady – state approximation for the concentration of the first excited singlet energy state [S_1], which assumes that the rate of absorption of light is equal to the combined rates of deactivation of S_1.

$$I_{abs} = (k_{IC} + k_{ISC} + k_F)\ [S_1] \qquad \text{eqn 1.3}$$

The ruthenium complexes in this thesis deal with phosphorescence, which occurs from the triplet state [T_1]. Shown in equation 1.4 is the steady – state approximation for the process which assumes that the rate of formation of triplet states is equal to their rates of deactivation.

$$K_{ISC}\ [S_1] = (k_{ISC} + k_P)\ [T_1] \qquad \text{eqn 1.4}$$

For phosphorescent complexes under steady – state conditions, the quantum yield of key processes can be described as the ratio of the decay rates to the total deactivation rates of that state. Shown in equation 1.15 is the expression of the quantum yields for these transitions.

$$\phi_{IC} = k_{IC} / (k_F + k_{ISC} + k_{IC}) \qquad \text{eqn 1.5}$$

$$\phi_{ISC} = k_{ISC} / (k_F + k_{ISC} + k_{IC}) \qquad \text{eqn 1.6}$$

$$\phi_P = \phi_{ISC} \times k_{IC} / (k_P + k_{ISC}) \qquad \text{eqn 1.7}$$

The quantum yield can also be related to the lifetime (τ) of the complex.

As shown in equation 1.8, the singlet lifetime (τ_S) is equal to the inverse of the sum of all rates that deactivate [S_1]. It is important to note that these expressions assume that the only deactivating processes are the radiative and non-radiatiave photophysical pathways.

The triplet lifetime (τ_T) is equal to the inverse of the sum of the rates that deactivate the energy level [T_1] and is shown in equation 1.9.

$$\tau_S = 1 / (k_F + k_{ISC} + k_{IC}) \quad \text{eqn 1.8}$$

$$\tau_T = 1 / (k_P + k_{ISC}) \quad \text{eqn 1.9}$$

Therefore, the expression of key quantum yield states may be defined from the following three equations.

$$\phi_{IC} = (k_{IC}) (\tau_S) \quad \text{eqn 1.10}$$

$$\phi_{ISC} = (k_{ISC}) (\tau_S) \quad \text{eqn 1.11}$$

$$\phi_P = (\phi_{ISC}) (k_P) (\tau_T) \quad \text{eqn 1.12}$$

Experimentally, values of τ_S and τ_T may be evaluated directly by measurement of the decay of [S_1] and [T_1] as a function of time. The most convenient method to monitor [S_1] is usually by measuring the fluorescence intensity emitted from [S_1]. Hence, τ_S is generally the same as the measured fluorescence lifetime, τ_F, but the measured values do not provide information on the pure radiative lifetime of fluorescence from the singlet energy state. However, measurement of the phosphorescence lifetime, τ_P, provides a direct measure of the excited triplet energy state, τ_T, as shown in equation 1.12.[3]

The fluorescence yield ϕ_f and singlet lifetimes τ_S of organic molecules are sometimes found to vary with temperature.[1] An increase in temperature typically leads to a decrease in both the quantum yield and lifetime of a molecule as non-radiative decay through such as vibrations, rotations and collisions become more likely. The population of the geometrically distorted ^{3}MC states are thermally induced in ruthenium polypyridyl complexes, which can lead to decomposition of the complex, depending on the s-donor ability, i.e. ligand field splitting of the coordinating ligands.[4, 5]

1.1.3 Photophysics of Ruthenium (II) Polypyridyl Complexes

Ru(II) is a d^6 transition metal where the polypyridyl ligands usually have σ donor orbitals on the nitrogens and π donor and π *acceptor orbitals are delocalised on the aromatic rings[6]. Shown in figure 1.3 is $[Ru(bpy)_3]^{2+}$ (where bpy = bipyridine), one of the most widely studied of ruthenium polypyridyls.

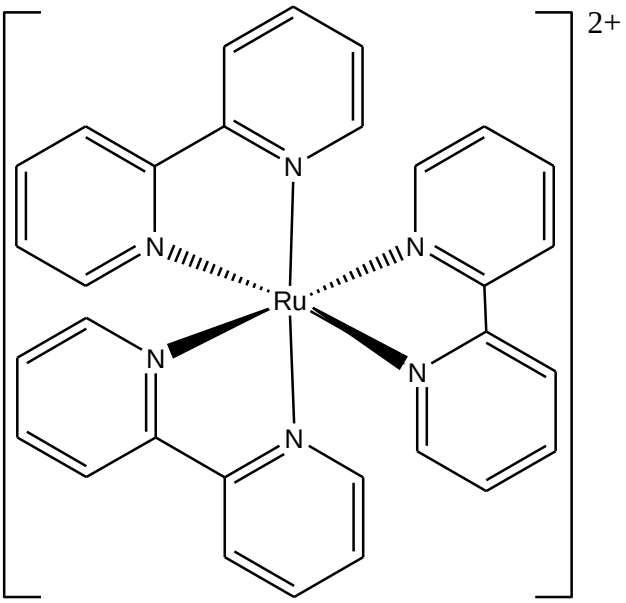

Figure 1.3: structure of $[Ru(bpy)_3]^{2+}$

Figure 1.4 shows the molecular orbital diagram for an octahedral metal complex, Ru(II) polypyridyl complexes can be considered as pseudo-octahedral.

Ruthenium polypyridyl complexes display intense absorption bands in the visible and near IR regions of the electromagnetic spectrum. These absorbance bands are typically assigned to electronic transitions such as metal centred (MC), ligand centred (LC) or charge transfer (CT). In general, the σ_L and π_L ligand orbitals are full for d^6 complex ground states. Depending on the oxidation state of the metal, the π_M orbitals are partially filled and the remaining orbitals are usually empty.

Metal - centred transitions involve the molecular orbitals which are mainly composed of the central metal d-orbitals and their wavelength commonly corresponds to the wavelength of visible light. d-d transitions in octahedral complexes involve a rearrangement populating the low-lying t_{2g} orbital to the e_g orbital. Ligand centered transitions such as p-p transitions occur at higher energy than metal centered and charge transfer transitions. Metal to ligand charge transfer (MLCT) is a common transition observed in Ru(II) complexes coordinated to organic ligands, such as polypyridyl derivatives and involves promotion of electrons from the highest occupied molecular orbital (HOMO) to the lowest unoccupied molecular orbital (LUMO)[7].

The multiplicity of each of the resulting excited states may be singlet or triplet, although spin – orbit coupling causes singlet – triplet mixing in metal centred complexes and results in the formation of ^{3}MLCT excited states in Ru(II) complexes.[8]

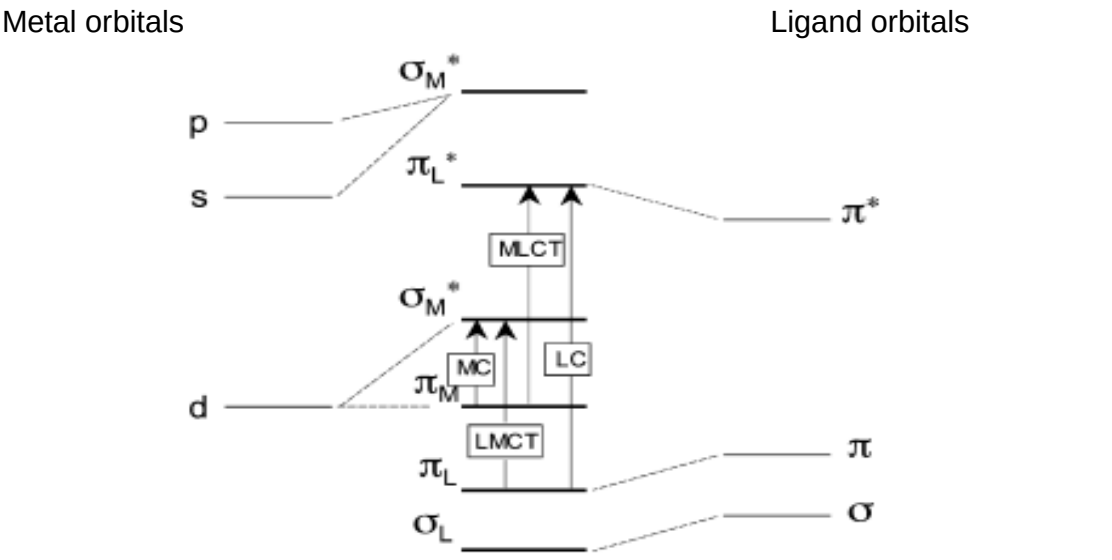

Figure 1.3: Molecular orbital diagram for an octahedral metal complex. The arrows indicate the four types of transitions based on localized MO configurations[4].

As previously mentioned, $[Ru(bpy)_3]^{2+}$ is one of the most widely studied of the ruthenium polypyridyls, with extensive research into the molecule's photophysical and redox characteristics found in the literature.[4, 5, 8, 9] It has been

commonly used as a reference to explain similar processes occurring in other ruthenium(II) complexes[9] and is used to rationalise the behaviour of the ruthenium(II) complexes studied in this thesis. Shown in figure 1.4 is the typical absorbance and emission spectra for $[Ru(bpy)_3]^{2+}$ in acetonitrile solution.

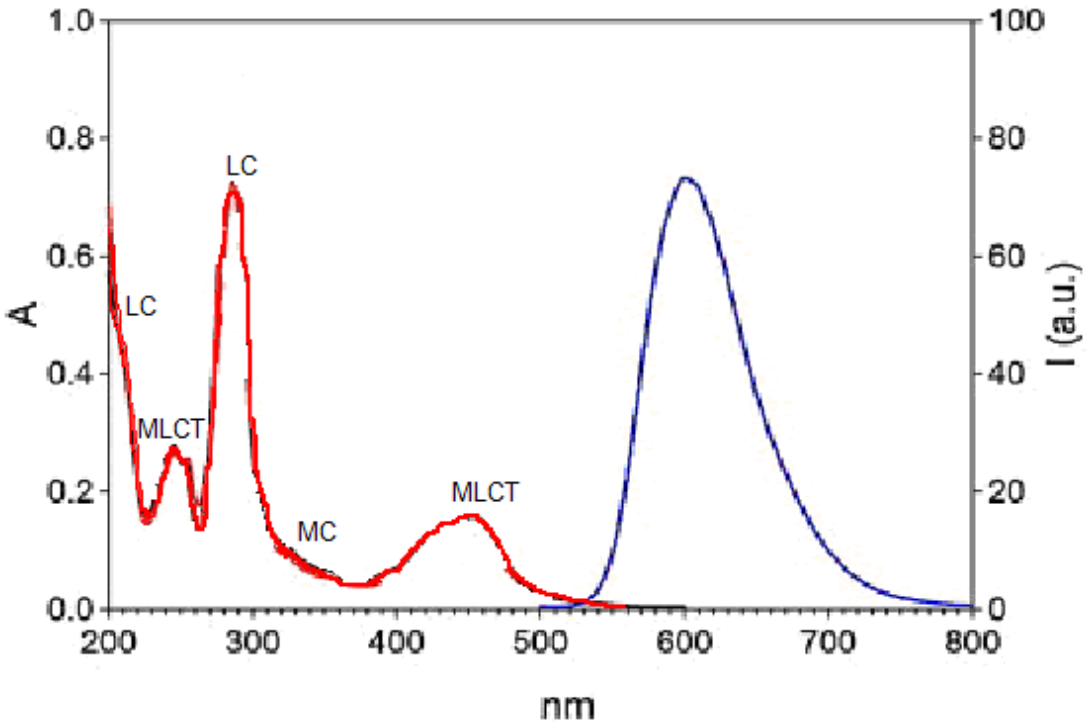

Figure 1.4: Absorbance and emission spectra of $[Ru(bpy)_3]^{2+}$ (10μM) in acetonitrile solution.

The absorbance spectrum of $[Ru(bpy)_3]^{2+}$ exhibits a characteristic ruthenium (dπ orbital) to bipyridyl ligand (π* orbital) metal to ligand charge transfer (MLCT) at 455 nm. An additional MLCT transition occurs at higher energy at 240 nm. There are two shoulders present at 322 nm and 342 nm which are not incontrovertibly assigned but are thought to be due to MC d → d transitions. The strong absorbance at approximately 285 nm in the spectrum is assigned to π-π* transitions within the bipyridyl ligands.

Excitation into the MLCT at 455 nm of the $[Ru(bpy)_3]^{2+}$ absorption band leads to an intense emission at approximately 610 nm which originates from a triplet MLCT state. Inter-system crossing is promoted by the heavy Ru nucleus in this complex and occurs with unity quantum yield.

1.1.4 Ruthenium complexes with pH Sensitive Ancillary Ligands

Quaranta et al.[10] have previously shown that the ionisation state of a benzimidazole group in a ruthenium complex can modify its luminescence behaviour. More recently however, the ionisable Pic ligand has been the focus of much interest when it has been coordinated to a ruthenium metal centre.[11-13] Shown in figure 1.5 below, is the structure of 2-(4-nitrophenyl)imidazo[4,5f][1,10]phenanthroline) [(picNO$_2$)], a common Pic – ligand. The ligand possesses two ionisable sites: each nitrogen atom located on the imidazole ring. These sites give rise to well defined acid-base characteristics and the terminus can be designed with a functionality that allows for efficient conjugation to biomolecules such as polypeptides. In this thesis, a range of Pic ligands have been synthesised to contain carboxyl, amino and nitro terminals and a photophysical comparison of their Ru(II) complexes is detailed and discussed in chapter 4.

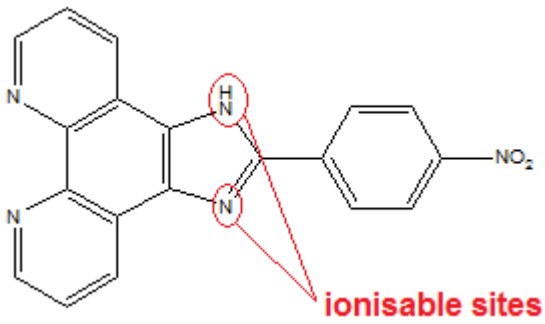

Figure 1.5: ionisable sites on 2-(4-Nitrophenyl)imidazo[4,5-f]1,10-phenanthroline [PicNO$_2$] ligand.

Pic ligands are of particular interest in relation to transition metals complexes, as when coordinated to a metal centre they display longer lifetimes and increased emission intensity, than their trisbipy derivatives. As these ligands are sensitive to their environment, they are potentially invaluable for probing complex biological structures. Neugebauer et al.[12] reported how intracellular pH

had a direct effect on both the lifetime and relative Raman peak intensities of the ruthenium(II) multimodal probe, containing this pH sensitive ancillary ligand, and is described further in section 1.3. This thesis heavily features ruthenium polypyridyl complexes with pH sensitive ancillary ligands and their photophysics are characterised in chapter 4.

1.2 Polypeptides as Suitable Transmembrane Transporters

1.2.1 Cell Penetrating Peptides

Peptides are biopolymers of amino acids which are linked through a peptide bond. A peptide bond, often referred to as an amide bond, is formed through the reaction of a carboxyl group of one molecule with the amino group of another molecule. This process is a condensation reaction as it leads to a loss of a water molecule and usually occurs between amino acids. Polypeptides are chains of amino acids which are held together by peptide bonds and are utilised in this thesis for the transport of novel probes across a cell membrane. Shown in figure 1.6 is the schematic representation of a peptide bond formation.

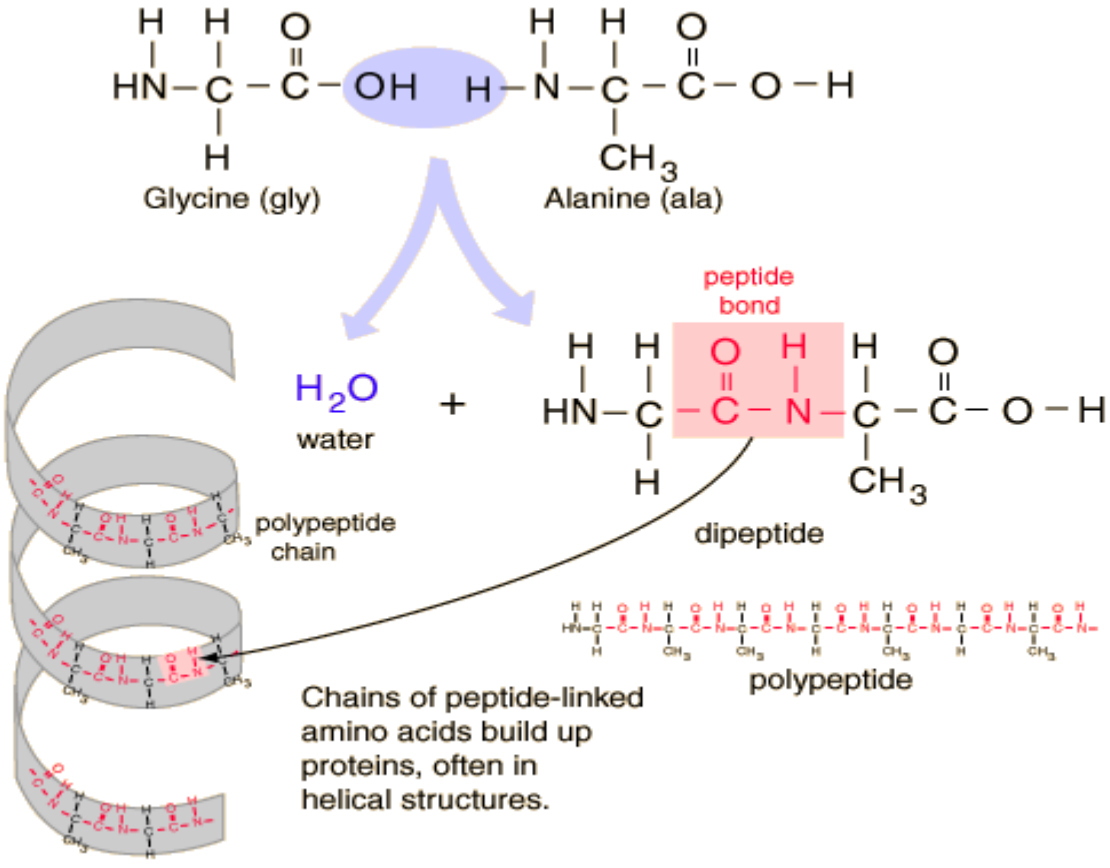

Figure 1.6: Peptide bond formation from the dehydration (condensation) reaction of glycine and aniline. [14]

A key aim of this thesis was to synthesise a transport carrying molecule which was capable of passive cell delivery, by the conjugation of a luminophore to a cell penetrating peptide. Certain naturally occurring molecules may enter the cell through a facilitated transport pathway mediated by receptors on the cell's surface. The nuclear transcription activator protein Tat is a protein which is encoded for by the Tat gene in HIV-1 and is an example of such a molecule.[15] Arginine is a commonly occurring, non – essential amino acid, meaning it can be produced in the body. It is cationic in nature, even under biological conditions, due to the presence of a guanidinium group which allows the peptide to form bidentate hydrogen bonds with anions such as phosphate. [16, 17] Previous studies by Wender.[15] demonstrated the importance of the guanidinium groups, as changing the cationic groups with neutral alanine residues led to a decrease in the cellular uptake which correlated directly with the number of arginine residues.

These results led to extensive research into polyarginine peptides as cell penetrating molecular cargo carriers. The number of guanidinium groups, and therefore overall polyarginine chain length greatly affects the ability of these peptides to diffuse across the cell membrane. The most efficient uptake was found in peptides with chain lengths ranging from R_6 – R_{11}. Polyarginine molecules with a chain length of less than six, show no significant uptake, while chain lengths exceeding eleven arginine groups show no increase in uptake.[15, 18] Shown in Figure 1.7 is the structure of an arginine molecule with guanidinium highlighted in red.

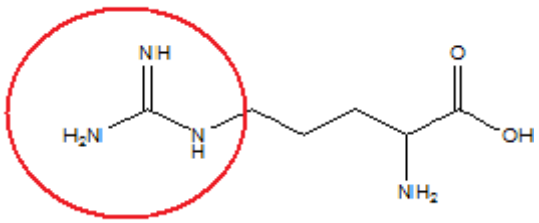

Figure 1.7: Arginine Structure ((S)-2-Amino-5-guanidinopentanoic acid) with guanidinium group highlighted in red

The four main routes to cellular uptake are endocytosis, active transport, facilitated diffusion and passive diffusion.[19] Endocytosis is thought to involve the cell membrane wrapping itself around the extra-cellular peptide and engulfing it. The peptide is then brought into the cell via small vesicles. Shown in figure 1.8 are the various endocytosis pathways.

Phagocytosis is the process where a cell membrane will change its shape to engulf particle solids to form an internal vesicle around the particle, known as a phagosome. The process is distinct from other forms of endocytosis as it is specific to the internalization of solids such as bacteria, as opposed to other processes which may internalize various liquids. In the human body, macrophages and neutrophils are two of the most effective phagocytic cells, where they are drawn toward an area of infection or inflammation by means of chemoattractants given off by the bacteria and the infected tissue.

Pinocytosis is another form of endocytosis where the plasma membrane forms an invagination and whatever substance is found within the area of invagination is brought into the cell's cytoplasm by tiny vesicles. This process is not involved in the ingestion of larger particulate material and is often referred to as "cellular drinking" as the materials ingested by the cell are liquids and material dissolved in liquids.

Receptor mediated endocytosis is a process by which cells internalize molecules or viruses. As its name implies, it depends on the interaction of that molecule with a specific binding protein in the cell membrane called a receptor. These receptors are brought into the plasma membrane by vesicles from the Golgi apparatus. After binding an endocytotic process occurs as a signal is sent through the membrane, leading to membrane coating, and formation of a membrane invagination. The molecule is then ingested by the cell. The protein involved in this process is the cytosolic protein clathrin, which contains receptor sites specific to the molecules being internalized.[20]

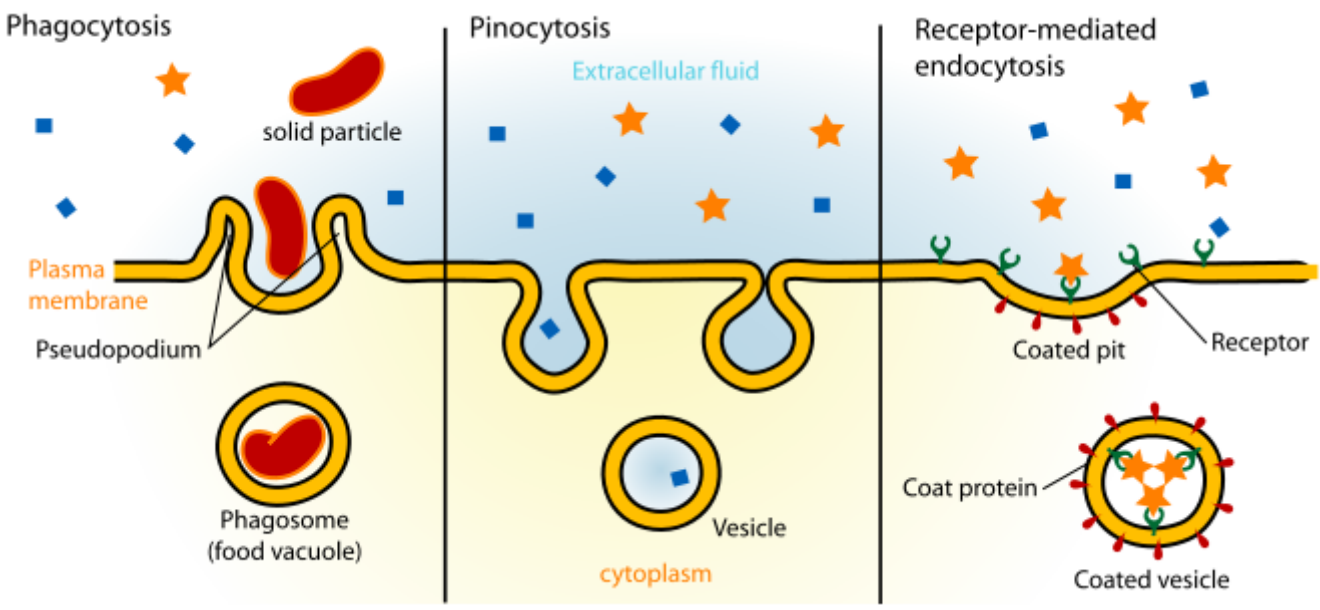

Figure 1.8: Schematic diagram of the various endocytosis pathways[21]

Electrostatic attraction is the first process in which the highly positively charged polypeptides are attracted to the negatively charged phosphate groups at the cell phospholipid membrane. Electrostatic attraction across the cell membrane draws some of the positive ions on the outside and some of the negative ions on the inside to the respective surfaces of the membrane. Heparan sulfate proteoglycan (HSPGs) located on the cell membrane then binds to these peptides and modulate Heparan sulphate mediated endocytosis. Macropinocytosis is reported as one of the major pathways of uptake for arginine rich peptides.[22, 23]

It is widely believed that endocytosis is the most likely mechanism of cellular uptake of arginine rich cell penetrating peptides as results have shown the process to be temperature and therefore, energy dependent which is indicative of endocytosis.[12, 22-24] Fuchs et al.[23] have previously reported the internalisation of a fluorescein labelled polypeptide by entocytoic means. Examining the internalization pathway of penetrating peptide into mammalian cells, nonaarginine was found in the cytosol as well as the nucleolus when cells were fixed, but observed only in the endocytic vesicles of live cells. Colocalization studies with vesicular markers confirmed the peptide was

internalized by endocytosis rather than passive diffusion across the plasma membrane.

Pellegrin[11] described the extensive photophysical characterisation of the ruthenium(II) polypyridyl complex, $[Ru(bpy)_2(picCOOH)]^{2+}$, containing a pH sensitive ancillary ligand. With the aim of exploiting the acid – base characteristics of this molecule for the exploration of cellular environments, the complex was subsequently conjugated to a polypeptide. Neugebauer[12] subsequently advanced this work by conjugating the pH sensitive probe to a cell penetrating peptide. Shown in figure 1.24 is a flow chart which depicts the uptake of the complex and its subsequent activity in a cellular environment. Consistent with endocytosis, the transport of the peptide conjugated dye across the cell membrane was found to be temperature dependent.[23] The use of this complex and other ruthenium probes in a cellular environment is discussed in further detail in section 1.3.1 below.

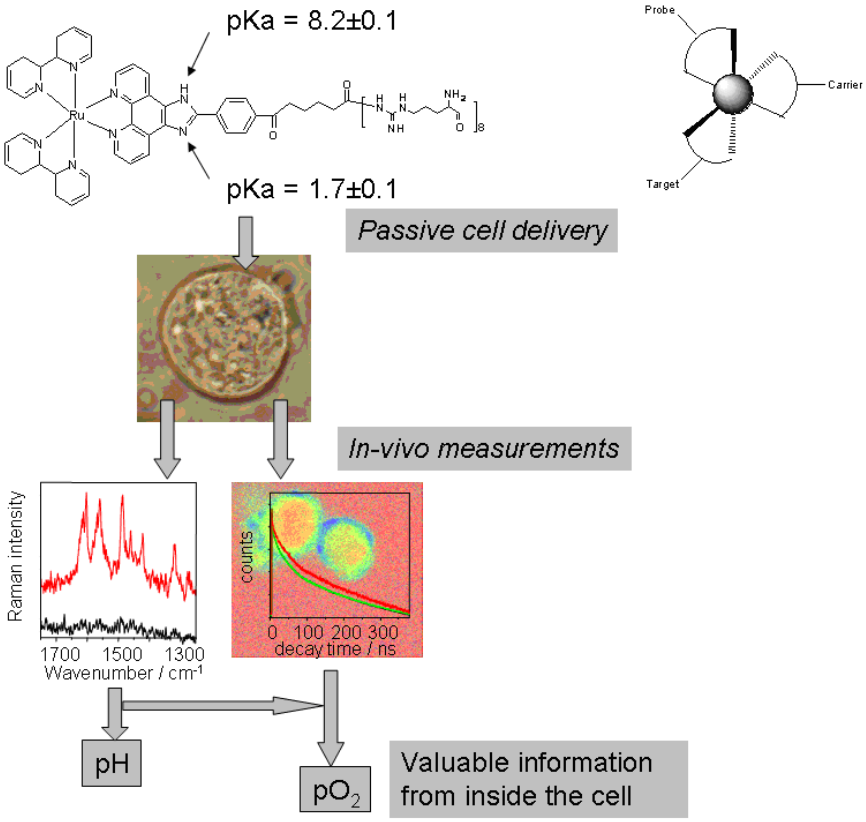

Figure 1.9: Flow diagram illustrating the cellular uptake and determination of intercellular pH (using Raman spectroscopy) and oxygen levels (using lifetimes) using the ruthenium (II) polypyridyl complex, $[Ru(bpy)_2(picCOOH)]^{2+}$.[25]

As endocytosis is thermally activated process, its efficiency is hindered at lower temperatures, for example 4°C instead of 37°C. It has been previously shown that in many systems endocytosis does not occur below 10°C. However, internalization of polypeptides has been reported at 4°C, where endocytic pathways do not function. A temperature independent pathway would suggest an uptake mechanism such as passive diffusion, which is energy independent, and in some examples both temperature dependent and independent pathways have been seen to co-occur.[24, 26]

Knipp et al.[27] have described hydrophobic peptides that are capable of permeating heterogenous human epithelial cells via passive diffusion. These peptides are more lipophilic when they exhibit significant beta – turn structure in solution which causes them to permeate the cell more readily.

Figure 1.10 illustrates an alternative mechanism which has been proposed for polyarginine uptake, called the translocation mechanism of polypeptides across the cell membrane via non-endocytotic pathways.[28] In this mechanism, the P – N dipole vector is in the plane of the membrane as shown in Figure 1.10 (a). Figure 1.10 (b) then illustrates the how the dipole bends towards the interior of the membrane when the peptide attracts the phosphate groups as it approaches the surface of the membrane. As this conformation is not favoured by the system, the peptide inserts into the interface between the hydrophilic head groups and the carbon chains. Figure 1.10 (c) shows how the peptide orients away from the choline groups. The cell membrane then becomes thinner as the density of the peptide increases, as illustrated in Figure 1.10 (d). The next stage of the process (Figure 1.10 (e)) involves translocation of an arginine amino acid with local bending of the membrane on both sides of the bilayer. This bending reduces the energetic barrier of the translocation. The final step in the mechanism is shown in Figure 1.10 (f) which illustrates the formation of a pore and the peptide translocates, bound to the interior of the bilayer surface.

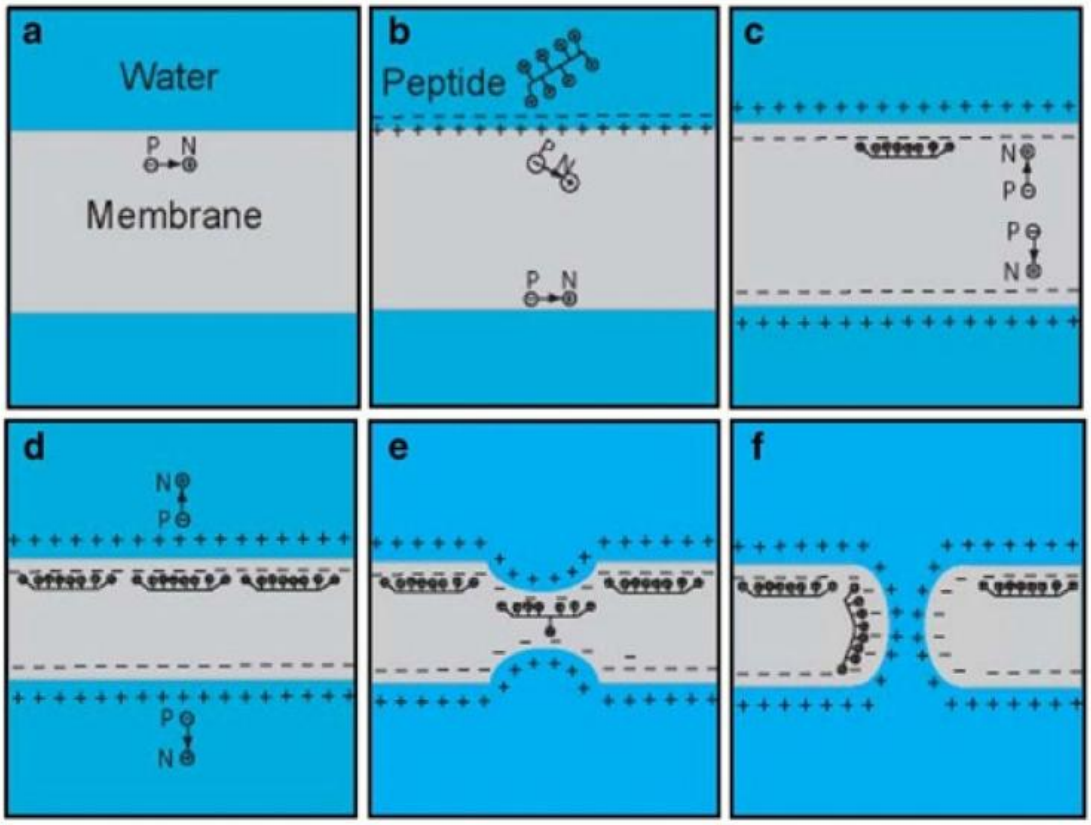

Figure 1.10: Schematic diagram illustrating qualitatively the steps involved in the translocation mechanism. The orientation of the dipole moment vector formed by the phosphate group (negatively charged) and the choline group (positively charged) denoted by P and N, respectively is shown.[28]

Despite endocytosis being widely believed to be the most likely mechanism of cellular uptake of cell penetrating peptides, evidence of passive (unactivated) diffusion and translocation methods of cellular uptake as potential uptake routes means the topic is still hotly debated. As the process has been demonstrated to be temperature and energy dependent, endocytosis seems a likely uptake mechanism. However, no method or process has been conclusively proven or universally accepted. Nonetheless, the results discussed suggest that polyarginine is very effective as a transmembrane molecular cargo carrier.

1.3 Metal Complexes as Bioanalytical Probes

Traditional organic probes used for diagnostic purposes have a number of limitations which reduce their suitability as probes for bioanalysis. Typically, organic fluophores have short-lived excited state lifetimes (<10 ns) and are susceptible to photobleaching when used in laser scanning microscopy. Such probes are also not suitable for resonance Raman as their relatively small Stoke's shift means fluorescence overwhelms the weaker Raman response.[13] Short lived probes are also unable to monitor important long lived biomolecular processes such as membrane diffusion, protein rotation and protein folding.

Overall, in order for a luminophore to be a suitable candidate for exploring a cellular environment it must be photostable, have a high quantum yield, be relatively non – toxic, cell permeable and have visible to near IR emission.

Many transition metal complexes offer numerous advantages over such organic fluorphores and have been exploited in cellular imaging,[11] diagnostics,[5] and supramolecular assemblies[29, 30] in recent years. Lo[31] have previously described a series of luminescent cyclometalated iridium(III) polypyridine complexes which exhibit a triplet metal-to-ligand charge-transfer (^{3}MLCT) emission. Shown in figure 1.31 is the absorbance (a) and emission (b) spectra of a range of iridium (III) complexes. As with many transition metal complexes, these Ir (III) luminophores exhibit significant flexibility where by changing the ligands the absorbance and emission characteristics of the complex can be tuned.

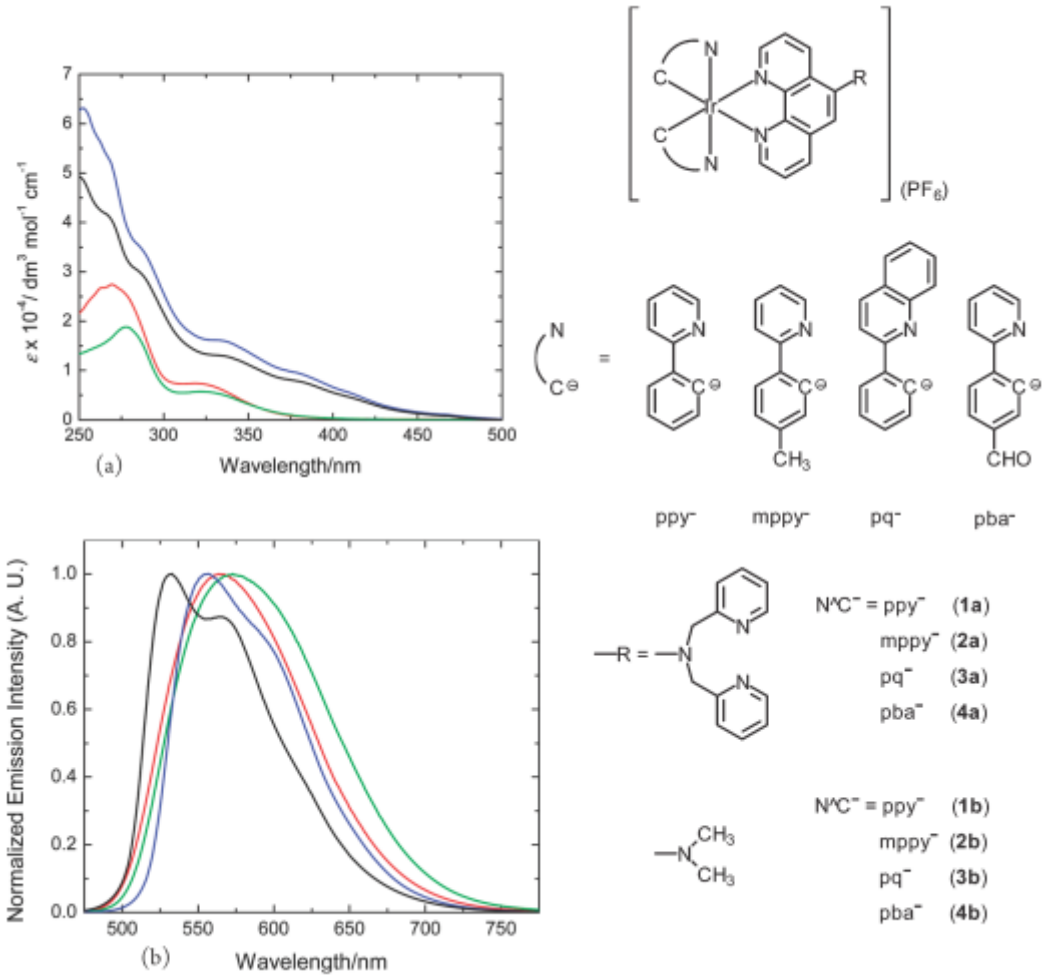

Figure 1.31: Structures of a series of iridium (III) polypyridine complexes with varying polpyridine ligands; electronic absorption spectra (a) and emission spectra (b) of a range of these complexes in CH_2Cl_2 at 25°C.[31]

A key objective of this thesis was to examine the cellular uptake, including the uptake speed, transport mechanism and localization, of a peptide conjugated ruthenium probe in two mammalian cell lines. The conjugation of a metal complex to a cell penetrating peptide facilitates efficient diffusion across mammalian cell membranes without destroying the lipid bilayer and without the need for membrane permeabilisation by artificial means such as detergent or organic solvent. The ability of a peptide conjugated ruthenium complex to penetrate mammalian cells was investigated using mouse Sp2/0-Ag14 myeloma cells. The myeloma is a cancerous plasma cell and was used as a model of a suspension mammalian cell.

Many transition metal complexes, containing ruthenium(II), osmium(II) or rhenium (I) with diimine ligands show characteristically long emission lifetimes (up to and beyond 1 μs) and can be synthesized to target key biological sites. One promising advancement involving a transition metal complex in cellular imaging is the recently reported synthesis of a zinc(II) complex containing Triapine. Shown in figure 1.31 is the structure of Triapine (3-aminopyridine-2-carboxaldehyde thiosemicarbazone), which is a a potent inhibitor of ribonucleotide reductase, the rate determining enzyme in the supply of DNA building blocks.

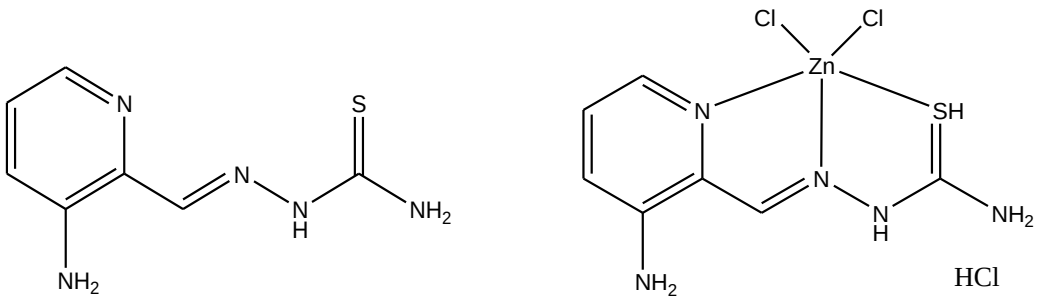

Figure 1.31: Structure of Triapine and coordinated zinc complex[32]

Coordination of the Triapine unit to a zinc(II) metal centre was found to increase the antineoplastic activity. Shown in figure 1.32 are live cell images of human colon carcinoma cells incubated with Triapine and the zinc(II) coordinated complex; the Zn (II) complex is shown to display selective affinity for the nucleoli of the cells. The false colour images in figure 1.32 (A) and (B) illustrates that the Triapine molecule and its Zn(II) complex localize to different areas of the cell. Co – localization studies using nucleolar protein fibrillarin shown in figure 1.32 (C) and (D) illustrate the preferential selectivity of the Zn(II) complex toward the nucleoli of the cells.[32]

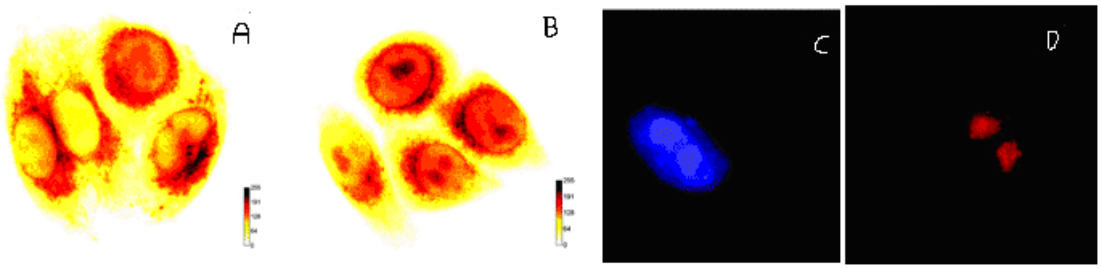

Figure 1.32: False colour images (A and B) of human colon carcinoma cells incubated with Triapine (0.25 mM) in PBS and Zn (II) Triapine complex (0.25 mM) in 0.5% DMSO/PBS; luminescence images (C and D) using nucleolar protein fibrillarin as a counter stain with Zn (II) Triapine complex (0.25 mM) in 0.5% DMSO/PBS.[32]

In another very recent study, Lo[33] reported on rhenium(I) complexes as novel trifunctional biological probes capable of bioconjugation and intracellular detection. The emission behaviour and cellular uptake properties of many luminescent rhenium (I) complexes have been reported in the literature[34], shown in figure 1.33 are novel trifunctional biological probes which were synthesised containing a fluorous moiety.

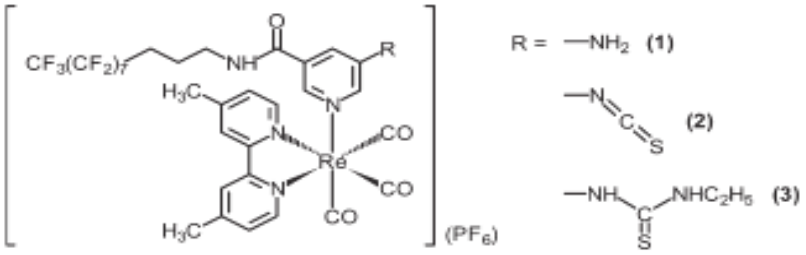

Figure 1.33: Structure of three rhenium (I) polypyridine complexes.[33]

The cellular uptake of the thiourea complex (3) in HeLa cells was examined using live–cell confocal imaging. As shown in figure 1.34, the complex was found to transport readily across the membrane and localize in the juxtanuclear region at 37°C, however uptake at 4°C led to less efficient uptake. This is evidence of uptake occurring through an energy dependent pathway such as endocytosis. Although not discussed in the paper, it is important to note that the Re(I) complex was incubated with 1% DMSO prior to imaging and that will have permeabilized the cell membrane making it difficult to assess if the compound is truly membrane permeable or to conclude anything about the uptake pathway.

Organic solvents, such as DMSO and ethanol, are frequently used in cellular uptake analysis. While DMSO is not toxic at this concentration, it causes the cell membrane to become less ridged, making it more susceptible to facilitate membrane diffusion.[46] DMSO will also permeabilize cells, meaning the dye is not penetrating a healthy cell membrane.[47, 48]

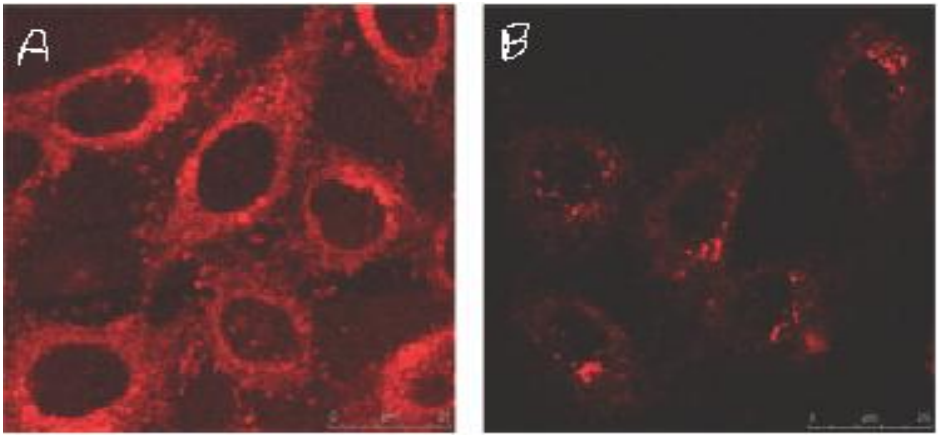

Figure 1.34: Luminescence images (λ_{ex} = 405 nm) of HeLa cells incubated with [Re(Me_2bpy)($CO)_3$(py-Rf-TU-C_2H_5))](PF_6) (5 μM) in 1% DMSO at 37°C (A) and 4°C (B).[33]

The punctuate emissive dots displayed in figure 1.34 were investigated further, as their proximity to the nucleus suggested they may be mitochondria. To confirm this, HeLa cells were counter – stained with MitoTracker Deep Red FM and examined using confocal microscopy, which is shown in figure 1.35. As is evidence from the significant overlap, the complex is found predominantly in the mitochondria of HeLa cells incubated at 37°C. The cationic charge of the complex, combined with it being highly hydrophobic in nature, is responsible for the mitochondrial – targeting properties of the complex.[35]

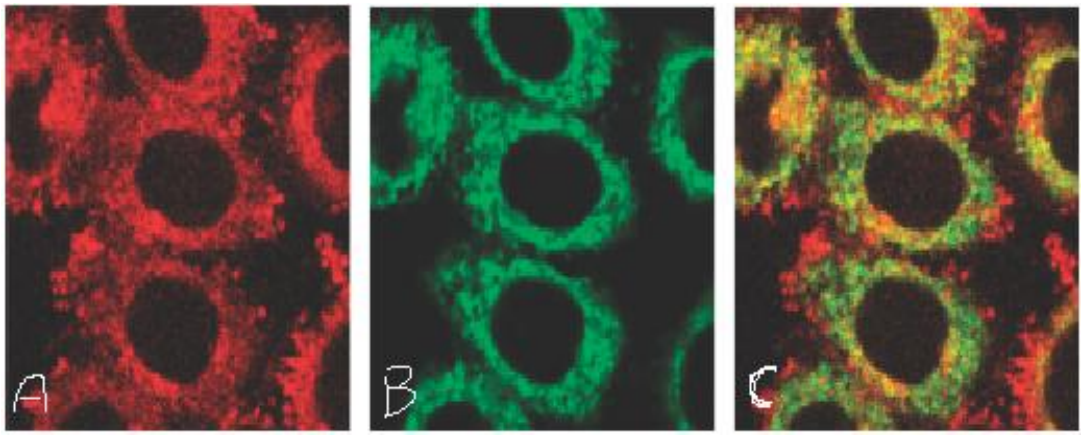

Figure 1.35: Luminescence confocal images (λ_{ex} = 405 nm, (a); (λ_{ex} = 633 nm, (b)) of HeLa cells incubated with [Re(Me_2bpy)($CO)_3$(py-Rf-TU-C_2H_5))](PF_6) (5 μM) in 1% DMSO for one hour (a) at 37°C and MitoTracker Deep Red FM (100 nM) for 20 minutes (b). Images are overlaid in (c).

Of the complexes synthesised, isothiocyanate complex (2) has been used to label bovine serum albumin (BSA) and glutathione (GSH). The complex may also be separated from a mixture of 20 amino acids using Fluorous Solid Phase Extraction (FSPE).[35] Investigation into the cytotoxicity of the amine complex (1) and the thiourea complex (3) was carried out using the MTT cell viability assay with HeLa cells as a model cell line. While both complexes were found to have high cytotoxicity (similar to related rhenium (I) complexes), their cytotoxicity can be readily modified with a choice of ligands with different lipophilicity.

While these novel trifunctional biological probes offer new and unique properties, it is noted that the isothiocyanate complex was omitted from the MTT assay because it is unstable in aqueous solution. The use of DMSO in a cellular environment raises doubts over the permeability of the cell and hence the suitability of the complex to live – cell imaging.

1.3.1 Use of ruthenium complexes in cellular imaging

The biological activity of ruthenium complexes has been of interest since the 1950's, when a range of tris (polypyridyl) complexes were found to have bacteriostatic and anti – viral activities.[36] More recently, two ruthenium(II) anticancer drugs (NAMI-A and KP1019) have reached clinical trials.[37,38] Several complexes were also shown to induce mitochondria mediated apoptosis in human cancer cells and interestingly display a lower toxicity than many traditional cisplatin based cancer treatments.[7]

These probes have also been utilised in protein hydrodynamics, where $[Ru(bpy)_2L]^{2+}$ and $[Ru(dpp)_2L]^{2+}$ based probes to explore the binding of an antibody to ruthenium-labelled HSA and their conjugation to immunoglobulins, ferritin, concavilin A, and plasmid DNA.[39-41] Very recently a ruthenium complex conjugated to estradiol was shown to be cell permeable, attributed to the lipophilicity of the steroid pendant.[42] Ruthenium(II) complexes have been used surprisingly little in biophotonics, given their optical and photophysical properties. In the past five years, ruthenium complexes have been utilised in conjunction with confocal microscopy to explore their cellular activity across a range of cell lines and environmental conditions.

Svensson[43] recently reported the ability of ruthenium polypyridyl complexes to transport across the cell membrane of Chinese Hamster Ovary (CHO) cells. The synthesis of a series of $[Ru(phen)_2(dppz)]^{2+}$ derivatives was described, where the alkyl chain length was altered to vary the compounds lipophilicity. Shown in figure 1.36 is the generic structure of the $[Ru(phen)_2(dppz)]^{2+}$ derivatives and associated chain lengths of the three complexes prepared.

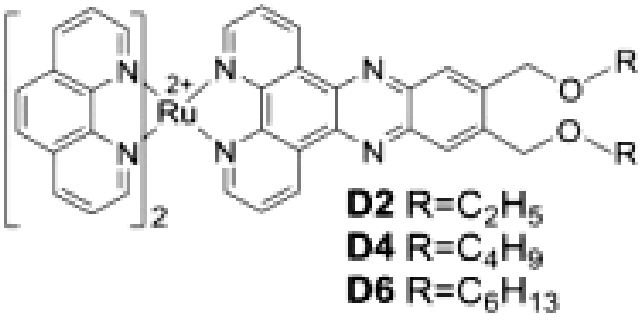

Figure 1.36: Range of $[Ru(phen)_2(dppz)]^{2+}$ complexes with varying lipophilicity altered by the alkyl chain length.[43]

The cellular uptake of the series of $[Ru(phen)_2(dppz)]^{2+}$ complexes in CHO-K1 cells was studied using confocal microscopy. Shown in figure 1.36 is the time dependent uptake and distribution of $[Ru(phen)_2(dppz)]^{2+}$ (D4) in CHO cells. Immediately after addition, D4 stains the cell membrane and remains in the plasma membrane. After 7 minutes, internalization of the dye was found to increase dramatically, accumulating in internal membranes. The time dependent nature of the dye uptake is consistent with endocytosis.[44]

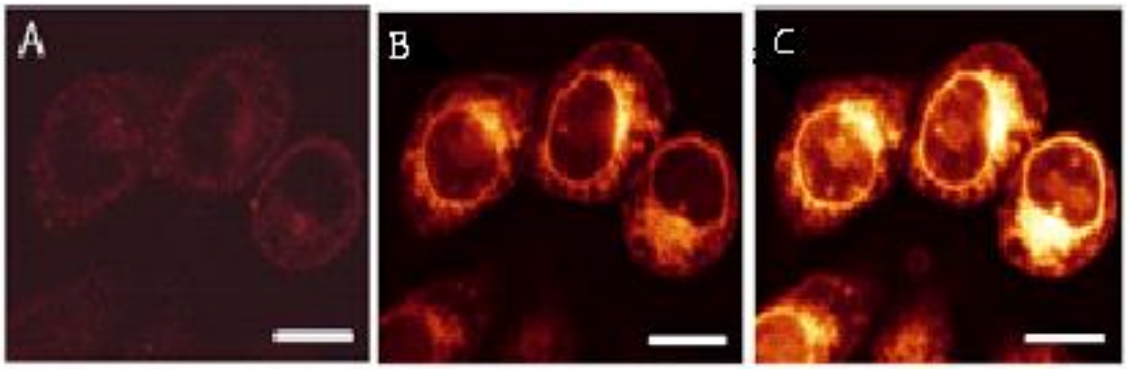

Figure 1.37: Luminescent confocal images (λ_{ex} = 488 nm) showing the time dependent uptake and cellular distribution of $[Ru(phen)_2(dppz)]^{2+}$ (D4) (10μM) in CHO – K1 cells after 3 minutes (A), 5 minutes (B) and 7 minutes (C). Scale bars are 10 μm.[43]

Shown in figure 1.37 is the distribution of the assorted dyes throughout the cell structure using confocal fluorescence microscopy. Ruthenium dipyridophenazine (dppz) complexes were found to localize in the endoplasmic reticulum or nucleus of fixed CHO cells. Slight modifications of the dppz ligand's

lipophilicity led to great variations in membrane binding. The least lipophilic complex (D2), was found predominantly in the nucleus, while complexes of increasing lipophilicity were found to be more homogenously distributed in the cells with comparable emission intensities inside the nucleus and in the cytoplasm.[43]

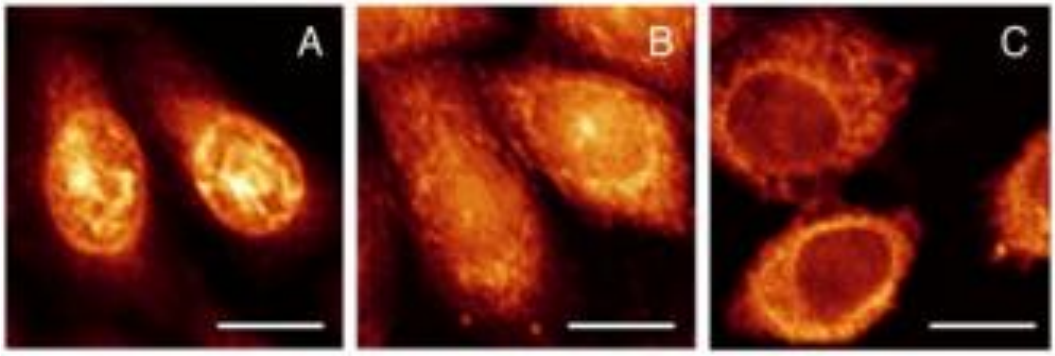

Figure 1.35: Luminescent confocal images (λ_{ex} = 488 nm) showing the cellular distribution of $[Ru(phen)_2(dppz)]^{2+}$ complexes in fixed CHO-K1 cells after 10 minutes. D2 (A), D4 (B), D6 (C) (10 μM) were added to cells fixed in methanol (−20 °C) for 15 minutes. Scale bars are 10 μm.[43]

Each dye was dissolved in media and DMSO (1% v/v), which is commonly used when imaging various metal complexes to aid solubility issues.[45] It is reported that uptake of the ruthenium complexes may occur through endocytosis or passive diffusion which would be expected for the more lipophilic complexes.[19, 49] The use of DMSO and the fixing of the CHO cells using ethanol bring into question the permeability of the cells and hence whether or not the complexes are genuinely cell permeable.

1.3.2 Ruthenium conjugated polypeptides in cellular imaging

As described in section 1.2.1, Neugebauer et al.[12] were the first to conjugate a ruthenium coordinated complex to a cell penetrating polypeptide, for the purpose of exploiting the complex in live cell imaging. Shown in Figure 1.36 are the structures of two novel ruthenium(II) polypeptides which were synthesized.

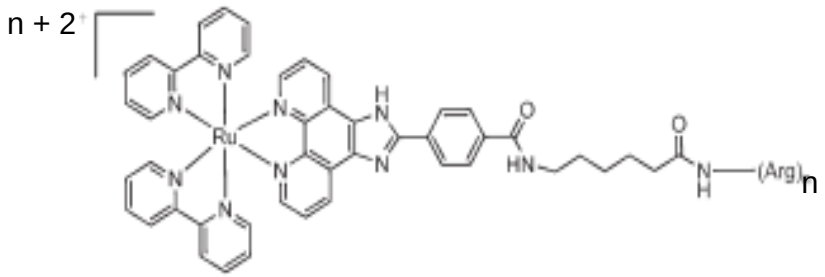

Figure 1.36: Structure of $[Ru(bpy)_2(picCOOH)Arg_n]^{2+n}$ (n is 5 or 8). In the parent complex, $[Ru(bpy)_2(picH_2)]^{2+}$, the aryl amide pendant on the imidazole ring was replaced by an aryl acid.

A key aim of this work was to assess whether the peptide conjugated ruthenium probe could passively transport across a cell membrane. The octaarginine dye conjugate $[Ru(bpy)_2(picCOOH)Arg_8]^{10+}$ was found to transport across the membrane of SP2 myeloma cells without the need to use organic solvents. To confirm that uptake into the cell was facilitated by the polypeptide, the parent complex, $[Ru(bpy)_2(picCOOH)]^{2+}$ was investigated and no luminescence was observed from within the cells, even after extensive incubation.

Interestingly, the short chain length $[Ru(bpy)_2(picCOOH)Arg_5]^{7+}$ also showed no evidence of distribution across the cell membrane, which indicates that polypeptide chain length has a huge bearing on its membrane permeabilisation abilities. Diffusion of the parent complex was achieved however, by introducing the detergent Triton, DMSO or ethanol which would permeabilise the cell.

SP2 cells in a buffered solution were exposed to $[Ru(bpy)_2(picCOOH)Arg_8]^{10+}$ with a final concentration of 3.5 x 10^{-5} M. Shown in figure 1.37 are luminescence images of SP2 cells which highlight the uptake capabilities of probe. In the absence of permeabilisation, the octaarginine dye – peptide was found to accumulates and preconcentrate inside the cell, with uptake confirmed to be irreversible and temperature dependent (Fig. 1.37(a) & (b)). The dye initially concentrates in the cell membrane, before distributing into the cell. Distribution of the dye inside the cell was not homogenous, resulting in brighter and darker areas, presumably due to different organelles.

After between 10 and 15 minutes the process was complete and no further changes were observed. In contrast, the parent complex was found to concentrate only on the cell membrane (Fig. 1.37(c)), before permeablisation of the cell membrane on exposure to Triton, allowed the dye to transport into the cell (Fig. 1.37(d)).

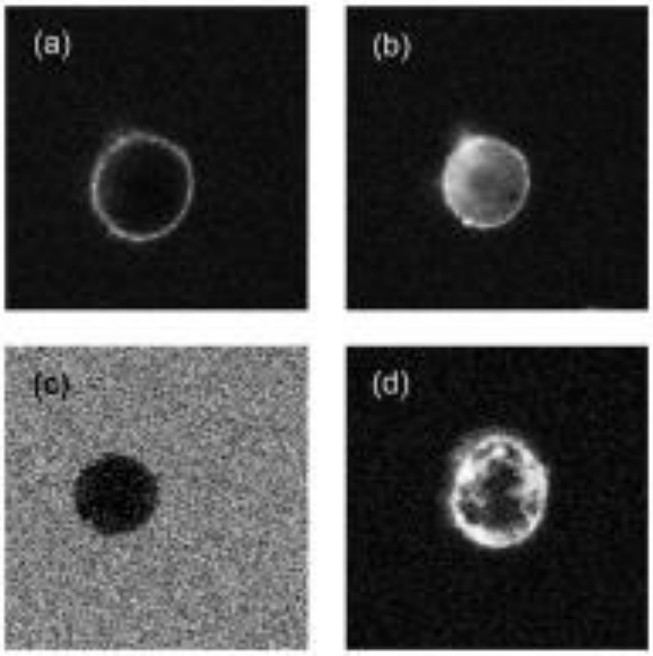

Figure 1.37: Luminescence images (λ_{ex} = 458 nm, λ_{em} = 610 nm) of SP2 myeloma cell incubated with $[Ru(bpy)_2(picCOOH)Arg_8]^{10+}$ (3.5 x 10^{-5} M) after (a) 3 minutes and (b) five minutes. (c) Myeloma cell incubated with the parent complex $[Ru(bpy)_2(picCOOH)]^{2+}$ (3.5 x 10^{-5} M) for 26 minutes and (d) for 5 minutes upon permeablizing the cell with Triton (1% v/v)

To assess the distribution of the dye in cellular organelles, myeloma cells were counterstained with commercial cell permeable dyes which exhibit specific staining. 3,3'-dihexyloxacarbocyanine iodide ($DiOC_6(3)$) selectively stains mitochondria at low concentrations and other structures in the cell, including the lysozomes and endoplasmatic reticulum at higher concentrations.[50] Shown in figure 1.38 are luminescence images of SP2 myeloma cells stained with $[Ru(bpy)_2(picCOOH)Arg_8]^{10+}$ and counter stained with $DiOC_6(3)$. From both figures, it is shown there is no overlap between $[Ru(bpy)_2(picCOOH)Arg_8]^{10+}$ and $DiOC_6(3)$ it can be concluded that $[Ru(bpy)_2(picCOOH)Arg_8]^{10+}$ does not localize in the mitochondria, lysozomes or endoplasmic reticulum of myeloma cells.[25]

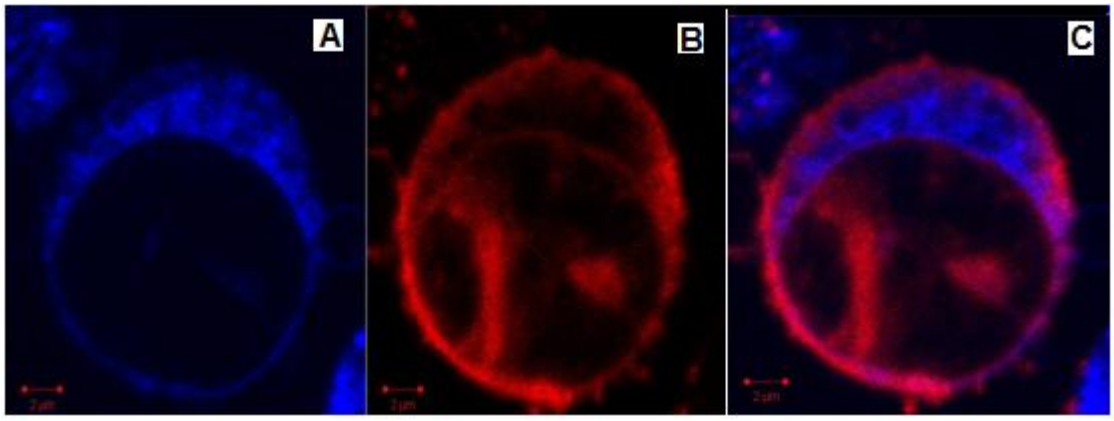

Figure 1.38: Luminescence images (λ_{ex} = 458 nm, λ_{em} = 515nm(a), 615 nm(b)) of SP2 cells incubated with $[Ru(bpy)_2(picCOOH)Arg_8]^{10+}$ (3.5×10^{-5} M) (b) and $DiOC_6(3)$ (5 μM) (a) in PBS (pH 7.4). Overlay (c).

To ensure that $[Ru(bpy)_2(picCOOH)Arg_8]^{10+}$ was capable of penetrating live cells without leading to their destruction, it was necessary to perform cell viability assays. Sytox green is a probe which only penetrates cells with compromised plasma membrane and was used to assess if the ruthenium stained cells were still viable. Shown in figure 1.39 are SP2 cells stained with the ruthenium peptide dye and in which the external buffer contains 0.5 μg/mL of Sytox green. Both dyes were excited with 458nm laser irradiation. The Sytox green fluorescence was collected with a band pass filter from 490nm – 515nm, while $[Ru(bpy)_2(picCOOH)Arg_8]^{10+}$ was collected through a 615 nm longpass filter.

The results indicate that Sytox green does not enter SP2 cells stained with $[Ru(bpy)_2(picCOOH)Arg_8]^{10+}$ labelled indicating that at least over the time-scale of these experiments (several hours) the ruthenium labelled cells remain viable. Importantly, these results demonstrate the ability of a peptide conjugated ruthenium probe to passively transport across the cell membrane of live myeloma cells and distribute throughout the cell's cytoplasm without causing cell apoptosis.

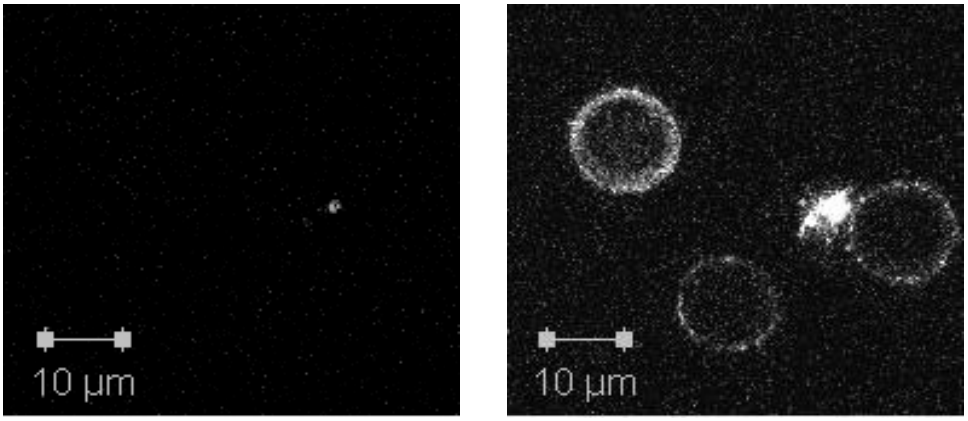

Figure 1.39: Luminescence images (λ_{ex} = 458 nm, λ_{em} = 505(A), 615 nm(B)) of SP2 cells incubated with $[Ru(bpy)_2(picCOOH)Arg_8]^{10+}$ (3.5×10^{-5} M) in which the external buffer contains 0.5 µg/mL of Sytox green.

A key advantage of ruthenium polypyridyl complexes when compared to traditional fluorescent imaging dyes is their long lived excited states, making them far more sensitive to their environment. The long lived fluorescent lifetime of $[Ru(bpy)_2(picCOOH)Arg_8]^{10+}$ is of particular interest, as it allows for discrimination from the shorter-lived background fluorescence present in many biological samples. Another advantage of the large Stokes shift of the dye is that it reduces the likelihood of self – quenching. FLIM imaging, where the contrast of the image is generated from variations in the measured emission lifetimes, is independent of concentration, light scattering, light path length and laser excitation power. As its emission is also removed from regions of the spectrum where autofluorescence of biological samples can occur, this allows for the use of fluorescent light imaging (FLIM). A long lifetime that is distinguishable from cellular autofluorescence is important for FLIM imaging.[51]

Shown in Figure 1.40 (a) is the fluorescence intensity map of a myeloma cell incubated for 12 minutes with $[Ru(bpy)_2(picCOOH)Arg_8]^{10+}$ and (b) a false colour lifetime image of the same cell. From Fig. 1.40 (a) is it determined that the dye residing in the outer membrane displays the shortest lifetime. This is expected as the higher solubility of O_2 in the membrane will result in greater quenching of the ruthenium probe.[52] The complex could potentially have applications as a luminescence O_2 mapping agent.

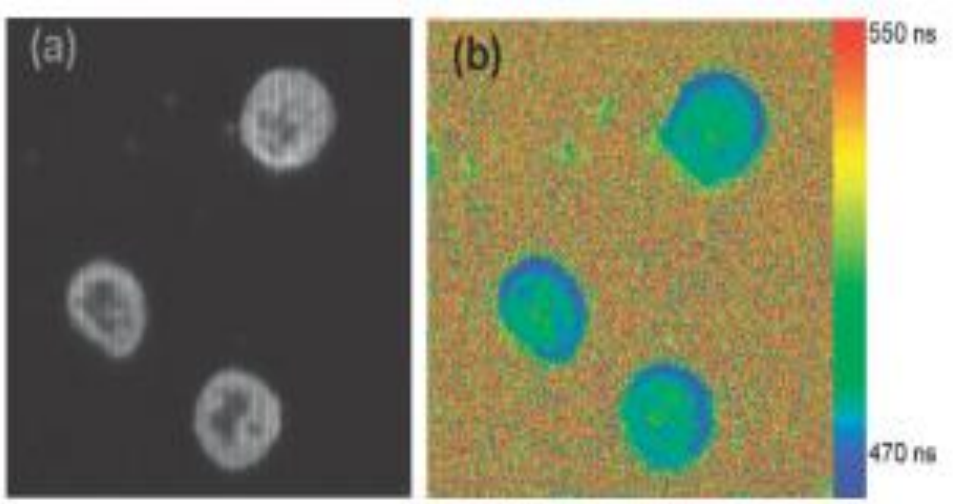

Figure 1.40: (a) Fluorescence intensity image and (b) false colour FLIM image of $[Ru(bpy)_2(picCOOH)Arg_8]^{10+}$ (3.5×10^{-5} M in aqueous PBS buffer) upon incubation in an SP2 myeloma cell for 15 minutes

As the $[Ru(bpy)_2(picCOOH)Arg_8]^{10+}$ probe was found to be pH and oxygen dependent, it was possible to exploit this sensitivity to measure both parameters in a single environment.[25] From FLIM images shown in Figure 1.41, it was possible to calculate the oxygen concentration within the cell, based on the luminescent lifetimes obtained. Once pH was defined from resonance Raman spectroscopy, the same ruthenium complex can be used to probe the O_2 concentration using FLIM. Luminescence intensity is not a reliable measure of oxygen concentration without an internal reference as it depends on the concentration of the dye, which varies throughout the cell. However, the luminescence lifetime reflects oxygen concentration and is not affected by local concentrations of dye.

Three regions of distinct luminescence lifetime inside the cell were identified from these images by comparison with Raman and confocal luminescence images. These were identified as the cellular membrane, the cytoplasm and the nucleus. A lifetime of 513 (± 21) ns was obtained for the background medium, 453 (± 25) ns for the outer cellular layer, 540 (± 12) ns for the cytoplasm, and 620 (± 8) ns for the nucleus. A key advantage of these dyes is their long lived excited state, in relation to many conventional imaging dyes.

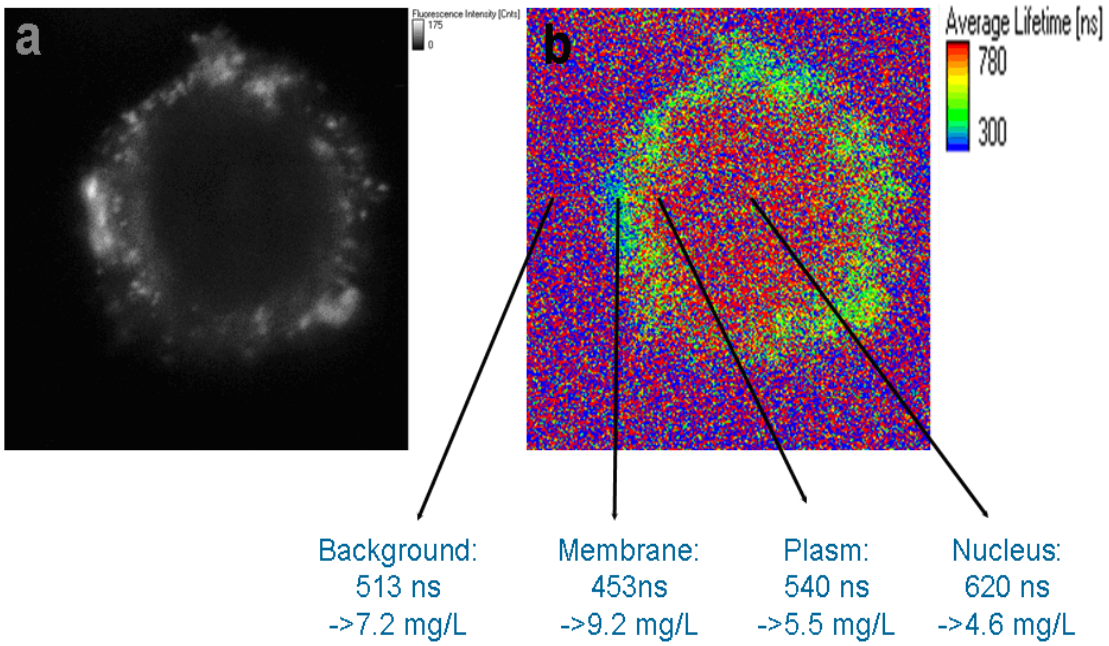

Figure 1.41: (a) Fluorescent intensity map of an SP2 myeloma cell incubated for 12 minutes with $[Ru(bpy)_2(picCOOH)Arg_8]^{10+}$ in PBS and (b) a false colour lifetime image of the same cell.[25]

Raman spectroscopy is a fundamentally weak phenomenon, as only 1 in 10^6 photons are inelastically scattered. However if the excitation laser coincides with an intense optical transition of the molecule, the signal may be significantly enhanced. Ruthenium polypyridyl complexes exhibit up to 200 nm separation between their absorbance and emission maxima which allows the collection of intense interference free resonance Raman spectra at a wavelength that also excites emission.[53]

While the electronic spectroscopy in the visible region for $[Ru(bpy)_2(picCOOH)Arg_8]^{10+}$ exhibits relatively weak pH dependence, the resonance Raman spectra show significant sensitivity to pH. Shown in Figure 1.42 is the Resonance Raman spectra of $[Ru(bpy)_2(picCOOH)Arg_8]^{10+}$ at a range of pH intervals following irradiation at 458 nm. As shown in the figure below, the ratio of the height/area of the pH dependent [Pic-COOH] ligand modes (at 1608 and 1550 cm^{-1}) and the height/area of the pH independent bipyridyl ligand modes (at 1488 and 1317 cm^{-1}) can be used to produce a pH plot. The bipyridyl ligand modes were found to be well resolved and were found, in terms of both intensity and wavelength to be unaffected by pH over the range explored. These modes were therefore selected as internal reference bands.

Resonance Raman signals were collected and mapped from SP2 myeloma cells containing $[Ru(bpy)_2(picCOOH)Arg_8]^{10+}$ in PBS buffer, as described in section 1.3.3. From the pH dependent Raman calibration curve, the cellular membrane was found to have a pH of 6.7, while the nucleus and cytoplasm had values of pH 6.8 and pH 7.2 respectively. The results obtained from this technique are in agreement with values previously reported by Machen et al.[54]

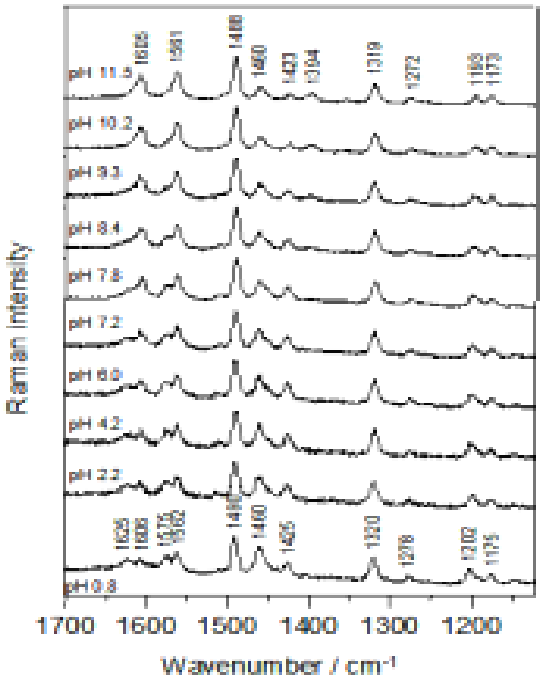

Figure 1.42: Resonance Raman spectra of $[Ru(bpy)_2(picCOOH)Arg_8]^{10+}$ collected at a range of pH values

Puckett[55] has also published results recently detailing the ability of a peptide conjugated ruthenium probe to passively permeate HeLa cells after incubation for 30 minutes at 37°C. Similarly to results published by Neugebauer[12] the parent complex $[Ru(phen)(bpy)(dppz)]^{2+}$ showed no evidence of crossing the cell membrane. However, once conjugated to octaarginine the dye was found to distribute throughout the cell after 30 minutes. At higher concentrations, the localization of the ruthenium-Arg_8-fluoroscein changes significantly. At concentrations up to 10 μM, the complex is restricted to punctate structures in the cytoplasm, whereas, at 15–20 μM the population of the cells was found to be heterogeneous. The punctate distribution implicates endocytosis,[56] which as previously discussed is a proposed internalization mechanism for polypeptides. As shown in figure 1.43, these results show the uptake of a ruthenium-Arg_8-fluoroscein probe being far more efficient than that of a ruthenium-Arg_8 probe alone. It is believed that the greater lipophilicity of the fluorescein moiety compared to the ruthenium increases the interactions with the cell membrane, which in turn may give rise to additional uptake methods for the fluoroscein probe.

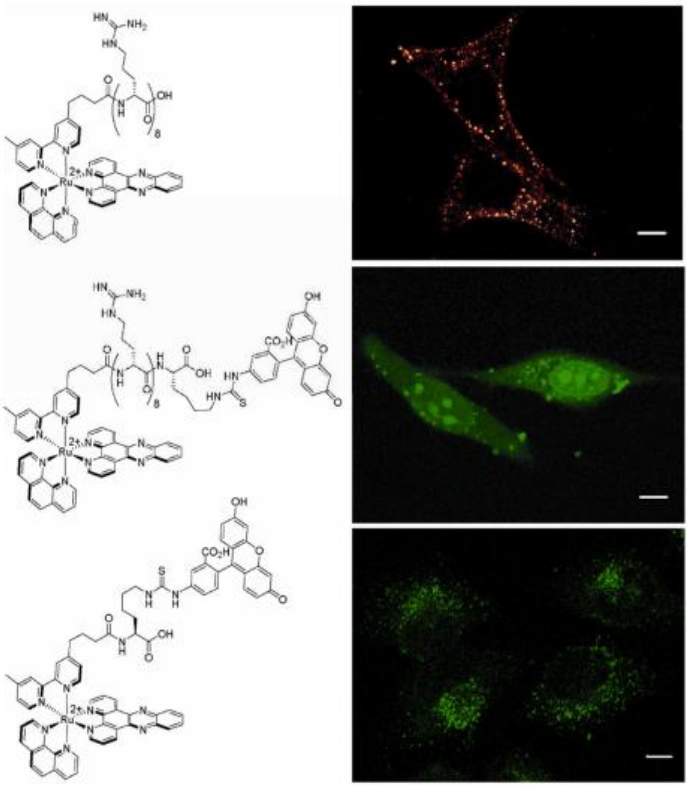

Figure 1.43: structures and corresponding luminescence images of complexes synthesised by Puckett et al. in HeLa cells at 37°C

1.3.3 Ruthenium conjugated polypeptides in Raman Mapping

Label free Raman mapping of cells has the ability to provide detailed concentrations of key biochemicals within the cell and as such has been the focus of a number of studies.[13] The low sensitivity of conventional Raman requires long acquisition times, leading to potentially damaging dwell times of the laser on a single spot.[57] Unlike luminescence, Raman is not influenced by oxygen concentration or other environmental parameters unless they directly affect a compound's structure (e.g. protonation). Through the introduction of an external label into the cell, excited under resonance absorption conditions, the dye's distribution and, unique to Raman, its structure, can be probed with excellent sensitivity. It is possible to develop a single label dye which can be used for both luminescence and resonance Raman imaging of cells. As discussed in this chapter, fluorescent organic dyes are not suitable for this purpose since their small Stokes shift means fluorescence overwhelms the weaker Raman response. The enhanced vibrations are restricted to those involving the chromophores participating in the optical transition so tend to lead to simplified Raman spectra.[58]

A key advantage of ruthenium polypyridyl complexes with regards to Raman spectroscopy is their capacity to make their photo-physical properties dependent on their environment. For example, a single ruthenium dye can be used to probe both pH and oxygen concentration in a single environment. If the pH of a complex is defined from resonance Raman spectroscopy, luminescence lifetime imaging of the same ruthenium complex can be used to probe the O_2 concentration.[58]

Raman mapping is a technique which generates detailed images based on a compound's Raman spectrum. A complete spectrum is acquired at multiple designated pixels of an image and these spectra are then interrogated to generate false colour images. A resonance Raman image is generated by analysing the intensity of individual or multiple bands in a spectrum. The plot intensity represents the intensity of these vibrational modes and therefore the relative dye concentration around the cell.[13]

A typical experiment uses sequential sample movement and spectrum acquisition, with acquisition time for one spectrum a crucial value, as it influences the acquisition time of the image which can consist of thousands of Raman spectra. From an image, it is possible to determine a compound's concentration and distribution, which is not possible with standard microscopy.[59, 60]

In a recent study, Cosgrave[13] investigated the use of a peptide conjugated ruthenium probe for the purposes of multimodal cellular imaging. Shown in Figure 1.43 is the structure the novel environmentally sensitive $[Ru(dppz)_2(pic)Arg_8]^{10+}$. The dppz ligands confer 'molecular light switch' properties on the ruthenium complex due to hydrogen bonding to the phenazine nitrogens, which leads to emission quenching in aqueous environments. Upon increasing addition of water aliquots to $[Ru(dppz)_2(pic)Arg_8]^{10+}$ in acetonitrile, the emission steadily decreased and was completely extinct at 18% v/v water.

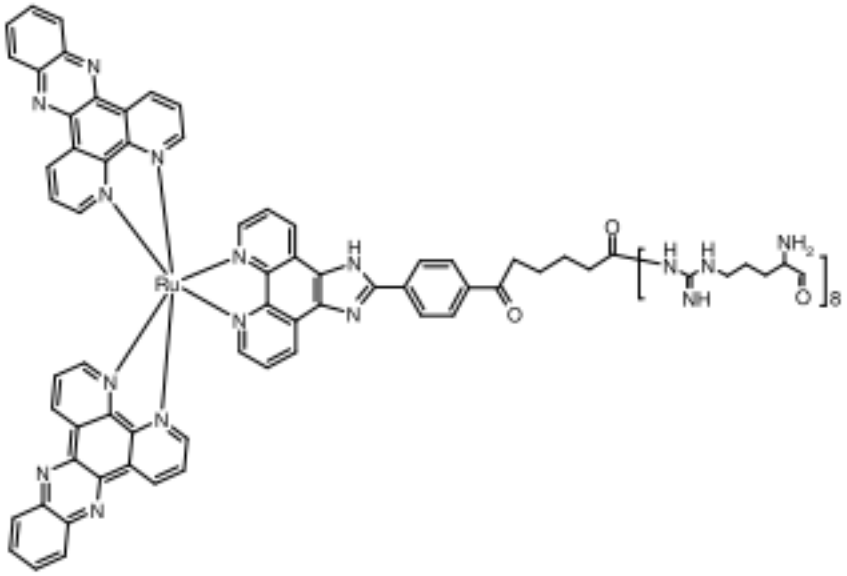

Figure 1.43: Structure of $[Ru(dppz)_2(pic)Arg_8]^{10+}$.[13]

Shown in Figure 1.44 is Raman intensity plot of an SP2 myeloma cell constructed from the intensity of ruthenium(II) vibrational modes and hence the relative dye concentration within the cell. Fig. 1.44(a) and (b) show white light images of the myeloma cells investigated, while Fig. 1.44(c) shows that the dye is clearly distributed throughout the cell but that the parent dye remains in the outer cell membrane as shown in Fig. 1.44(d). The concentration of $[Ru(dppz)_2(pic)Arg_8]^{10+}$ is highest close to the centre of the cell in the cytoplasm.

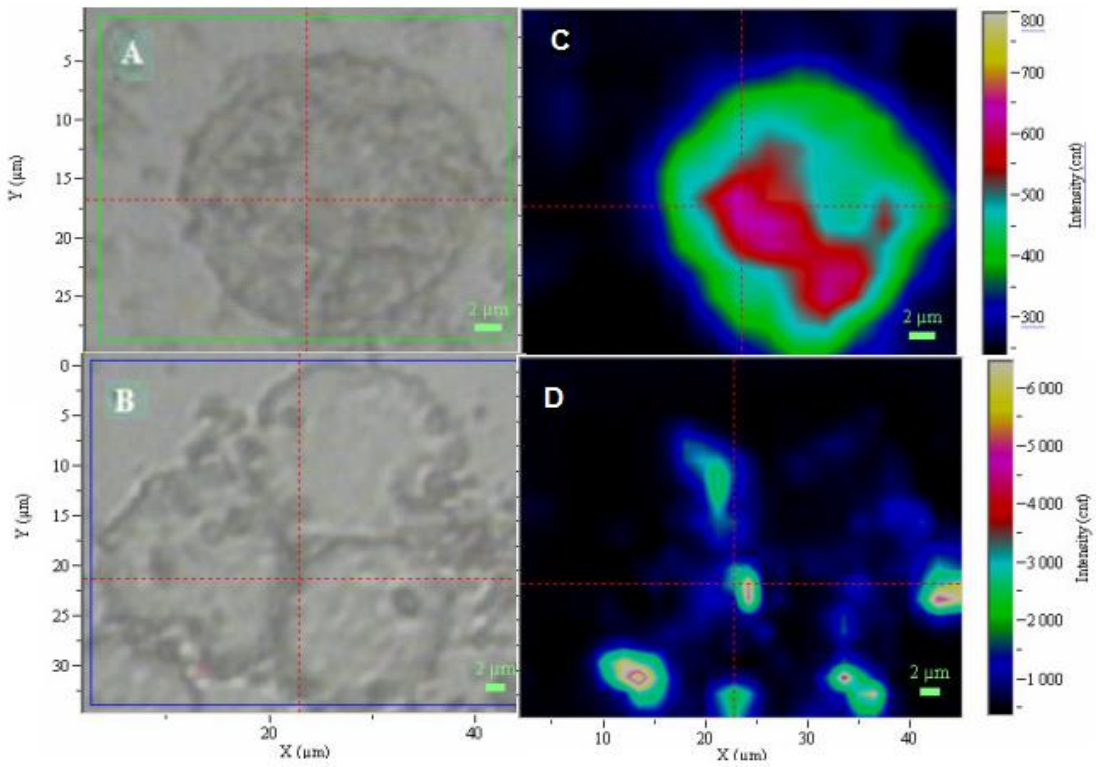

Figure 1.44: Resonance Raman intensity map of live SP2 myeloma cells after incubation with $[Ru(dppz)_2(pic)Arg_8]^{10+}$ (c) and the unconjugated parent dye (d) after excitation at 458 nm. (a) and (b) represent white light images of the cells in PBS.[13]

1.3.4 Mechanism of cellular uptake of ruthenium dyes

As mentioned in section 1.2, while endocytosis is widely believed to be the most likely mechanism of cellular uptake of cell penetrating peptides and also other metal complexes, there is still much debate around the topic.

Puckett and Barton[19] have previously examined the mechanism of cellular entry for a ruthenium(II) polypyridyl complex in HeLa cells. Using flow cytometry, the extent of uptake of $Ru(DIP)_2dppz^{2+}$ (where DIP = 4,7-diphenyl-1,10-phenanthroline) was determined. Transport of the dye across the cell membrane was first assessed using confocal microscopy. As shown in Figure 1.45, the ruthenium complex was found to accumulate inside the cell rather than associating solely at the membrane surface.

To determine whether the uptake mechanism was energy dependent, the complex was incubated with HeLa cells after ATP depletion by deoxyglucose (a glucose analog that inhibits glycolysis) and oligomycin (an inhibitor of oxidative phosphorylation).[61, 62] Fluorescently labelled transferrin was used as a positive control as it is known to be internalized by clathrin-mediated endocytosis. HeLa cells were pretreated for one hour with deoxyglucose (50 mM) and oligomycin (5 μM), then rinsed and incubated with $Ru(DIP)_2dppz^{2+}$ (5 μM) or transferrin-AlexaFluor488 for one hour.

Shown in Figure 1.46 are flow cytometry confocal microscopy images measuring the effect of metabolic inhibition on the uptake of $Ru(DIP)_2dppz^{2+}$ in HeLa cells. The mean luminescence was determined to be 659 ± 12 compared to 675 ± 10 for the cells not treated with deoxyglucose and oligomycin. This suggests the ruthenium complex is entering the cells via an energy independent pathway. The endocytosis of transferrin was found to display a significant fluorescence decrease under metabolic inhibition. The mean fluorescence was shown to decrease from 3034 ± 52 to 210 ± 5, which is in contrast to the results for $Ru(DIP)_2dppz^{2+}$. While transferrin is known to cross the cell membrane through endocytotic pathways, the large difference in the mean fluorescence decrease between complexes suggests differing uptake mechanisms.

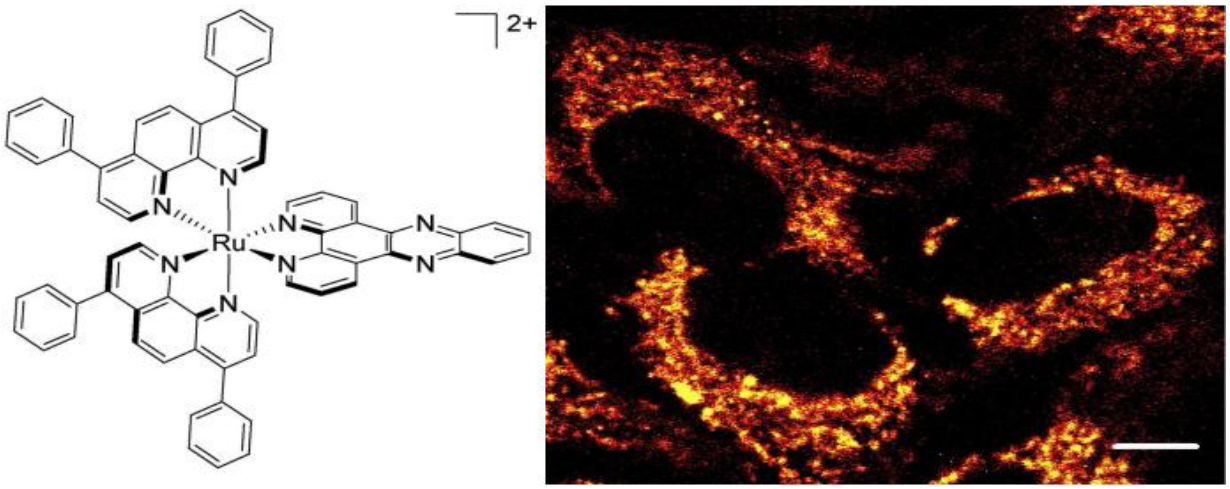

Figure 1.45: Chemical structure of $Ru(DIP)_2dppz^{2+}$; Luminescence confocal image of HeLa cells incubated with $Ru(DIP)_2dppz^{2+}$ (5 μM) for four hours.[19]

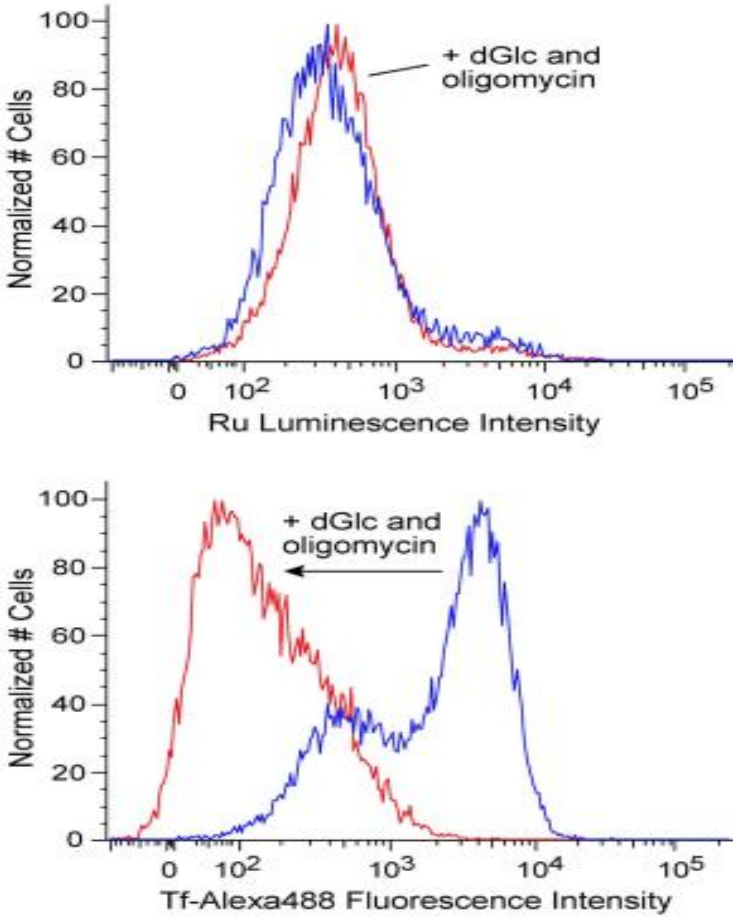

Figure 1.46: Flow cytometry measuring the effect of metabolic inhibition on uptake of $Ru(DIP)_2dppz^{2+}$ in HeLa cells. Cells treated with inhibitors (red) are compared to control cells (blue). Top: $Ru(DIP)_2dppz^{2+}$ uptake. Bottom: transferrin-AlexaFluor488 uptake.[19]

As shown in Figure 1.37, Svensson[43] recently reported the ability of a series of ruthenium polypyridyl complexes to transport across the cell membrane of CHO cells. Uptake of the dyes was found to increase dramatically with time with distribution in internal membranes complete after seven minutes. The time dependent nature of this internalization suggests that the Ru(II) complexes cross the cell membrane via endocytosis.[44]

However, an aspect of both the research of Svensson,[43] Barton[19] and many other reported studies on coordination compounds that must be considered is their use of DMSO (1%) to aid the solubility of metal complexes.

As discussed in section 1.3.2, Neugebauer et al.[12] synthesized a cell penetrating ruthenium polypeptide, with the parent complex showing no signs of entering the cell. This suggests that results obtained using DMSO are in fact studying permeabilized cells, meaning the dye is not penetrating a healthy cell membrane.[47, 48]

It is widely believed that endocytosis is the most likely mechanism of cellular uptake of arginine rich cell penetrating peptides as results have shown the process to be temperature and energy dependent which is indicative of endocytosis.[12, 22-24] This process involves the cell membrane wrapping itself around the extra-cellular peptide and engulfing it. The peptide is then brought into the cell via small vesicles. Fuchs et al.[24] have previously reported the internalisation of a fluorescein labelled polypeptide by entocytoic means. Internalization of complexes in myeloma cells has been reported to follow clathrin mediated endocytosis[63], while CHO cells internalize complexes predominantly through caveolin – mediated pathways, with clathrin inhibition showing no effects on uptake.[64]

Clathrin dependent endocytosis is a process by which cells internalize molecules through the inward budding of proteins coated with the cytosolic protein clathrin, which contains receptor sites specific to the molecules being internalized.[20] Caveolin form a unique endocytic and exocytic compartment at the surface of most cells and are capable of importing molecules and delivering

them to specific locations within the cell.[65] However, it has also been reported that obstruction of caveolin mediated pathways did not completely eliminate the uptake of fluorescently labelled alginate – chitosan complexes in CHO cells, evidence that other internalization pathway(s) are involved.[64]

As the process has been demonstrated to be temperature and energy dependent, endocytosis seems a likely uptake mechanism. However, no method or process has been conclusively proven or universally accepted.

1.4 Ruthenium complexes as intracellular sensors

1.4.1 Ruthenium(II) complexes as pH and O_2 sesnors

There is currently considerable interest in luminescence imaging of essential biological parameters such as pH, pO_2, hydrogen peroxide and calcium.[66-71] Intracellular pH is of particular importance for the activity of enzymes, synthesis of macromolecules (protein, DNA, RNA), the conductivity of ion channels and controlling the cell cycle.[72] The pH of cellular tissue could be used as a marker of disease in tumor cells which have been found to display abnormally acidic cytoplasmic pH.[73, 74] Fluorophores sensitive to pH undergo changes in emission intensity or spectral shift upon protonation. At appropriate wavelength the fluorescence intensity of such sensor is a function of the pH of the surrounding environment. Therefore, a probe capable of measuring intracellular pH could be invaluable in live cell imaging.

Acidotropic partition dyes are a range of fluorescent dyes whose presence in acid compartments can be detected from fluorescence alone. Acridine orange will enter acidic compartments such as lysozomes, becoming protonated and sequestered, and will emit orange light when excited by blue light. However, a limitation to the use of this probe in live cell imaging is the frequent occurrence of dye photoconvertion during image acquisition.[125] The structure of acridine orange is shown in figure 1.47.

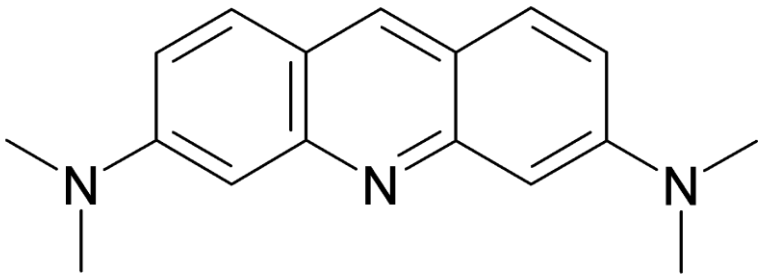

Figure 1.47: Structure of Acridine Orange

As described in section 1.3.2, Neugebauer et al.[25] have previously described the resonance Raman spectroscopy of $[Ru(bpy)_2(pic\text{-}arg_8)]^{10+}$ over a range of pH values. Using both a pH dependent and independent Raman features as internal references, the ratio of two modes was used to estimate the pH in different regions of an SP2 myeloma cell.

Shown in figure 1.48 is the peak ratio plot of the pH-sensitive pic-Raman-band at 1575 cm^{-1} and the pH-independent bpy-band at 1317 cm^{-1} versus pH. The solid line shows the fitted Henderson – Hasselbalch model which provided a pKa of 8.5 ± 0.2, which was in agreement with values obtained from UV/vis absorption spectroscopy. Using confocal scanning microscopy, the outer cellular membrane was found to have a pH of 6.7, while the nucleus and cytoplasm had values of pH 6.8 and pH 7.2 respectively. Typical values for the pH within the cytoplasm are between 7.0 and 7.4.[72] This technique may provide insights into intracellular activity, as the relative low value inside the nucleus suggests a low activity of DNA and RNA synthesis, as the optimal range is between 7.0 and 8.0.[72]

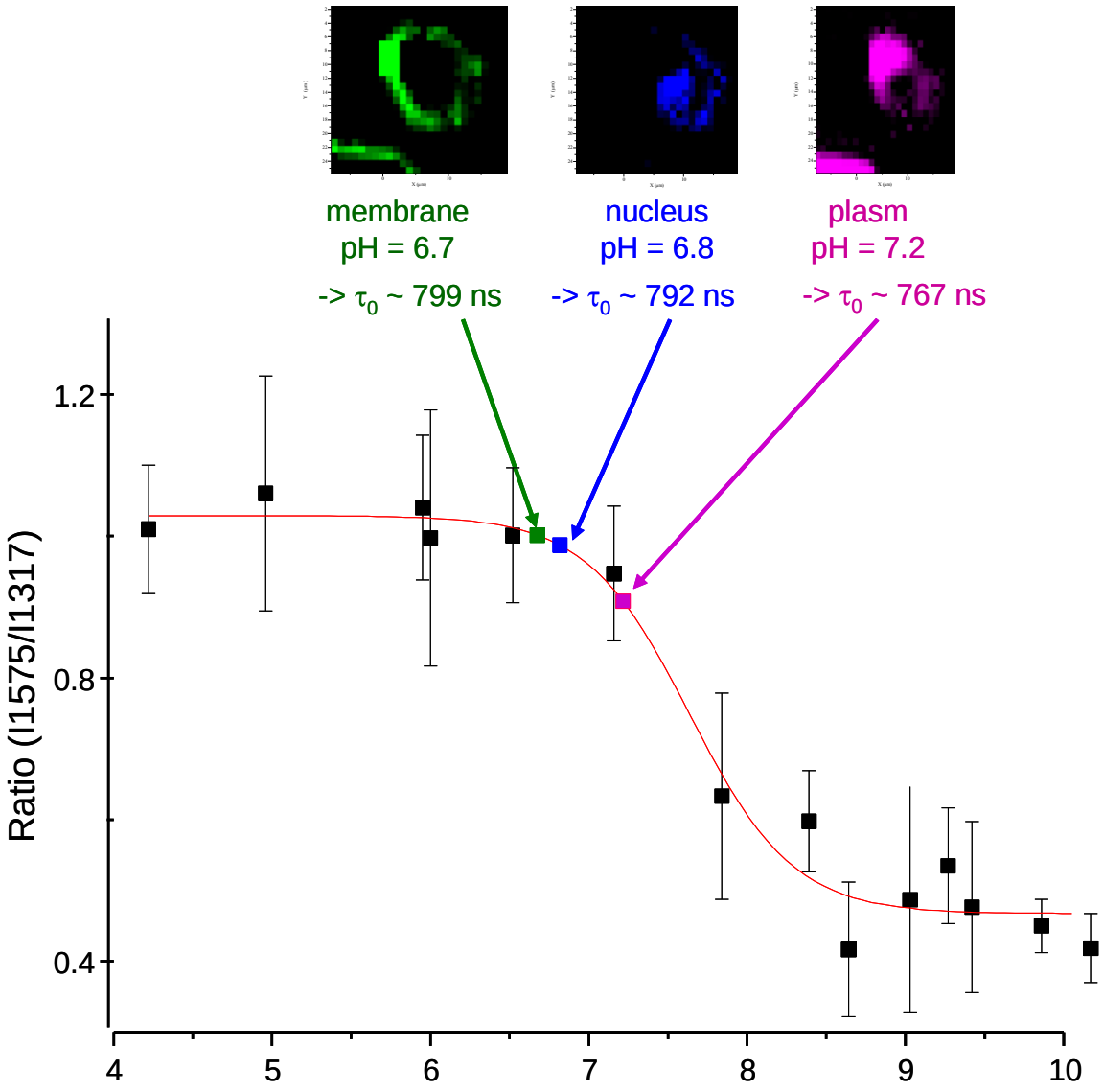

Figure 1.48: Plot of the change of the relative intensities of two Raman bands from $[Ru(bpy)_2(pic\text{-}arg_8)]^{2+}$ centered at 1575 cm^{-1} and 1317 cm^{-1} with pH.[25]

A recent study has described the activity of an intracellular oxygen sensitive probe based on phosphorescent porphyrin dyes conjugated to cell-penetrating peptides.[75] Shown in figure 1.49 is the structure of one of the probes, comprised of uncharged derivatives of Pt(II)-coproporphyrin I covalently linked to positively charged TAT-derived peptides. Both the rate of consumption and concentration of cellular oxygen are linked to physiological processes such as oxidative phosphorylation, generation of ATP, production of reactive oxygen species (ROS), nitric oxide (NO), oxidative burst, and adaptive responses to

hypoxia.[76-79] As conjugation to the cell penetrating peptide allows for passive transport across the cell membrane, these probes provide a simple and versatile tool for O_2 monitoring in live cells and in tissue. Shown in Figure 1.49 is the phosphorescence lifetime of the probe in respiring and nonrespiring cells.

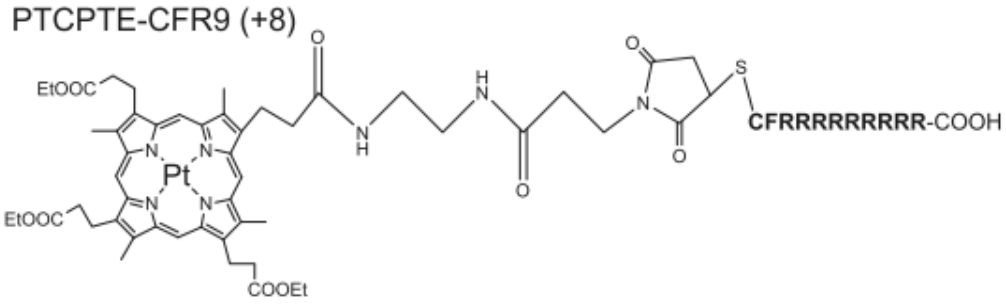

Figure 1.49 Chemical structure of phosphorescent porphyrin probe.[75]

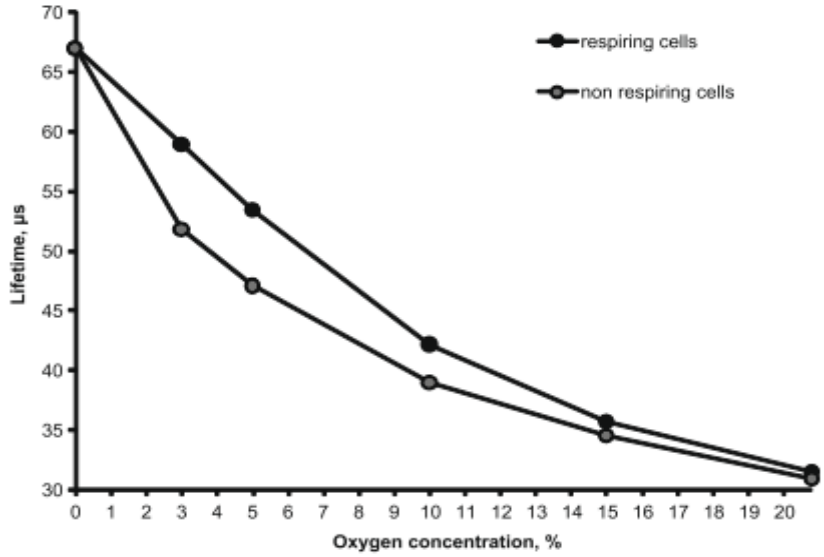

Figure 1.50: Phosphorescence lifetime at different O_2 concentrations for the resting dPC12 cells loaded with PtCPTE-CFR9 probe (10 μm) for 16 hours and for the same cells treated with antimycin A.[75]

1.4.2 BODIPY complexes as biological probes

Borondipyrromethenes (BODIPY) derivatives are a synthetically versatile class of fluorophore which have attracted much interest for their function as molecular probes,[80] light-harvesting molecular arrays[81] and photo – dynamic therapy via singlet oxygen generation.[82] They are known for their robust photophysical properties, such as strong absorption of visible light high fluorescence quantum yield and good photostability.[83] Several BODIPY derivatives have been commercialized for biological labelling.

Shao et al.[84] have recently described a dinitrobenzenesulfonyl (DNBS) BODIPY probe capable of specific detection of cysteine over other biological molecules, such as glutathione and amino acids. Cysteine was reported to cleave the DNBS moiety, which resulted in a 46 – fold emission enhancement. Shown in Figure 1.51 is the skeletal structure of BODIPY, which has several positions on the chromophore available for functionalisation. Functionalisation is commonly achieved through pyrrole substitution with a phenyl or alkyl group or attachment of functional groups such as ligands or biomolecules via the aryl group highlighted on position 8 below.[85]

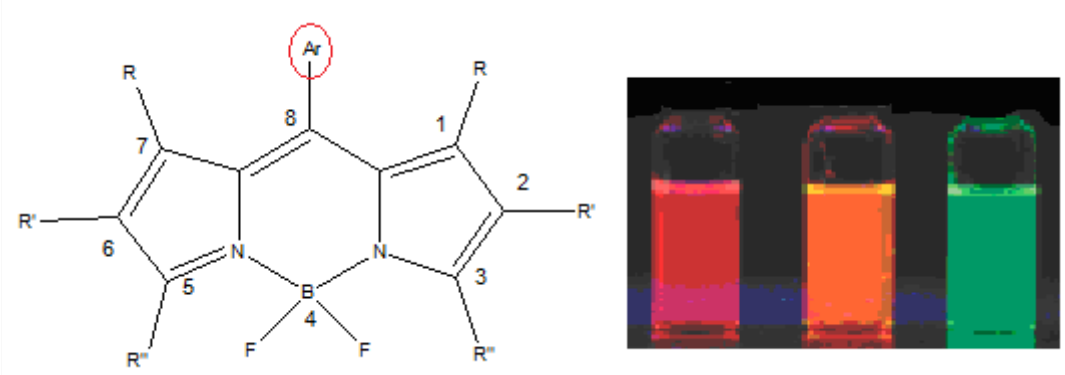

Figure 1.51: Skeletal structure of the BODIPY system showing 8 available positions for functionalisation (left); fluorescent photographs of BODIPY derivatives taken under UV light (hand-held UV lamp, 365 nm) in toluene at room temperature.[83]

An initial aim of this project was to produce a ruthenium – peptide conjugate with both an oxygen or pH sensitive and insensitive fluorophore as a self-referenced sensor for confocal microscopy. In a cellular environment, it may be difficult to identify whether certain probes have been converted to another species, as fluorescence intensity is a less reliable reporter than emission lifetime for sensing but is a much more commonly applied technique.

Ruthenium probes are useful in cell O_2 sensors due to their large long-lived emissive triplet state which is readily quenched quantitatively by molecular oxygen. Other properties which make them good probes are their Stokes shifts, good photostability and red emission wavelengths (away from possible autofluorescence of biological material).[12]

However, by combining with a pH or oxygen insensitive probe, the ratio of luminescence at two wavelengths (one sensitive, one insensitive to its environment) will be unaffected by the concentration of the dye and will therefore have potential application as an intracellular sensor in conventional microscopy.

Shown in figure 1.52 is a theoretical display of how such a sensor could be utilised to determine oxygen concentration based on emission intensity ratio.

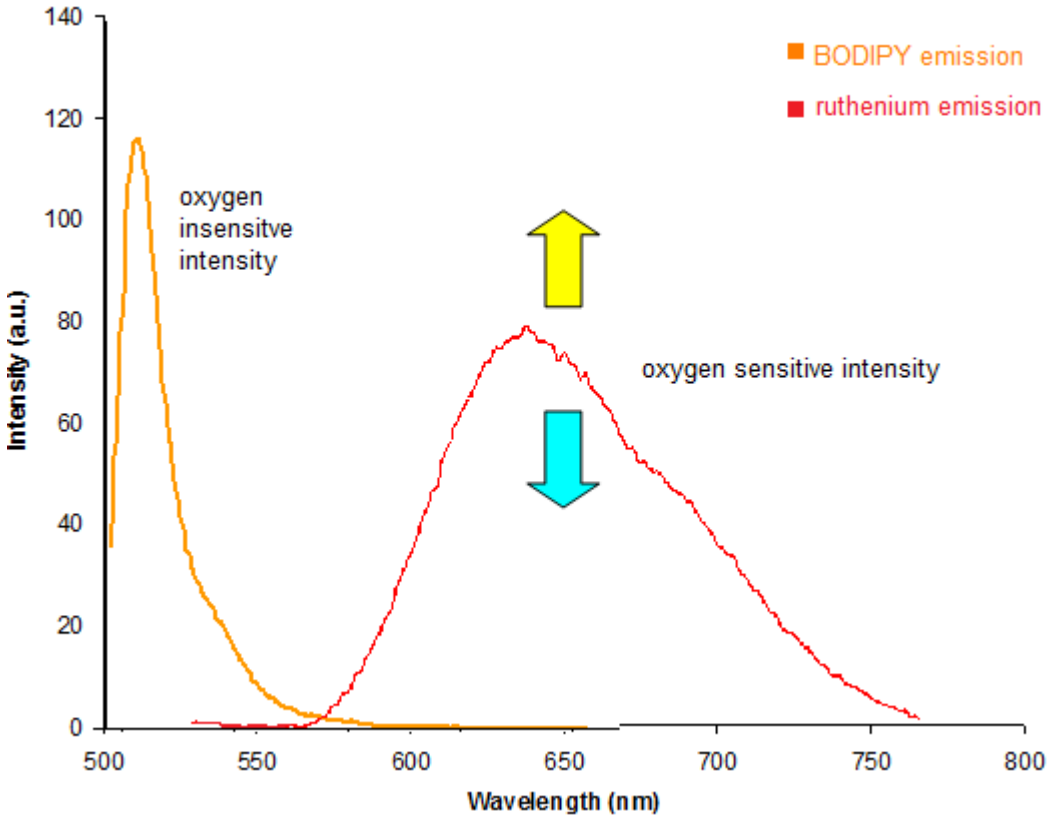

Figure 1.52: Theoretical emission spectrum of a BODIPY – conjugated ruthenium complex, showing an orange oxygen insensitive BODIPY peak at 515 nm and an oxygen sensitive ruthenium peak at 641 nm. Such a complex should be excited using a 458 nm laser. The graph was obtained by overlaying a spectra of a BODIPY-COOH (15 μM) complex with one of $[Ru(NO_2phen)_2(picNH_2)]^{2+}$ (20 μM), after both were excited using a 458 nm laser. The graph was subsequently normalised using MATLAB Spectrum Analyzer.

The target complex in this project was designed with the aim of attaching two cell penetrating peptides and one BODIPY reference probe to a single supramolecular unit. This approach had two major advantages: (I) the second CPP would lead to a greatly increased overall charge on the complex and (II) only a single reference was to be used as two highly luminescent BODIPY probes may dwarf the ruthenium emission. The ruthenium complex was designed to have on amino terminus in order to exploit this group for EDC/NHS coupling to a carboxyl functionalised BODIPY dye.

This reaction scheme is shown in Figure 1.53, where the EDC crosslinker activates the carboxyl group, which readily allows reaction with primary amines. The intermediate formed is susceptible to hydrolysis and is unstable in aqueous environments. The intermediate is stabilized by the addition of an NHS ester which forms a more stable amine – reactive ester which may be coupled with an amine.

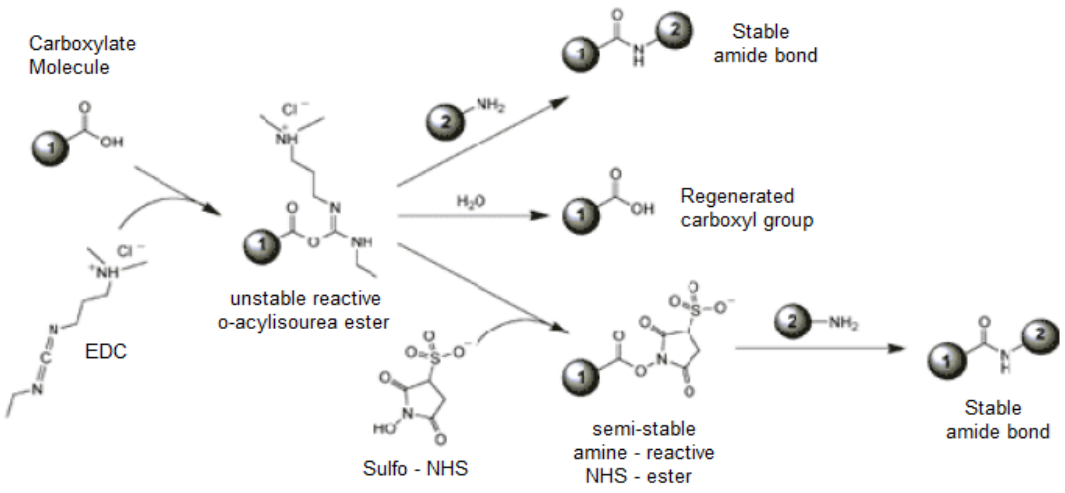

Figure 1.53: Schematic representation of the EDC/NHS coupling mechanism[86]

Shown in Figure 1.54 is the chemical structure of the ruthenium(II) complex designed for conjugation to a BODIPY dye and two cell penetrating peptides. The nitro containing phenanthroline ligands attached to the metal centre can be reduced, which provides for the possibility of conjugating a BODIPY group at the pic - NH_2 terminus; with two cell penetrating peptides then conjugated to the complex at the NO_2 groups after reduction. As described in section 4.2.1, the reduction of $[(Ru(NO_2phen)_2Cl)]^{2+}$ has a high yield (> 85%) and the nitro functionality can be readily reduced to NH_2 groups. The ruthenium complex may be conjugated to a cell penetrating peptide with a resin – bound peptide and spacer.

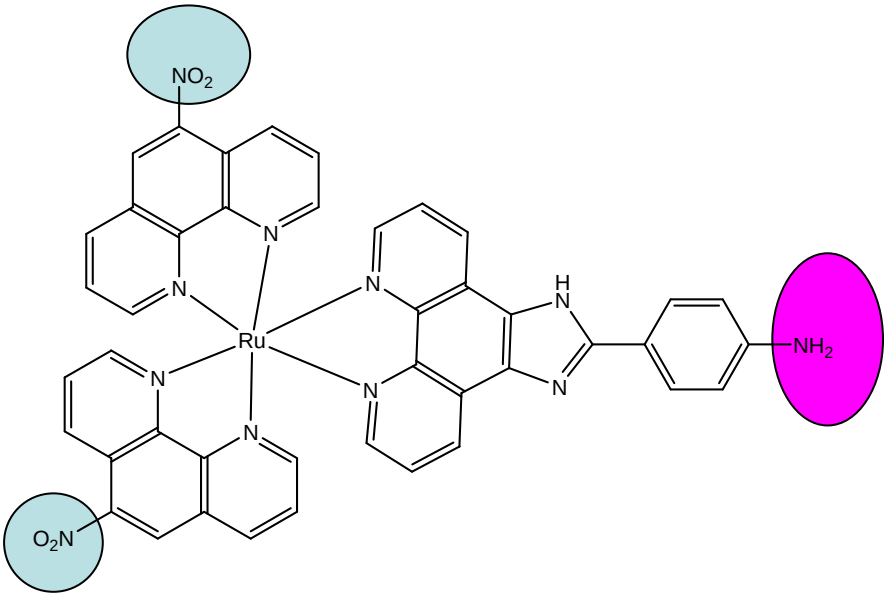

Figure 1.54: Structure of ruthenium(II) complex designed for conjugation to a BODIPY dye and two cell penetrating peptides. Highlighted in blue are the two sites intended to link cell penetrating peptides; highlighted in pink is the site designated for linking to a BODIPY dye

Chapter 2: Experimental

2.1 Experimental Methods and Instrumentation

- 2.1.1 Chemicals
- 2.1.2 Nuclear Magnetic Resonance Spectroscopy
- 2.1.3 Absorbance Spectroscopy
- 2.1.4 Fluorescence Spectroscopy
- 2.1.5 Calculating Quantum Yields
- 2.1.6 Lifetime Measurements
- 2.1.7 Chromatographic Techniques
- 2.1.8 Resonance Raman Spectroscopy

2.2 Cell Culture

- 2.2.1 Cell enumeration and viability assay
- 2.2.2 Sp2/0-Ag14 culture protocol
- 2.2.3 CHO-k1 culture protocol

2.3 Cellular Imaging

- 2.3.1 Confocal Fluorescence Microscopy
- 2.3.2 Resonance Raman Mapping

2.1 Experimental Methods and Instrumentation

2.1.1 Chemicals

All chemicals and reagents were purchased from Sigma Aldrich Ireland and used without any further purification steps. All reactions were performed in air unless otherwise stated.

2.1.2 Nuclear Magnetic Spectroscopy (NMR) Spectroscopy

^{1}H-NMR was performed on a Brucker AC 400 MHz using deuterated DMSO-d_6 or deuterated Methanol (MeOD) as solvent unless otherwise specified. Peak positions are relative to TMS (0 ppm chemical shift). All NMR spectra were processed and analysed using Topspin NMR software.

2.1.3 Absorption Spectroscopy

UV-Vis spectra were recorded on a Varian Cary 50 spectrophotometer. Samples were analysed in a quartz cuvette with a path length of 1 cm with a spectral range of 200 – 600 nm unless otherwise stated. The background was corrected for blank solvent absorbance prior to every measurement and was collected at room temperature.

2.1.4 Fluorescence Spectroscopy

Emission spectra were recorded on a Varian Cary Eclipse fluorescence spectrophotometer with an excitation slit width of 5 nm and an emission slit width of 5 nm, PMT detector voltage was 600 V. All experiments were performed using a 1 cm path length quartz cuvette. The background was corrected for blank fluorescence before each measurement and was collected at room temperature.

2.1.5 Calculating Quantum Yields

The phosphorescent quantum yield for ruthenium(II) complexes were estimated by matching the MLCT absorbance transition of both the complex and standard $[Ru(bpy)_3]^{2+}$ [ϕ_P = 0.0642 in acetonitrile].[87] Both solutions were excited into the MLCT region of maximum absorbance and the corresponding emission recorded. The luminescent quantum yield was calculated using the formula shown in Equation 2.11.

$$\phi_{P(x)} = (A_x/A_s)\,(F_s/F_x)\,(n_x/n_s)^2\,\phi_{P(s)} \qquad \text{eqn 2.11}$$

where ϕ_P is the phosphorescent quantum yield, A is absorbance at the excitation wavelength, F is the area under the corrected emission spectrum and n is the refractive index of the solvents used. X and s refer to the unknown and standard respectively. All quantum yield experiments were carried out three times and the average quantum yield was then reported.

2.1.6 Lifetime Measurements

Luminescent lifetimes were obtained using a Picoquant Fluotime 100 Time Correlated Single Photon Counting (TCSPC) system exciting at 450 nm and using a 510 nm narrow band pass dielectric filter for ruthenium complexes. The instrument response function was determined by using ledox AM30 colloidal silica solution with an excitation source (picosecond pulse diode lasers) of 450 nm for ruthenium samples respectively.

10,000 counts were collected for each lifetime measurement and all measurements were performed in triplicate using Nanoharp software to confirm results. Typical pulse rates of the excitation source were 1 x 10^5 s^{-1} with typical pulse widths of 300 ps. The aerated and degassed lifetime was recorded for each sample, with degassed samples being degassed with nitrogen for 20 minutes prior to analysis.

The calculation of the luminescent lifetimes were carried out by fitting an exponential decay function to each decay plot to extract the lifetime information using FluoFit software. Due to the inherently long lifetimes of ruthenium(II) complexes all data was fitted to mono/bi-exponential decay functions to the baseline of the decay curve using tail-fit with an x2 value of between 0.9-1.1.

2.1.7 Chromatographic Techniques

All products were purified using an automated flash chromatography system (Varian Intelliflash 310 series) using a Basic Alumina (Al_2O_3), 125 μm particle size, 112 mm, 24 gram column; or a Silica Gel, 50 μm particle size, 98 mm, 15 gram column. This allowed purification by separation of compounds into fractions and separation was followed using UV detection (200 – 400 nm) and an auto collector. The detection wavelength monitored was dependent on the maximum absorbance of the compound in the detector limitations, while also collecting peaks above a slope sensitivity of 0.5.

Thin layer chromatography (TLC) was performed to follow progress of reactions on glass silica gel (Merck, 250 μm thickness) or alumina (Alumina GF, Aldrich, 250 μm thickness). The sample plate was then placed in a TLC chamber containing the selected mobile phase and analysed under UV light (254 and 365 nm).

2.1.8 Resonance Raman Spectroscopy

Resonance Raman spectra were obtained on a HORIBA Jobin – Yvon Labram HR 1000 spectrometer coupled to a Digital Instruments Bioscope II with an inverted microscope. The Raman band of a silicon wafer at 520 cm^{-1} was used for calibration. The area of the laser spot on the samples was 1 μm in diameter and laser power was set from 1 to 2 mW using the laser power control. Data acquisition times were set to 2 seconds and 5 acquisitions were carried out for each spectra.

2.2 Cell Culture

Cells were maintained in a 37°C incubator with 5% CO_2 and 95% humidified air. Sp2/0-Ag14 cells were grown in complete Dulbecco's Modified Eagle's Medium, while CHO-K1 cells were grown in ATCC-formulated F-12K Medium. Both media were supplemented with 10% Fetal Bovine Serum, which is widely used for the in vitro cell culture of eukaryotic cells[88]. Due to the high growth of the CHO cells, the FBS was reduced to 5% after passage 10. Supplemented media was subsequently stored at 4°C. All cells and supplements were purchased from LGC Standards.

2.2.1 Cell enumeration and viability assay

Cell viability was assessed using the trypan blue exclusion method.[89] This method is based on the principal that dead or dying cells which do not have an intact cell membrane will take up the dye and subsequently be stained blue. 100 µL of cell suspension was mixed with 150 µL PBS and 250 µL of trypan blue solution (0.4% (v/v)). After approximately two minutes cells were applied to a brightline haemocytometer (Sigma®) and examined under high-power magnification (× 40) using an inverted microscope (Olympus CKX31, Olympus Corporation, Tokyo, Japan). Cells that were inside the central grid of 25 squares were counted.

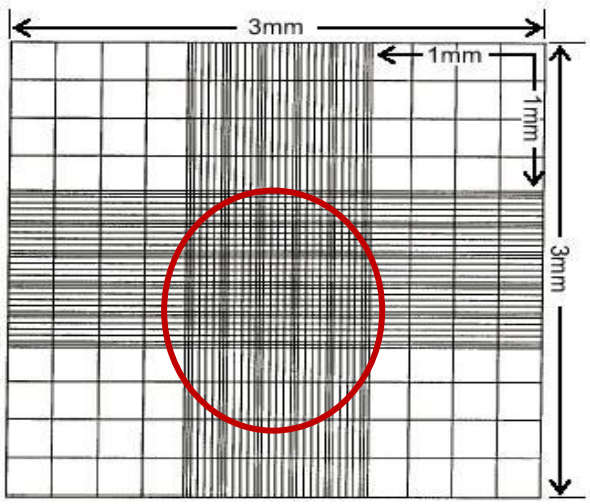

A viable cell count was achieved by using the following formula:

$$\text{Cells / ml} = N \times 5 \times 10^4$$

Where N = total number of cells counted, 5 = dilution factor and 10^4 = constant.

2.2.2 Sp2/0-Ag14 culture protocol

After removal from liquid nitrogen and rapid thawing, cells were decontaminated by spraying with 70% ethanol. The contents of the vial were transferred to a centrifuge tube containing 9 cm^3 complete culture medium and spun at 100 rpm (approx. 125xg) for 6 minutes. The cell pellet was resuspended in 10cm^3 of media and transferred to a 25cm^2 culture flask. Cells were seeded at a concentration between 1 x 10^5 and 5 x 10^5 cells/ml each time and culture flasks were left in the incubator. Depending on cell density fresh medium was added every 2 – 4 days and cell concentration was never allowed to exceed 1 x 10^6cells/ml. The base medium for this cell line is ATCC formulated Dulbecco's Modified Eagle's Medium (30-2002). This medium was made complete by the addition of fetal bovine serum (ATCC: 30-2020) to a final concentration of 10%.

2.2.3 CHO-k1 culture protocol

After removal from liquid nitrogen and rapid thawing, cells were decontaminated by spraying with 70% ethanol. The contents of the vial were transferred to a centrifuge tube containing 9 cm^3 complete culture medium and spun at 100 rpm for 6 minutes. The cell pellet was resuspended in 15 cm^3 of media and transferred to a 75cm^2 culture flask. Cells were subcultured by removing the medium and rinsing the cell layer with 0.25%(w/v) Trypsin- 0.53mM EDTA solution to remove all traces of serum which contains Trypsin inhibitor. After rinsing, 3 cm^3 of Trypsin-EDTA solution was added to the flask and placed in an incubator for five minutes to disperse the cell layer. The flask was removed from the incubator and 7 cm^3 of medium was added, transferred to a centrifuge tube and spun spun at 100rpm for 6 minutes. Cells were seeded at a concentration between 1 x 10^5 and 2 x 10^5 cells/ml each time and culture flasks were left in the incubator.

2.3.1 Confocal Fluorescence Microscopy

Confocal microscopy is an imaging technique that uses point illumination and a spatial pinhole which eliminates light thicker than the focal plane. The resulting higher z-resolution and reduced out-of-focus blur make confocal pictures crisper and clearer. Shown in Figure 2.31 is a schematic representation of a confocal microscope.

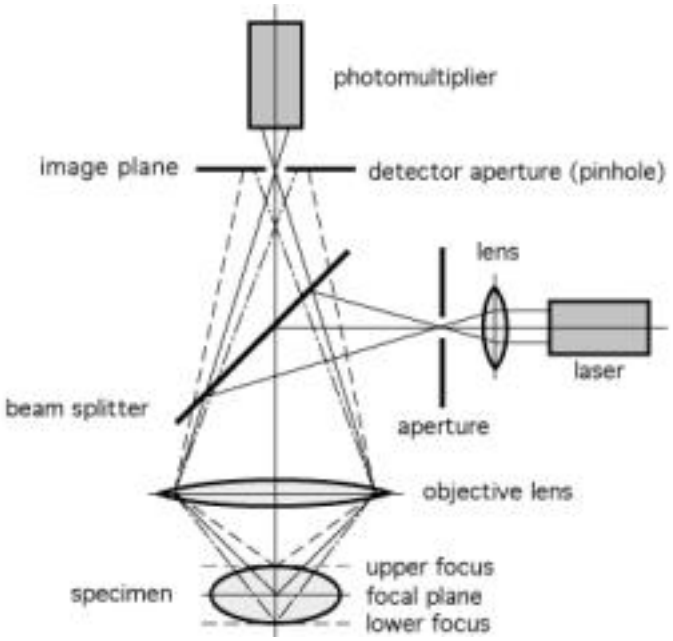

Figure 2.31: Schematic diagram illustrating the components of a confocal microscope.[90]

The objective lens focuses the incident light into a cone shaped beam so that the maximum intensity of the beam strikes a single spot within the sample. The luminescence from the sample is then focused by the dichroic beam splitter mirror onto a pinhole aperture, eliminating out-of-focus light or glare in specimens whose thickness exceeds the immediate plane of focus. A key advantage of confocal microscopy compared with traditional widefield microscopy is that single optical sections are projected on one plane, resulting in a clean image without any out-of-focus noise. While selecting a small pinhole diameter, it is only possible to image a thin optical section, although this will achieve the highest resolution possible.[90] Throughout this thesis, the standard pinhole size used was 1 airy unit; the microscope used was a Zeiss LSM510 META Confocal Imaging System.

Shown in Figure 3.22 is an example of the higher resolution images achieved with confocal microscopy in comparison to traditional microscopy and also a visualisation of the difference in incident light between the two techniques. Any noise that is present in an image can be greatly reduced via the acquisition of several frames which may be accumulated and averaged.

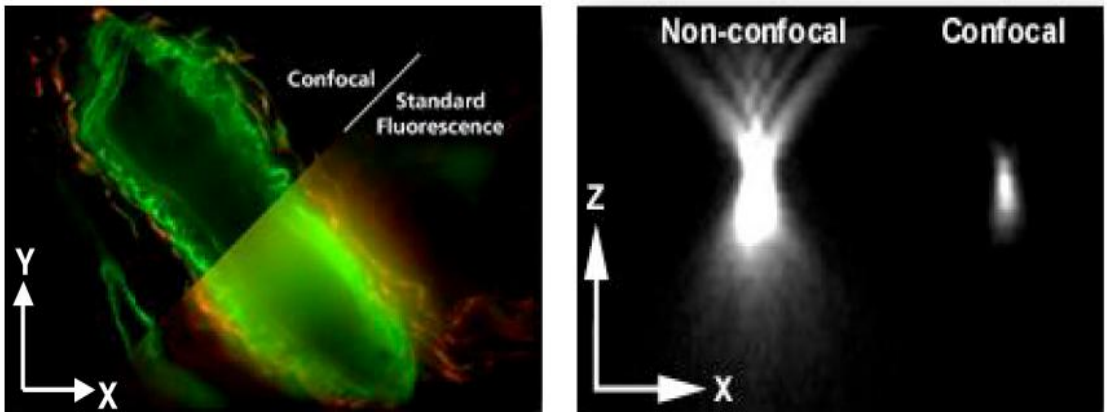

Figure 3.22: Comparison of the standard fluorescence image (left) and the incident light (right) of confocal and widefield microscopy.[91]

The co – localization studies described in Chapter 3 are made possible through multi – channel detection. In this mode, only one laser line is active, exciting one fluorophore at a time which then emits its signal and is collected by one active photo-multiplier tube PMT. Then Laser & PMT are switched off and the next laser line and PMT are activated in order to capture the next channel.

Also described in Chapter 3 is the z – stack technique, which is possible due to the automatically adjustable microscope stage. This technique allows for the acquisition of data images of varying optical depth. The number of optical sections defines the resolution in the data set.

2.3.2 Resonance Raman Mapping

Raman mapping is a technique which generates detailed images based on a compound's Raman spectrum. A resonance Raman image is generated by analysing the intensity of individual or multiple bands in a spectrum wherein the Raman excitation wavelength is resonant with an optical absorption of the sample.

Resonance Raman maps were obtained on a HORIBA Jobin – Yvon Labram HR 1000 spectrometer coupled to a Digital Instruments Bioscope II with an inverted microscope. The Raman band of a silicon wafer at 520 cm^{-1} was used for calibration. An individual cell of interest was identified and then a white light image of this cell was recorded. The Raman maps shown in this thesis were obtained for live cells without the use of an incubator, and thus at approximately 25°C. The total number of data points may be selected before each acquisition, however to ensure cell viability, images were collected in a time not exceeding twenty minutes.

The Raman maps shown in this thesis were obtained through the use of sequential sample movement and spectrum acquisition, with the final image consisting of thousands of Raman spectra.

Chapter 3: Synthesis and Characterisation of ruthenium complexes suitable for bioconjugation

3.0 Introduction

3.1 Experimental Procedure

- 3.1.1 Synthesis of pic ligands
- 3.1.2 Synthesis of BODIPY dye
- 3.1.3 Synthesis of ruthenium complexes
- 3.1.4 Synthesis of ruthenium – peptide conjugate
- 3.1.5 Synthesis of ruthenium – BODIPY conjugate

3.2 Results and Discussion

- 3.2.1 Synthesis
- 3.2.2 ^{1}HNMR Discussion
- 3.2.3 Characterisation of ruthenium complexes
  - 3.2.3.1 Absorbance
  - 3.2.3.2 Photophysics
  - 3.2.3.3 Emission Lifetime
- 3.2.4 Characterisation of ruthenium – peptide conjugate
  - 3.2.4.1 Absorbance
  - 3.2.4.2 Photophysics
  - 3.2.4.3 pH Dependence Studies
  - 3.2.4.4 Resonance Raman Spectroscopy
  - 3.2.4.5 Photostability – UV irradiation
- 3.2.5 Synthesis of ruthenium – BODIPY sensor

3.3 Conclusions

3.0 Introduction

As described, ruthenium polypyridyl complexes have numerous unique photophysical properties which make them potentially invaluable for cellular imaging such as their intense polarised luminescence, large Stokes shift, red emission wavelengths as well as their environmental sensitivity.[12] A key advantage of many ruthenium (II) complexes is that they are not susceptible to much of the degradation exhibited by organic fluorophores. The focus in this thesis was on two Ru(II) polypyridyl complexes, both with ionisable ligands, one an imidazole and the other triazole.

The complex $[Ru(bpy)_2(picCOOH)]^{2+}$, where picCOOH is 2-(4-Carboxylphenyl)imidazo[4,5-f]1,10-phenanthroline has been synthesized and its photophysical properties explored recently by a number of groups, including our own.[11,12, 92] One of the attractive properties of this complex, is that unlike most common fluorophores its emission intensity and lifetime are enhanced in an aqueous compared to non-polar environment. Conjugation of $[Ru(bpy)_2(picCOOH)]^{2+}$ to a cell penetrating peptide was carried out via the carboxyl terminus and the dye was subsequently found to be a useful probe for cellular imaging.

An initial aim of this work was to synthesise a BODIPY – conjugated ruthenium dye and attach this complex to a cell-penetrating peptide, to produce a molecule capable of reporting on pH and oxygen concentrations in a cellular environment (Ru centre), with self-referencing to a non-environmentally sensitive luminophore (BODIPY). The conjugation of a metal complex to a cell-penetrating peptide facilitates efficient diffusion across mammalian cell membranes without destroying the lipid bilayer. The synthetic approach taken was to design a ruthenium(II) complex with two nitrophenanthroline ligands capable of linking to a cell penetrating peptide, and also containing an amino terminus in order to exploit this group for EDC/NHS coupling to a carboxyl functionalised BODIPY dye.

Peptide – conjugated ruthenium(II) probes have previously been shown to transport passively across a myeloma cell membrane (believed to occur via endocytosis) and distribute throughout the cell.[12] BODIPY complexes are known for their robust photophysical properties, such as strong absorption of visible light high fluorescence quantum yield, good photostability and are also pH and O_2 insensitive which make them useful as reference compounds.

The first part of this chapter presents detailed and comparative photophysical and spectroscopic studies for two nitrophenanthroline – ruthenium(II) – pic complexes with different terminal functionality, as well as the phenanthroline parent complex. Mass spectrometry was used in conjunction with NMR (^{1}H-NMR / COSY) to confirm the purity and structure of the complexes synthesised. Although the final complex was not completed these novel complexes form the first two components of the route to the novel chromophores from where future work will commence.

The second part of this chapter describes the synthesis of a ruthenium(II) – triazole complex and it's subsequent conjugation to a cell penetrating peptide. The cellular activity of this probe and it's parent complex is described in Chapter 4. Here, a complete photophysical, resonance Raman and photostability study is described to support the cellular imaging results discussed in the following chapter and also to provide a comparison between the parent and the peptide – conjugated complex.

3.1.1 Synthesis of Pic ligands

Chemicals

All chemicals and reagents were purchased from Sigma Aldrich Ireland and used without any further purification steps. All reactions were performed in aerated media unless otherwise stated.

The preparation of 2-(4-carboxylphenyl)imidazo[4,5-f]1,10-phenanthroline [(picCOOH)]

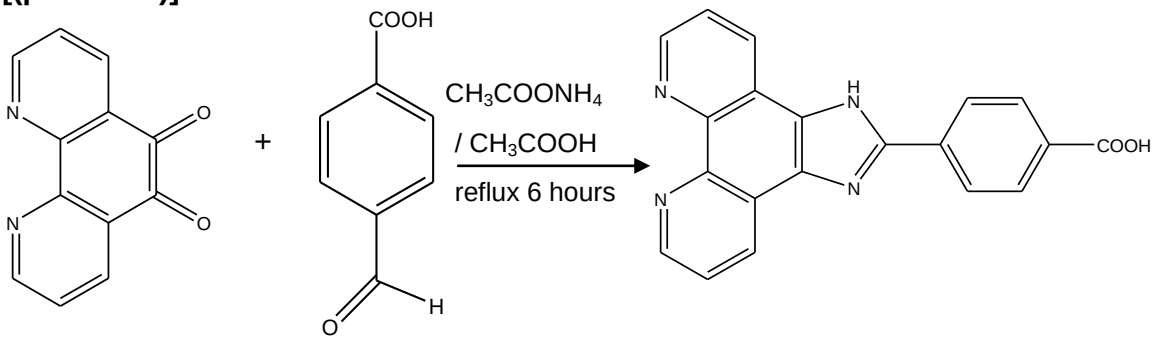

phendione 4-carboxybenzaldeyde 2-(4-carboxylphenyl)imidazo [4,5-f]1,10-phenanthroline

The ligand was prepared using a modification to a method previously described in the literature.[11] 1,10-Phenanthroline-5,6-dione (0.21 g, 1 mmol), 4-carboxybenzaldeyde (0.15 g, 1 mmol) and ammonium acetate (1.5 g, 20 mmol) were suspended in glacial acetic acid (20 cm^3) and refluxed overnight. The reaction vessel was cooled down and water (100 cm^3) was added to the reaction mixture to induce crystallisation and was stored at 4°C overnight. The product precipitated as yellow solid and was collected by filtration. The solid was washed with water and methanol and dried in air. Yield (79%, 0.269 g)

^{1}H NMR (400 MHz, DMSO-d_6): (ppm) **13.99** (s, 1H), **9.06** (d, 2H), **8.95** (d, 2H, J = 2.4 Hz), **8.41** (d, 2H, J = 8.4 Hz), **8.20** (d, 2H, J = 8.4 Hz), **7.87** (m, 2H).

The preparation of 2-(4-Nitrophenyl)imidazo[4,5-f]1,10-phenanthroline [PicNO$_2$]

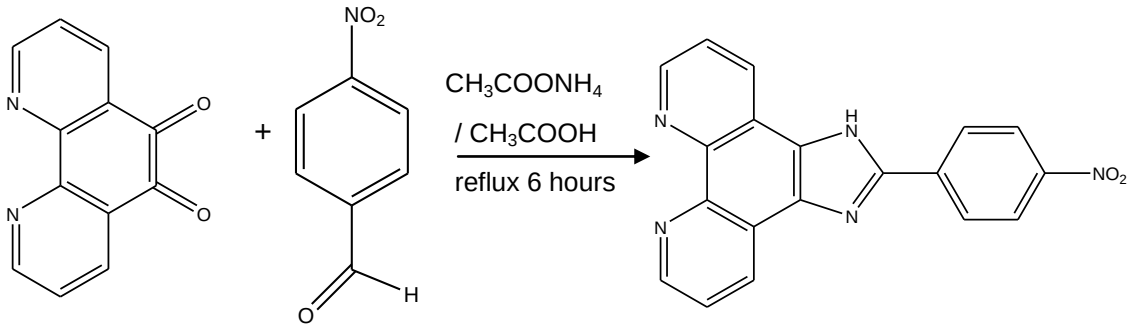

phendione 4-nitrobenzaldeyde 2-(4-nitrophenyl)imidazo [4,5-f]1,10-phenanthroline

1,10-Phenanthroline-5,6-dione (0.406 g, 1.93 mmol), 4-nitrobenzaldeyde (0.345 g, 2.32 mmol) and ammonium acetate (2.975 g, 38.6 mmol) were suspended in glacial acetic acid (35 cm^3) and left to reflux at 130°C for eight hours. The reaction vessel was cooled down and water (200 cm^3) was added to the reaction mixture to induce crystallisation and was stored at 4°C overnight. The product precipitated as yellow solid and it was collected by filtration. The solid was washed with water and methanol and dried in air (0.567 g, 86*%).*

^{1}H NMR (DMSO-d$_6$): (ppm) **9.07** (d, 2H, J = 1.6 Hz), **8.89** (d, 2H, 1.6 Hz), **8.51** (m, 4H, J = 8.8 Hz, J = 7.2 Hz, J = 9.2 Hz), **7.86** (m, 2H).

The preparation of 2-(4-Aminophenyl)imidazo[4,5-f]1,10-phenanthroline [PicNH$_2$]

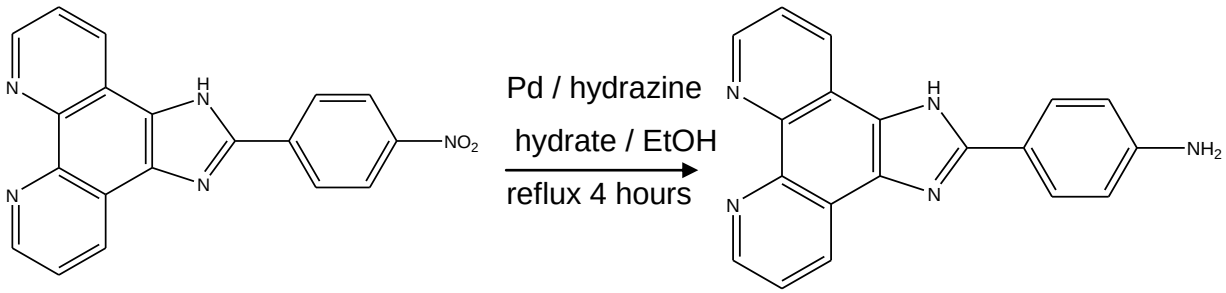

2-(4-nitrophenyl)imidazo [4,5-f]1,10-phenanthroline

2-(4-aminophenyl)imidazo [4,5-f]1,10-phenanthroline

2-(4-nitrophenyl)imidazo[4,5-f]1,10-phenanthroline [(PicNO$_2$)] (1.500 g, 4.3 mmol) was dissolved in absolute ethanol (35 cm^3) and to this solution palladium 5% wt on activated carbon (0.130 g) was added. Hydrazine hydrate (1.13 cm^3, 2.54 mmol) was added dropwise via a syringe and the resulting solution was left to reflux at 90°C for four hours. The solution was filtered through celite (compacted with ethanol / dichloromethane), to remove the palladium, and evaporated to dryness. The solid was then purified using an alumina (basic) chromatographic column using 10% (v/v) methanol : dichloromethane mobile phase to yield a dark yellow product. (1.285 g, 94%).

^{1}H NMR (DMSO-d$_6$): (ppm) **13.32** (s, 1H), **8.98** (d, 2H), **8.91** (d, 2H), **7.97** (d, 2H, J = 8.8 Hz), **7.81** (m, 2H), **6.73** (d, 2H, J = 8.4 Hz), **5.63** (s, 2H).

3.1.2 Synthesis of BODIPY dye

The preparation of 8-benzoic acid-4,4-difluoroboradiazaindacene [BODIPY-COOH]

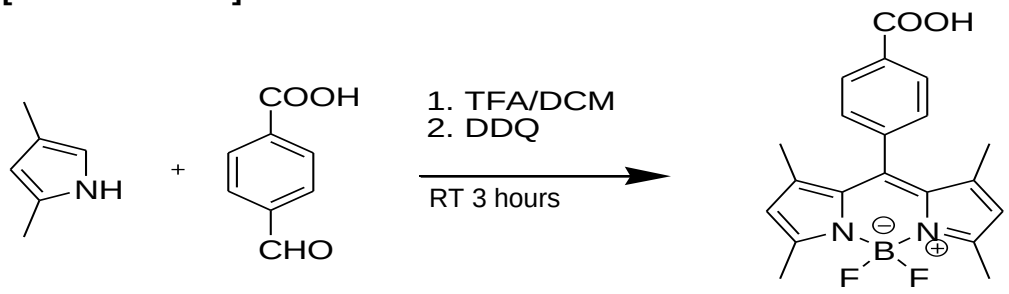

Dimethylpyrrole 4-formylcarboxylic acid

8-benzoic acid-4,4-difluoro boradiazaindacene

The ligand was prepared using a modification to a method previously described in the literature.[124] 2,4-dimethylpyrrole (0.428 g, 4.5mmol) and 4-formylcarboxylic acid (0.301 g, 2.0 mmol) were dissolved in dichloromethane (150 cm^3). One drop of trifluoroacetic acid was added and the solution was left to stir at room temperature. The reaction was monitored by TLC until complete consumption of the carboxylic acid was confirmed. 2,3-Dichloro-5,6-dicyano-1,4-benzoquinone (DDQ) (0.454 g, 2.0 mmol) was added to the mixture followed by the addition of triethylamine (4 cm^3). The mixture was stirred for another two hours, washed with water, dried and the solvent evaporated under reduced pressure. The resulting solid was then purified using a silica chromatographic column using 40% (v/v) hexane : ethyl acetate mobile phase to yield a purple product. Yield (66%, 0.484 g). Mol Wt 367.15$gmol^{-1}$

^{1}H NMR (400 MHz, acetone-d_6): (ppm) **8.25** (d, 2H), **7.60** (d, 2H), **6.15** (s, 2H), **2.52** (s, 6H), **1.42** (s, 6H).

3.1.3 Synthesis of ruthenium complexes

The preparation of ruthenium-(bis-1,10-phenanthroline)dichloride [$Ru(phen)_2Cl_2$]

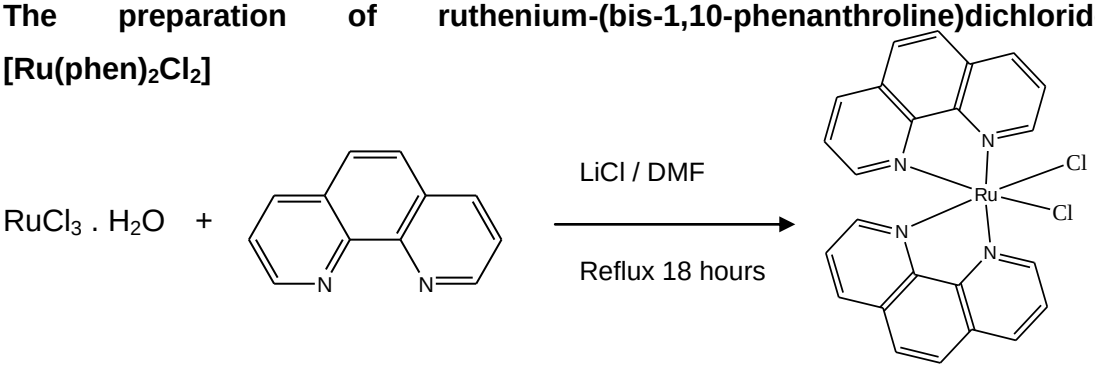

Ruthenium tri chloride hydrate

1,10-phenanthroline

ruthenium-(bis-1,10-phenanthroline)dichloride

Dimethylformamide (21 cm^3) was degassed under nitrogen for two hours. $RuCl_3.3H_2O$ (0.5 g, 1.91 mmol), was dissolved in the degassed DMF in a three neck round bottomed flask. To this lithium chloride (0.55 g, 12.99 mmol) was added followed by 1,10 phenanthroline (0.690 g, 3.83 mmol) in equal portions over 30 minutes. The reaction was refluxed at 140°C under nitrogen for 20 hours.

The reaction mixture was allowed to stand to cool to room temperature and acetone (15 cm^3) was added to promote precipitation, before storing the flask at 4°C overnight. The precipitate was then filtered and the solid washed with acetone, water and diethyl ether giving a dark purple solid. Yield: 71% (0.76g) MW: 532$gmol^{-1}$.

^{1}H NMR (400 MHz, DMSO-d_6): (ppm) **10.21** (d, 2H), **8.65** (d, 2H), **8.24** (d, 2H), **8.17** (m, 4H), **8.08** (d, 2H), **7.68** (d, 2H), **7.28** (dd, 2H).

The preparation of ruthenium-(bis-1,10-5-nitrophenanthroline)dichloride [$Ru(NO_2\ phen)_2Cl_2$]

Dimethylformamide (21 cm^3) was degassed under nitrogen for two hours. $RuCl_3.3H_2O$ (0.58 g, 2.22 mmol), was dissolved in the degassed DMF in a three neck round bottomed flask. To this lithium chloride (0.71 g, 15.09 mmol) was added followed by 5-nitro-1,10-phenanthroline (1.001 g, 4.44 mmol) in equal portions over 30 minutes. The reaction was refluxed at 140°C under nitrogen for 20 hours.

The reaction mixture was allowed to stand to cool to room temperature and acetone (15 cm^3) was added to promote precipitation, before storing the flask at 4°C overnight. The precipitate was then filtered and the solid washed with acetone, water and diethyl ether. This solid was then purified using a silica chromatographic column using 10% methanol : dichloromethane mobile phase to yield a dark purple product. Yield: 68% (0.808g) MW: 621$gmol^{-1}$

^1H NMR (400 MHz, DMSO-d_6): (ppm) **10.34** (d, 2H), **9.35** (s, 1H), **9.20** (s, 1H), **9.03** (d, 1H), **8.94** (d, 1H), **8.61** (d, 1H), **8.48** (d, 1H)., **8.31** (m, 2H), **8.01** (dd, 2H), **7.45** (m, 2H)

ESI-MS (CH3OH, m/z): 854.3.
ESI-MS: M2+ 1105.6 m/z, M2+/2 553.5 m/z

The preparation of ruthenium-(bis-1,10-5-aminophenanthroline)dichloride [$Ru(NH_2\ phen)_2Cl_2$]

Ruthenium-(bis-2,2-5-nitrophenanthroline) dichloride [$Ru(NO_2phen)_2Cl_2$] (0.120 g, 0.19 mmol) was dissolved in absolute ethanol (10 cm^3) and to this solution palladium 5% wt on activated carbon (0.014 g) was added. Hydrazine hydrate (0.071cm^3, 1.46mmol) was added dropwise via a syringe and the resulting solution was left to reflux at 90^0C for four hours.

The solution was filtered through celite (compacted with ethanol/ dichloromethane), to remove the palladium, and evaporated to dryness. The solid was then purified using an alumina (basic) chromatographic column using 10% methanol : dichloromethane mobile phase to yield a light purple product. (0.104g, 83%).

^{1}H NMR (400 MHz, DMSO-d_6): (ppm) **9.98** (m, 1H), **9.57** (m, 1H), **9.08** (m, 1H), **8.61** (d, 1H), **8.43** (d, 1H), **8.25** (m, 1H), **8.01** (dd, 2H), **7.64** (d, 1H), **7.46** (m, 1H), **7.24** (d, 2H), **7.13** (s, 1H), **6.98** (s, 1H), **6.89** (s, 2H), **6.74** (s, 2H).

The preparation of ruthenium (bis-2,2-phenanthroline)-2(4-carboxyphenyl)imidazo[4,5-f]1,10-phenanthroline
$[(Ru(phen)_2 PicCOOH)]^{2+}$

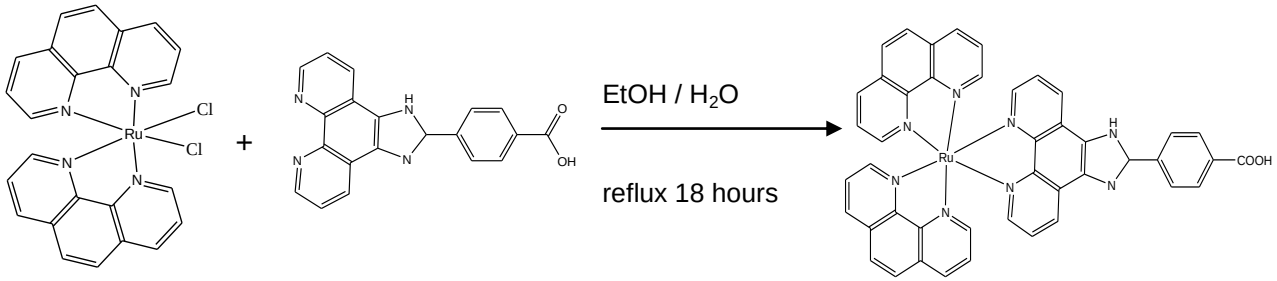

ruthenium-(bis-1,10, phenanthroline dichloride

2(4-carboxyphenyl)imidazo [4,5-f]1,10-phenanthroline

(bis-1,10-phenanthroline)-2(4 carboxyphenyl) imidazo[4,5-f]1,10-phenanthroline

$[Ru(phen)_2Cl_2]$ (0.125 g, 0.23 mmol) and 2(4-carboxyphenyl)imidazo[4,5-f]1,10-phenanthroline [PicCOOH] (0.088 g, 0.25 mmol) were placed in a 25 cm^3 round bottomed flask and left to reflux at 85^0C in ethanol (10 cm^3) for 18 hours.

The reaction was allowed to stand until it had cooled to room temperature. A saturated solution of $NaCl_4$ was added and the precipitate was collected. The solid was then washed with diethyl ether and chloroform to yield a dark orange solid.

The product was then dissolved in acetonitrile and filtered to remove any unreacted $PicNH_2$. The filtrate was then collected and dried leading to an orange solid. Yield (0.140g, 78%) Mol Wt: 803.7$gmol^{-1}$.

^{1}H NMR (400 MHz, DMSO-d_6): (ppm) **14.51** (s, 1H), **9.09** (d, 2H), **8.80** (d, 2H), **8.73** (d, 2H), **8.46** (d, 2H), **8.40** (m, 4H). **8.24** (d, 2H), **8.14** (m, 2H), **8.08** (d, 2H), **8.02** (d, 2H), **7.77** (m, 4H).

ESI-MS (CH_3OH, m/z): 903.27

The preparation of ruthenium (bis-1,10-5-nitrophenanthroline)-2(4-Aminophenyl)imidazo[4,5-f]1,10-phenanthroline [$(Ru(NOphen)_2PicNH_2)]^{2+}$

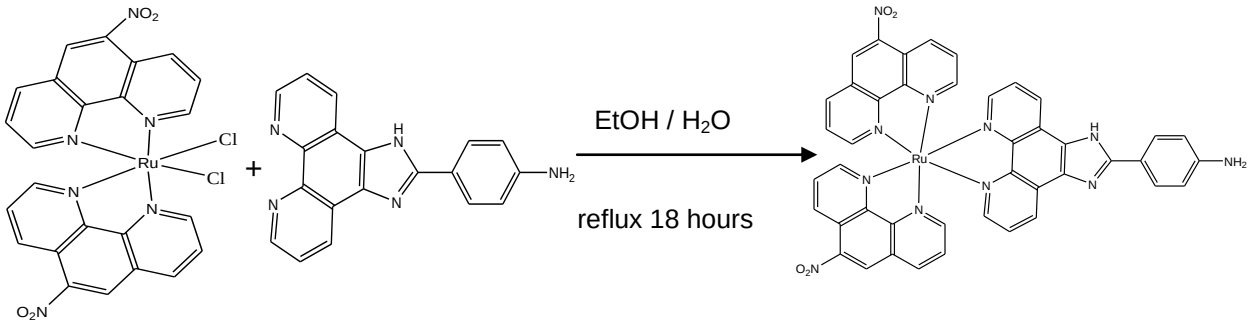

ruthenium-(bis-1,10, 5-nitrophenanthroline dichloride

2(4-carboxyphenyl)imidazo [4,5-f]1,10-phenanthroline

(bis-1,10-phenanthroline)-2(4-aminophenyl) imidazo [4,5-f]1,10-phenanthroline

Ru $(NO_2phen)_2Cl_2$ (0.285g, 0.45mmol) and 2(4-Aminophenyl)imidazo[4,5-f]1,10-phenanthroline [$PicNH_2$] (0.171 g, 0.54 mmol) were placed in a 50 cm^3 round bottomed flask and left to reflux at 85°C in ethanol (25 cm^3) for 18 hours.

The reaction was allowed to stand until it had cooled to room temperature. A saturated solution of sodium perchlorate was added and the precipitate was collected. The solid was then washed with diethyl ether and chloroform to yield a dark orange solid.

The product was then dissolved in acetonitrile and filtered to remove any unreacted $PicNH_2$. The filtrate was then collected and dried leading to an orange solid. Yield (0.302g, 78%) Mol Wt: 862.1$gmol^{-1}$.

^{1}H NMR (400 MHz, DMSO-d_6): (ppm) **9.21** (d, 2H), **9.10** (t, 2H), **9.01** (ds, 2H), **8.77** (t, 2H), **8.24** (t, 2H), **7.94** (d, 2H). **7.88** (m, 2H), **7.76** (m, 4H), **7.61** (dt, 2H), **6.74** (d, 2H), **5.39** (s, 2H).

ESI-MS (CH3OH, m/z): 961.89

The preparation of ruthenium (bis-1,10-5-nitrophenanthroline)-2-(4-Carboxylphenyl)imidazo[4,5-f]1,10-phenanthroline $[(Ru(NOphen)_2PicH_2)]^{2+}$

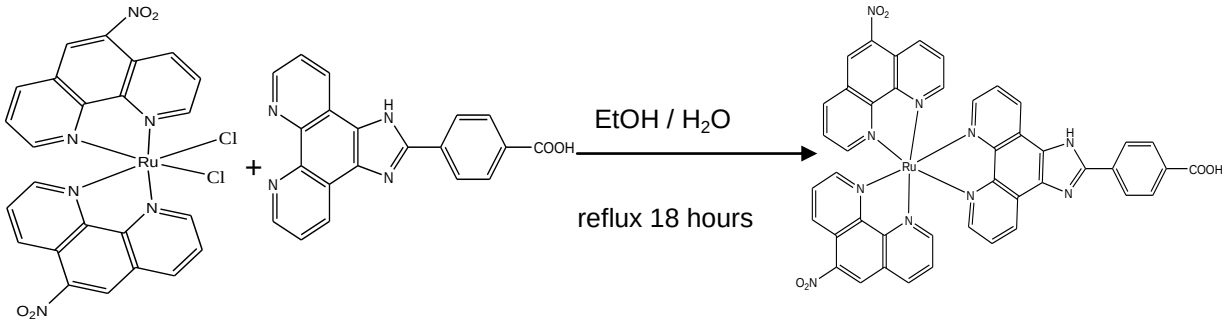

ruthenium-(bis-1,10, 5-nitrophenanthroline dichloride

2(4-carboxyphenyl)imidazo [4,5-f]1,10-phenanthroline

(bis-1,10-phenanthroline)-2(4-aminophenyl) imidazo [4,5-f]1,10-phenanthroline

$Ru(NO_2phen)_2Cl_2$ (0.170 g, 0.19 mmol) and 2-(4-Carboxylphenyl)imidazo[4,5-f]1,10-phenanthroline [$PicH_2$] (0.112 g, 0.23 mmol) were placed in a 50 cm^3 round bottomed flask and left to reflux at 85°C in ethanol for 18 hours.

The reaction was allowed to stand until it had cooled to room temperature. A saturated solution of sodium perchlorate was added and the precipitate was collected. The solid was then washed with diethyl ether and chloroform to yield a dark orange solid.

The product was then dissolved in acetonitrile and filtered to remove any unreacted [pic] ligand. The filtrate was then collected and dried leading to an orange solid. Yield (0.137 g, 81%) Mol Wt: 892.1 $gmol^{-1}$.

^{1}H NMR (400 MHz, DMSO-d_6): (ppm) **14.47** (s, 1H), **8.03** (d, 2H), **7.95** (m, 2H), **7.88** (m, 2H), **7.64** (m, 2H), **7.06** (m, 4H). **7.04** (m, 2H), **6.91** (dd, 2H), **6.79** (dt, 2H), **6.58** (m, 4H), **6.51** (d, 2H).

ESI-MS (CH3OH, m/z): 990.37 ([M- ClO4]$^{2+}$): 891.23

3.1.4 Synthesis of ruthenium peptide conjugate

Synthesis of 2-(5-(5-bromo-2-methoxyphenyl)- 4H-1,2,4-triazol-3-yl) pyridine

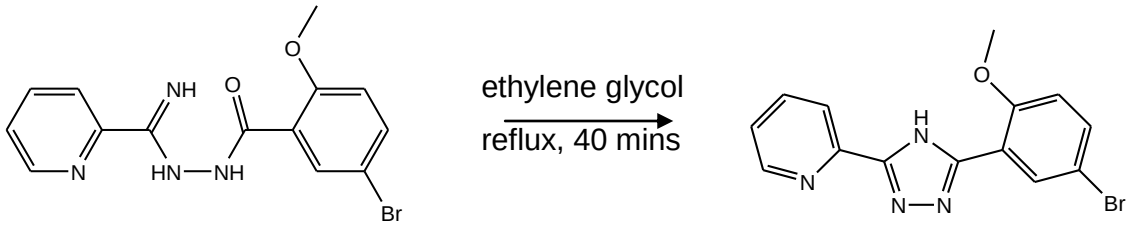

N'-(imino(pyridin-2-yl)methyl)-5-bromo-2-methoxybenzohydrazide

2-(5-(5-bromo-2- methoxyphenyl) 4H-1,2,4-triazol-3-yl)pyridine

The ligand N'-(imino(pyridin-2-yl)methyl)-5-bromo-2-methoxybenzohydrazide was prepared using modification to a method previously described in the literature.[93, 94] A slurry of the ligand (10.4 g, 29.78 mmol) was refluxed in ethylene glycol (30 cm^3) for one hour. The solution was then cooled to approximately 90°C and water (30 cm^3) added, and the mixture was stored at 4°C for 18 hours. The precipitate was collected, washed with water, and dried under vacuum at 80°C for one hour (3.7 g, 37.51%). The crude product was used in next step.

^{1}H NMR (400 MHz, DMSO-d_6): (δppm) **3.75** (s, 3 H), **7.00** (d, 1 H), **7.10** (m, 1 H), **7.38** (d, Hz, 1 H), **7.78** (t, 1 H), **8.14** (s, 1 H), **8.15** (s, 1 H), **8.29** (m, 1 H).

ESI-MS (CH3OH, m/z): calculated (M) 331.1, found 332.1 ($M + H^+$)

Synthesis of ruthenium bis(2,2-bipyridyl) {2-[5-5-(5-bromo-2-methoxyphenyl)-4*H*-1,2,4-triazol-3-yl] pyridine}

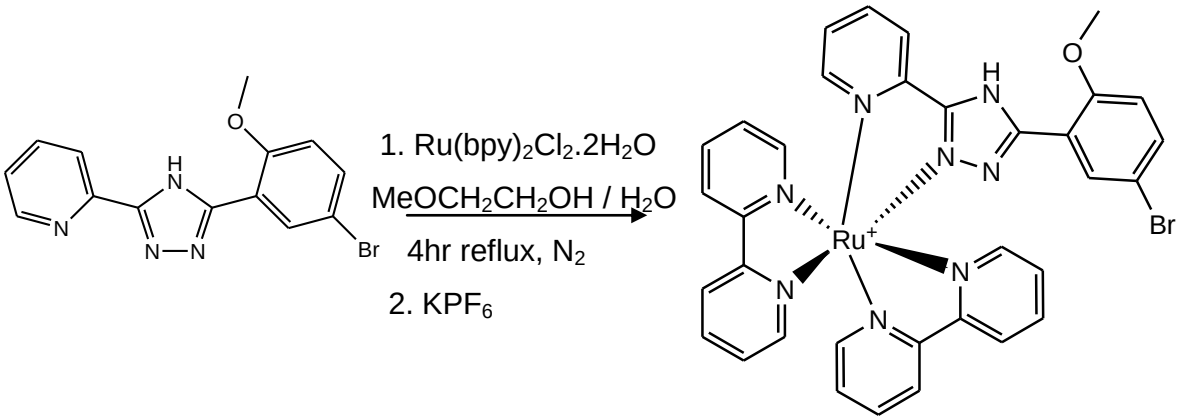

2-(5-(5-bromo-2- methoxyphenyl) 4H-1,2,4-triazol-3-yl)pyridine

ruthenium bis(2,2-bipyridyl) {2-[5-5-(5-bromo-2-methoxyphenyl) -4*H*-1,2,4-triazol-3-yl] pyridine}

$[Ru(bpy)_2Cl_2]$ (0.529 g, 1.09 mmol) and 2-(5-(5-bromo-2- methoxyphenyl) 4H-1,2,4-triazol-3-yl)pyridine (0.406 g, 1.22 mmol) were placed in a 100 cm^3 round bottomed flask containing 2-methoxyethanol (60 cm^3) and water (20 cm^3) which was deoxygenated with nitrogen for ten minutes. The mixture was then refluxed under nitrogen for four hours. After cooling to room temperature, the solvents were evaporated and to the resulting orange residue water (20 cm^3) was added. Potassium hexafluorophosphate (KPF_6) (1.5 g) was then added to the solution and the precipitated product was extracted with DCM, organic solution was dried with magnesium sulfate and the solvent was evaporated under vacuum. The solid was then purified using a silica chromatographic column using 10% v/v methanol : dichloromethane mobile phase to yield an orange product (0.70 g, 72%).

^{1}H NMR (400 MHz, acetonitrile-d_3) δ ppm **8.44** (d, 1 H), **8.46** (d, 1 H), **8.39** (d, 1 H), **8.42** (d, 1 H), **8.13** (d, 1 H), **7.98** (m, 1 H), **7.97** (dd, 1 H), **7.91** (m, 3 H), **7.86** (m, 2 H), **7.76** (m, 3 H), **7.52** (d, 1 H), **7.41** (m, 2 H), **7.36** (m, 2 H), **7.29** (dd, 1 H), **7.23** (m, 1 H), **7.19** (d, 1 H), **7.15** (dd, 2 H), **6.95** (d, 1 H), **3.71** (s, 3 H)

ESI-MS (CH_3OH, m/z): calculated (M) 745.1, found 745.1 (M)

Synthesis of ruthenium bis(2,2-bipyridyl) [(2*E*)-3-{4-methoxy-3-[5-(pyridinyl)- 1,2,4-triazol-3-yl] phenyl} propenoic acid]

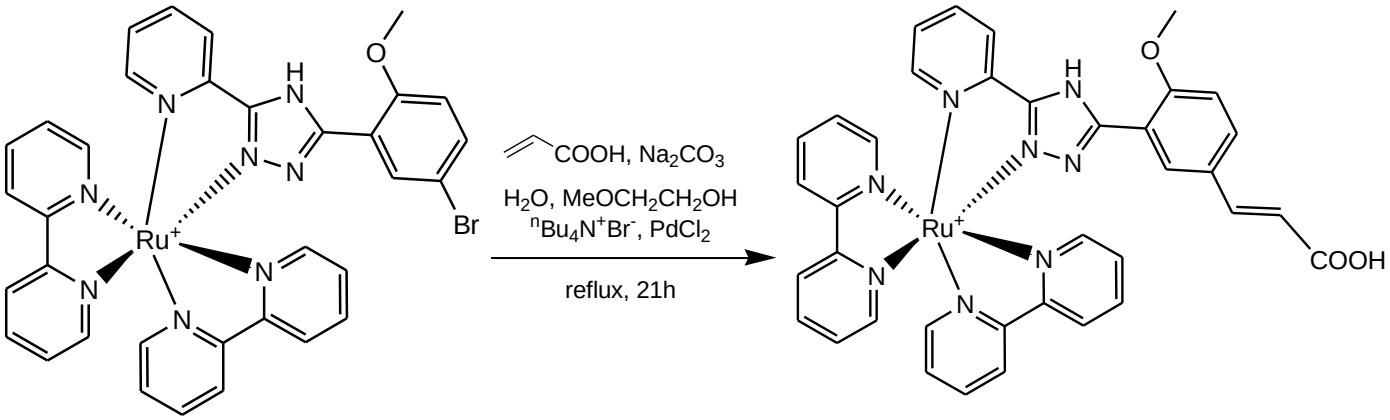

ruthenium bis(2,2-bipyridyl) {2-[5-5-(5-bromo-2-methoxyphenyl) -4*H*-1,2,4-triazol-3-yl] pyridine}

ruthenium bis(2,2-bipyridyl) [(2*E*)-3-{4-methoxy-3-[5-(pyridinyl)- 1,2,4-triazol-3-yl] phenyl} propanoic acid

Ruthenium bis(2,2-bipyridyl) {2-[5-5-(5-bromo-2-methoxyphenyl)-4*H*-1,2,4-triazol-3-yl] pyridine**}** (0.261 g, 0.29 mmol), sodium carbonate (0.420 g, 5.04 mmol), tetrabutylammonium bromide (0.1 g, 0.31 mmol), palladium (II) chloride (0.03 g, 0.17 mmol) and acrylic acid (0.045 g, 0.63 mmol) were added to a 100 cm^3 round bottomed flask containing water (25 cm^3) and 2-methoxyethanol (15 cm^3) and the mixture refluxed under nitrogen for twenty hours. The solvents were removed by rotary evaporation and the orange residue was collected. The solid was then dissolved in water (40 cm^3) and extracted three times with dichloromethane. The organic layer was discarded and to the aqueous solution concentrated hydrochloric acid (to pH=1) and KPF_6 (1 g) were added. The product was extracted with DCM and the solvent evaporated under vacuum (0.162 g, 63%).

^{1}H NMR (400 MHz, acetonitrile-d_3) δ ppm = **8.47** (t, 2 H), **8.4**0 (d, 1 H), **8.35** (d, 1 H), **8.29** (d, 1 H), **8.05** - 7.99 (m, 2 H), **7.98** (m, 2 H), **7.91** (m, 2 H), **7.84** (m, 2 H), **7.80** (d, 1 H), **7.74** (d, 1 H), **7.60** (m, 2 H), **7.46** (m, 2 H), **7.41** (m, 3 H), **7.26** (dd, 1 H), 7.24 (t, 1 H), **7.06** (d, 1 H), **6.17** (d, 1 H), **3.79** (s, 3 H)

ESI-MS (CH3OH, m/z): calculated $(M)^+$ 735.1; found 735.1 $(M)^+$

Synthesis of ruthenium bis(2,2-bipyridyl) [(2*E*)-3-{4-methoxy-3-[5-(pyridinyl)- 1,2,4-triazol-3-yl] phenyl} prop-2-enoyl]oxy}pyrrolidine-2,5-dione)

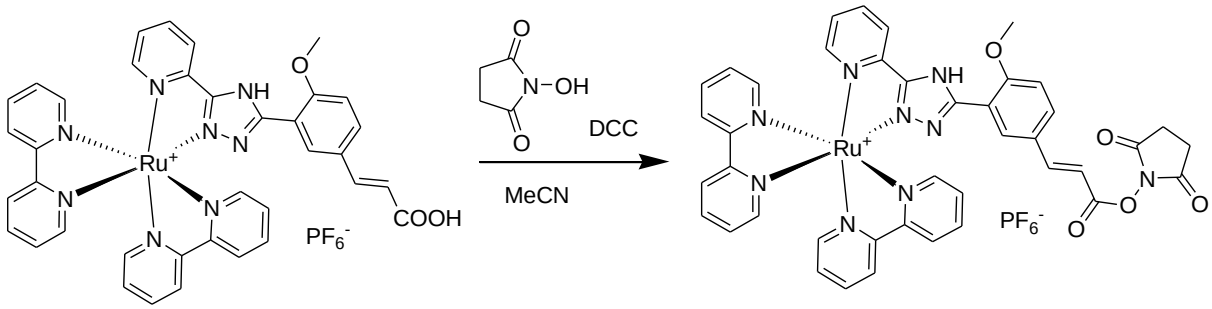

ruthenium bis(2,2-bipyridyl) [(2*E*)-3-{4-methoxy-3-[5-(pyridinyl)-1,2,4-triazol-3-yl] phenyl} propanoic acid

ruthenium bis(2,2-bipyridyl) [(2*E*)-3-{4-methoxy-3-[5-(pyridinyl)-1,2,4-triazol-3-yl] phenyl} prop-2-enoyl]oxy}pyrrolidine-2,5-dione)

To a solution of ruthenium bis(2,2-bipyridyl) [(2*E*)-3-{4-methoxy-3-[5-(pyridinyl)-1,2,4-triazol-3-yl] phenyl} propenoic acid**]** (0.042 g, 0.05 mmol) in anhydrous acetonitrile (3 cm^3), dicyclohexylcarbodiimide (DCC) (0.02 g, 0.09 mmol) were added. The resulting mixture was stirred at room temperature for five minutes and N-hydroxysuccinimide (0.01 g, 0.84 mmol) in anhydrous acetonitrile (1 cm^3) was added. After stirring at room temperature for twenty four hours the solvent was evaporated an the crude product purified on silica using gradient acetonitrile – 1,5%$_{aq}$ KNO_3 (starting from 0% to 20% of $KNO_{3(aq)}$). The product was dissolved in DCM (20 cm^3) and a solution of potassium hexafluorophosphate (0.2 g, 1.08 mmol) in water (5 cm^3) was added. The organic solution was dried with magnesium sulfate, filtered and the solvent was evaporated (0.032 g, 64%). The active ester was used in next step immediately.

^{1}H NMR (400 MHz, acetonitrile-d_3) δ ppm = **8.50** (m, 5 H), **8.10** (m, 1 H), **8.03** (m, 10 H), **7.82** (m, 2 H), **7.69** (dd, 1 H), **7.53** (m, 1 H), **7.44** (dd, 1 H), **7.39** (dd, 2 H), **7.23** (m, 1 H), **7.16** (m, 1 H), 7.10 (d, 1 H), **6.57** (d, 1 H), **5.45** (s, 2 H), **3.78** (s, 3 H)

ESI-MS (CH3OH, m/z): calculated $(M)^+$ 832.2; found 832.2 $(M)^+$

Synthesis of ruthenium bis(2,2-bipyridyl) [(2*E*)-3-{4-methoxy-3-[5-(pyridinyl)- 1,2,4-triazol-3-yl] phenyl} prop-2-enoyl]amino}ethyl)-2,5-dioxopyrrolidin-3-yl]- L-cysteinyl-L-arginyl-L-arginyl-L-arginyl-L-arginyl-L-arginyl-L-arginyl-L-arginyl-L-arginyl-L-argininamide}

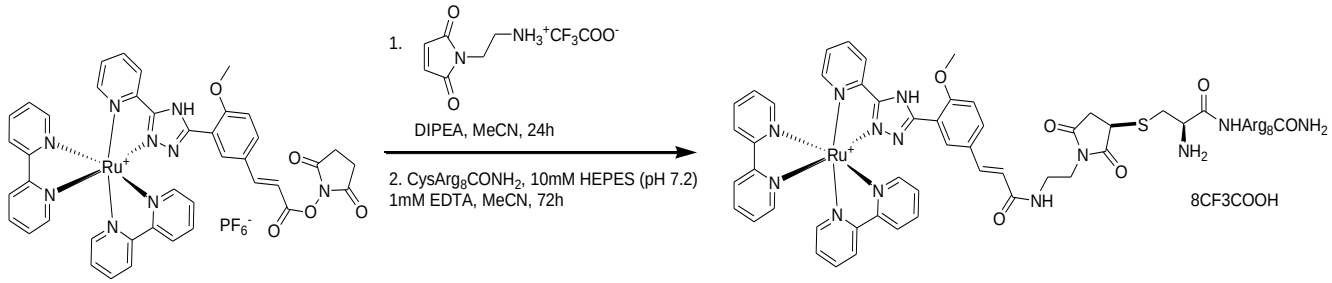

ruthenium bis(2,2-bipyridyl) [(2*E*)-3-{4-methoxy-3-[5-(pyridinyl)- 1,2,4-triazol-3-yl] phenyl} prop-2-enoyl]oxy}pyrrolidine-2,5-dione)

ruthenium bis(2,2-bipyridyl) [(2*E*)-3-{4-methoxy-3-[5-(pyridinyl)- 1,2,4-triazol-3-yl] phenyl} prop-2-enoyl]amino}ethyl)-2,5-dioxopyrrolidin-3-yl]- octaarginine

To a solution of ruthenium bis(2,2-bipyridyl) [(2*E*)-3-{4-methoxy-3-[5-(pyridinyl)- 1,2,4-triazol-3-yl] phenyl} prop-2-enoyl]oxy}pyrrolidine-2,5-dione) (0.019 g, 0.021 mmol) in anhydrous acetonitrile (2 cm^3) N-(2-aminoethyl)maleimide trifluoroacetate (0.006 g, 0.02 mmol) and diisopropylethylamine (0.05 cm^3, 0.07 mmol) were added and the mixture stirred at room temperature for twenty one hours. The solvents were evaporated under vacuum and the crude product was dissolved in acetonitrile (1 cm^3) (This stock solution was used in next step immediately). To a solution of $NH_2CysArg_7ArgNH_2$ (0.019 g, 0.015 mmol) in HEPES buffer (3 cm^3, 10 mmol, pH 7.2) containing EDTA (1 mmol) a stock solution of active ester was added and the resulting solution was stirred at room temperature for seventy-two hours. The solvents were then evaporated under vacuum the crude product was dissolved in water (5 cm^3), the insoluble fragments discarded and trifluoroacetic acid (0.1 cm^3) was added to the solution before freeze drying. Then the crude product was purified twice on silica gel C-18 (2 x 10 g) using water-acetonitrile (0,1% of TFA) 3-2 as eluent. The first fraction was collected and freeze-dried (0.04 g, 59 %).

MALDI-MS: calculated for $C_{94}H_{140}N_{44}O_{13}RuS$ $(M+H)^+$: 2228.0478; found 2228.8857 Da $(M+H)^+$

3.1.5 Synthesis of ruthenium – BODIPY conjugate

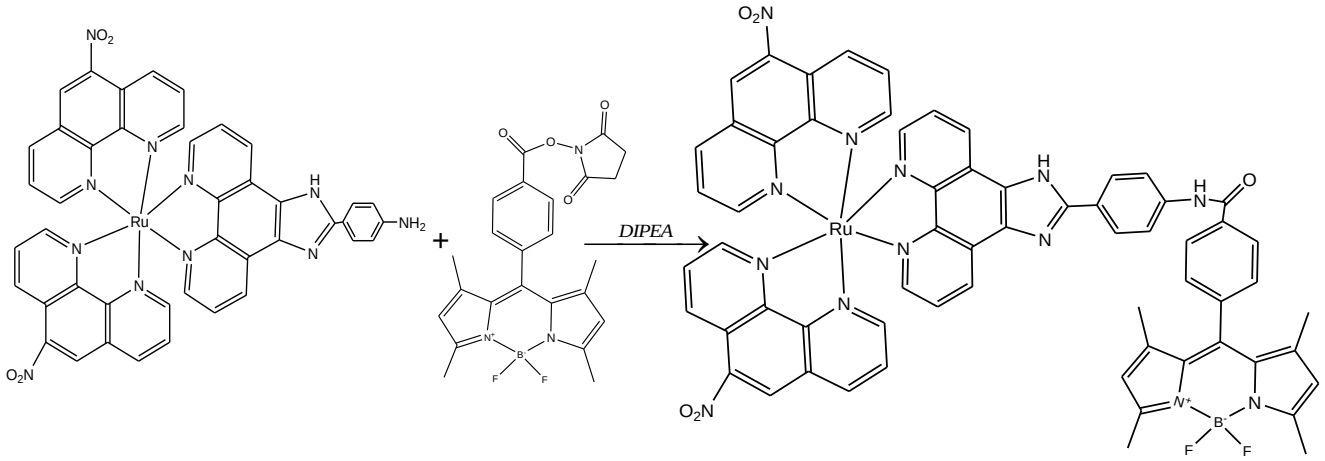

$[Ru(NO_2phen)_2(picNH_2)]^{2+}$ (0.201 g, 0.232 mmol), 8-benzoic acidpyrrolidine-2,5-dione-4,4-difluoroboradiazaindacene [BODIPY-NHS] (0.85 g, 0.182 mmol) and N,N-Diisopropylethylamine (135 μL) were added to a 10 cm^3 round bottomed flask containing dichloromethane (4 cm^3) and acetonitrile (15 cm^3) and the mixture stirred for eighteen hours.

The solvents were removed by rotary evaporation and the orange residue was collected. The solid was then purified using an alumina (basic) chromatographic column using 10% methanol : dichloromethane mobile phase. A separate purification was attempted using a silica chromatographic column using 40% (v/v) hexane : ethyl acetate mobile phase. Pure product was never isolated.

conjugation using EDC/NHS coupling reagents

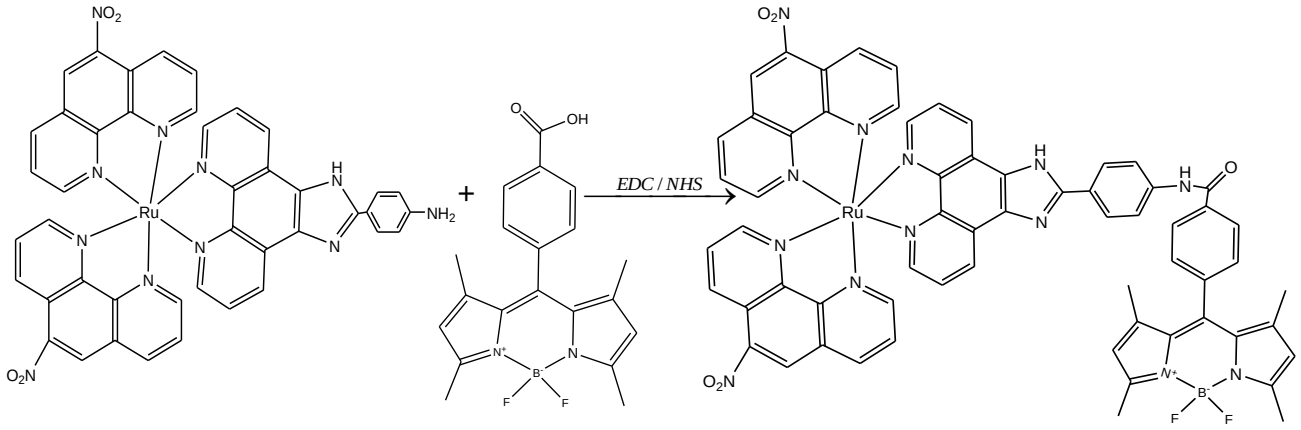

8-benzoic acid-4,4-difluoroboradiazaindacene [BODIPY-COOH] (0.027 g, 0.074 mmol) and 1-ethyl-3-[3-dimethylaminopropyl] carbodiimide hydrochloride [EDC] (0.012 g, 0.074 mmol) were added to a 10 cm^3 round bottomed flask containing PBS buffer pH 7.0 (5 cm^3) and stirred for 10 minutes. Then, N-hydroxysulfosuccinimide [NHS] sodium salt (0.008 g, 0.074 mmol) was added to the solution and it was left to stir for an additional 30 minutes.

$[Ru(NO_2phen)_2(picNH_2)]^{2+}$ (0.077 g, 0.089 mmol) and N,N-Diisopropylethylamine (381 μL, 0.223 mmol) were added was then added to the reaction mixture and left stirring overnight.

The solvents were removed by rotary evaporation and the orange residue was collected. The solid was then purified using an alumina (basic) chromatographic column using 10% methanol : dichloromethane mobile phase. A separate purification was attempted using a silica chromatographic column using 40% (v/v) hexane : ethyl acetate mobile phase. Pure product was never isolated.

3.2 Results & Discussion

3.2.1 Synthesis

The synthesis of the imidazole (pic) ligand was reported previously and is dependent on the acid catalysed reaction of 1,10-phenanthroline 5,6-dione with the excess ammonium acetate to provide the critical 1,10-phenanthroline 5,6-di-imine intermediate (1) . This intermediate was then reacted with a chosen aldehyde to undergo an aldol-type of condensation, forming a second intermediate. This step is followed by a two hydrogen shift leading to the loss of a water molecule forming the imidazole complex as shown in figure 3.11[95]

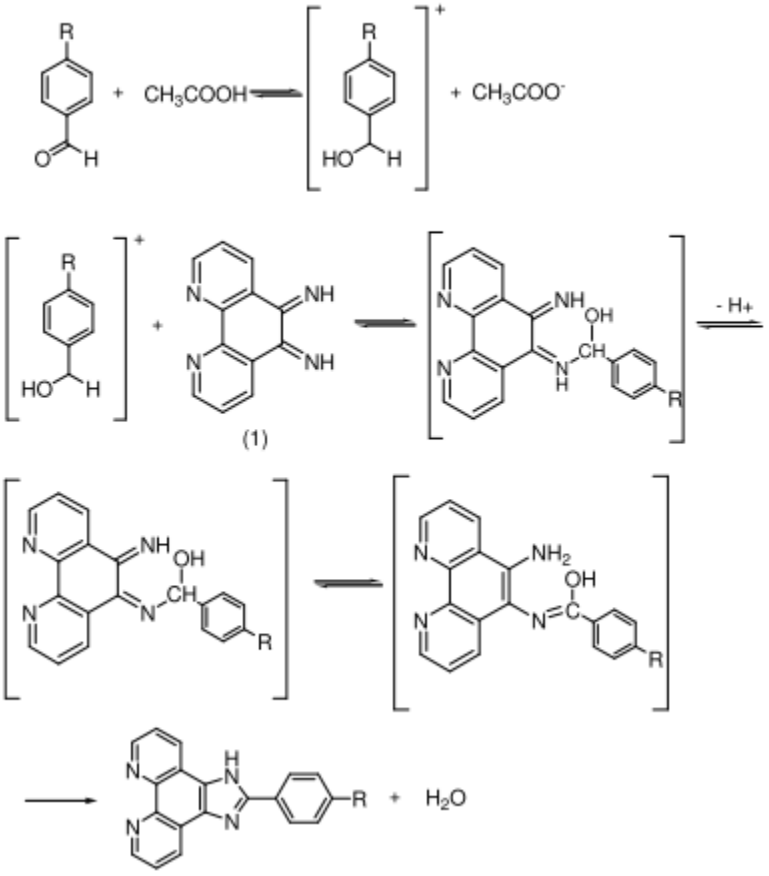

Figure 3.11: Mechanism illustrating the formation of the imidazole ligand.[95]

The synthesis of $[(Ru(phen)_2L\text{-}L)]^{2+}$ and $[(Ru(NO_2phen)_2L\text{-}L)]^{2+}$ (where L-L are bidentate polypyridyl ligands) complexes from $[(Ru(phen)_2L\text{-}L)]^{2+}$ and$[(Ru(phen)_2L\text{-}L)]^{2+}$ proceeds by the replacement of two chloride atoms with water molecules under reflux in water. Lability of the water ligands in the resulting complexes allows a facile attachment of a designated Pic ligand. The first chloride atom can be replaced at low temperatures in organic solvents such as acetone and ethanol. There is a difference in lability of the two chloride atoms and the second atom must be replaced using a solvent with a high boiling point or with the addition of water[96]. All complexes were synthesised under reflux using an ethanol / water (1:1) mixture and purified by column chromatography on alumina.

The initial route to the synthesis of $[Ru(NH_2\ phen)_2Cl_2]$ followed similar reactions to those reported in the literature using $[RuCl_3]$ and (NH_2phen) and proved to be unsuccessful.[97] It was then decided to attempt an alternative, novel approach via the preparation of $[(Ru(NO_2phen)_2Cl)]^{2+}$ and subsequent reduction of the nitro to amine groups. Reduction of the aminophenantrholine ligand after it had been already coordinated to the metal centre was successful with the reduction step giving a high yield (>85%).

The ease of synthesis of Pic ligands with selective functional terminal group grants the possibility of linking further complexes to additional ligands. The COOH and NH_2 groups allow for the facile extension of the functionality of the molecule. The nitro containing phenanthroline ligands attached to the metal centre are modifiable for reduction, which provides for the possibility of conjugating one moiety at the pic terminus with one or more different groups at the NO_2 after reduction.

3.2.2 ^{1}H-NMR Spectroscopy

Fig. 3.12: structural representations of $[Ru(phen)_2Cl_2]$(I) and $[Ru(NO_2phen)_2Cl_2]$(II)

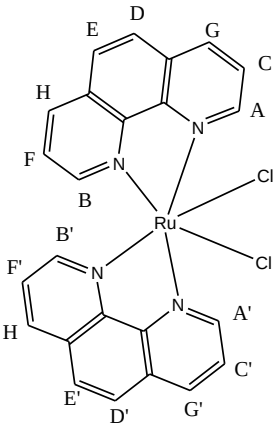

(I)

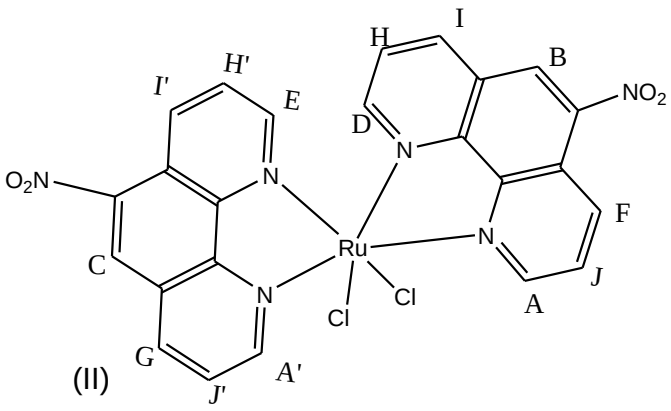

(II)

Phen proton	$[Ru(phen)_2Cl_2]$ ppm	NO_2phen proton	$[Ru(NO_2phen)_2Cl_2]$ ppm
H^A / $H^{A'}$	10.21 (d, 2H)	H^A / $H^{A'}$	10.34 (m, 2H)
H^B / $H^{B'}$	8.65 (d, 2H)	H^B	9.35 (s, 1H)
H^C / $H^{C'}$	8.24 (d, 2H)	H^C	9.20 (s, 1H)
H^D / $H^{D'}$ /H^E/$H^{E'}$	8.17 (m, 4H)	H^D	9.03 (d, 1H)
H^F / $H^{F'}$	8.08 (d, 2H)	H^E	8.94 (d, 1H)
H^G / $H^{G'}$	7.68 (d, 2H)	H^F	8.61 (d, 1H)
H^H / $H^{H'}$	7.28 (dd, 2H)	H^G	8.48 (d, 1H)
		H^H / $H^{H'}$	8.31 (m, 2H)
		H^I	8.01 (m, 2H)
		H^J / $H^{J'}$	7.45(dt, 2H)

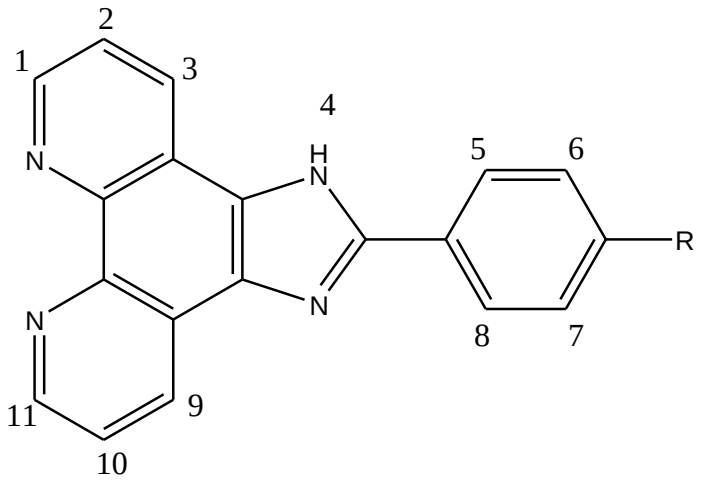

Figure 3.12: [pic-R] ligand illustrating numbering scheme for ^{1}H-NMR analysis

proton	[picCOOH] ppm	proton	[picNO$_2$] ppm	proton	[picNH$_2$] ppm
carboxyl-H	13.91 (s, 1H)	H_1, H_{11}	9.07 (d, 2H)	H_4	13.38 (s, 1H)
H_1, H_{11}	9.06 (d, 2H)	H_3, H_9	8.92 (d, 2H)	H_1, H_{11}	9.06 (d, 2H)
H_3, H_9	8.95 (d, 2H)	H_5, H_6, H_7, H_8	8.52 (m, 4H)	H_3, H_9	8.96 (d, 2H)
H_6, H_7	8.41 (d, 2H)	H_2, H_{10}	7.86 (m, 2H)	H_5, H_8	8.02 (d, 2H)
H_5, H_8	8.20 (d, 2H)			H_2, H_{10}	7.88 (d, 2H)
H_2, H_{10}	7.87 (m, 2H)			H_6, H_7	6.81 (d, 2H)
				amino-NH$_2$	5.72 (s, 2H)

Table 3.11: ^{1}H-NMR resonances for [pic-R] ligand with various functional groups, carried out in DMSO-d_6. The integration and peak splitting are shown in brackets.

Mass spectrometry was used in conjunction with NMR (^{1}H-NMR / COSY) to confirm the purity and structure of the complexes synthesised. Table 3.11 shows the full ^{1}H-NMR data for each of the three pic ligands synthesised. The R-group on each of the ligands contains constituents that differ in their electron donating and electron withdrawing properties. As a result the protons showing the largest change in chemical shift are located on the phenyl ring of the pic ligand. The nitro and carboxylic acid groups are electron withdrawing and draw electron density away from nearby protons; thus deshielding other protons on the rings resulting in a chemical shift downfield.

In the amino-pic ligand, the electron donating NH_2 group has lone pairs adjacent to the phenyl ring which increase the electron density on the ring, leading to an upfield shift of the phenyl protons. This is most notably observed in the comparison of the electron donating amino group and the electron donating nitro group. The protons located at positions H6 and H7 on the amino functionalised pic ligand are shifted upfield to 6.81 ppm, while the corresponding atoms on the nitro-pic ligand have a chemical shift of 8.52 ppm. The protons on the imidazole ligand were not observed in the [picCOOH] or [picNO_2] ligands, presumably due to the protons being very active and therefore readily exchangeable between the two nitrogens on the imidazole ring and deuterium in the solvent.[98]

The ^{1}H-NMR spectra for the [Ru(phen)$_2$Cl$_2$] and [Ru(NO_2phen)$_2$Cl$_2$] showed signals at 10.21 and 10.34 ppm respectively, each integrating for 2H. These peaks are attributed to the protons neighbouring the two chlorine atoms, as the electron density is decreased around each proton and they are shifted downfield. These peaks would only be expected at such a frequency is bis-complexes, as displacement of the chlorine atoms will change the chemical environment of the protons. The coordinating pic ligand leads to greater electron density around these protons, resulting in greater shielding of the external magnetic field, and a shift upfield of approximately 1 ppm.

$[Ru(NO_2phen)_2 picCOOH]^{2+}$		$[Ru(NO_2phen)_2 picNH_2]^{2+}$	
NO_2phen protons ppm	picCOOH protons ppm	NO_2phen protons ppm	$picNH_2$ protons ppm
H^B / H^C 7.88 (m, 2H)	H_1, H_{11} 8.03 (d, 2H)	H^J / $H^{J'}$ 9.10 (t, 2H)	H_1, H_{11} 9.21 (d, 2H)
H^F / H^G 7.64 (m, 2H)	H_5, H_8 7.95 (m, 2H)	H^B, H^C 9.01 (ds, 2H)	H_5, H_8 7.94 (d, 2H)
H^I / $H^{I'}$ 7.06 (m, 4H)	H_3, H_9 7.06 (m, 4H)	H^H / $H^{H'}$ 8.77 (t, 2H)	H_3, H_9 7.76 (m, 4H)
H^F / H^G 7.04 (m, 2H)	H_2, H_{10} 6.91 (dd, 2H)	H^A / $H^{A'}$ / H^D / H^E 8.24 (m, 4H)	H_2, H_{10} 7.61 (dt, 2H)
H^J / $H^{J'}$ 6.91 (dd, 2H)	H_6, H_7 6.51 (d, 2H)	H^I / $H^{I'}$ 7.88 (m, 2H)	H_6, H_7 6.74 (d, 2H)
H^H / $H^{H'}$ 6.79 (dt, 2H)		H^F / H^G 7.76 (m, 4H)	NH_2 5.39 (s, 2H)
H^A / $H^{A'}$ / H^D / H^E 6.58 (m, 4H)			

Table 3.12: ^{1}H-NMR resonances for [pic-R] ligand with various functional groups, carried out in methanol-d_4. The integration and peak splitting are shown in brackets.

Table 3.13 shows the relative shift in ppm of the free [pic] ligand compared to the metal coordinated [pic] ligand. The greatest change for the pic ligands were located at H3 and H9 following the ligand's coordination to the ruthenium center. This change is attributed to an increase in electron density around each proton as they are shifted upfield. The ruthenium complex has a d^6 filled shell and it's coordination increases the electron density on the pic ligand, which causes a delocalised shielding effect focused on the protons at H3 and H9. As with the free ligands, the protons on the imidazole ligand were not observed for either metal, again presumably due to the protons being very active and can be readily exchanged between the two nitrogens on the imidazole ring.

Proton	$[Ru(NO_2phen)_2 picCOOH]^{2+}$ Δ ppm	$[Ru(NO_2phen)_2 picNH_2]^{2+}$ Δ ppm
H_1	0.02	0.04
H_2	0.12	0.01
H_3	-1.18	-1.21
H_5	0.02	-0.08
H_6	0.59	-0.06
H_7	0.57	-0.07
H_8	0.02	-0.08
H_9	-1.16	-1.20
H_{10}	0.12	0.02
H_{11}	0.02	0.04

Table 3.13: Δ ppm of ^1H NMR shifts of coordinated complexes compared to free ligand

3.2.3 Optical Characterisation of ruthenium complexes

3.2.3.1 Absorbance

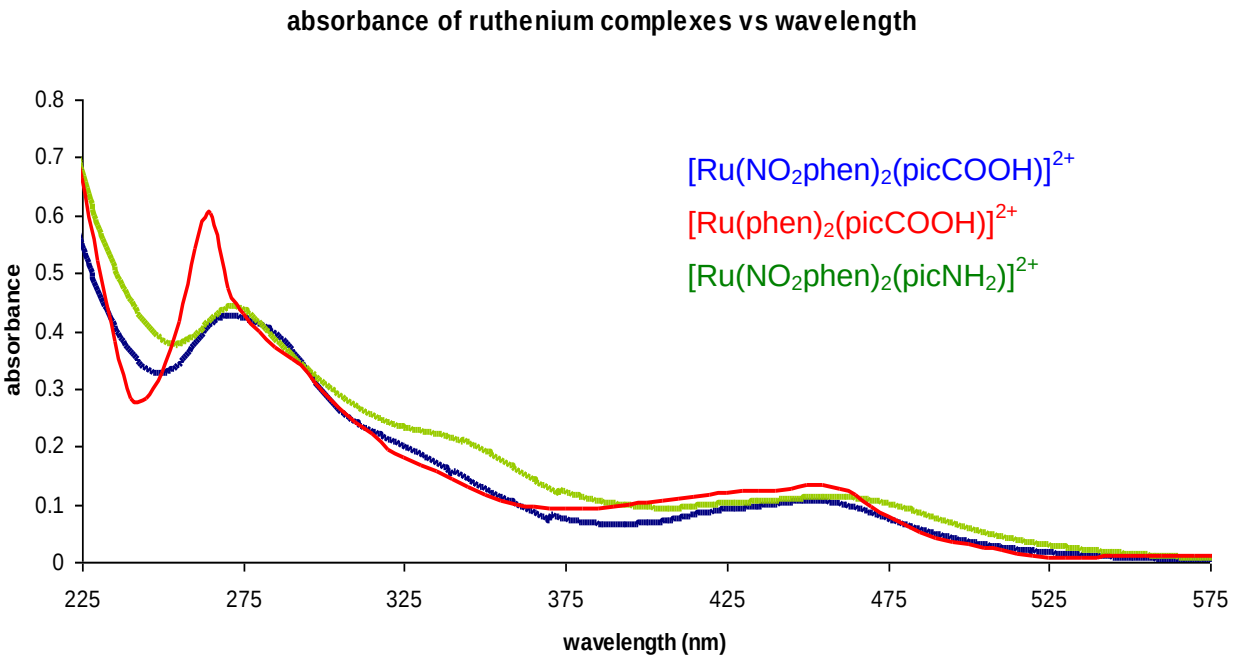

Figure 3.13: Overlaid absorbance spectra of ruthenium (II) polypyridyl complexes (10μM) in acetonitrile solution.

Shown in Figure 3.13 is an overlay of the absorbance spectra for the three novel ruthenium(II) pic complexes. The UV-vis spectra of all three complexes are distinguished by a ruthenium dπ to ligand π* metal to ligand charge transfer (MLCT) at 457 nm (phen-carboxyl), 457 nm (nitrophen-carboxyl) and 462 nm (amino) band respectively. The shift in the λ_{max} of the amino complex of approximately 5 nm to longer wavelength compared to the carboxyl complexes, is consistent with the fact that the amino ancillary ligand is a slightly better σ-donating ligand.[99] This shift to longer wavelength suggests a decrease in the HOMO-LUMO band gap for the t_{2g} to ligand π* transition.

The strong absorbance peak at approximately 265 nm in the spectrum of $[Ru(phen)_2(picCOOH)]^{2+}$ may be assigned to π-π* transitions within the phenanthroline ligands. This peak has shifted approximately 9 nm to a longer wavelength for both complexes containing nitro functionalised phenanthroline ligands, when compared to $[Ru(phen)_2(picCOOH)]^{2+}$. These peaks are found at a wavelength approximately 10 – 15 nm shorter than $[Ru(bpy)_2(picCOOH)]^{2+}$, described previously in the literature.[11] The wavelength of the peak is clearly dependent on the phenanthroline ligand, which confirms the peak as a π-π* transition of the NO_2phen ligands. These ILCT π-π* transitions permit hyperconjugation between the electronic structures and aromatic rings which increases the stability of the complexes. This causes a decrease in the HOMO-LUMO energy gap which results in a shift to longer wavelengths.[100, 101]

The other transitions in the UV/VIS spectra of each complex at approximately 340 nm are attributed to π-π* transitions of the [pic-R] ligands. This is confirmed as these bands exhibit a strong pH dependence, as expected as the pic ligands contain two ionisable protons on the imidazole ring, as discussed in the introduction. The 260 nm transition is thought to have MLCT character as a high energy CT transition was observed in $[Ru(bpy)_3]^{2+}$.[5]

3.2.3.2 Photophysics

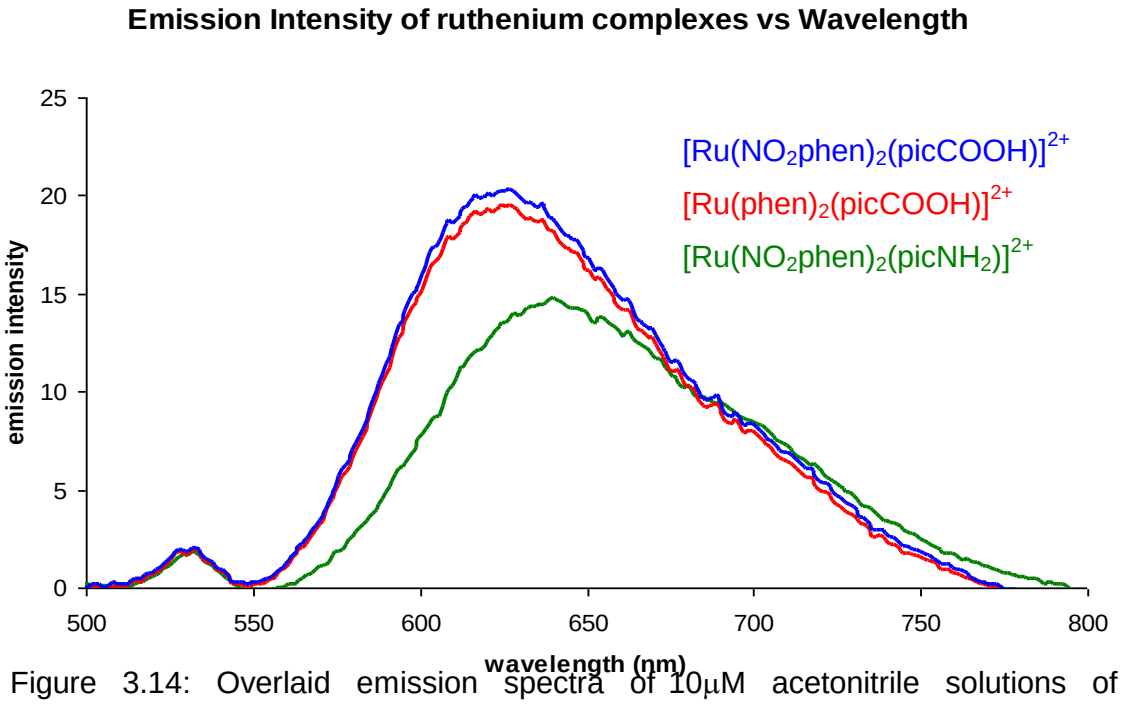

Figure 3.14: Overlaid emission spectra of 10μM acetonitrile solutions of $[Ru(NO_2phen)_2(picCOOH)]^{2+}$ (excited at 457 nm), $[Ru(phen)_2(picCOOH)]^{2+}$ (excited at 457 nm) and $[Ru(phen)_2(picNH_2)]^{2+}$ (excited at 462 nm). Emission slit: 5 nm, excitation slit: 5 nm, PMT detector voltage: 600V. Samples are not absorbance matched.

Shown in Figure 3.14 are the emission spectra for the synthesised ruthenium(II) complexes. Table 3.21 summarizes the spectroscopic data for the three complexes. The emission spectrum of $[Ru(NO_2phen)_2(picCOOH)]^{2+}$ exhibits a maximum emission at 621 nm when excited into the MLCT absorbance band at 457 nm. Excitation into the $[Ru(phen)_2(picCOOH)]^{2+}$ MLCT band also resulted in an intense emission at 619 nm. The emission spectrum of $[Ru(NO_2phen)_2(picNH_2)]^{2+}$ exhibits a slight red shift to 634 nm. This is again a result of the electron donating nature of the amino substituent, which leads to a decrease in the LUMO energy for the $picNH_2$ ligand. Importantly, the Stokes shift for all synthesized complexes exceeds 150 nm, reducing the possibility for concentration quenching or self-absorption by the complex where these complexes are used in imaging. The Stokes shift also allows the possibility for the acquisition of resonantly enhanced Raman spectra without interference from the emission of the complex when exciting into the MLCT band.

3.2.3.3 Emission Lifetime

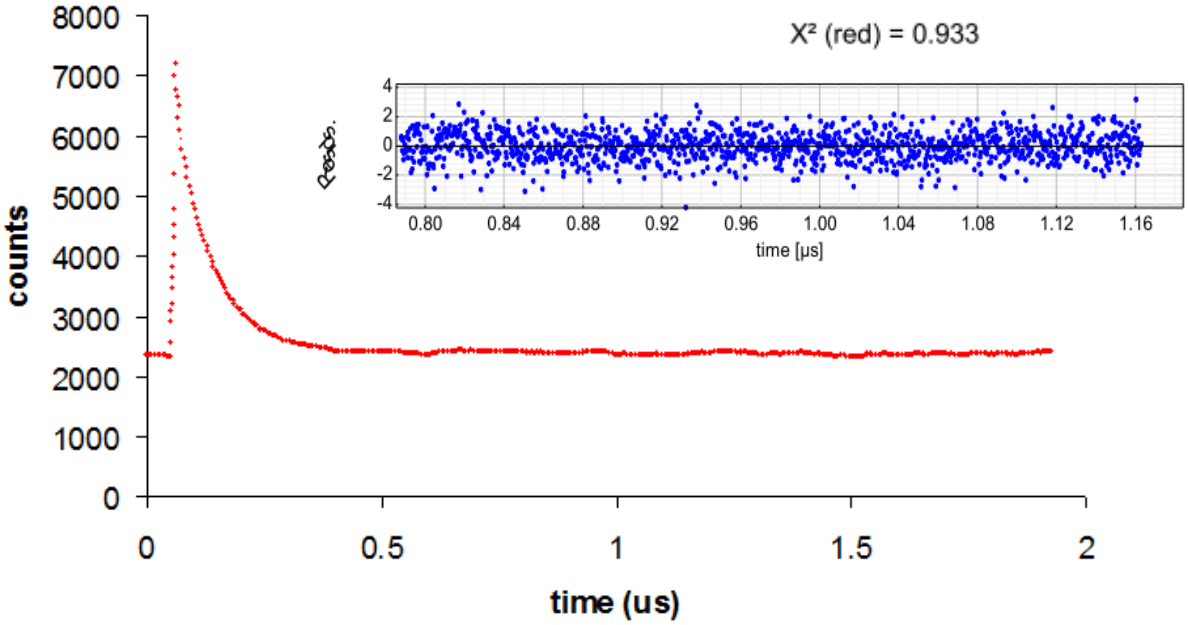

Figure 3.15: Emission lifetime of $[Ru(NO_2phen)_2(picCOOH)]^{2+}$ (20 μM) in acetonitrile solution

The emission decays of all three complexes follow mono-exponential kinetics in aerated and in degassed acetonitrile (using argon). The lifetime of $[Ru(NO_2phen)_2(picCOOH)]^{2+}$ was 159 ns in aerated acetonitrile and 451 $\pm$ 3 ns in degassed acetonitrile, while the lifetime of $[Ru(phen)_2(picCOOH)]^{2+}$ was 151 ns in aerated acetonitrile and 430 $\pm$ 5 ns in degassed acetonitrile. The observed lifetime increase in the absence of oxygen is indicative of the triplet MLCT character of the emission. The quenching mechanism is expected to be triplet to triplet energy transfer to oxygen resulting in loss of emission at the ruthenium centre and production of singlet oxygen. The lifetime of $[Ru(NO_2phen)_2(picNH_2)]^{2+}$ was 61 ns in aerated acetonitrile and 79 ns in degassed acetonitrile. As oxygen quenching is a diffusion controlled process the oxygen sensitivity is lower in short lived complexes.

Table 3.21: Optical properties of Ruthenium (II) Complexes Synthesised. Absorbance measurements were carried out at room temperature at concentrations of 20 x 10^6 M. Lifetime values were measured in aerated / degassed acetonitrile at room temperature and fit to monoexponential decay plots. Photoluminescent quantum yield (ϕ) measured in degassed acetonitrile at room temperature, using $[Ru(bpy)_3]^{2+}$ as a standard.

compound	Absorbance λ_{max} (ε, $dm^3mol^{-1}cm^{-1}$)	Emission λ_{max}	τ (ns) aerated / degassed	ϕ
$[Ru(phen)_2(picCOOH)]^{2+}$	457 nm (13,193) 336 nm (20,090) 265 nm (51,297)	611 nm	159 / 451	0.048
$[Ru(NO_2phen)_2(picCOOH)]^{2+}$	457 nm (11,871) 338 nm (21, 304) 274 nm (44,611)	611 nm	151 / 430	0.042
$[Ru(NO_2phen)_2(picNH_2)]^{2+}$	462 nm (11,984) 337 nm (27,545) 274 nm (45,135)	632 nm	61 / 79	0.031

3.2.4 **Ruthenium triazolate complexes and their Polypeptide conjugates**

3.2.4.1 Absorbance

Shown in figure 3.21 is the UV/VIS absorbance of the $[Ru(bpy)_2htrz\text{-}arg_8]^{9+}$ and its parent dye which exhibits four electronic transitions at approximately 227 nm, 258 nm, 290 nm and 458 nm. The molar extinction coefficients of the ruthenium peptide conjugate were calculated to be 78,9426 $M^{-1}cm^{-1}$, 64,037 $M^{-1}cm^{-1}$ 117,611$M^{-1}cm^{-1}$ and 19,800 $M^{-1}cm^{-1}$ respectively. Conjugation of the ruthenium(II) dye to the peptide did not cause any significant alterations to the wavelength of absorbance and emission of the conjugate when compared to the parent dye.

The UV-vis spectra of both complexes are distinguished by a ruthenium $d\pi$ to ligand π^* a metal to ligand charge transfer (MLCT) at 458 nm, with the tail of the dye – peptide extending to a slightly longer wavelength. The shoulder at approximately 340 nm is attributed to π-π* transitions of the triazole ligand. As reported in section 1.1.4, these bands exhibit strong pH dependence as the ligands contain two ionisable protons on the triazole ring. The strong absorbance peak at approximately 289 nm may be assigned to π-π* transitions within the bipyridine ligands.

The absorption band at 458 nm is similar to that of ruthenium triazole complexes previously described by Lees et al.[102] who reported MLCT transitions at 460 nm and 461 nm. In these complexes, a red shift of approximately 25 nm was observed for pyridine based complexes explained by the strong σ-donor effect of the pyridine ring. $[Ru(bpy)_2htrz\text{-}arg_8]^{9+}$ and its parent dye also show the same spectral properties as those of the corresponding $[Ru(bpy)_2(2\text{-}ppt)]$ complex where ppt is 5-(pyridin-2-yl)-1,2,4-triazole.[103]

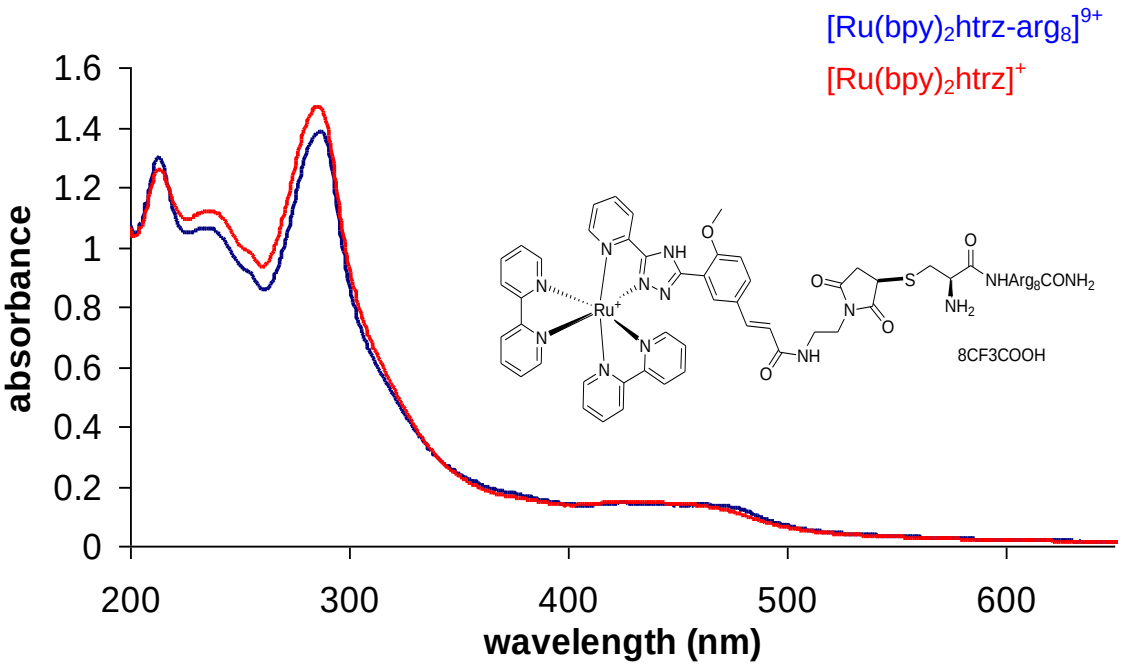

3.21: Absorbance spectra of $[Ru(bpy)_2htrz\text{-}arg_8]^{9+}$ and $[Ru(bpy)_2htrz]^{+}$ (20×10^{-6} M) in PBS buffer (pH 7.4) solutions

3.2.4.2 Photophysics

Shown in Figure 3.22 is the emission spectrum of $[Ru(bpy)_2htrz\text{-}arg_8]^{9+}$ and its parent dye. The emission spectrum of the parent complex exhibits a maximum emission at 651 nm when excited into the MLCT absorbance band at 458 nm with a quantum yield of 0.005 in PBS. The emission decays follow monoexponential kinetics with the excited state lifetime of $[Ru(bpy)_2htrz\text{-}arg_8]^{9+}$ in the presence of oxygen in PBS reduced from 147 ns to 91 ns, with the parent complex being reduced from 139 ns to 84 ns. The decrease in lifetime in the presence of oxygen is also an indication of the triplet MLCT character of the emission.[12] Table 3.22 compares the photophysical results of the parent ruthenium dye and the ruthenium – peptide conjugate. The lifetimes and quantum yields are very similar in the comparison of the free ruthenium (II) dye with the conjugated complex indicating that the peptide had little effect on the photophysics of the luminophore. These results correspond well with previous studies into ruthenium bipyridyl peptide conjugates which also showed little impact on optical or photophysical properties when conjugated.[12] Ruthenium triazole complexes containing two carboxy-bipyridine ligands reported by Lees et al. had an emission maxima of over 670 nm, a red shift of 20 nm with respect to the values observed for bpy derivatives.[102] Emission in ruthenium polypyridyl complexes occurs from a triplet metal to ligand charge transfer (^{3}MLCT) state. Detailed resonance Raman studies, excited state pKa measurements and isotopic labelling studies have shown that for pyridine triazole complexes this emitting state is bpy-based, irrespective of the state of protonation of the triazole ring.[104]

Compound	Absorbance λ_{max} (ε, $dm^3mol^{-1}cm^{-1}$)	Emission λ_{max}	τ (ns) aerated / degassed	ϕ
$[Ru(bpy)_2htrz]^{2+}$	**457 nm (19,626) 290 nm (116,931) 258 nm (64,129) 227 nm (78,302)**	**651 nm**	**84 / 139**	**0.005**
$[Ru(bpy)_2htrz\text{-}arg_8]^{10+}$	**458 nm (19,800) 291 nm (117,611) 258 nm (64,037) 227 nm (78,942)**	**651 nm**	**91 / 147**	**0.006**

Table 3.22: Optical properties of ruthenium peptide conjugate and parent complex. Absorbance measurements were carried out at room temperature at concentrations of 20 x 10^6 M. Lifetime values were measured in aerated / degassed PBS at room temperature and fitted to monoexponential decay plots. Photoluminescent quantum yield (ϕ) were measured in degassed PBS at room temperature, using $[Ru(bpy)_3]^{2+}$ as a standard.

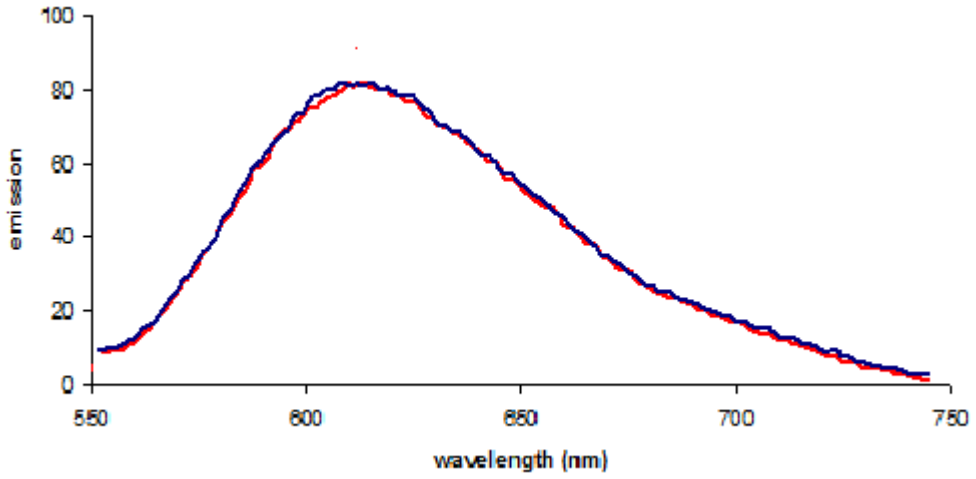

3.22: Overlaid emission spectra of $[Ru(bpy)_2htrz\text{-}arg_8]^{9+}$ and $[Ru(bpy)_2htrz]^{+}$ (20 x 10^{-6} M) in PBS buffer (pH 7.4) solutions. Emission slit: 5 nm, excitation slit: 5 nm.

3.2.4.3 pH Dependence Studies

$[Ru(bpy)_2(htrz)]^+$ contains a triazole moiety, and is therefore ionizble – comparable ligands have been discussed previously and the protonation state of the trizole, dramatically affects the optical properties of the complex.[104] This is due to the triazole ring being directly bonded to the metal and its protonation state affects the s-donor properties of the ligand. Vos[105] has previously reported a Ru (II) bipyridyl triazole complex where deprotonation of the triazole ligand resulted in lower oxidation potentials and in a red shift of the lowest energy dπ-π* absorption band. This effect is due to the stronger σ-donor ability of the deprotonated ligand. The acid – base behaviour of the triazole also has a profound effect on the photostability of the complex and this is discussed further in chapter 4.

In order to measure the effect of pH on the absorbance and emission spectra, $[Ru(bpy)_2(htrz)]^+$ was dissolved in phosphate buffered saline (pH 7.4) and pH was increased using sodium hydroxide; a separate aliquot of the same solution was decreased in pH with the gradual addition of perchloric acid. The absorbance and emission spectra were recorded at 0.5 pH unit intervals. To avoid spectral changes due to volume adjustment, working solutions of 20 cm^3 were used in conjunction with μL aliquots of acid or base.

Shown in Figure 3.23 are the three ionisable sites exhibited by $[Ru(bpy)_2(htrz)]^+$, two on the triazole and one on the carboxylic acid. Monitoring the electronic absorption spectra allows the protonation and deprotonation of these sites to be studied which can provide insight into the extent of electronic communication within the metal complex as a function of pH[11].

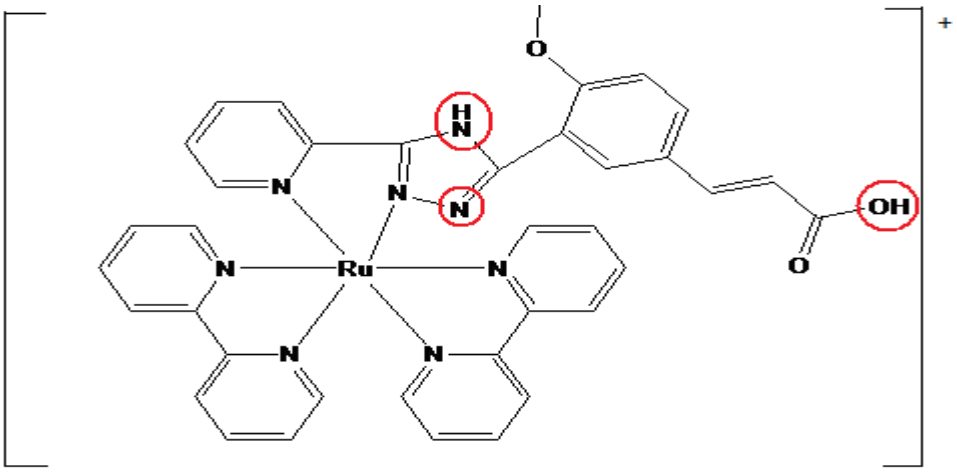

Figure 3.23: Available ionisable sites on $[Ru(bpy)_2htrz]^+$

Shown in figure 3.24 the ligand centered π-π* transition of the protonated species at 342 nm is shifted slightly to a shorter wavelength compared to the deprotonated species. The shift to lower wavelength and therefore higher energy suggests an increase in the HOMO-LUMO energy gap due to carboxylate formation.[11] The bpy π-π* transition appears slightly shifted from 284 nm to 281 nm.

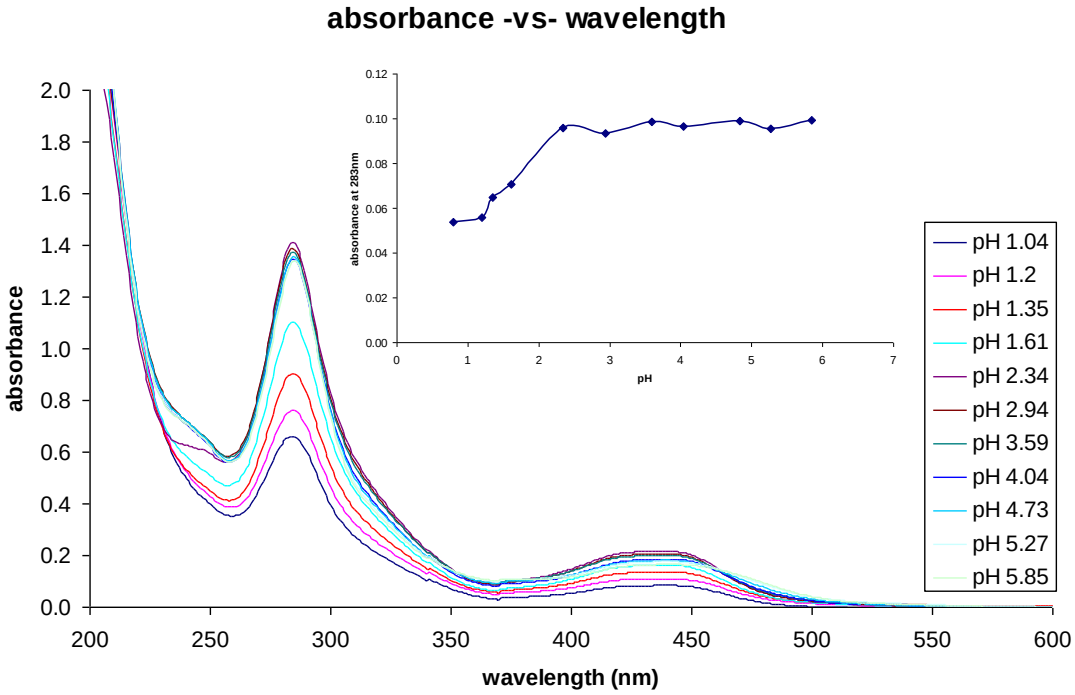

Figure 3.24: Absorbance spectra of $[Ru(bpy)_2(htrz)]^+$ (10μM) in PBS buffer solution, upon addition of μl aliquots of perchloric acid solution.(inset) pH titration curve of $[Ru(bpy)_2(htrz)]^+$ in PBS solution, monitoring the changes in absorbance at 283 nm upon addition of perchloric acid.

Deprotonation of the species leads to the triazolate complex above pH 6, showing a red shift in the MLCT from 449 nm to 472 nm, LC (htrzCOOH) π-π* transition at 345 nm and a shift in bpy π-π* transition from 284 nm to 287 nm. As the triazole ring is directly bound to the ruthenium centre, deprotonation of the ligand leads to increased s-donation ability and therefore increased ligand field splitting causing the t_{2g} level to be reduced, which results in the observed red shift. These effects have been previously noted in imidazole and triazole ligands.[11]

The ground state pKa values were determined by monitoring the spectral changes at 283 nm in the absorbance spectrum across a pH range of 0.8 – 12.7. Shown in figures 3.24 inset and 3.25 inset are plots of absorbance at 340 nm versus pH and from this data the point of inflection was determined by differentiation. The pKa values were estimated to be 1.9 and 6.9 respectively. Protonation of the triazole, to give the triazolium, occurs at low pH so the pKa value can only be given as an estimate. This protonation at low pH is believed to be due to coulombic repulsion between the positively charged triazolium ring and the positive metal centre.[11]

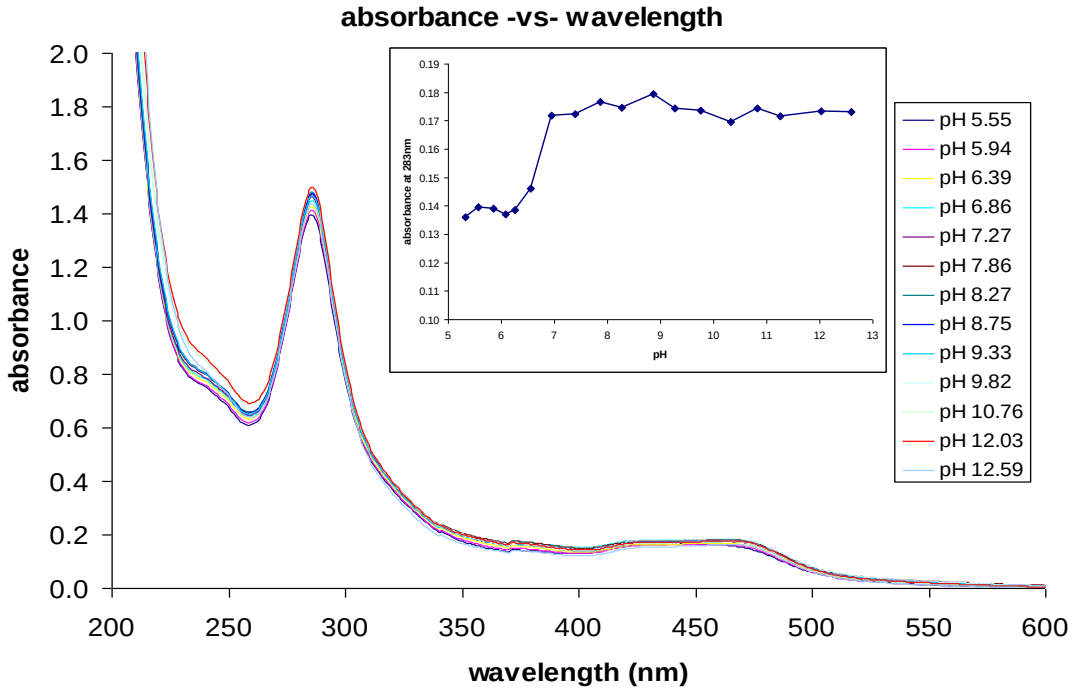

Figure 3.25: Absorbance spectra of $[Ru(bpy)_2htrz]^+$ (10μM) in PBS buffer solution, upon addition of μl aliquots of 7M sodium hydroxide solution.(inset) pH titration curve of $[Ru(bpy)_2htrz]^+$ in PBS solution, monitoring the changes in absorbance at 283 nm upon addition of 7M sodium hydroxide solution.

Protonation of the triazole on the ancillary ligand greatly affects both luminescent intensity and emission wavelength when compared to $[Ru(bpy)_2htrz]^+$. The red shift observed is greater than that observed in the equivalent absorbance spectra and may therefore due to a stabilising electrostatic interaction between the MLCT generated bpy anion radical and the extra positive charge of the triazolium.[11] The excited state pKa* values were estimated to be 1.6 and 8.5, respectively, from the graphs in Figures 3.26 (inset) and 3.27 (inset). These values were calculated using the Förster cycle.

The pKa values for the ground and excited state are similar, which suggests that the location of the excited state is not on the ionisable ligand but on the bipyridine ligands. This is also consistent with the excited state pKa* studies on comparable triazole complexes. Vos et al. have previously demonstrated that a large change in pKa values would be expected if the excited state was on the triazole ligand.[103]

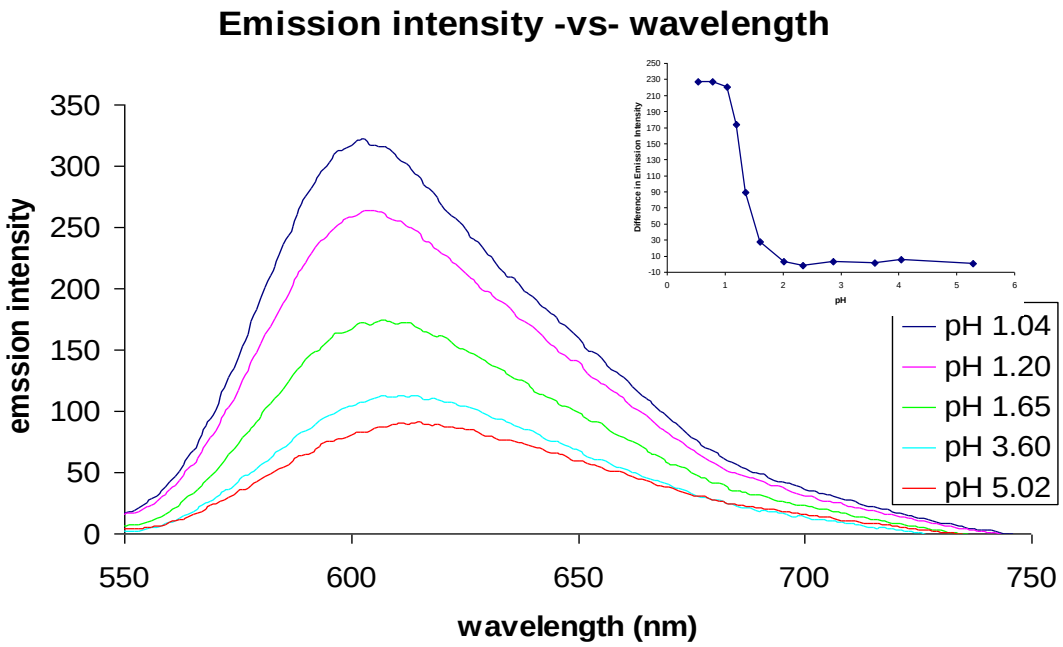

Figure 3.26: Overlaid emission spectra of $[Ru(bpy)_2htrz]^+$ (10μM) in PBS buffer upon addition of perchloric acid. Emission slit: 5 nm, excitation slit: 5 nm, PMT detector voltage: 600v, (inset) pH titration curve of $[Ru(bpy)_2htrz]^+$ in PBS solution, monitoring the difference in emission intensity upon addition of perchloric acid.

A significant red shift is observed upon deprotonation with sodium hydroxide from 629 nm to 652 nm. This spectral shift is most likely due to the stabilising electrostatic interaction between the MLCT generated bpy anion radical and the extra positive charge of the triazolium.

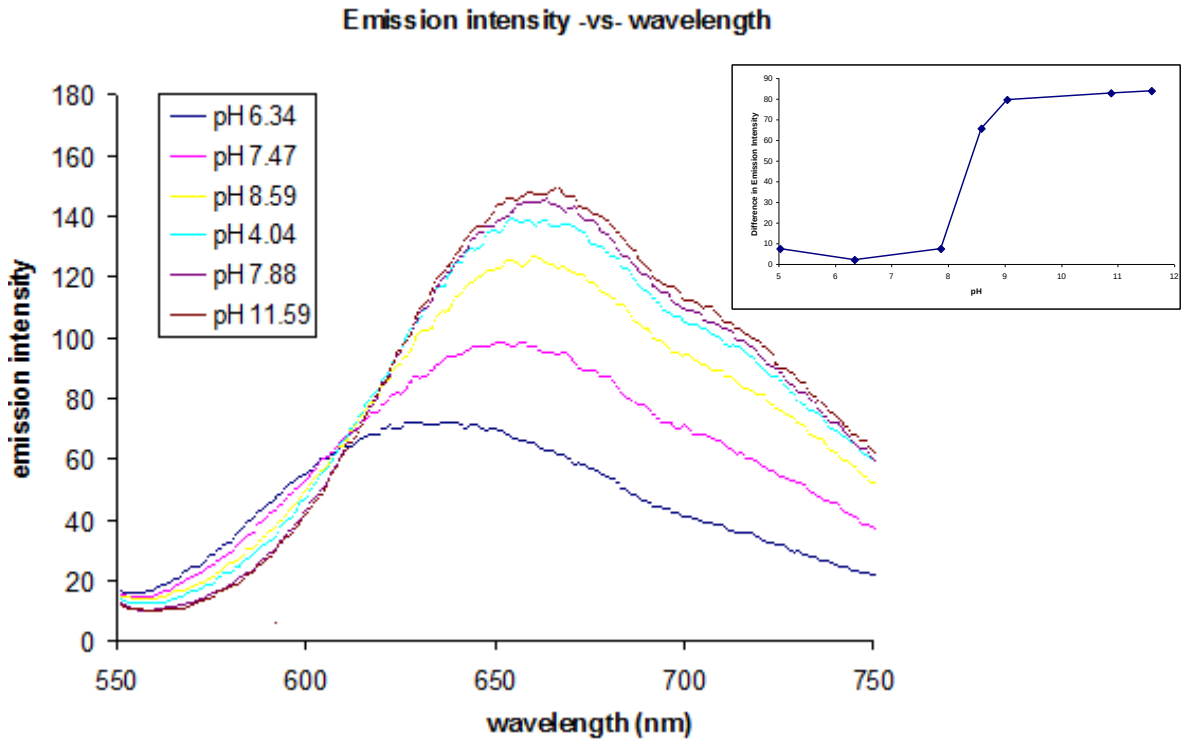

Figure 3.27: Overlaid emission spectra of $[Ru(bpy)_2htrz]^{2+}$ (10μM) in PBS buffer upon addition of sodium hydroxide solution. Emission slit: 5 nm, excitation slit: 5 nm, PMT detector voltage: 600v, (inset) pH titration curve of $[Ru(bpy)_2htrz]^{+}$ in PBS solution, monitoring the difference in emission intensity upon addition of 7M sodium hydroxide solution.

3.2.4.4 Resonance Raman Spectroscopy

Raman spectroscopy is a fundamentally weak phenomenon, as only 1 in 10^6 photons are inelastically scattered. However if the excitation laser coincides with an intense optical transition of the molecule, the signal may be significantly enhanced. This phenomenon, known as resonance Raman spectroscopy provides an enhancement of 10^3 up to 10^7 in signal in the vibrations of the chromophores involved in the transition, as described in greater detail in the general introduction. It has been used in biosensors to detect dye labelled targets as dyes can provide strong resonance Raman signals.[106, 107] Resonance with the MLCT transitions of ruthenium (II) polypyridyl complexes can yield intense Raman spectra with excellent signal-to-noise ratio. One of its key applications in studying coordination compounds with mixed ligands has been in the assignment of the optical transitions.

$[Ru(bpy)_2(htrz)]^+$ was irradiated with 458, 488 and 514 nm laser lines. The 458 nm laser line is coincident with the main visible MLCT absorption of the complex (as described in the UV-vis absorbance spectrum) and under these resonance conditions the vibrational modes associated only with the chromophores are enhanced. No pre-resonance lines of higher energies were used in this analysis.

Shown in figure 3.28 is an overlay over the resonance Raman spectra of the complex irradiated at 458, 488 and 514 nm. The signature bipyridyl vibrational modes are observed in each with no significant changes observed between the data, the frequencies and approximate assignments are shown in table 3.23. This suggests that the lowest energy optical transition in each case, arises from a ruthenium ($d\pi$) to bipyridyl ligand (π^*) MLCT transition. There is also evidence of a weak ruthenium-nitrogen stretch at 375 cm^{-1} also consistent with this assignement. All the Raman modes were collected in solution and assigned according to the published data. [108, 109]

Shown in figure 3.29 is an overlay of the resonance Raman spectra of the complex at pH 12 irradiated at 458, 488 and 514 nm. This pH range allowed exploration of the deprotonated species, two additional Raman peaks at 1082cm^{-1} and 1126cm^{-1} are observed at this pH with 514 nm excitation. While they appear at pH 12 when excited using the 458 nm and 488 nm laser lines, the peaks are much weaker and appear with far greater intensity with 514 nm excitation. As these peaks are more pronounced in the 514 nm spectrum, they may be attributed to lower energy Raman signals due to pyridyl in-plane twisting modes.

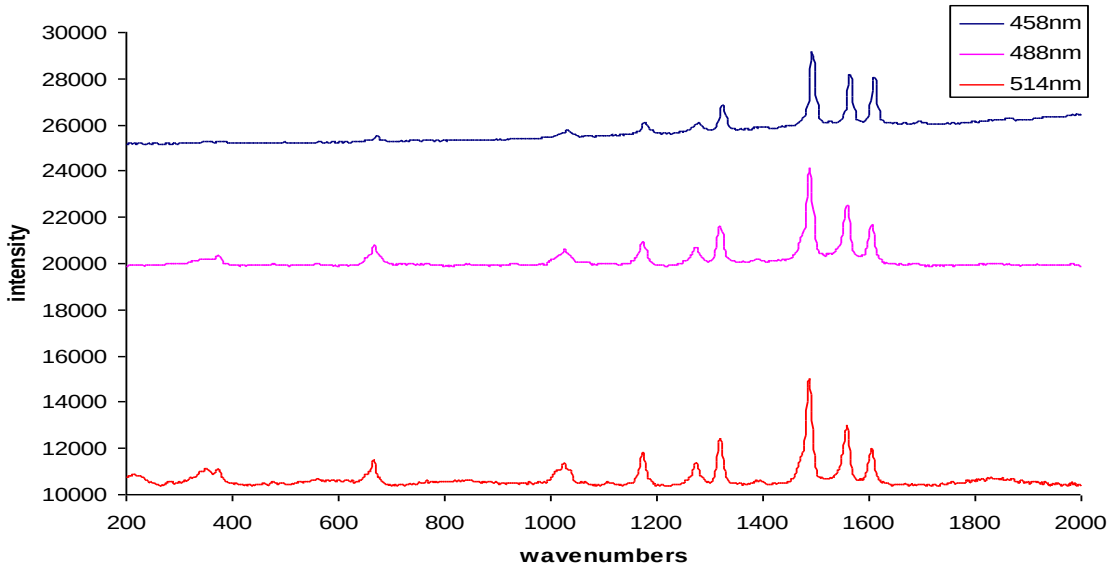

Figure 3.28: Stacked Raman spectra of $[Ru(bpy)_2(htrz)]^+$. Samples were measured in their solid state using 458 nm (top), 488 nm (middle) and 514 nm (bottom) excitation laser lines. All spectra were gathered with 5 acquisitions and an exposure time of 2 seconds with a laser power of 10mW

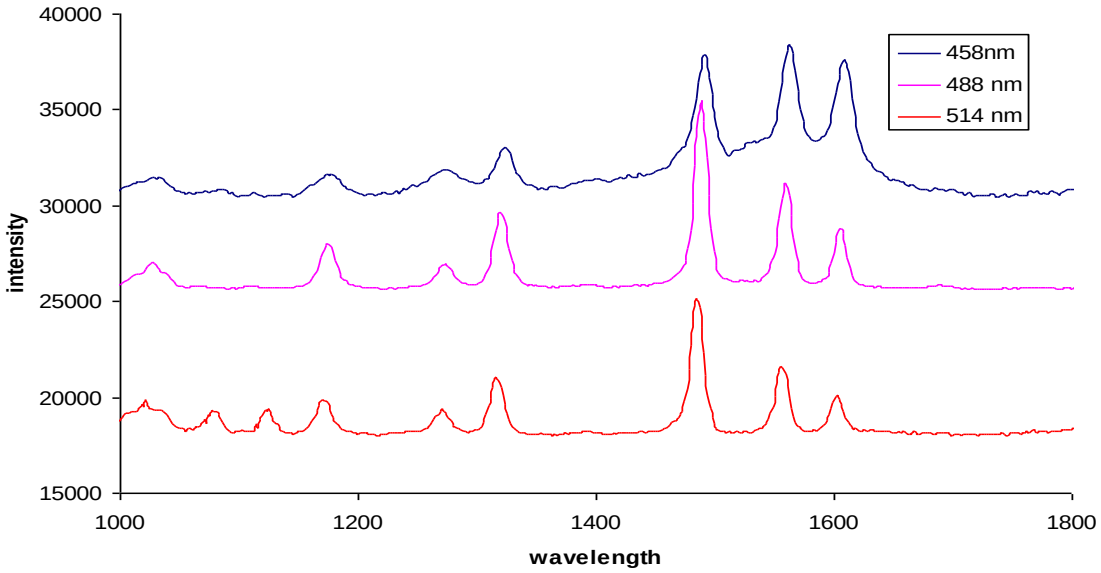

Figure 3.29: Stacked Raman spectra of $[Ru(bpy)_2(htrz)]^+$ at pH 12. Solid Samples were measured in their solid state using 458 nm (top), 488 nm (middle) and 514 nm (bottom) excitation laser lines. All spectra were gathered with 5 acquisitions and an exposure time of 2 seconds with a laser power of 10mW.

Table 3.23: General assignment of Raman vibrational modes of the ruthenium (II) complexes synthesised using 458 nm excitation.

458 nm excitation	(cm^{-1})	Assignment
Bipyridyl vibrational modes:	~ 1609	C = C stretch
	~ 1564	C = C stretch
	~ 1490	C = C stretch
	~ 1315	C = C stretch
	~ 1281	C-C (inter-ring bending)
	~ 1189	CCH (in-plane bending)
	~ 1030	Ring breathing
	~ 668	Pyridyl in-plane twisting
ruthenium – ligand vibrational modes:	~ 375	Metal-ligand stretch

3.2.4.5 Photostability – irradiation under white light

One of the key disadvantages of conventional organic fluorophores used in cell imaging, such as fluorescein and its derivatives is the very poor photostability. This can severely restrict their usefulness in monitoring dynamic processes in cells where continuous irradiation over seconds or minutes is required. Neugebauer[12] has previously reported the improved photostability of Ru(II) complexes in cell applications compared to such probes. However, Ru(II) triazole complexes in particular have been reported to exhibit very high photostability.[102-104] Therefore, here we examined and compared the order to determine the stability of $[Ru(bpy)_2(htrz)]^+$ under white light irradiation in acetonitrile (which can act as a coordinating ligand and destabilise the complex) and in PBS buffer, i.e. conditions like those in cell imaging. 10μM samples in acetonitrile (and PBS) were placed in front of a white light lamp for six hours. As a reference, $[Ru(bpy)_3]^{2+}$ was used and the absorbance of both samples were measured.

A key advantage of many ruthenium (II) complexes is that they are not as susceptible to photobleaching as many organic based molecular probes. The photobleaching of $[Ru(bpy)_2htrz\text{-}arg_8]^{9+}$ in myeloma cells is discussed in section 4.3.5, where the sample was irradiated using a 458 nm laser line. Studies of the temperature dependence of the emission of ruthenium – bipyridyl complexes containing triazole ligands indicate that thermal population of the deactivating triplet metal – centered state does not occur.[104] As a consequence of this, these compounds are expected to be photostable. This photostability is most likely caused by the strong σ - donor properties of the deprotonated triazole ligand, which induces strong ligand field splitting in the complex.[110]

Shown in Figure 3.30 is the absorbance spectra of and $[Ru(bpy)_3]^{2+}$ in PBS buffer (pH 7.4) solution and shown in Figure 3.31 is the absorbance spectra of $[Ru(bpy)_2htrz]^+$ in PBS buffer (pH 7.4) solution; both samples were absorbance matched.

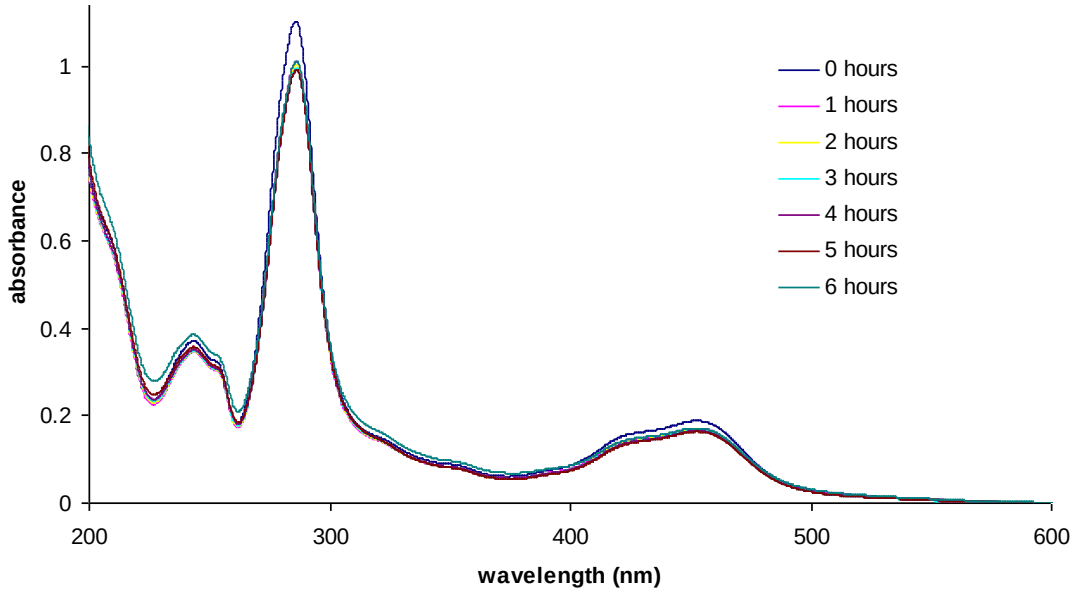

Figure 3.30: Absorbance spectra of and $[Ru(bpy)_3]^{2+}$ in PBS buffer (pH 7.4) solution. Sample was absorbance matched with $[Ru(bpy)_2htrz]^{+}$

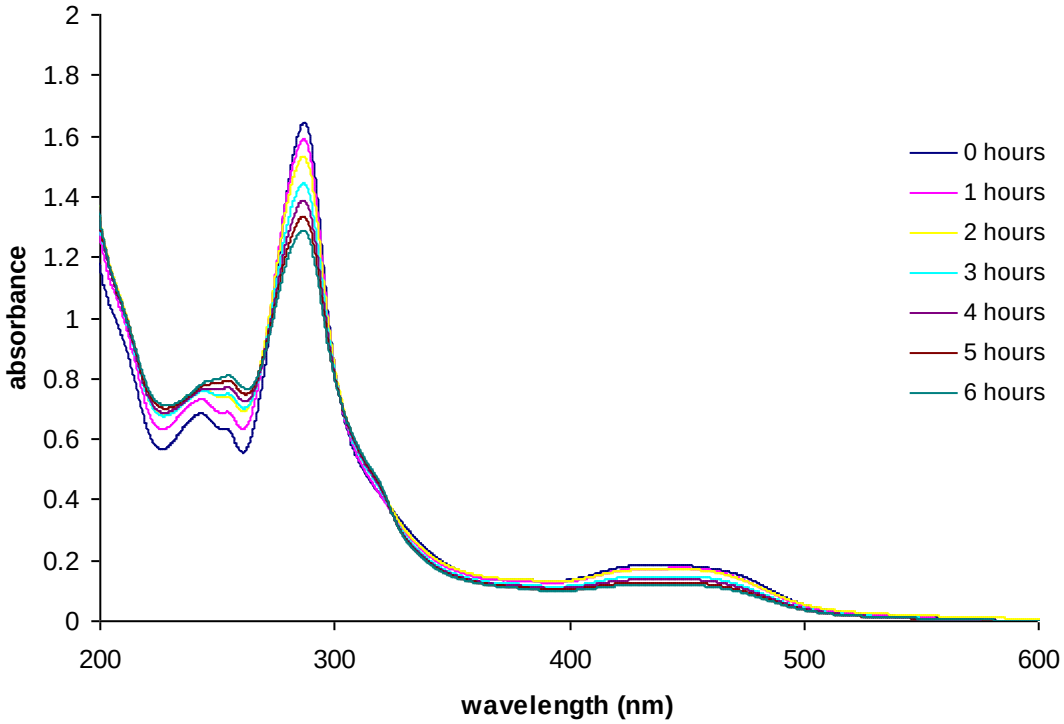

Figure 3.31: Absorbance spectra of $[Ru(bpy)_2htrz]^{+}$ in PBS buffer (pH 7.4) solution. Sample was absorbance matched with $[Ru(bpy)_3]^{2+}$

Shown in Figures 3.30 and 3.31 are the reduction in the absorbance of $[Ru(bpy)_3]^{2+}$ and $[Ru(bpy)_2htrz]^{+}$ respectively in PBS buffer (pH 7.4) solution. Monitoring the MLCT band, samples were absorbance matched and both complexes found to reduce by approximately 20% each over six hours. That the degradation occurs over such a large time range shows the large advantage that these inorganic complexes have over organic fluorophores, which would be expected to be completely destroyed in a matter of minutes.[12, 111]

As previously described, ruthenium triazole complexes are known to be stable compared to those of $[Ru(bpy)_3]^{2+}$, so the fact that both complexes showed similar stability here is surprising.[112] As this experiment was carried out using a UV lamp, it is perhaps not the most accurate method of comparing the photostability of the two complexes. A more accurate test is the photobleaching experiment described in section 4.3.5. To further investigate the stability of both dyes under UV irradiation, it is suggested to expose the samples to a greater power source, while varying solvent to obtain a broader data set. The stability shown is however, again evidence that these complexes are extremely useful for cell imaging and studying the dynamics of cellular processes.

3.2.5 Synthesis of ruthenium – BODIPY sensor

An initial aim of this project was to produce a ruthenium – peptide conjugate that also contained a pH and oxygen insensitive fluorophore as a reference molecule to the environmentally sensitive ruthenium centre. The BODIPY derivative prepared was BODIPY-NHS ester, which was prepared according to a method previously described for this compound but in this case modified to yield the for the NHS ester which was new and synthesised with a 61% yield. The NHS ester was prepared with the intention of coupling to the NH_2 terminus of the starting material $[Ru(NO_2phen)_2(picNH_2)]^{2+}$ complex described above.

After encountering a number of synthetic difficulties the final BODIPY – conjugated ruthenium complex was not successfully isolated. Two ruthenium nitrophenanthroline complexes were however successfully synthesised with an amino and carboxyl terminus on respective ancillary ligands. Carboxy and amino terminated BODIPY probes were also successfully synthesised however these complexes were ultimately never conjugated with the ruthenium dye. The attempted amine coupling via reactive esters only led to starting materials being recovered. The reaction of the ruthenium dye with the BODIPY – NHS ester may in future be achieved in a different solvent system, with DMF or DMF / water 90/10 mix possible systems worth investigating. The reaction time and pH for these processes are also important as the reaction may become more acidic over time; this can drive the reaction backwards by hydrolysing the NHS ester.[113] Constant monitoring by TLC may be a method of determining if this is the process undergone and increasing the starting materials may be necessary.

Following failure of the NHS ester coupling approach a second synthetic strategy described previously in this chapter was attempted to exploit the BODIPY molecule's carboxyl reactivity with the NH2 terminus of the ruthenium(II) complex, $[Ru(NO_2phen)_2(picNH_2)]^{2+}$. This approach was attempted via a EDC/NHS coupling reaction.[114] However, this method failed to produce the BODIPY – ruthenium conjugate. It is surprising that this reaction was unsuccessful considering it is a well known often used technique.

Each reaction was carried out a total of ten times but the only products recovered were starting materials. For future work different coupling reagents may be attempted. (2-(7-Aza-1H-benzotriazole-1-yl)-1,1,3,3tetramethyluroniumhexafluorophosphate) [HATU] is used in peptide synthesis to introduce the active ester and is an alternative coupling reagent, in addition to using DIPEA as base to ensure the pH is raised to 7.5. [HATU] has previously been used for the robust coupling of peptides and allows greater experimental flexibility than the EDC/NHS coupling for more challenging synthesis.[115]

3.3 Conclusions

The synthesis and characterisation of ruthenium (bis-2,2-5-nitrophenanthroline)-2(4-aminophenyl)imidazo[4,5-f]1,10-phenanthroline $[(Ru(NOphen)_2PicNH_2)]^{2+}$ and ruthenium (bis-2,2-5-nitrophenanthroline)-2-(4-carboxylphenyl)imidazo[4,5-f]1,10-phenanthroline $[(Ru(NOphen)_2PicH_2)]^{2+}$, two novel nitrophenanthroline – ruthenium – pic complexes with different terminal functionality, as well as the phenanthroline parent complex were described. Both the carboxyl and amino functionalised complexes behave very similarly and may be characterised by their comparable absorbance and emission.

The amino and carboxy terminated ruthenium complexes were compared using spectroscopic methods, with the MLCT band in the absorbance spectrum of $[(Ru(NOphen)_2PicNH_2)]^{2+}$ exhibiting a shift of approximately 5 nm to longer wavelength compared to the carboxyl complexes, is consistent with the amino ancillary ligand as a slightly better σ-donating ligand. Transitions at 340 nm were found to be pH dependent and were attributed to π-π* transitions of the [pic-R] ligands, contain two ionisable protons on the imidazole ring.

$[Ru(bpy)_2htrz]^{+}$, prepared by Dr D Plazuk was characterised by pKa titration, Raman spectroscopy and UV irradiation. Deprotonation of the complex above pH 8.5 led to a spectral shift due to the stabilising electrostatic interaction between the MLCT generated bpy anion radical and the extra positive charge of the triazolium moiety. Raman spectra showed no significant changes observed at different excitation laser lines. This suggests that the optical transition arises mainly from a ruthenium (dπ) to bipyridyl ligand (π*) MLCT transition. This complex was designed for conjugation to a cell penetrating peptide and exploited as a tool for resonance Raman mapping in a cellular environment. Resonance Raman of the complex in its solid form showed signature bipyridyl vibrational Raman modes which were observed using 458, 488 and 514 nm laser lines, with no significant changes between the data. This suggested that the lowest energy optical transition arises from a ruthenium (dπ) to bipyridyl ligand (π*) MLCT transition.

The photostability of $[Ru(bpy)_2htrz\text{-}arg_8]^{9+}$ was compared with $[Ru(bpy)_3]^{2+}$ by monitoring the MLCT band. Both samples were exposed to UV irradiation for six hours, over which times both complexes degraded by approximately 20% each over six hours. Due to the high photostability of previously reported ruthenium – triazole complexes, the similar degradation of both dyes is surprising. However the fact that it occurs over such a large time range shows the large advantage that these inorganic complexes have over typically photo-unstable organic fluorophores.

The initial aim of this work, to produce a BODIPY – conjugated ruthenium complex was not achieved, as the target molecule was never successfully isolated. An attempt to conjugate the ruthenium(II) dye with the BODIPY – NHS ester may in future be achieved in a different solvent system or using alternative reaction conditions. The well – known EDC/NHS coupling reaction was used in an attempt to conjugate the carboxyl group on the BODIPY dye to the amino terminus of $[Ru(NO_2phen)_2(picNH_2)]^{2+}$, however this also proved unsuccessful. This strategy may be revisited with the use of different coupling reagents. Another strategy may be to attach the BODIPY dye to a peg – linker with an amino or carboxyl terminus. The reaction may be more sterically favoured and could proceed with a ruthenium – pic complex with a carboxyl or amino terminus with the use of a coupling reagent.

Chapter 4: Ruthenium – Peptide Conjugates for Cellular Imaging

4.1 Introduction

Live cell imaging has been revolutionised by advances in luminescence microscopy, in particular laser scanning and confocal microscopy. In addition, such technology has revolutionised Raman spectroscopy and confocal Raman microscopes can be used to scan a surface in a similar manner to a luminescence confocal microscope, but provide information on structure and composition of the material which is beyond the scope of luminescence.

Raman is however, limited by its low sensitivity and the long acquisition times needed. This means that in imaging the long dwell-times of the laser on a single spot are required for each step scan leading potentially to photodamage to the sample. In the case of cells, if they are non-adherent they may possibly move during long acquisition times. Nonetheless, the key advantage of Raman is that it directly probes structure and in the case of resonance Raman the sensitivity and consequently acquisition times can be dramatically improved. If the resonance Raman probe has a structural marker of environment for example of protonation status it can be used to sense environmental change within a cell.

Many organic based molecular probes which have been used for sensing diagnostic roles typically have the disadvantage of short-lived fluorescent lifetimes (<10 ns) and are susceptible to photobleaching when used in laser scanning microscopy. Such probes are also not suitable for resonance Raman as their relatively small Stoke's shift means fluorescence overwhelms the weaker Raman response. Short lived probes are unsuitable as they are unable to monitor other long lived processes such as membrane diffusion, protein rotation and protein folding.

A key advantage of ruthenium(II) polypyridyl and related luminescent metal complexes when compared to traditional fluorescent imaging dyes is their long lived triplet excited states, which make them far more sensitive to their environment, particularly to molecular oxygen which is itself triplet in the ground state. The long lived fluorescent lifetime of these complexes is of particular interest, as it allows for discrimination from the shorter-lived background

fluorescence (typically less than 10 ns) present in many biological samples. The possible barriers of concentration quenching or self-absorption of the complex are removed by their large Stokes shift. Additionally, their emission is red shifted and removed from regions of the spectrum where autoluminescence of biological samples can occur. This can facilitate the use of fluorescent light imaging (FLIM) and confocal microscopy measurements. As the Stoke's shift of Ru(II) complexes is typically up to 200 nm, the collection of intense interference free resonance Raman spectra is permitted at a wavelength that also excites emission.[116] Resonance Raman mapping allows the total spatial distribution of the dye in the cells to be determined.

The difficulty in transporting luminescent metal complexes across the cell membrane of living cells without disrupting the cell was discussed in chapter 1. As described, octaarginine as a molecular cargo carrier a derivative of naturally occurring of the cell penetrating peptide Tat can be attached to a ruthenium complex to facilitate passive transport of the dye across the cell membrane. The ability of these peptides to diffuse across the cell membrane is highly dependent on the arginine chain length, with a chain length of Arg_5 – Arg_{11} necessary but octa – and nona – arginine showing the greatest carrying ability.[13] This work details the cellular activity of a ruthenium octaarginine peptide conjugate, using confocal microscopy, fluorescent light imaging and resonance Raman mapping to determine the uptake, cytotoxicity, and localization of the dye within SP2 myeloma cells and Chinese Hamster Ovary cells.

SP2 and CHO lines were both used as examples of mammalian cells. The characteristics of these cell lines are discussed in section 1.41, but one of the main differences between the lines is that SP2 myeloma cells are a suspension line, whereas CHO cells are adherent and will only grow when they are attached to a surface. The surface protein composition of each cell type is expected to be quite different which may affect uptake.[117] The differences arising as a result of the biochemical nature of these cell lines is examined using commercially available probes which exhibit targeted localization within specific organelles.

4.2 Experimental Procedure

To examine and compare the cellular uptake of $[Ru(bpy)_2htrz\text{-}arg_8]^{9+}$ and it's parent (unconjugated) complex, SP2/0-Ag14 myeloma and Chinese Hamster Ovary (CHO) cells were investigated as models of mammalian cells. The uptake and distribution throughout each cell type was compared by examining the luminescence distribution from the metal complex using confocal laser scanning microscopy, fluorescent lifetime imaging (FLIM) and resonance Raman mapping. In a typical protocol for the non-adherent SP2 cells, 10 μL of an aqueous solution of the Ru-complex $[Ru(bpy)_2htrz]^{2+}$ or $[Ru(bpy)_2htrz\text{-}arg_8]$ (1.4×10^{-4} M) were added to 50 μL of the cell suspension to yield a final dye concentration of 2.8×10^{-5} M.

The adherent CHO cells were seeded at a concentration of 1×10^5 cells / cm^3 and grown for two days in a six well flask at 1 cm^3 per well before imaging. Immediate cellular uptake of dye observed for the myeloma cells was not observed with the CHO cell line, so to each 1 cm^3 well, 65 μL of an aqueous solution of the Ru-complex $[Ru(bpy)_2htrz]^{+}$ or $[Ru(bpy)_2htrz\text{-}arg_8]^{9+}$ (1.1×10^{-3} M) were added to yield a final dye concentration of 2.8×10^{-5} M and the cells were incubated for six hours. The growth medium was removed by washing the cells with PBS buffer (pH 7.4) and the cells were imaged immediately.

4.2.1 Cell Imaging

Using confocal laser scanning microscopy, $[Ru(bpy)_2htrz]^{2+}$ and $[Ru(bpy)_2htrz\text{-}arg_8]$ were excited using a 458 nm argon ion laser line, corresponding to the MLCT absorbance of each complex and the emission images were recorded through a 615 nm longpass filter, which cuts out any light below 615 nm. For co-localization studies, the commercially available nuclear targeting 3,3'-dihexyloxacarbocyanine iodide ($DiOC_6(3)$) was used to investigate the cellular localization of the peptide conjugated dye in both cell lines. Aqueous solutions of $DiOC_6(3)$ were added to the final cell suspension to yield a final concentration of 0.5 μM (to target mitochondria) and 5 μM (to target lysozomes and the endoplasmatic reticulum). This counter staining probe was also excited at 458 nm and the emission images recorded using a band pass filter from 505 nm – 530 nm.

The nuclear targeting 4′,6-Diamidino-2-phenylindole dihydrochloride (DAPI) was prepared with a final concentration of 300 nM in PBS buffer solution. Myeloma cells were washed with PBS and incubated with the DAPI standard solution for five minutes, before further rinsing and imaging was immediately carried out. The emission was collected with a band pass filter from 425 nm – 530 nm. The same protocol was used for imaging of the DAPI counter stain with CHO cells.

4.2.2 Fluorescent Lifetime Imaging

Myeloma and CHO cells were prepared as described in section 3.2.1. and using a 458 nm pulsed diode laser line fluorescent light images were collected using a 610 nm longpass filter. To achieve a high resolution, yet also ensure the cells retained their viability, 128 x 128 pixel scans were recorded over approximately twenty minutes. Specific regions of interest were investigated using a zoom of up to x 849 to increase the lifetime count per pixel.

4.2.3 Cell Mapping Using Resonance Raman Spectroscopy

Myeloma and CHO cells were prepared as described in section 3.2.1. and using a 457.9 nm argon ion laser line resonance Raman mapping was performed. This excitation wavelength was selected as it matches the MLCT absorbance for the Ru(II) complexes. The mapping technique involves obtaining Raman spectra step wise across a grid of predefined area where Raman spectra are collected at discrete step sizes, e.g. 1 um steps . Each image was garnered using five accumulations and a sixty second exposition time. A complete map of each cell was recorded in approximately twenty minutes. The step size was set at 0.5 μm and the grid size was set at 21 μm.

4.3 Results & Discussion

4.3.1 Confocal Fluorescence Microscopy – Probe Uptake in Myeloma cells

As described, a major limitation of inorganic dyes is their inability to passively transport across a cell membrane without membrane permeabilisation. The ability of $[Ru(bpy)_2htrz\text{-}arg_8]^{9+}$ to penetrate mammalian cells was investigated using mouse Sp2/0-Ag14 myeloma cells. The myeloma is a cancerous plasma cell and was used as an example of a suspension mammalian cell. As described in section 4.2.1., the peptide conjugated complex was added to a cell suspension and imaged using confocal fluorescence microscopy. For all cells studied in this section, $[Ru(bpy)_2htrz\text{-}arg_8]^{9+}$ was subject to a final concentration of 2.8×10^{-5} M in the incubation medium which resulted in uptake and bright luminescence in the cell membrane within one minute.

The cellular imaging results in this section reveal that conjugation of a metal complex to the cell penetrating peptide facilitates efficient diffusion across mammalian cell membranes without destroying the lipid bilayer. The ability of the ruthenium complex to passively transport across the membrane of SP2 cells, only when conjugated to a peptide was confirmed by comparing uptake with the parent, unconjugated dye. Shown in figure 4.11 (a) is a luminescence confocal image of the parent ruthenium dye which shows no evidence of membrane penetration after incubation for 30 minutes at 37°C. Neugebauer et al. have previously demonstrated that a ruthenium complex with a 2+ charge in the absence of peptide cannot penetrate an intact cellular membrane. However, diffusion of the ruthenium parent dye into the cell could be achieved upon permeablizing the cell with Triton (1% v/v).[12] Shown in 4.11 (b) is a luminescence confocal image of the parent ruthenium dye in a PBS solution containing triton (1% v/v). This illustrates the complex can be incorporated into the cell through permeablisation of the cell membrane. These “rainbow images” utilise a custom false colour coding to accentuate cellular image. However, Triton and in other examples in the literature organic solvents such as DMSO or ethanol, damage the cell membrane and are therefore not an ideal approach to promote dye entry to a cell.

To determine the ability of $[Ru(bpy)_2htrz\text{-}arg_8]^{9+}$ to transport passively across the cell membrane, the dye was added to a suspension of SP2 cells and imaged using confocal fluorescence microscopy. To maintain cellular conditions, uptake of the dye was monitored at 37°C, where it was found to penetrate the cell membrane extremely rapidly (the process seemed to be complete in approx 1min). Our group has previously demonstrated the ability of a ruthenium – peptide conjugate to penetrate a cell membrane in less than 5 minutes,[12] but the results reported in this thesis are to our knowledge some of the fastest uptake rates reported for such metal complexes. The rapid migration of dye into the cell made monitoring individual biological processes difficult and limited the detail in which dye uptake could be studied. To examine if the uptake process was energy dependent, uptake was also examined at a lower, temperature i.e. 25°C. Interestingly, this slowed uptake, suggesting the process occurs via an energy dependent pathway such as endocytosis.[13] Furthermore slowing uptake, allowed the transport across the biological membrane, as well as distribution throughout organelles within the cell to be more closely examined. Shown in figure 4.12 is the time dependent ability of the ruthenium peptide conjugate to passively transport across the cell membrane. Shown in (a) is a luminescent confocal image of an SP2 myeloma cell incubated with $[Ru(bpy)_2htrz\text{-}arg_8]^{9+}$ at 25° for one minute, while (b) shows the same cell after six minutes. Cell uptake of the dye was found to be irreversible and was complete after six to eight minutes. Shown in figure 4.13 is a z-stack of a myeloma cell which has been incubated with the ruthenium peptide dye. Shown in figure 4.14 is the detailed dye uptake in an SP2 cell over 20 minutes at 25°C. The distribution of the dye throughout the cell was confirmed through these experiments, with the dye showing evidence of localization within specific organelles.

Previous studies of ruthenium polypyridyl complexes reported the ability of $[Ru(bpy)_2(picCOOH)Arg_8]^{10+}$ to transport across a cell membrane of SP2 myeloma cells via a cell penetrating peptide.[12] The plasma membranes of viable cells exhibit a membrane potential (−50 to −70 mV), with the inside of the cell negative with respect to the outside. The concentration of the negatively charged phosphatidyl serine leads to this negative charge on the cells inner membrane. Therefore a complex with a larger charge will have a greater driving force across

the membrane assuming the mechanism is energy dependent. Interestingly, $[Ru(bpy)_2htrz\text{-}arg_8]^{9+}$ was found to transport rapidly across the membrane, in a time frame which was even faster than $[Ru(bpy)_2(picCOOH)Arg_8]^{10+}$.

It has previously been reported that while a positive net charge of hydrophilic peptides enhances the speed of their transport across the cell membrane, with increasing molecular size the overall charge of the molecule becomes less significant.[118] Another possibility is that two different uptake pathways occur for each dyes. While $[Ru(bpy)_2(picCOOH)Arg_8]^{10+}$ was found to transport across the cell membrane in five minutes, the uptake of $[Ru(bpy)_2htrz\text{-}arg_8]^{9+}$ in SP2 cells was even faster and was observed at room temperature. However, both dyes exhibited temperature dependence in their uptake, suggesting an endocytic pathway.

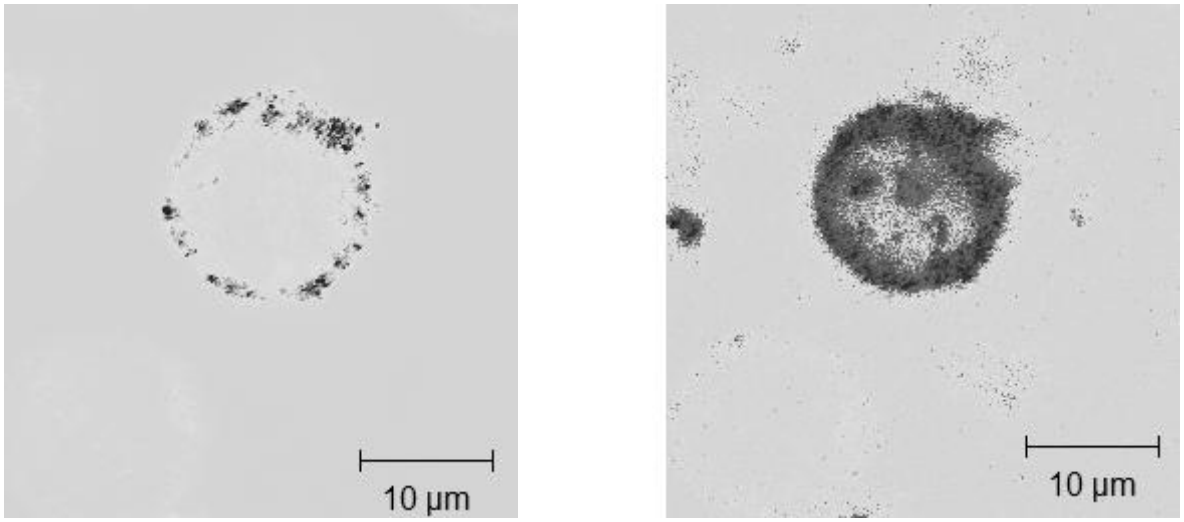

(a) (b)

Figure 4.11: Luminescence confocal rainbow images (explain in text what this is) (λ_{ex} = 458 nm, λ_{em} = 615nm) (a) of live SP2 myeloma cell incubated with parent complex $[Ru(bpy)_2htrz\text{-}arg_8]^{9+}$ (2.8 x 10^{-5} M) in PBS buffer (pH 7.4) for 30 minutes and (b) for 7 minutes after permeablizing the cell with Triton (1% v/v).

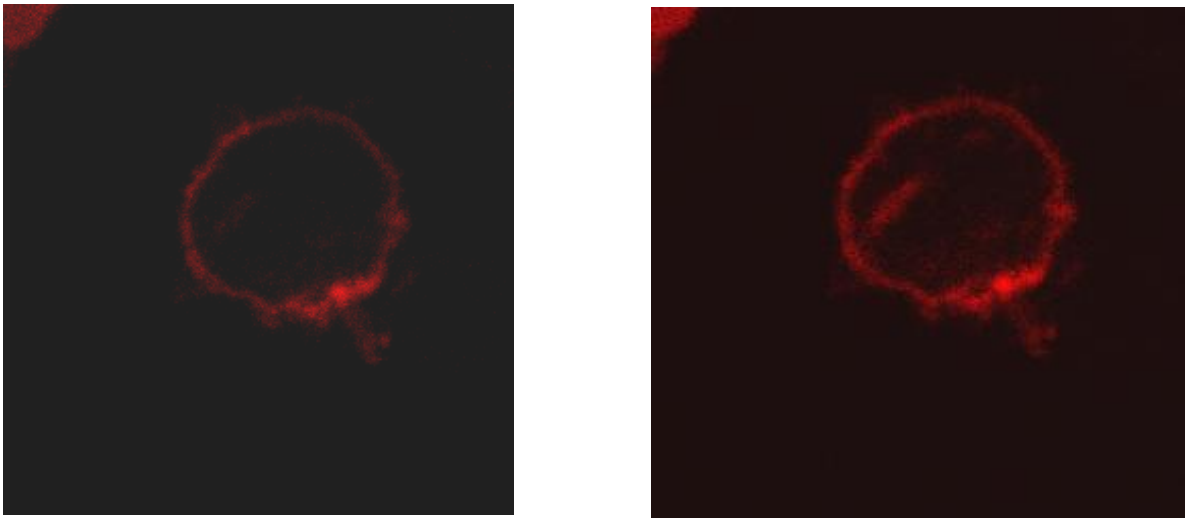

(a) (b)

Figure 4.12: Luminescence images (λ_{ex} = 458 nm, λ_{em} = 615nm) of SP2 myeloma cell incubated with $[Ru(bpy)_2htrz\text{-}arg_8]^{9+}$ (2.8 x 10^{-5} M) in PBS (pH 7.4) after (a) 1 minute and (b) six minutes.

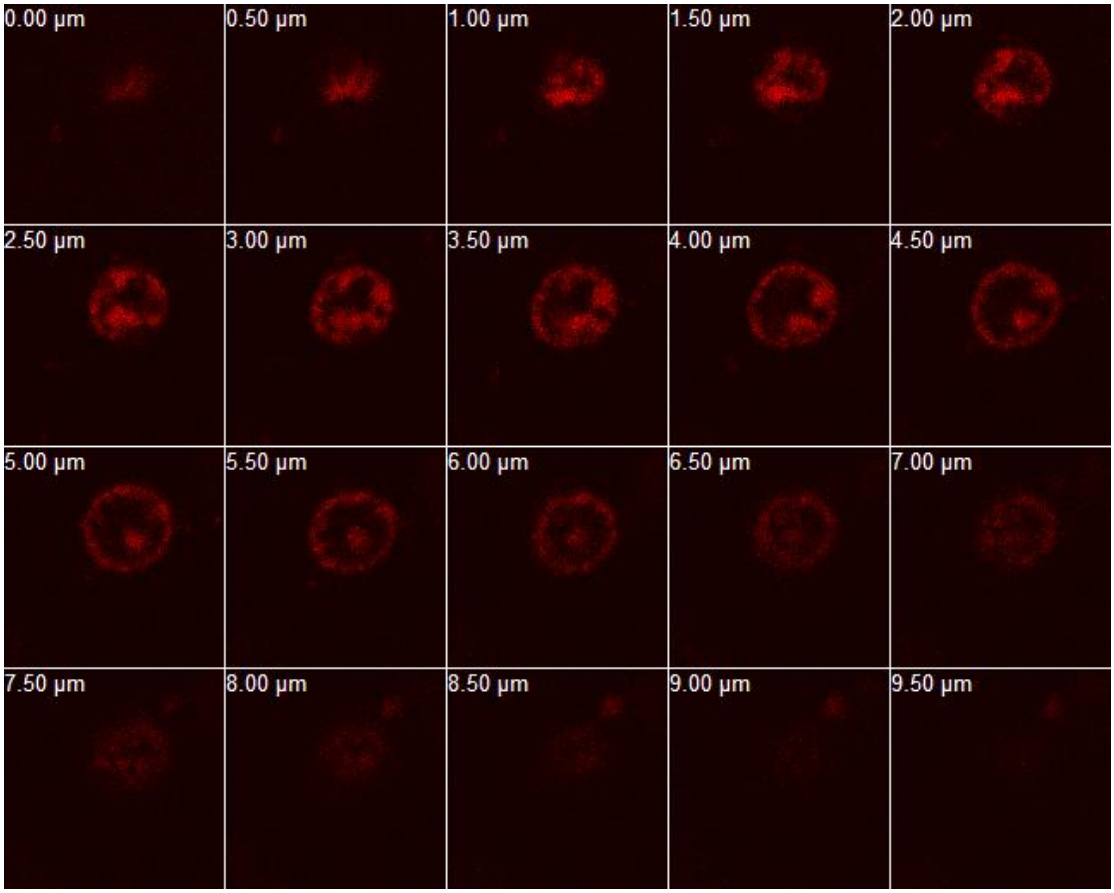

Figure 4.13: Luminescence confocal z-stack images (λ_{ex} = 458 nm, λ_{em} = 615nm) of SP2 myeloma cell incubated with $[Ru(bpy)_2htrz\text{-}arg_8]^{9+}$ (2.8 x 10^{-5} M) in PBS (pH 7.4) after 20 minutes at room temperature.

To assess the distribution of the dye in cellular organelles, myeloma cells were counterstained with commercial cell permeable dyes which exhibit specific staining. 3,3'-dihexyloxacarbocyanine iodide ($DiOC_6(3)$) selectively stains mitochondria at 0.5µM and structures in the cell, including the lysozomes and endoplasmatic reticulum at 5µM.[50] Shown in figure 4.14 are luminescence images of SP2 myeloma cells stained with $[Ru(bpy)_2htrz\text{-}arg_8]^{9+}$ and counter stained with $DiOC_6(3)$ (0.5 µM). Shown in figure 4.15 is a z-stack of cells stained with the ruthenium peptide dye and counter stained with a higher concentration of $DiOC_6(3)$ (5 µM).

From both figures, it is evident that there is no overlap between $[Ru(bpy)_2htrz\text{-}arg_8]^{9+}$ and $DiOC_6(3)$ it can therefore be concluded that $[Ru(bpy)_2htrz\text{-}arg_8]^{9+}$ does not localize in mitochondria, lysozomes or endoplasmic reticulum of the myeloma cells. It is clear that although the dye permeates throughout the cell the highest intensity emission come from the outer membrane or other membrane bound structures within the cell. One possibility is that luminescence is promoted when the complex binds to lipid membrane. Both parent and conjugated dyes were excited with 458nm laser irradiation. The green $DiOC_6(3)$ luminescence was collected with a band pass filter from 505nm – 530nm, while the red luminescence of $[Ru(bpy)_2htrz\text{-}arg_8]^{9+}$ through a 615 nm longpass filter.

Cells were also stained with the nuclear targeting 4′,6-Diamidino-2-phenylindole dihydrochloride (DAPI) to further investigate the distribution of dye. DAPI stains nuclei specifically, with little or no cytoplasmic labelling. Shown in figure 4.16 are luminescence images of SP2 myeloma cells stained with $[Ru(bpy)_2htrz\text{-}arg_8]^{9+}$ and counter stained with DAPI (300 nM). DAPI was excited with 375nm laser irradiation, while $[Ru(bpy)_2htrz\text{-}arg_8]^{9+}$ was excited at 488nm. The blue DAPI luminescence was collected with a band pass filter from 425nm-530nm, while the red luminescence of $[Ru(bpy)_2htrz\text{-}arg_8]^{9+}$ through a 615 nm longpass filter. Shown in Figure 4.17 is luminescence confocal z-stack images of SP2 cells stained with the ruthenium – peptide conjugate and then counter stained with DAPI. While the extent of co-localization appears unclear from the single confocal image, the z-stack images clearly show that the ruthenium probe does not show significant overlap with the DAPI emission, but appears to localize just outside the nucleus.

A problem which may arise from these co-localization studies is the quenching of $DiOC_6(3)$ and DAPI by the ruthenium dye. In it's excited state $DiOC_6(3)$ emits in the region of 452 nm to 535 nm, while DAPI has an emission maxima at 460 nm. When either $DiOC_6(3)$ or DAPI are in their excited state, they may act as a donor molecule, transferring energy to the ruthenium dye, a ground state acceptor molecule. This non – radiative energy transfer may be by Förster resonance energy transfer (FRET), a mechanism based transition dipoles

between the donor and acceptor, or may even occur through a trivial mechanism. The extent of energy transfer is determined by the distance between the donor and acceptor, and the extent of spectral overlap. It is important to note that if this is occurring it may reduce the intensity of the localisation stain at regions where the ruthenium is co-localised and may enhance the emission of the ruthenium dye.

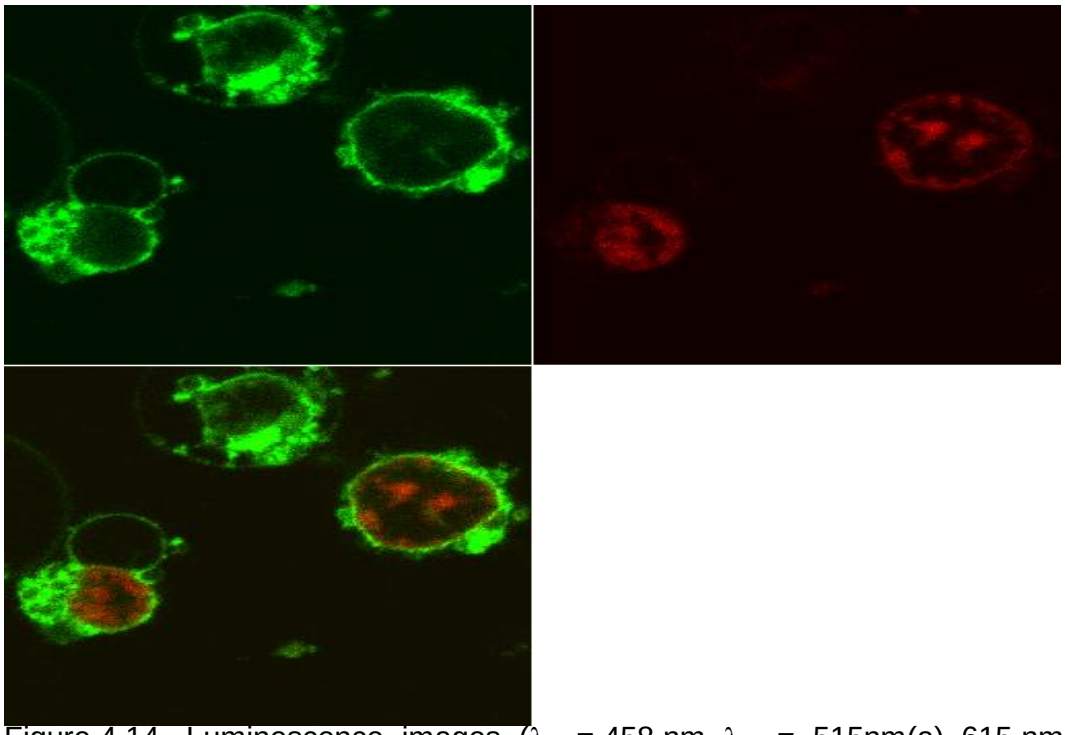

Figure 4.14 Luminescence images (λ_{ex} = 458 nm, λ_{em} = 515nm(a), 615 nm(b)) of SP2 cells incubated with $[Ru(bpy)_2htrz\text{-}arg_8]^{9+}$ (2.8 x 10^{-5} M) (b) for ten minutes at room temperature before addition of $DiOC_6(3)$ (5 μM) (a) in PBS (pH 7.4).

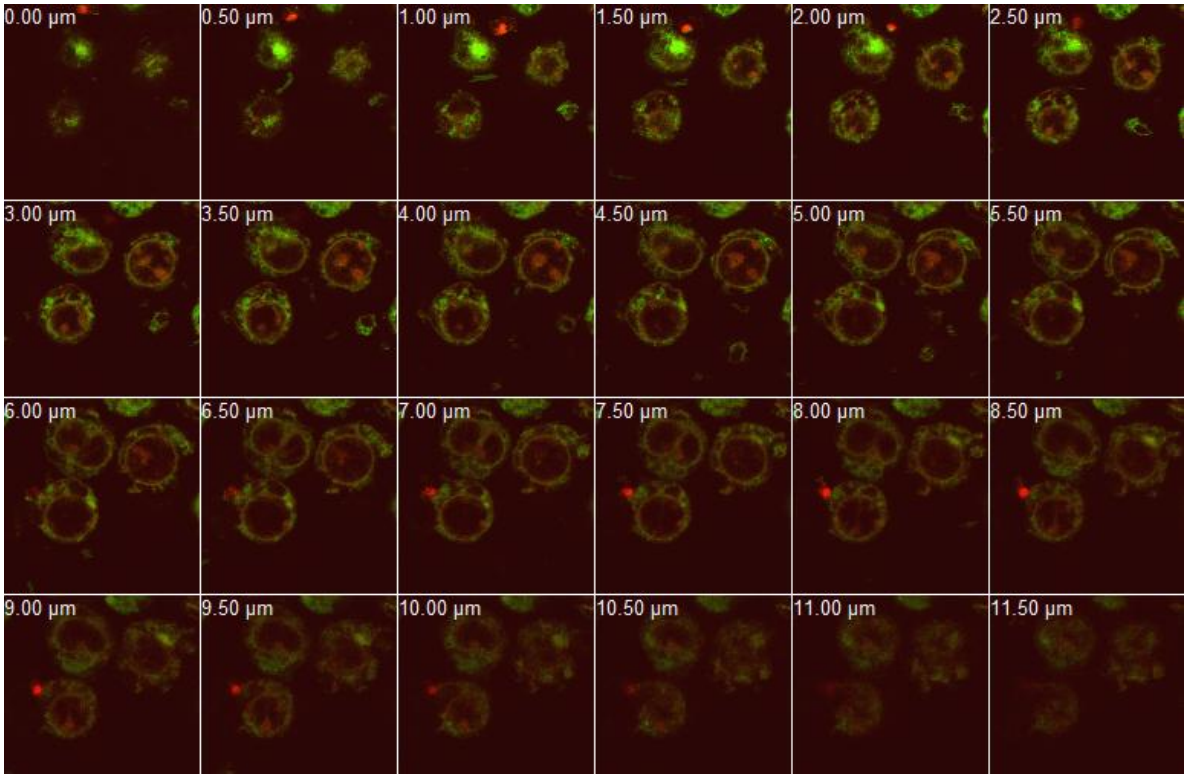

Figure 4.15 Luminescence z-stack images (λ_{ex} = 458 nm, λ_{em} = 515nm(a), 615 nm(b)) of SP2 cells incubated with $[Ru(bpy)_2htrz\text{-}arg_8]^{9+}$ (2.8 x 10^{-5} M) (b) for ten minutes at room temperature before addition of $DiOC_6(3)$ (5 μM) (a) in PBS (pH 7.4).

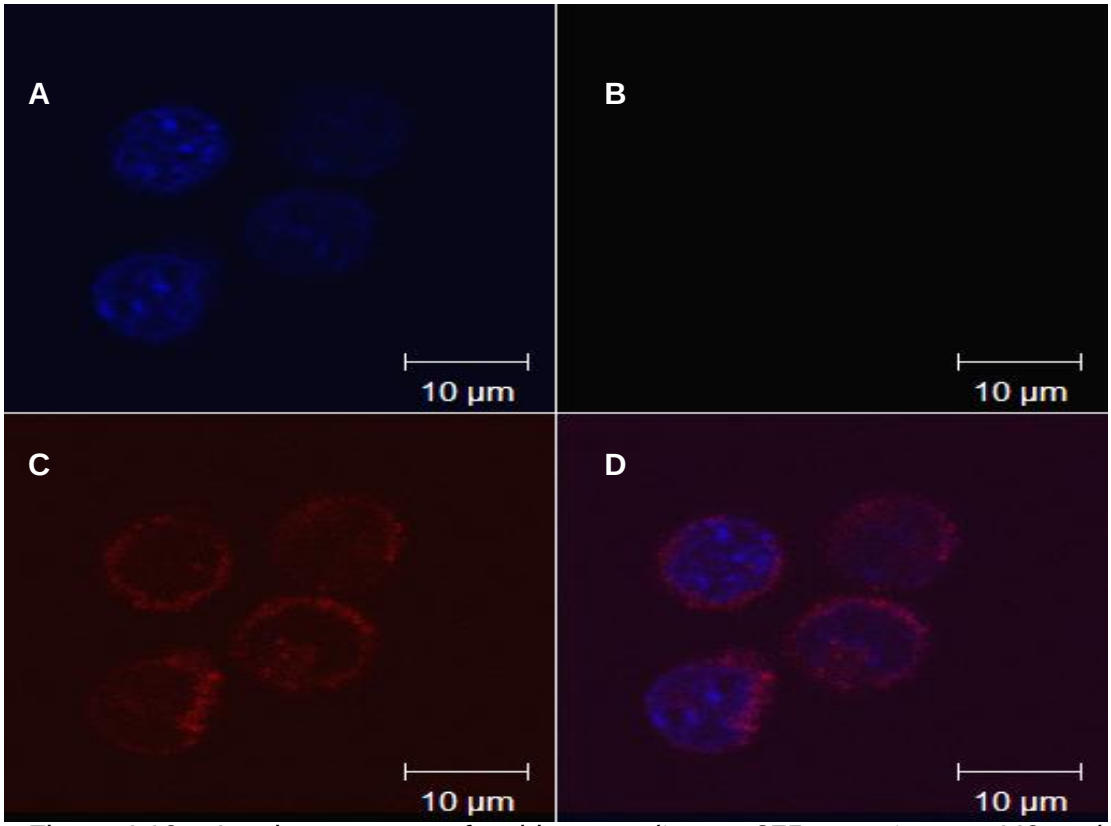

Figure 4.16: Luminescence confocal images (λ_{ex} = 375 nm, λ_{em} = 440 nm(a), (λ_{ex} = 488 nm, λ_{em} = 615 nm(b)) of SP2 cells incubated with $[Ru(bpy)_2htrz\text{-}arg_8]^{9+}$ (2.8×10^{-5} M) (b) for ten minutes at room temperature before addition of DAPI (300 nM) (a) to the same cells in PBS (pH 7.4).

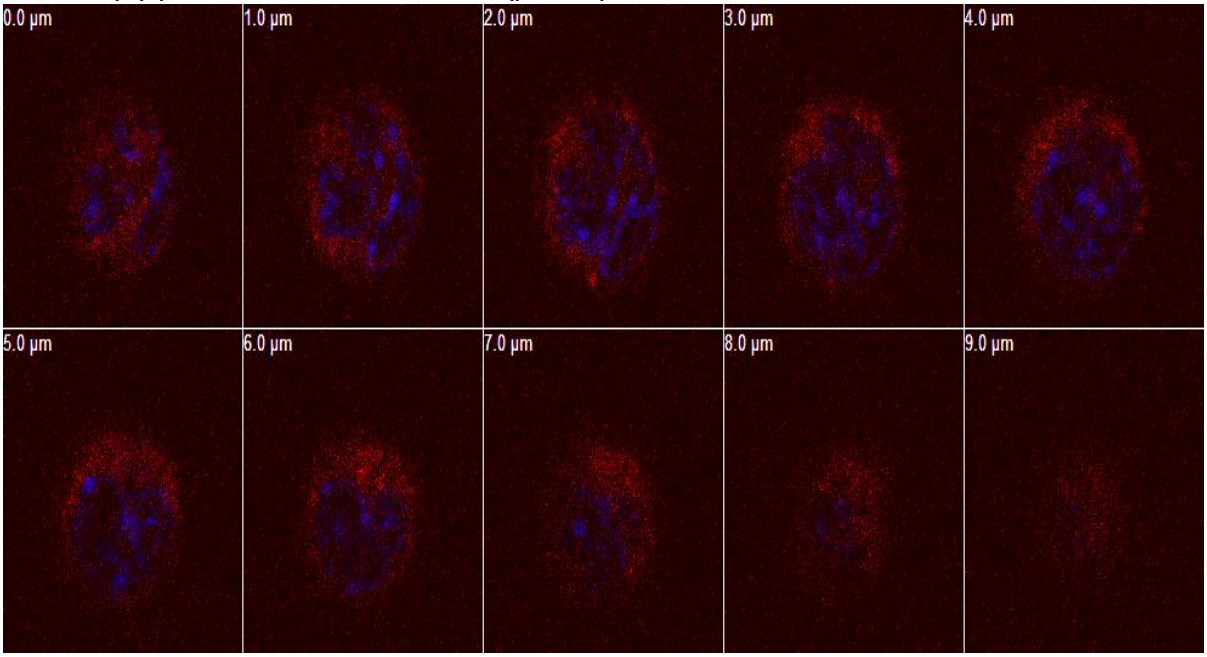

Figure 4.17: Luminescence confocal z-stack images (λ_{ex} = 375 nm, λ_{em} = 440 nm(a), (λ_{ex} = 488 nm, λ_{em} = 615 nm(b)) of SP2 cells incubated with $[Ru(bpy)_2htrz\text{-}arg_8]^{9+}$ (2.8×10^{-5} M) (b) for ten minutes at room temperature before addition of DAPI (300 nM) (a) to the same cells in PBS (pH 7.4).

To ensure that $[Ru(bpy)_2htrz\text{-}arg_8]^{9+}$ penetration into live cells occurred without leading to their destruction, it was necessary to perform cell viability assays. Sytox green is a probe which only penetrates cells with compromised plasma membrane and it is therefore a reliable probe of cell viability. Shown in figure 4.17 are SP2 cells stained with the ruthenium peptide dye and counter stained with Sytox green. A cell suspension containing $[Ru(bpy)_2htrz\text{-}arg_8]^{9+}$ (2.8×10^{-5} M) was incubated at 37°C for one hour to ensure transport across the cell membrane. The cells were then washed with PBS and left in which the external buffer containing Sytox green (10 μM).

$[Ru(bpy)_2htrz\text{-}arg_8]^{9+}$ and Sytox green were both excited with 458nm laser irradiation. The Sytox green luminescence was collected with a band pass filter from 490nm – 515nm, while $[Ru(bpy)_2htrz\text{-}arg_8]^{9+}$ was collected through a 615 nm longpass filter. Figure 4.17 (A) shows the Sytox green luminescence within the cells, the red channel (B) shows the luminescence arising from $[Ru(bpy)_2htrz\text{-}arg_8]^{9+}$. From these Figures, it is clear that the ruthenium dye is present in the cytoplasm of an SP2 cell where there is no Sytox present, demonstrating the ability of the ruthenium – peptide conjugate to penetrate live myeloma cells. Formation of vesicles at the cell membrane known as blebbing is observed in figure 4.17 and figure 4.18 and such structures are usually an indication of cell death and correspondingly an overlap is observed between the ruthenium dye and the Sytox green in these images when blebbing is observed. This demonstrates the ability of the ruthenium – peptide conjugate to penetrate cells once their membrane has been permeabilized, which the parent complex was already shown to do in figure 4.11. The important thing to note from this figure is the ability of the dye to penetrate live cells. This work was carried out on a time scale not exceeding one hour, in line with previous experiments, so as to confirm the viability over that period.

It has previously been reported in the literature that a similar ruthenium polypyridyl labelled cell penetrating peptide shows approximately 30% cell death upon incubation for two days with SP2 myeloma cells. Despite this, the cell culture was still found to be viable and suitable for imaging purposes.[13] Inorganic metal complexes are known to produce singlet oxygen typically

through an energy transfer process from its excited triplet state to triplet oxygen ($^3O_2$). Singlet oxygen is known to react with the DNA base guanosine as well as a number of amino acids and may lead to cell apoptosis.[119] Although the cells here appear viable over the time scale of the experiment explored. Long term exposure of the cells with the complex present under irradiation are likely to lead to cell death through this mechanism.

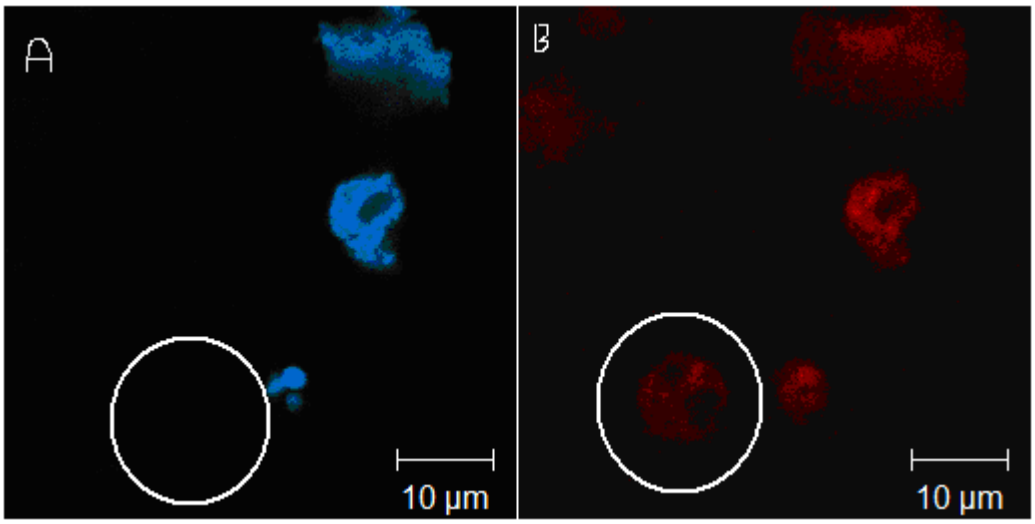

Figure 4.17: Luminescence images (λ_{ex} = 458 nm, λ_{em} = 520(A), 615 nm(B)) of SP2 cells incubated with Sytox green (10 µM) and $[Ru(bpy)_2htrz\text{-}arg_8]^{9+}$ (2.8 x 10^{-5} M) in PBS (pH 7.4)

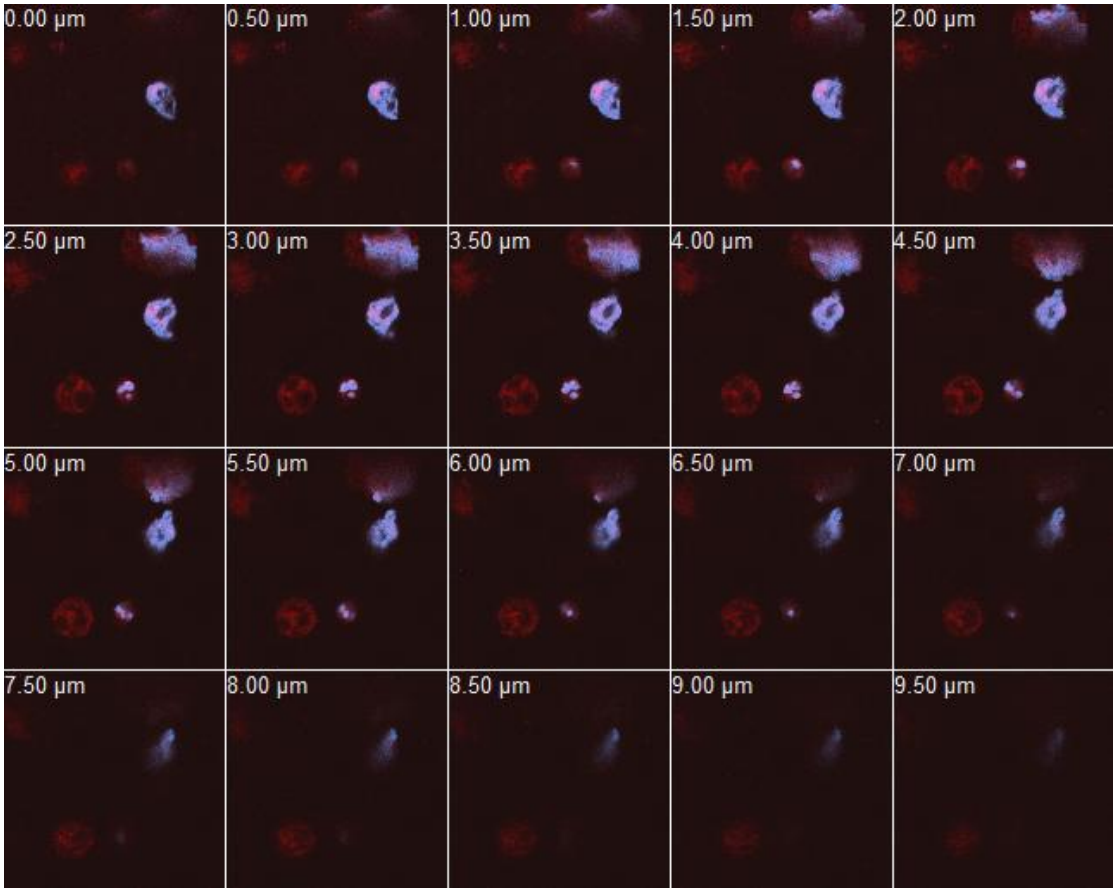

Figure 4.18: Luminescence z-stack images (λ_{ex} = 458 nm, λ_{em} = 520(A), 615 nm(B)) of SP2 cells incubated with Sytox green (10 µM) and $[Ru(bpy)_2htrz\text{-}arg_8]^{9+}$ (2.8 x 10^{-5} M) in PBS (pH 7.4)

4.3.2 Cellular Uptake of $[Ru(bpy)_2htrz\text{-}arg_8]^{9+}$ in CHO Cells

As described in section 1.3.2, Svensson has previously described the ability of ruthenium polypyridyl complexes to transport across the cell membrane of Chinese Hamster Ovary (CHO) cells.[43] Each dye was dissolved in medium and DMSO (1% v/v), which is commonly used when imaging various metal complexes to aid solubility issues.[45] While DMSO is not toxic at this concentration, it does permeabilize cells, meaning the dye is not penetrating a healthy cell membrane.[47, 48] Ruthenium dipyridophenazine (dppz) complexes were found to localize in the endoplasmic reticulum or nucleus of CHO cells. Slight modifications of the dppz ligand's lipophilicity led to great variations in membrane binding. The least lipophilic complex was found predominantly in the nucleus, while complexes of increasing lipophilicity were found to be more homogenously distributed in the cells with comparable emission intensities inside the nucleus and in the cytoplasm.[43] The cell membrane binding, uptake and intracellular localization of $[Ru(bpy)_2htrz\text{-}arg_8]^{9+}$ in CHO-K1 cells were studied with confocal microscopy.

Interestingly the behaviour was quite different to that of the SP2 cells. In this instance, incubation of the peptide bound ruthenium dye with CHO cells at room temperature, no cellular uptake was observed, with little or no luminescence seen after an hours incubation. The minimum incubation time found which was suitable for imaging was four hours at 37°C, after which bright luminescence results in the cell. For comparison purposes, the concentration of $[Ru(bpy)_2htrz\text{-}arg_8]^{9+}$ was kept at (2.8×10^{-5} M), as in the SP2 myeloma experiments. As with the SP2 cells, dye uptake was found to be irreversible, however uptake was considerably less efficient, and the final intensity was identical once uptake was complete in CHO cells. Remarkably, in SP2 cells the dye was found to passively cross the cell membrane in less than ten minutes at room temperature, however even after one hour this was not observed in CHO cells. While some uptake of the ruthenium – peptide conjugate was observed in CHO cells after two hours, the intensity shown in SP2 uptake after ten minutes was not reached via CHO uptake for four hours. This result suggests that uptake is approximately 20 times faster in the SP2 myeloma cell line than in CHO cells.

To the best of our knowledge, there are no examples in the literature of similar comparative studies of uptake speed between cell lines where such differences are observed.

Shown in figure 4.21 are confocal images of CHO cells after incubation with $[Ru(bpy)_2htrz\text{-}arg_8]^{9+}$ at room temperature for one hour. The dye appears to distribute throughout the cellular plasma but shows little affinity for individual CHO cells or specific organelles.

Shown in figure 4.22 are confocal images of CHO cells following incubation with $[Ru(bpy)_2htrz\text{-}arg_8]^{9+}$ at 37°C for four hours. The ability of the ruthenium peptide conjugate to passively transport across the cell membrane is again demonstrated here. The red luminescence was collected through a 615 nm longpass filter. In contrast to the SP2 cells, the ruthenium peptide dye appears to localize in the cellular cytoplasm. Shown in figure 4.23 is a z-stack of a CHO cell which has been incubated with the ruthenium peptide dye for four hours, which confirms the internalisation of the dye in the cell.

Ruthenium dyes in DMSO (1% v/v) have previously been shown to internalise in CHO cells after five minutes[43] but as discussed earlier, these cells may have been permeabilized. Shown in figure 4.24 is a luminescent confocal image of CHO cells after incubation for five minutes with $DiOC_6(3)$ (5 μM). The green $DiOC_6(3)$ luminescence was collected with a band pass filter from 505nm – 530nm. The outer membrane of the cells are found to be approximately 20 μm each with nuclear radii of 12 μm when measured using the Zeiss LSM Image Browser program. While $DiOC_6(3)$ is known to penetrate live cells, what is significant here is the rapid uptake seen, which was also observed for the SP2 cells. The rapid diffusion shown by the probe may be due to it's small size allowing faster transport.[13]

Uptake of the ruthenium dye in CHO cells was considerably less efficient than for the myeloma cells. $[Ru(bpy)2htrz\text{-}arg_8]^{9+}$ was found to passively cross the cell membrane of SP2 myeloma cells in less than ten minutes at room

temperature, however even after one hour this was not observed in CHO cells. One of the main differences between the cell types are that SP2 myeloma cells are a suspension line, whereas CHO cells are adherent and will only grow when they are attached to a surface. It has been previously reported that trypsinization had no effect on the binding of alginate – chitosan complexes in CHO cells.[64] However, it is possible that the decrease in $[Ru(bpy)2htrz\text{-}arg_8]^{9+}$ uptake speed may be due to specific trypsin – cleavable proteins involved in the internalization.[120] Although internalization was effective in both cell lines, the significant difference in uptake speed and localization suggests alternative uptake pathways in each cell line.[117] Significantly, the speed of uptake in both cell types was found to be temperature dependent, which is consistent with endocytosis.[44]

As both cell lines express both clathrin and caveolin proteins, the reasons for alternative uptake pathways are not immediately evident. Previous studies have reported that complex size may be a determining factor in clathrin – mediated or caveolin – dependent uptake.[117] However, the pathway dependencies observed here cannot be explained by complex size, nor can these results be explained by the composition of the complex as both cell lines were treated with one dye at identical concentrations. While the reasons for cell line dependence remain unconfirmed, these results infer that cell physiology is critical in complex internalization.

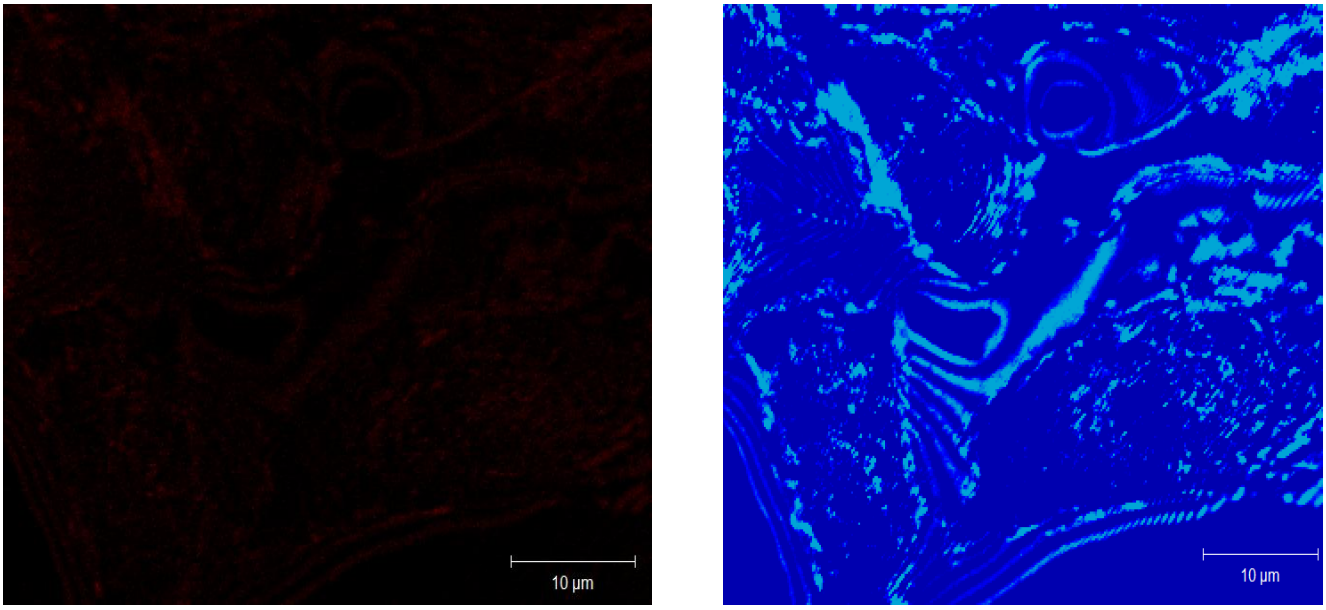

(a) (b)

Figure 4.21: Luminescence confocal image (a) and rainbow image (b) (λ_{ex} = 458 nm, λ_{em} = 615nm) of live CHO cells incubated with $[Ru(bpy)_2htrz\text{-}arg_8]^{9+}$ (2.8×10^{-5} M) after one hour in PBS (pH 7.4) at room temperature.

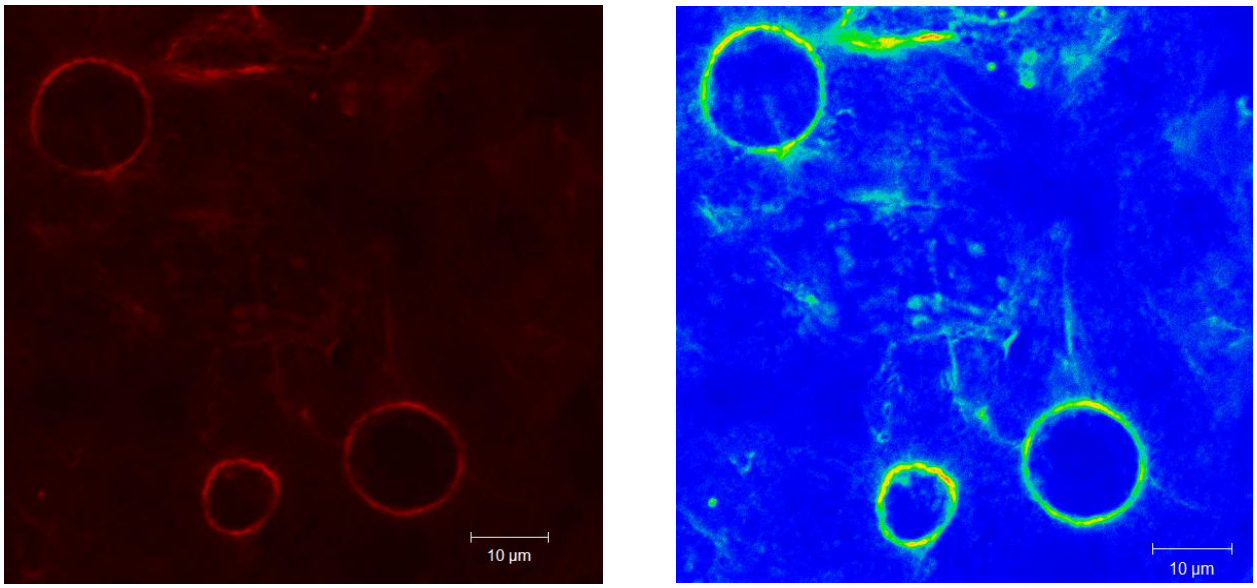

(a) (b)

Figure 4.22: : Luminescence confocal image (a) and rainbow image (b) (λ_{ex} = 458 nm, λ_{em} = 615nm) of live CHO cells incubated with $[Ru(bpy)_2htrz\text{-}arg_8]^{9+}$ (2.8×10^{-5} M) for four hours in PBS (pH 7.4) at 37°C.

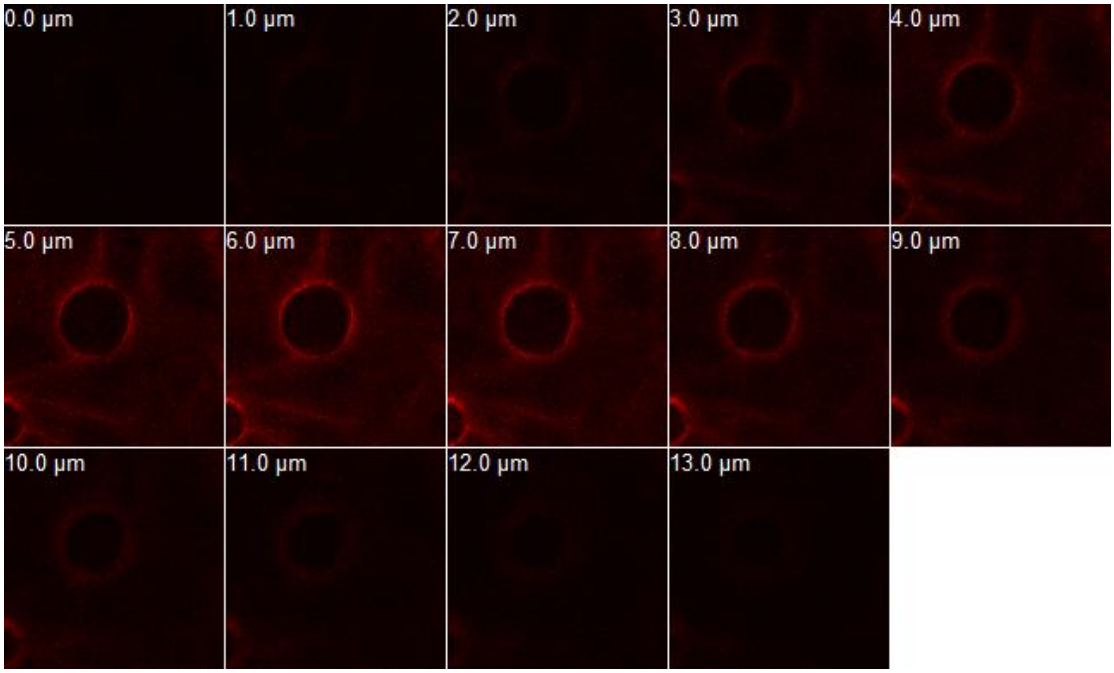

Figure 4.23: : Luminescence z-stack confocal image (λ_{ex} = 458 nm, λ_{em} = 615nm) of live CHO cells incubated with $[Ru(bpy)_2htrz\text{-}arg_8]^{9+}$ (2.8 x 10^{-5} M) for four hour in PBS (pH 7.4) at 37°C.

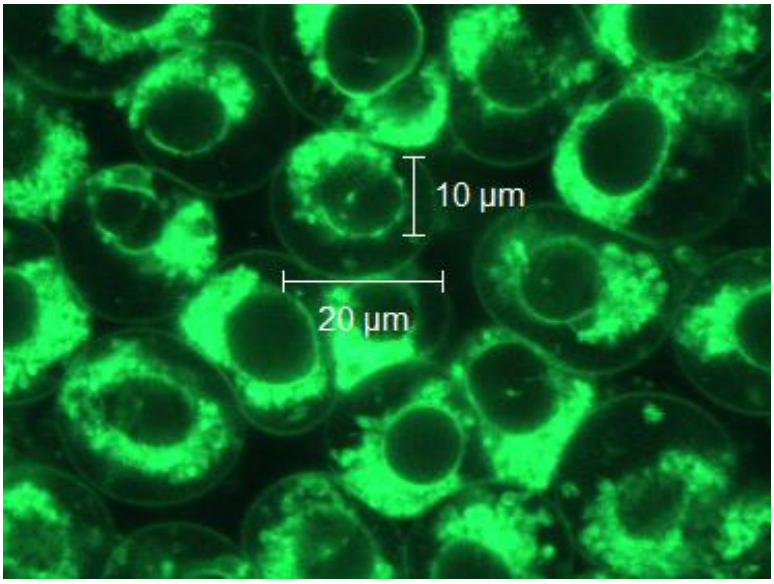

Figure 4.24: Luminescence confocal image (λ_{ex} = 458 nm, λ_{em} = 515 nm) of live CHO cells incubated with $DiOC_6(3)$ (5 µM) for five minutes in PBS (pH 7.4) at room temperature. At this concentration, the dye localizes in lysozomes and the endoplasmatic reticulum.

To ensure that $[Ru(bpy)_2htrz\text{-}arg_8]^{9+}$ was penetrating live CHO cells, it was necessary to perform a cell viability assay as for the SP2 cell line to see if Ru and Sytox uptake were coincidental. Sytox green was again used to determine viability. Shown in figure 4.24 is CHO cells stained with the ruthenium peptide dye and counter stained with Sytox green. Both dyes were excited with 458nm laser irradiation. The Sytox green luminescence was collected with a band pass filter from 490nm – 515nm, while $[Ru(bpy)_2htrz\text{-}arg_8]^{9+}$ was collected through a 615 nm longpass filter. As shown in (c), the ruthenium dye is present in the cytoplasm of an SP2 cell where there is no Sytox present. Channel (b) shows the presence of a cell with a damaged membrane that Sytox green has successfully localised in the nucleus. As confirmed in channel (c) the ruthenium dye is able to penetrate live cells, with no evidence of any Sytox counter staining present.

As mentioned previously in this section, ruthenium dipyridophenazine (dppz) complexes with alkyl ether chains localize in the endoplasmic reticulum of CHO cells when permeabilized with DMSO (1% v/v). Shown in figure 3.25 is a confocal image of CHO cells stained with $[Ru(bpy)_2htrz\text{-}arg_8]^{9+}$ (2.8×10^{-5} M) and counter stained with DAPI (300 nM). 4′,6-Diamidino-2-phenylindole dihydrochloride (DAPI) stains nuclei specifically, with little or no cytoplasmic labelling. These results demonstrate the ability of the ruthenium dye to enter the cell, via a cell penetrating peptide without requirement for permeablisiation. A major advantage of the peptide bound dye is its ability to diffuse passively across a cell membrane, ensuring no damage occurs to the cell. Another key advantage of a conjugated peptide is that they render the ruthenium complex water soluble in cases where the parent is not. The cell membrane may become permeabilized when DMSO is used due to the toxic nature of it and other organic solvents.

DAPI was excited with 375nm laser irradiation, while $[Ru(bpy)_2htrz\text{-}arg_8]^{9+}$ was excited at 488nm. The blue DAPI luminescence was collected with a band pass filter from 425nm – 530nm, while the red luminescence of $[Ru(bpy)_2htrz\text{-}arg_8]^{9+}$ through a 615 nm longpass filter. As there is no overlap between $[Ru(bpy)_2htrz\text{-}arg_8]^{9+}$ and DAPI it can be concluded that $[Ru(bpy)_2htrz\text{-}arg_8]^{9+}$ does not penetrate the nucleus. Conversely, comparison of confocal images of

the ruthenium probe in CHO cells with $DiOC_6(3)$, which localizes in the endoplasmatic reticulum at 5 μM concentration, suggests that $[Ru(bpy)_2htrz\text{-}arg_8]^{9+}$ localizes in the endoplasmatic reticulum. The non – continuous nature of the distribution is in agreement with previously mentioned studies which show ruthenium dyes in CHO cells which localize endoplasmic reticulum which has a large convoluted membrane structure.[43]

(a) (b)

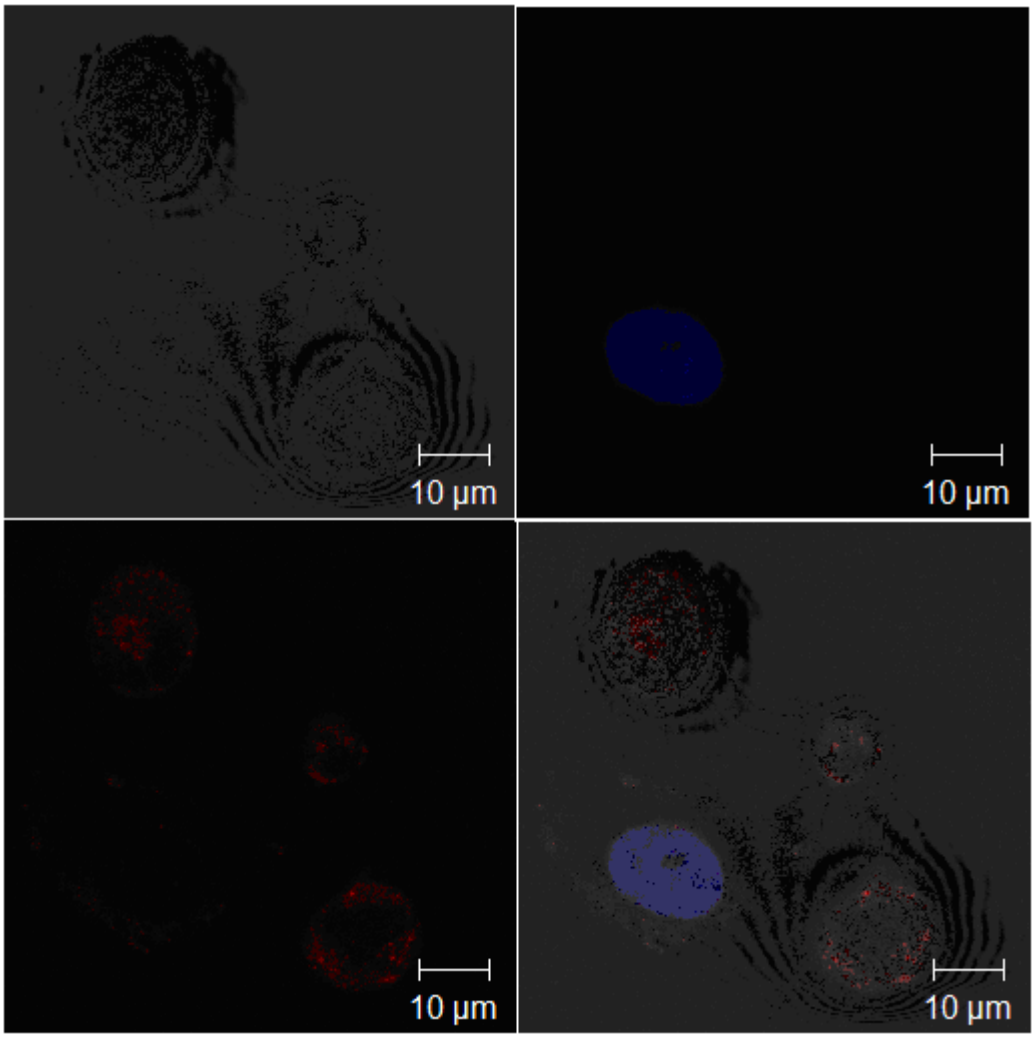

(c) (d)

Figure 4.24: Luminescence images (λ_{ex} = 458 nm, λ_{em} = 470 nm (a), 520 nm (b), 615 nm(c)) of CHO cells incubated with $[Ru(bpy)_2htrz\text{-}arg_8]^{9+}$ (2.8×10^{-5} M) (c) for four hours before addition of Sytox green (10 μM) (b) in PBS (pH 7.4).

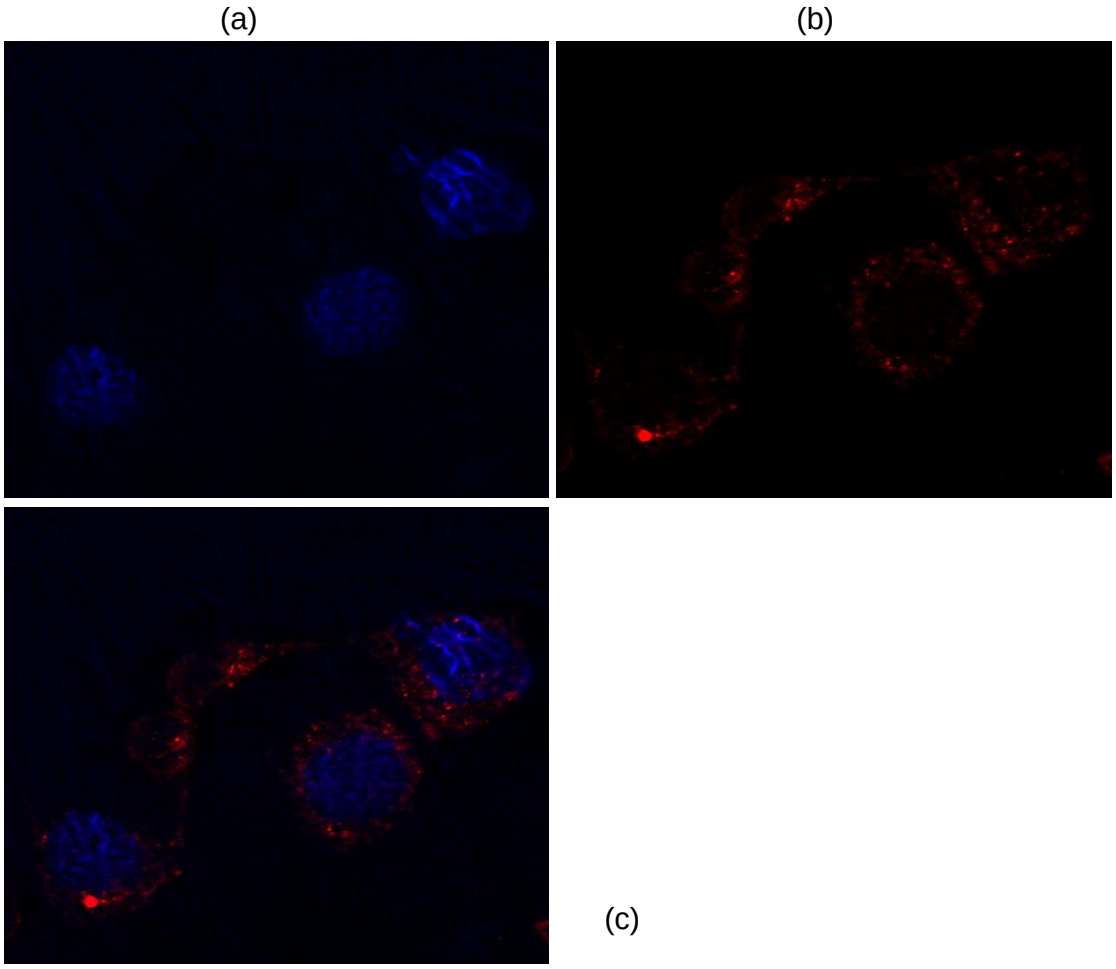

Figure 4.25 Luminescence images (λ_{ex} = 375 nm, λ_{em} = 440 nm(a), (λ_{ex} = 488 nm, λ_{em} = 615 nm(b)) of CHO cells incubated with $[Ru(bpy)_2htrz\text{-}arg_8]^{9+}$ (2.8×10^{-5} M) (b) for four hours before addition of DAPI (300 nM) (a) in PBS (pH 7.4).

4.3.3 Fluorescence Lifetime Imaging Microscopy

A key advantage of ruthenium polypyridyl complexes when compared to traditional luminescent imaging dyes are their long lived excited states due to the phosphorescent character of their emission, making them far more sensitive to their environment. For example a reduction of over 70% is observed for the lifetimes of $[Ru(dppz)_2Pic]^{2+}$ and $[Ru(bpy)_3)]^{2+}$ in the presence of oxygen in acetonitrile compared with deaerated solution.[5] As the emission lifetime is independent of luminophore concentration, it is ideal for measurements in a cellular environment where the exact concentration of dye may be difficult to determine as uptake may vary or the dye may accumulate preferentially in different domains within single cells. From chapter 3, the excited state lifetime of $[Ru(bpy)_2htrz\text{-}arg_8]^{9+}$ in the presence of oxygen in PBS is reduced from 147 ns to 91 ns, with the parent complex reduced from 139 ns to 84 ns in an air saturated solutions.

As described, the luminescence intensity and lifetime of $[Ru(bpy)_2htrz\text{-}arg_8]^{9+}$ exhibits oxygen dependence. Shown in figure 4.11 (a) and (c) is the luminescence intensity of $[Ru(bpy)_2htrz\text{-}arg_8]^{9+}$ in SP2 and CHO cells respectively. Both cell lines were prepared for fluorescence lifetime imaging as described for confocal microscopy experiments described previously. Shown in figure 4.11 (b) and (d) is the luminescence lifetime image of these cells. These false colour images reflect the average lifetime of the probe throughout the cell. As can be seen from the fluorescent lifetime images, it is difficult to observe significant variations in lifetime. The lifetime of $[Ru(bpy)_2htrz\text{-}arg_8]^{9+}$ was measured at specific regions of each cell, with values varying between 119 ns and 138 ns.

The luminescence lifetime image of myeloma cells are shown in Fig. 4.26, with (b) showing the outer membrane of the cell; and (d) showing internal structures are a lower depth. For image (b), a longer lifetime appears at some of the external membrane structures, while in contrast the lifetime shown internally in the cell in image (d) appears to be fairly uniform. Interestingly, in the CHO cell (f), the lowest lifetime appears on the outer structure of the cell, which is consistent with previous studies by Neugebauer[12] which showed that oxygen sensitive peptide labelled ruthenium luminophore exhibits its shortest lifetime when residing the membrane of a cell. This is expected as the higher solubility of O_2 in the membrane will result in greater quenching.[52] The CHO cell also exhibited no fluorescent lifetime within the nucleus of the cell, which is consistent with confocal microscopy images shown in section 4.3.2 which showed that the ruthenium – peptide conjugate did not enter the nucleus.

As the ruthenium complex does not exhibit as significant a reduction in lifetime as other long lived ruthenium complexes in the presence of oxygen, this approach makes it difficult to differentiate various components of the cell.[13] It must also be considered that the lifetime within the cell may change as a result of something other than O_2 e.g. association with membrane, DNA or ROS.

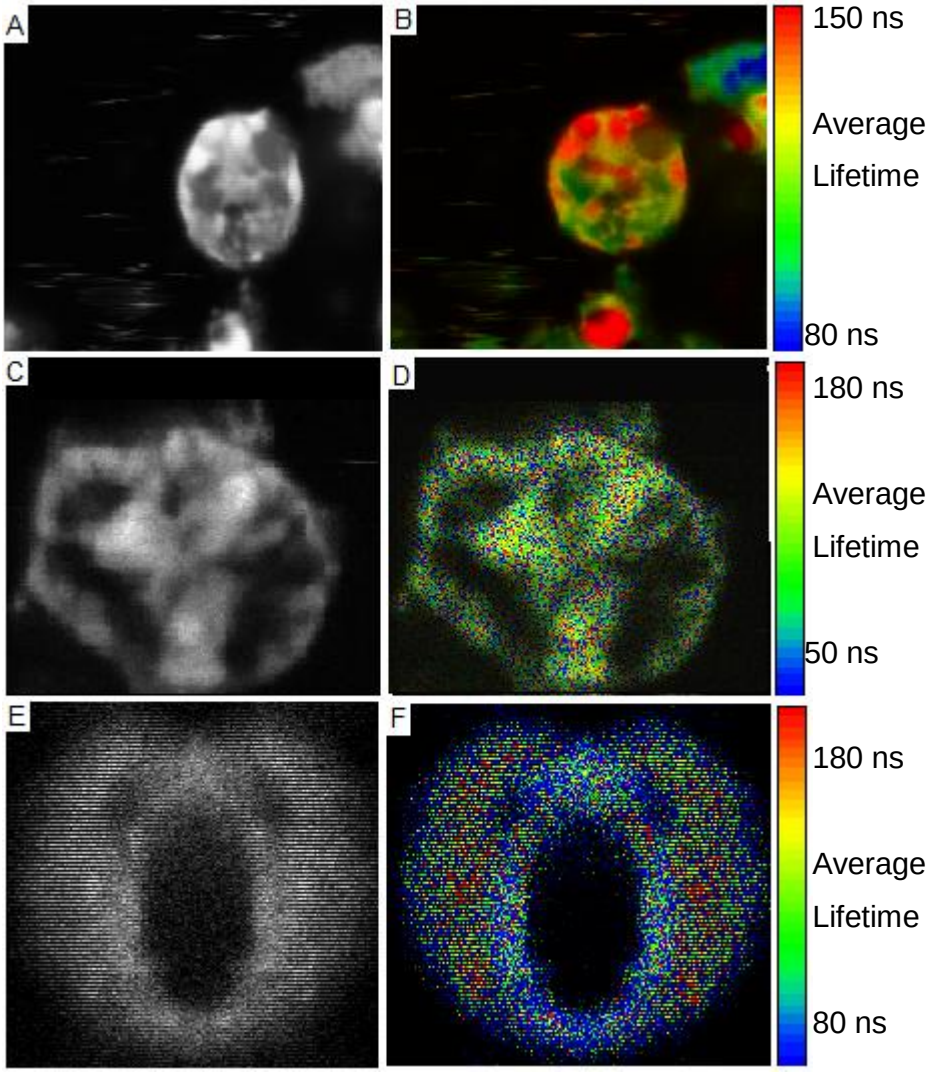

Figure 4.26 (a) Luminescence Intensity Image of SP2 Myeloma cells after incubation for 10 minutes with $[Ru(bpy)_2htrz\text{-}arg_8]^{9+}$ (2.8×10^{-5} M) in PBS (pH 7.4),

(b) Fluorescent Lifetime image of the same cell (λ_{ex} = 458 nm, λ_{em} = 615nm);

(c) Luminescence Intensity Image of SP2 Myeloma cell after incubation for 10 minutes with $[Ru(bpy)_2htrz\text{-}arg_8]^{9+}$ (2.8×10^{-5} M) in PBS (pH 7.4),

(d) Fluorescent Lifetime image of the same cell (λ_{ex} = 458 nm, λ_{em} = 615nm);

(e) Luminescence Intensity Image of CHO cell after incubation for four hours with $[Ru(bpy)_2htrz\text{-}arg_8]^{9+}$ (2.8×10^{-5} M) in PBS (pH 7.4),

(f) Fluorescent Lifetime image of the same cell (λ_{ex} = 458 nm, λ_{em} = 615nm)

4.3.4 Cell Mapping Using Resonance Raman

Raman mapping is a technique which generates detailed images based on a compound's Raman spectrum and is discussed in greater detail in section 1.3.3. A complete map is acquired by collecting Raman spectra in a step wise fashion from a grid established over the area to be imaged. Each spectrum forms a pixel of the final image and similar spectra/pixels are then used to generate false colour images. From an image, it is possible to interrogate a compound's structure as well as its distribution, which is not possible with standard fluorescence microscopy.[59, 60]

In order to investigate the dye's distribution and structure following uptake by living cells, Raman maps were obtained of $[Ru(bpy)_2htrz\text{-}arg_8]^{9+}$ under 473 nm laser excitation in both SP2 and CHO cells. To investigate the presence of the complex within the cell, individual cells were analysed using resonance Raman mapping. This was achieved by recording the Raman spectra at a series of intervals across the cell. The step size was set at 0.5 μm and the grid size was set at 21 μm.

The successful transport of $[Ru(bpy)_2htrz\text{-}arg_8]^{9+}$ across the plasma membrane evident from confocal fluorescence microscopy is confirmed from a Raman map of a myeloma cell and is shown in figure 4.42. Shown in figure 4.41 is a white light image of the myeloma cell prior to mapping. As the myeloma cells investigated are a suspension cell line, it was possible that the cell may drift and change it's position throughout the scan. To ensure this did not happen, the cell was held between two cover slips, ensuring a uniform position and more accurate final map. The resonance Raman image was generated by analysing the intensity of the 1490, 1561 and 1601 cm^{-1} bands at each point in the map. The plot intensity represents the intensity of these vibrational modes and therefore the relative dye concentration throughout the cell. Shown in figure 4.44 is a Raman map of a CHO cell which clearly confirms that the dye penetrates and is distributed throughout both cell types investigated.

The most intense Raman signal, corresponding to the greatest concentration of dye, can be observed in the center of the cell (represented by the pink and yellow regions). The least intense peaks (indicated by the blue regions) were observed outside the cell membrane which is a further indication of the dye's cell penetrating ability. While the mapping of three peaks is shown for both maps, each cell line was mapped from individual peaks across the Raman spectra, with each band showing the same map.

Shown in figure 4.43 is an overlay of individual spectra from selected regions of varying Raman intensity within an SP2 cell. The greatest signal intensity according to Raman signal was found to be at the center of the cell, but there was little difference between the peak frequency of the three regions, suggesting the dye exhibits little change due to environmental pH in these regions. In both cell lines, the dye appeared to localize in the centre of the cell, which was not expected from the results obtained from confocal imaging. A possible reason for this may be the low resolution of the Raman maps. The maps were generated from spectra from 20 designated pixels of an image, a higher resolution could be generated with a greater number of data points across each cell. The image is rather low resolution therefore and this may also account for the similarities in the spectra across the sample. A disadvantage of Raman and to a greater extent Raman mapping is that it is a slow process when compared to other spectroscopic techniques. Acquisition of Raman maps can, in some cases, extend to several days.[121] Each map was acquired in approximately 20 minutes; the slow speed of the technique limits the level of detail of each cell map primarily for two reasons: the relatively long dwell time of the laser on a single spot required is potentially damaging to both the cell and the dye; the short lifetime of the cells in question when removed from an incubator. Furthermore, this technique as it currently stands is not appropriate for studying dynamic processes in cells. However one way around is to combine this method directly with fluorescence to identify the region of interest and just collect Raman from selected regions, e.g. organelles. While the results shown here confirm the cell-penetrating ability of the octoarginine peptide and also highlights the effectiveness of our dye as a resonance Raman probe, it did not allow for a clear distinction of specific cellular regions.

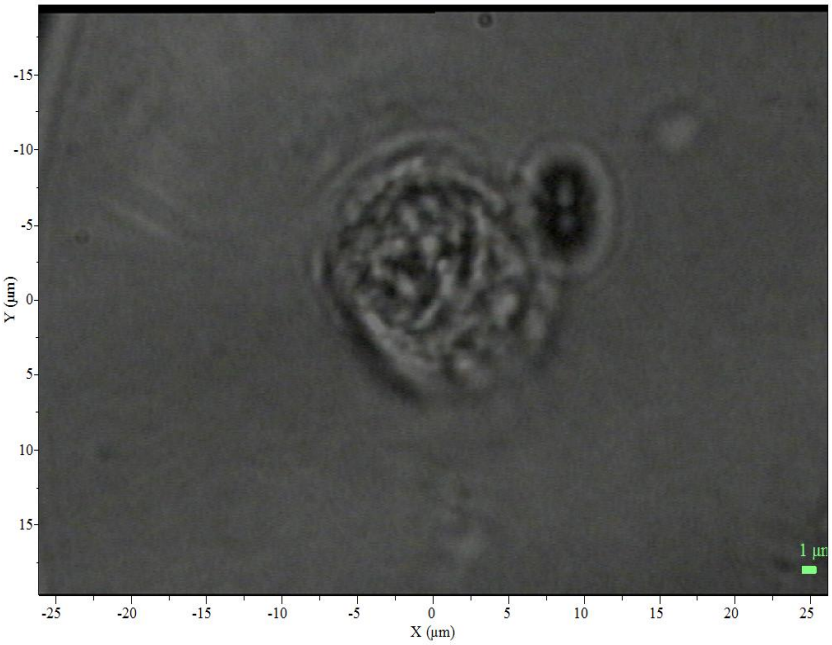

Figure 4.41: Image of myeloma cell mapped with $[Ru(bpy)_2htrz\text{-}arg_8]^{9+}$

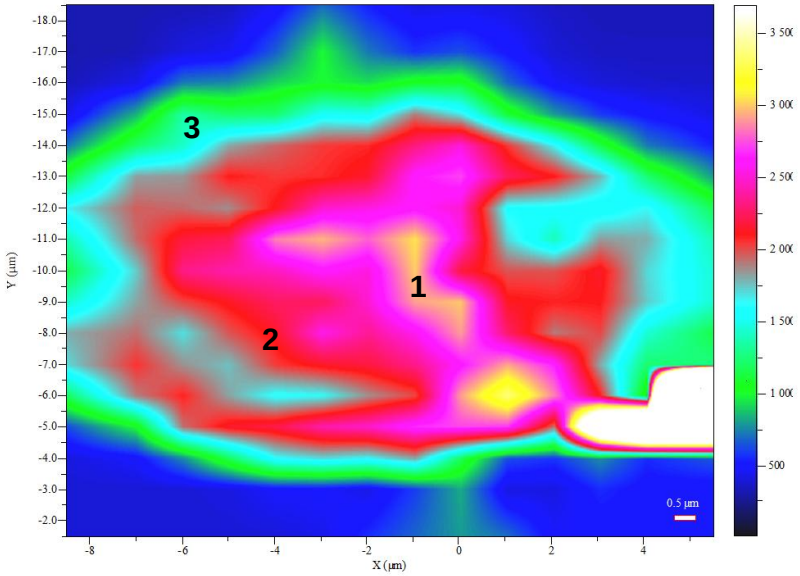

Figure 4.42: Raman intensity plot of a live SP2 myeloma cell constructed from the intensity of the peak at 1561 cm^{-1} in the spectrum of $[Ru(bpy)_2htrz\text{-}arg_8]^{9+}$ (2.8 x 10^{-5} M) after excitation at 473 nm. The colour bar indicates the relative Raman signal intensity that decreases from top to bottom.

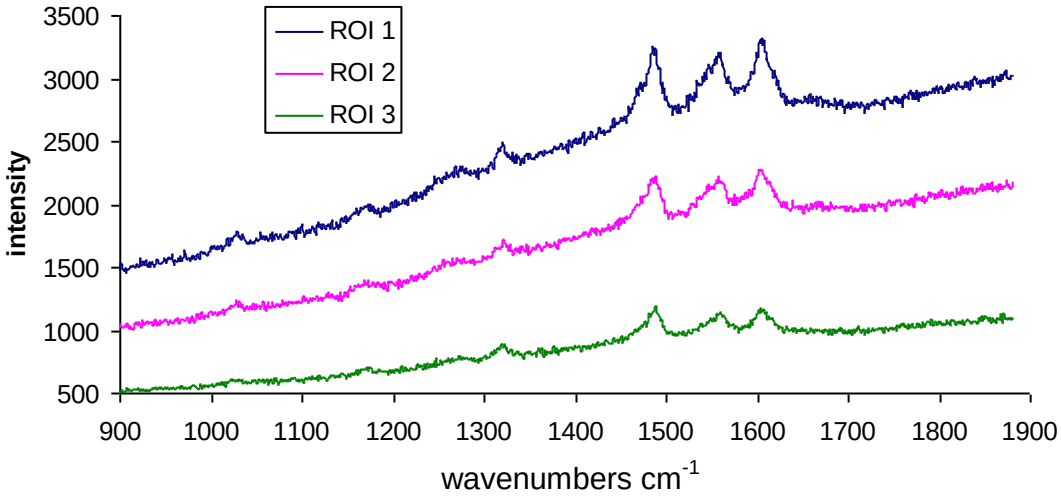

Figure 4.43: Raman Spectra of $[Ru(bpy)_2htrz\text{-}arg_8]^{9+}$ (2.8×10^{-5} M) after excitation at 473 nm inside the myeloma cell. Shown are individual spectra from regions of varying Raman intensity from map shown in Figure 4.42.

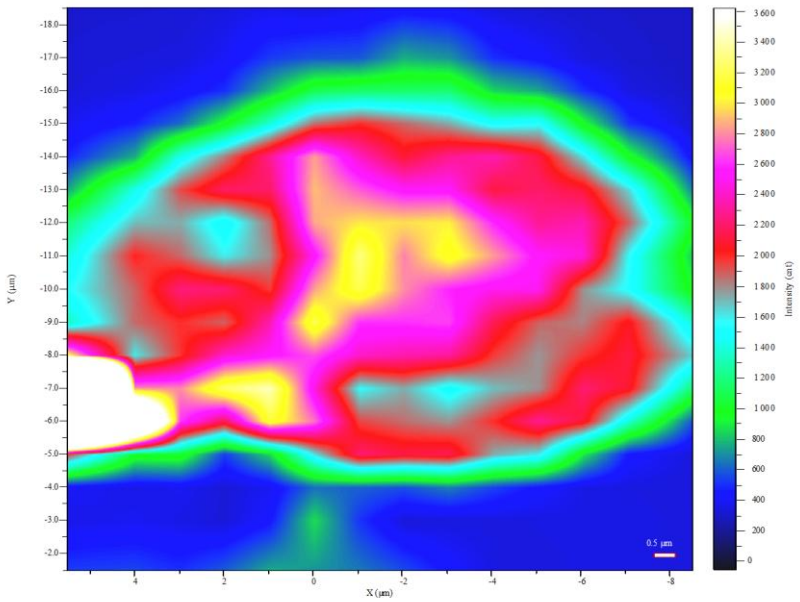

Figure 4.44: Raman intensity plot of a live CHO cell incubated with $[Ru(bpy)_2htrz\text{-}arg_8]^{9+}$ (2.8×10^{-5} M) for four hour in PBS (pH 7.4) at 37°C and constructed from the intensity of the peak at 1561 cm^{-1} in the spectrum of $[Ru(bpy)_2htrz\text{-}arg_8]^{9+}$ after excitation at 473 nm. The colour bar indicates the relative Raman signal intensity that decreases from top to bottom.

4.3.5 Photostability

4.3.5.1 Photostability of ruthenium complexes in myeloma cells

Photostability is a phenomenon which describes the ability (or inability) of a molecule to fluoresce after it has undergone repetitive excitation cycles. Most fluorophores can undergo a limited number of excitation and emission cycles, before their emission fades due to photodecomposition and eventually the fluorophore becomes inactive.[122] Many organic based molecular fluorophores commonly used for imaging purposes typically are susceptible to photobleaching when used in laser scanning microscopy. Such organic probes are not very well suited to examine environmental sensitivity in biological samples or to follow long lived dynamic processes such as membrane diffusion, protein rotation and protein folding. A key advantage of ruthenium(II) complexes is that they do not tend to exhibit such rapid degradation and have been reported to retain more than 50% of their initial luminescence intensity from within cells under 20 minutes continuous irradiation using a 458 nm argon ion laser line.[123]

As reported in section 3.2.4.4, upon monitoring the MLCT band of $[Ru(bpy)_2(htrz)]^+$ and $[Ru(bpy)_3]^{2+}$, both complexes found to reduce by approximately 20% each over six hours upon irradiation with UV light. In order to determine the photostability of $[Ru(bpy)_2(htrz)]^+$ in a cellular environment, the peptide conjugate was first internalized into SP2 myeloma cells. To encourage photobleaching, the 458 nm line of an argon ion laser was used for excitation at 100% transmission (overall power did not exceed 10 milliwatts). The sample was irradiated for 10 µs cycles, allowed to recover for and then irradiated again. In total, each sample was exposed to a 10 µs cycle six times in a second and were imaged for over 600 seconds.

To compare the photostability of the dye with another ruthenium(II) complex and an organic reference, the experiment was separately carried out using $[Ru(bpy)_3]^{2+}$ and 3,3'-dihexyloxacarbocyanine iodide ($DiOC_6(3)$). Shown in figure 4.51 is the photodegradation of the emission intensity of the three dyes under the conditions described. Shown in figure 4.52 is the loss of emission intensity of $[Ru(bpy)_2htrz]^+$ in the membrane of an SP2 cell, before (a) and after (b) irradiation (a separate cell is shown before (c) and after (d) irradiation in the same figure).

As expected, the organic $DiOC_6(3)$ was found to be almost completely photobleached after less than 150 seconds, while both ruthenium complexes were still found to luminesce after 800 seconds. Surprisingly, there was no distinct difference in the extent of bleaching experienced between $[Ru(bpy)_2htrz]^+$ and $[Ru(bpy)_3]^{2+}$.

The ruthenium – triazole complex was expected to have far greater photostability due to the strong σ - donor properties of the deprotonated triazole ligand, which induces strong ligand field splitting in the complex.[110, 112] The photostability of the triazole complex may be better demonstrated by varying the parameters of this experiment, such as increasing and decreasing the dwell time while bleaching or altering the number of excitation cycles the sample is exposed to. Further bleaching experiments could focus on solid samples of both complexes, which may provide a greater insight into the photostability of each complex.

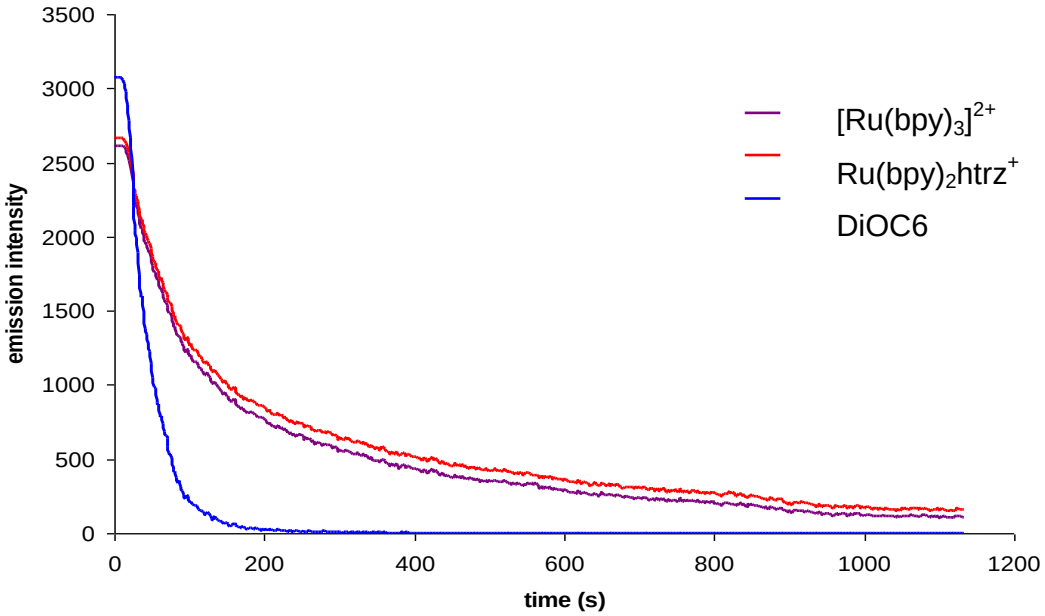

Figure 4.51: Luminescence emission intensity of $[Ru(bpy)_2htrz]^+$ (20μM), $[Ru(bpy)_3]^{2+}$ (20μM) and $DiOC_6(3)$ (5μM) in SP2 cells upon 10μs 100% irradiation cycles using a 458 nm argon ion laser line

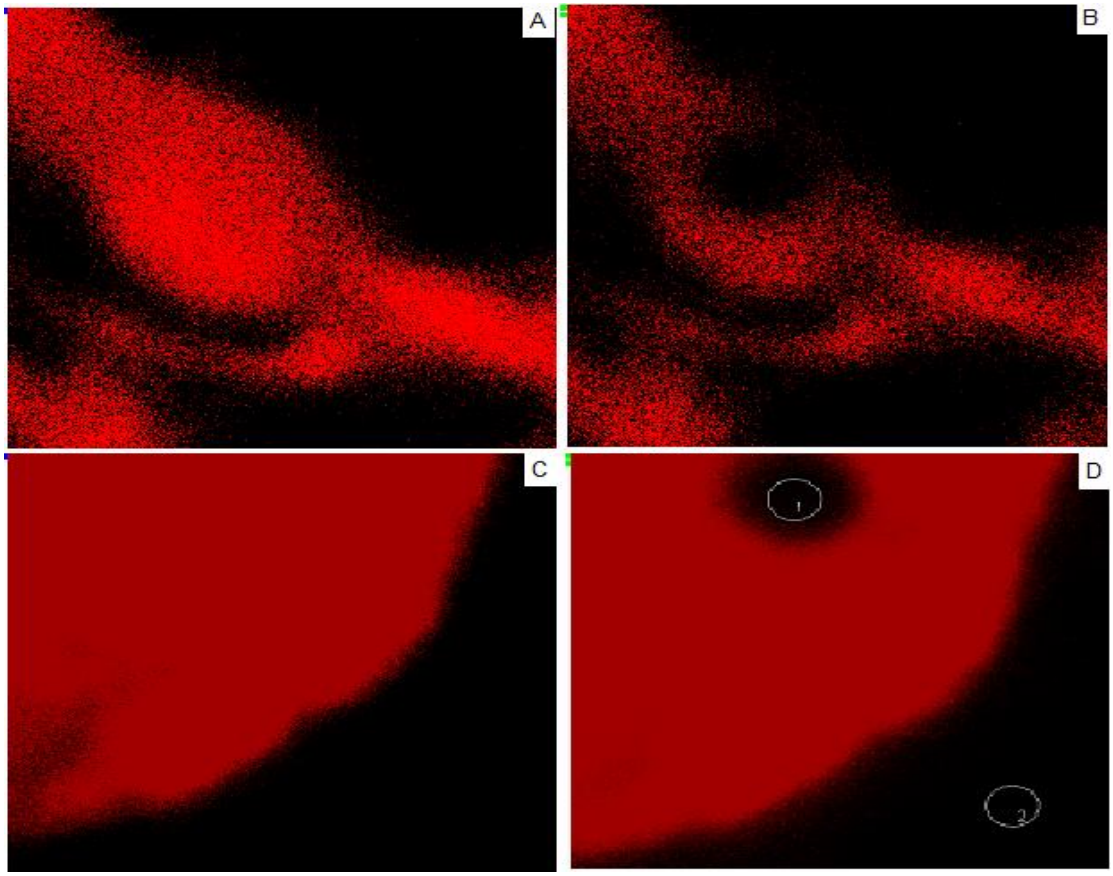

Figure 4.52: Luminescence images (λ_{ex} = 458 nm, λ_{em} = 615nm) of SP2 myeloma cell incubated with $[Ru(bpy)_2htrz\text{-}arg_8]^{9+}$ (20 μM) in PBS (pH 7.1) before (a) and after (b) 100% irradiation cycles using a 458 nm argon ion laser line

4.4 Conclusion

The results presented in this chapter report on the ability of the ruthenium peptide conjugate to diffuse passively across the cell membrane of two cell lines, SP2 myeloma and Chinese Hamster Ovary cells. Importantly, the parent ruthenium complex in the absence of peptide cannot penetrate the cellular membrane and only upon permeablizing the cell with Triton (1% v/v) can $[Ru(bpy)_2htrz]^+$ achieve this.

The peptide conjugated ruthenium complex was found to have a short lifetime (149 ns) relative to other Ru polypyridyl complexes (μs scale). As a result, it was difficult to differentiate various components of the cell using fluorescent light imaging. Resonance Raman mapping was used to investigate the presence of the complex within both cell types, by analysing individual cells. The most intense Raman signals, corresponding to the greatest concentration of dye, were observed in the center of each cell. Utilising commercially available specifically targeting cellular probes, the location of $[Ru(bpy)_2htrz\text{-}arg_8]^{9+}$ within both cell lines was investigated. The dye was found to bind to non specific organelles in the SP2 cells and was mainly found outside the nucleus of CHO cells, presumably in the endoplasmic reticulum.

The uptake speed in both cell types was found to be temperature dependent, which is consistent with endocytosis. Although internalization was effective in both cell lines, the significant difference in uptake speed and localization suggests alternative uptake pathways in each cell line. However, the different uptake speeds may arise from the difference in cell physiology between the SP2 and CHO cell lines.

The reasons for alternative uptake pathways were not determined in this thesis, as the pathway dependencies observed cannot be explained by complex size, or by the composition of the complex as both cell lines were treated with one dye at identical concentrations.

While the reasons for cell line dependence remain unconfirmed, these results showing different uptake speed and localization of $[Ru(bpy)_2htrz\text{-}arg_8]^{9+}$ in SP2 and CHO cell lines infer that cell physiology is critical in complex internalization.

Chapter 5: Conclusions and Future Work

5.1 Conclusions and Future Work

This MSc thesis focused on the synthesis of ruthenium probes which contained functional groups suitable for bioconjugation and detailed photophysical characterisation of these complexes as a function of their functional group. In the second part of this thesis, the spectroscopy, photophysics and cell uptake of a related Ru(II) polypyridyl complex conjugated to a polyarginine peptide was explored.

Chapter 3 detailed the synthesis and detailed comparative spectroscopic, photophysical and redox characterisation of two ruthenium (II) complexes of $[(Ru(NOphen)_2PicNH_2)]^{2+}$ and $[(Ru(NOphen)_2PicCOOH)]^{2+}$ from a family based on pic (define) developed in our group containing two nitrophenanthraline ligands and only differed in their terminal functionality on the pH sensitive pic ancillary ligand. The amino and carboxy terminated ruthenium complexes were compared using spectroscopic methods, with the shifts in the absorbance and emission spectra of $[(Ru(NOphen)_2PicNH_2)]^{2+}$ consistent with the electron donating nature of the amino substituent. Transitions at 340 nm were found to be pH dependent and were attributed to π-π* transitions of the [pic-R] ligands, which contains two ionisable protons on the imidazole ring, with a slight shift in this peak for the amino functionalised complex.

A further aim in chapter 3 was to produce a ruthenium – peptide conjugate with both an oxygen or pH sensitive and insensitive fluorophore as a self-referenced sensor for confocal microscopy. The purpose of synthesising both amino and carboxy functionalised luminophores was to allow increase the possible conjugation routes for this complex with a sensor. Attempts to produce a BODIPY – conjugated ruthenium complex proved unsuccessful, with the target molecule never successfully isolated. Conjugation of the ruthenium complex to a BODIPY probe was attempted ten times via an EDC/NHS coupling reaction. Despite this being a well known coupling technique, the only products recovered were starting materials.

Chapter 3 also described the optical characterisation of $[Ru(bpy)_2htrz]^+$, a ruthenium – bipyridyl complex containing a triazole ancillary ligand. The ground and excited state pKa, Raman spectroscopy and photostability of the complex was investigated under white light irradiation. Deprotonation of the complex above pH 8.5 led to a spectral shift due to the stabilising electrostatic interaction between the MLCT generated bpy anion radical and the extra positive charge of the triazolium. Signature bipyridyl vibrational Raman modes were observed using 458, 488 and 514 nm laser lines, with no significant changes between the data, suggesting the lowest energy optical transition arises from a ruthenium (dπ) to bipyridyl ligand (π*) MLCT transition. The effect of conjugation of the peptide, octaargine to the carboxy terminus of this complex on the optical properties of the complex was also explored and the influence found to be minimal

The conjugation of ruthenium complexes to cell penetrated peptide has previously reported by our group, with these probes capable of passively transporting across the cell membrane. In chapter 4 confocal microscopy was used to investigate the interaction of $[Ru(bpy)_2htrz]^+$ and its octaargnine conjugate on two mammalian cell lines; SP2 myeloma and CHO cells. It was found that the parent complex $[Ru(bpy)_2htrz]^+$ failed to transport across the cell membrane. The peptide conjugate of the complex was then added to a suspension of SP2 cells at 37°C, where it was found to rapidly penetrate the cell membrane. is the uptake rate was approximately four times faster than previous ruthenium probes reported and to our knowledge one of the fastest uptake rates for such metal complexes. Uptake of the ruthenium peptide conjugate in CHO cells was also investigated using confocal microscopy but the dye was only observed in the cell after four hours. The uptake in both cell lines was determined to be temperature dependent, which is indicative of an activated process such as endocytosis; however the significant difference in uptake speed suggests alternative uptake pathways in each cell line.

The localization of $[Ru(bpy)2htrz\text{-}arg_8]^{9+}$ in SP2 and myeloma cells was also determined to differ when cells were stained with the complex and then counter stained with nuclear targeting and endoplasmic reticulum targeting

probes. Upon counter staining both cell lines with $DiOC_6$, $[Ru(bpy)_2htrz\text{-}arg_8]^{9+}$ was found not localize in the endoplasmic reticulum of myeloma cells, but appears to localize in the endoplasmatic reticulum of CHO cells. The nuclear targeting DAPI probe was used to determine that $[Ru(bpy)_2htrz\text{-}arg_8]^{9+}$ localizes just outside the nucleus in both SP2 and CHO cells. As dye concentration and imaging conditions were kept constant, these results infer that cell physiology is critical in complex internalization.

Resonance Raman mapping was also used to confirm the successful transport of $[Ru(bpy)_2htrz\text{-}arg_8]^{9+}$ across the plasma membrane of both SP2 and CHO cells. The resonance Raman image was generated by analysing the intensity of the 1490, 1561 and 1601 cm^{-1} bands at each point in the map. In both cell lines, the dye appeared to localize in the centre of the cell, which was not expected from the results obtained from confocal imaging.

Future work emerging from this thesis should focus on developing a new approach to conjugate the ruthenium – bisnitrophenanthraline – pic complex to the pH and O_2 insensitive BODIPY probe. The BODIPY – NHS reaction may proceed using a different solvent system, for example DMF or a DMF water mixture. Alternatively, the conjugation may become more sterically favoured by attaching the BODIPY dye to a peg – linker with an amino or carboxyl terminus, before coupling to the ruthenium complex. The exploitation of a different coupling reagent is another possibility; [HATU] has been used for the robust coupling of peptides and allows greater experimental flexibility than the EDC/NHS coupling.

There is currently an intense interest in the use of metal complexes in live cell imaging and further work can expand on both the results and techniques shown here. Confocal microscopy confirmed $[Ru(bpy)_2htrz\text{-}arg_8]^{9+}$ passively crossed the cell membrane of both SP2 and CHO cells yet the results suggested that cell physiology may affect the uptake mechanism. The uptake of the dye in both cell lines may be further investigated using AlexaFluor 350, which emits at 425 nm and selectively stains the plasma membrane. This could be used to gain a more precise idea of the time taken for the dye to transport through the membrane for each cell type. The Raman mapping described was limited by

image resolution and acquisition time, which if increased, could lead to far more informative images. While whole cell mapping involves monitoring an area of at least 100 μm, focusing on individual cellular compartments may produce a greater insight into the localization and concentration of a metal complex within a cell.

Chapter 6: References

(1) Jablonski diagram http://www.photobiology.info/photochem.html (accessed 29/01/2012),.

(2) Lakowicz, J.R., **2006**. Principles of Fluorescence Spectroscopy.

(3) Nicholas, J.; Ramamurthy, V.; Scaiano, J.C. **2009**. Principles of Molecular Photochemistry - An Introduction; University Science Books.

(4) Balzani, V. and Campagna, S., **2007**. Photochemistry and Photophysics of Coordination Compounds I.

(5) Juris, A.; Balzani, V.; BargellettI, F.; Campagna, S.; Belser, P.; Von Zelewsky, A. Coord. Chem. Rev. **1988**, 85-277. .

(6) Rajkumar, E.; Rajagopal, S.; Ramamurthy, P; Vairamani, M. **2009**. Inorganica Chimica Acta, 362(5), pp. 1629-1636.

(7) Steed, A. Supramolecular Chemistry; Wiley: **2000**.

(8) Barigelletti, F.; Juris, A.; Balzani, V.; Belser, P.; Von Zelewsky. A., Inorg. Chem. **1987**, 26, 4115-4119.

(9) Rillema, P; Conrad, D. *Inorg. Chem.*, **1983**, *22* (11), pp 1617–1622.

(10) Quaranta, A.; Lachaud, F.; Herrero, C.; Guillot, R.; Charlot, M.F.; Leibl, W.; Aukauloo, A., **2007**. Chem. Eur. J. 13. , pp. 8201.

(11) Pellegrin, Y., Forster, R.J. and Keyes, T.E., **2009**. Inorganica Chimica Acta, 362(6), pp. 1715-1722.

(12) Neugebauer, U.; Pellegrin, Y.; Devocelle, M.; Forster, R. J.; Signac, W.; Moran, N.; Keyes, T. E. *Chem. Commun.* **2008**, 5307-5309.

(13) Cosgrave, L., Devocelle, M., Forster, R.J. and Keyes, T.E., Chem. Commun., **2010**, 46, 103–105.

(14) Peptide bonds

http://hyperphysics.phy-astr.gsu.edu/hbase/organic/amino.html (accessed 6/17, 2012)

(15) Wender, P.A., - Mitchell, D.J., - PattabiramaN, K., - Pelkey, E.T., - Steinman, L. and - Rothbard, J.B., Nat. Acad. Of Sci. **2000** 97, 13003.

(16) Rothbard, J.; Jessop, T.; Wender, P. Adv Drug Deliv Rev. **2005** 28;57(4):495-504.

(17) Rothbard, J.; Jessop, T.; Wender, P. *J. Am. Chem. Soc.*, **2004**, *126* (31), pp 9506–9507

(18) Mitchell, D.J.; Steinman, L.; Kim, D.T.; Fathman, C.G.; Rothbard, J.B. **2000**. Joun. of Peptide Research Vol 56, Issue 5, pages 318–325..

(19) Puckett, C. A.; Barton, J. K. *Biochemistry (N. Y.)* 2008, 47, 11711-11716.

(20) Chayen, J., **1975**. An Introduction to Cell Biology.

(21) http://php.med.unsw.edu.au/cellbiology/index.php?title=Cell_Import_-_Endocytosis (accessed 31/3/2011)

(22) Fuchs, S.; Raines, R. Cell Mol. Life Sci. 63 **2006**. 16, pp. 1819.

(23) Fuchs, S.M.; Raines, R.T., *Biochemistry*, **2004**, *43* (9), pp 2438–2444.

(24) Fukati, S.; Niwa, M.; Nakase, I.; Tadokoro, A.; Suguira, Y. *Bioconjugate Chem.*, **2004**, *15* (3), pp 475–481.

(25) Neugebauer, U., Cosgrave, L., Pellegrin, Y., Devocelle, M., Forster, R. and Keyes, T.E., unpublished results.

(26) Silverstein, S.C.; Steinman, R.M.; Cohn. Z.A., **1977**. Annual Review of Biochemistry. 46, pp. 669.

(27) Knipp, G.T.; Van Der Velde, D.G.; Siahaan, T.J.; Borchardt, R.T. **1997**. Pharm Res. 14(10):1332-40.

(28) Herce, H.; Garcia, A. Journ. of biological physics **2007**, Volume 33, 5-6, pp 345-356

(29) McCusker, J.K. *Acc. Chem. Res.*, **2003**, *36* (12), pp 876–887

(30) Damrauer, N.H.; Cerullo, G.; Yeh, A.; Boussie, T.R.; Shank, C.V.; McCusker, J.K., Science 3, **1997**: Vol. 275 no. 5296 pp. 54-57

(31) Lee, P.; Lo, K. *Inorg. Chem.*, **2011**, *50* (17), pp 8570–8579

(32) - Kowol, C.R.; Trondl, R.; Arion, V.B.; Jakupec, M.A.; Lichtscheidl, I.; Keppler, B.K. *Dalton Trans.*, **2010**,39, 704-706.

(33) Louie, M.; Lo, K. *Inorg. Chem.*, **2011**, *50* (19), pp 9465–9471

(34) Lo, K; Louie, M.; Zhang, K. Coord Chem Rev. Vol 254, 21, **2010**, Pages 2603–2622

(35) Amoroso, A.J.; Coogan, M.P.; Dunne, J.E.; Fernandez-Moreira, V.; Hess, J.B.; Hayes, A.J.; Lloyd, D.; Millet, C.; Pope, S.J.A.; Williams, C *Chem. Commun.*, **2007**, 3066-3068

(36) Dwyer, F.P., Gyarfas, E.C., Rogers, W.P. and Koch, J.H., **1952**. Biological activity of complexions. Nature[PubMed: 12982853].

(37) Hartinger, C.; Keppler, B. Journ. of Inorg. Biochem. Volume 100, Issues 5–6, **2006**, 891–904

(38) Bergamo, A.; Sava, G. *Dalton Trans.*, **2007**, 1267-1272.

(39) Szmacinski, H. **1998**. Biochimica Et Biophysica Acta-Protein Structure and Molecular Enzymology, 1383(1), pp. 151.

(40) Lakowicz, J.R.; Szmacinski, H.; Terpetschnig, E., 1996. Abstracts of Papers of the American Chemical Society, 1996. 211: p. 218-BIOT.

(41) Jimenez-Hernandez, M.E., **2000**. Photochemistry and Photobiology, 72, pp. 28.

(42) Lo, K.; Lee, T.K.; Lau, J.S.; PooN, W.L.; Cheng, S.H., **2008**. 47, pp. 200.

(43) Svensson, F.R., Matson, M., LI, M. and Lincoln, P., **2010**. Biophysical chemistry, 149(3), pp. 102-106.

(44) Lissi E. A.; Caceres T. J. Bioenerg. Biomembr. 1989. 21, pp. 375.

(45) Yu, M.; Zhao, Q.; Shi, L.; LI, F.; Zhou, Z.; Yang, H.; Yi, T.; Huang, C. Cationic iridium(iii) complexes for phosphorescence staining in the cytoplasm of living cells. ***Chem. Commun.***, 2008, 2115-2117

(46) Notman, R.; Noro, M., O'Malley, B.; Anwar, J., **2006**. J. Am. Chem. Soc. 128, pp. 13982.

(47) Notman, R.; Noro, M.; Anwar, J. *J. Am. Chem. Soc.*, **2006**, *128* (43), pp 13982–13983

(48) Yu, Z.; Quinn, P.J. Mol Membr Biol. **1998** Apr-Jun;15(2):59-68.

(49) Dobrucki, J.W. **2001**, J. Photo-chem. Photobiol., B 65, pp. 136.

(50) Terasaki, M., Loew, L., Lippincott-Schwartz, J. and Zaal, K., 2001. Fluorescent Staining of Subcellular Organelles: ER, Golgi Complex, and Mitochondria. Current Protocols in Cell Biology. John Wiley & Sons, Inc.

(51) Fernandez-Moreira, V.; Thorp-Greenwood, F.L.; Coogan, M.P., **2010** ChemInform Abstract: Application of d6 Transition Metal Complexes in Fluorescence Cell Imaging..

(52) Lissi, E.A.; Caceres, T., **1989**. 21(3), pp. 375.

(53) Piszczek, G. Archives of Biochemistry and Biophysics, Vol. 453, Issue 1, **2006**, Pages 54–62

(54) Machen, T.E.; Leigh, M.J.; Taylor, C.; Kimura, T.; Asano, S.; Moore, H. Am. J. Physiol Cell Physiol 2003, 285, C205-C214.

(55) Puckett, C.; Barton, J., **2009**. J Am Chem Soc. , pp. 8738.

(56) Nakase, I.; Takeuchi, T.; Tanaka, G.; Futaki, S., **2008**. Adv Drug Delivery Rev. 2008;60:598–607.

(57) Uzunbajakava, N.; Lenferink, A.; Kraan, Y.; Volokhina, E.; Vrensen, G.; Greve, J.; Otto, C. Biophys. Journ. Vol 84, Issue 6, **2003**, 3968–3981.

(58) Esposito, A.; Gralle, M.; Wouters, F. *Biochemistry*, **2008**, *47* (49), pp 13115–13126.

(59) Steele, S.; Young, P.; Price, R.; Lewis, D., The AAPS Journal **2004**. 6(4)

(60) G.I.T. Imaging & Microscopy. **2007**. (4), pp. 34.

(61) Barban, S.; Schulze, H., **1961.** J. Biol. Chem. 236, pp. 1887-1890.

(62) Slater, E.C. **1967**. Application of inhibitors and uncouplers for a study of oxidative phosphorylation. MethodsEnzymol. 10, pp. 48-57.

(63) Rollason, R.; Korolchuk, V.; Hamilton, C.; Schu, P.; Banting, G., 2007. Clathrin-mediated endocytosis of a lipid-raft-associated protein is mediated through a dualtyrosine motif. , pp. 3850.

(64) Douglas, K.; Piccirillo, C.; Tabrizian, M. European Journ of Pharm. and Biopharm. Vol 68, Issue 3, **2008**, Pages 676–687

(65) Anderson, R., Annu Rev Biochem. **1998**; 67, 199-225.

(66) Le, D. **2007**. In vivo imaging of hydrogen peroxide with chemiluminescentnanoparticles. Nat Mater 6:765–769. .

(67) Nagai, T.; Sawano, A.; Park, E.S.; Miyawaki, A. **2001**. Proc Natl Acad Sci USA 98:3197–3202.

(68) Nagai, T.; Yamada, S.; Tominaga, T.; Ichikawa, M.; Miyawaki, A. **2004**.. Proc Natl Acad Sci USA 101:10554–10559. .

(69) Nakai, J.; Ohkura, M.; Imoto, K. **2001**. Nat Biotechnol 19:137–141.

(70) Niethammer, P.; Grabher, C.; Look, A.T.; Mitchison, T.J. **2009**. Nature 459:996–999. .

(71) Zhang, G.; Palmer, G.M.; Dewhirst, M.W.; Fraser, C.L., **2009**. Nat Mater 8: 747–751.

(72) Madshus, I.H. Journ. Biochem. **1988**, 250, 1-8. .

(73) Schindler, M.; Grabski, S.; Hoff, E.; Simon, S.M. **1996**. Journ. of Biochemistry, 35, (9), 2811-2817.

(74) Svastova, E.; Hulikova, A.; Rafajova, M.; Zat'ovicova, M.; Gibadulinova, A.; Casini, A.; Cecchi, A.; Scozzafava, A.; Supuran, C.T.; Pastorek, J.; Pastorekova, S. **2004**. FEBS Letters 2004, 577, 439-445.

(75) Dmitriev, R.; Zhdanov, A.; Papkovsky, D. Journ. of Analytical Biochemistry**,** Vol 398, 1, **2010**, 24–33

(76) - Giulivi, C.; Kato, K.; Cooper, C.E., Am. J. Physiology. **2006**, vol 291

(77) Duchen, M. Molecular aspects of Medicine, Vol 25, 4, **2004**, 365–451

(78) Taylor, C.T., **2008**. Biochem. J. 409 (19–26)

(79) Robinson, J. Histochemistry and Cell Biology, **2009**, Vol 131, 4, pp 465-469

(80) Izumi, S.; Nagano, T. *J. Am. Chem. Soc.*, **2009**, *131* (29), pp 10189–10200

(81) Cotela, A.; Arbeloa, I. *J. Phys. Chem. A*, **2009**, *113* (28), pp 8118–8124

(82) Awuah, S.; Polreis, J.; You, Y. *Org. Lett.*, **2011**, *13* (15), pp 3884–3887

(83) Chen, Y.; Guo, H.; Xie, L. *J. Org. Chem.*, **2012**, *77* (5), pp 2192–2206

(84) Shao, J.; Guo, H.; Ji, S.; Zhao, J. J. Biosensors and Bioelectronics. Vol 26, 6, **2011**, 3012

(85) Rohand, T.; Boens, N.; Qin, W.; Dehaen. *Chem. Commun.*, **2006**, 266-268

(86) EDC/NHS coupling mechanism http://www.piercenet.com/browse.cfm?fldID=02030312 (Accessed 10/15, 2012).

(87) Bhasikuttan, A.; Suzuku, M.; Okada, T. *J. Am. Chem. Soc.*, **2002**, *124* (28), pp 8398–8405

(88) ATCC, CHO-K1 data sheet. http://www.atcc.org/ATCCAdvancedCatalogSearch/ProductDetails/tabid/452/Default.aspx?ATCCNum=CRL-1581&Template=cellBiology (Accessed 07/12/2010)

(89) Strober, W. Trypan Blue Exclusion Test of Cell Viability. **2001**, John Wiley & Sons, Inc.

(90) Gordon, K.C.; Al-Obaidi, A.H.R.; Jayaweera, P.M.; McGarvey, J.J.; Malone, J.F.; Bell, S.E.J. *J. Chem. Soc., Dalton Trans.*, **1996**, 1591-1596

(91) Introduction to Confocal Laser Scanning Microscopy http://www.zmb.uzh.ch/resources/download/CLSM.pdf (Accessed 06/14, 2012)

(92) Bai, GI.; Wang, KZ.; Jin, LP.; Gao, LH.; J. Inorg. Biochem. Vol 98, 12, **2004**, 2011–2015

(93) Bon-Suk Koo, Eun-Hoo Kim and Kee-Jung Lee, Synthetic Communications. **2001** 32(15), pp. 2275.

(94) Nishiyama, H.; Yoshiwara, H. *J. Org. Chem.*, **1992**, *57* (1), pp 407–410

(95) Steck, E.A.; Day, A.R. **1943**. J. Am. Chem. Soc. 65, pp. 452-456.

(96) Buchanan, B. E.; Degn, P.; Velasco, J. M. P.; Hughes, H.; Creaven, B. S.; Long, C.; Vos, J. G.; Howie, R. A.; Hage, R.; van Diemen, J. H.; Haasnoot, J. G.; Reedijk, J. *J. Chem. Soc.* , Dalton Trans. **1992**, 1177-1183.

(97) Jiang, CW.; Chao, H.; Li, RH.; Li, H.; Ji, LN. Polyhedron, Vol 20, 17, **2001**, 2187–2193

(98) Liu, Y., Zeng, C., Huang, H., He, L. and Wu, F., **2010**. *E. J. Med Chem*, 45(2), pp. 564-571.

(99) Chao, H., Li, R.; Ye, B., Li, H.; Feng, X., Cai, J.; Zhou, J.; Ji, L., *J. Chem. Soc.* , Dalton Trans. **1999**, 3711-3717.

(100) Veith, G. D.; Mekenyan, O. G.; Ankley, G. T.; Call, D. J. Chemosphere **1995**, 30, 2129-2142.

(101) Ackermann, M., Interrante, L. *Inorg. Chem.*, **1984**, *23* (24), pp 3904–3911

(102) Lees, A.C.; Evrard, B.; Keyes, T.E.; Vos, J.G.; Kleverlaan, C.J., Alebbi, M.; Bignozzi, C.A. **1999**. European Journal of Inorganic Chemistry, (12), pp. 2309-2317.

(103) Hage, R.; Haasnoot, J.; Reedijk, **1990**. Inorg. Chim. Acta. 174, pp. 77.

(104) Fanni, S.; Keyes, T.; O'Connor, C.; Vos, J. Coord chem rev. 208, 1, **2000**, 77

(105) Fennema, B.; Hage, R.; Haasnoot, J.; Reedijk, Inorg. Chim. Acta. Vol 171, 2, **1990**, 223–228.

(106) Vos, J.G., Forster, R.J. and Keyes, T.E., 2003; **2003**. Introduction. Interfacial Supramolecular Assemblies. John Wiley & Sons, Ltd, pp. 1-7.

(107) Mahajan, S., Richardson, J.; Brown, T. SERS-Melting: A New Method for Discriminating Mutations in DNA Sequences. *J. Am. Chem. Soc.*, **2008**, *130* (46), pp 15589–15601.

(108) Pellegrin, Y.; Keyes, T.; Forster, R. Inorg. Chim. Acta. **2008**, 361, 9, 2683

(109) Webb,M.; Knorr, F.J.; McHale, J.L. **2001** Journ. of Raman Spectroscopy. Vol 32, 6, 481–485

(110) Horn, S.; Ahmed, H.M.Y.; Hughes, H.P.; Soman, S.; Browne, W.R.; Vos, J.G. *Photochem. Photobiol. Sci.*, **2010**, 9, 985-990

(111) Fluorescent probes

http://www.piercenet.com/browse.cfm?fldID=4DD9D52E-5056-8A76-4E6E-E217FAD0D86B (Accessed 11/03, 2012).

(112) Hage, R.; Van Diemen, J.H.; Ehrlich, G.; Haasnoot, J.G.; Stufkens, D.J., Vos, J.G.; Reedijk, J. Inorganic Chemistry, Vol 29, 5, **1990**, 989

(113) Clugston, M.; Flemming, R. **2008**. Le Chatlier's Principle. Advanced Chemistry. Oxford, pp. 168-172.

(114) Gu, YJ.; Wong, WT. Journ. Tox. and applied pharm. Vol 237, 2, **2009**, Pages 196–204

(115) Miranda, L.P.; Alewood, P.F. PNAS. 16, **1999** vol. 96 no. 4 1181-1186

(116) Rothbard, J.; Jessop, T.; Wender, P. Advanced Drug Delivery Reviews, Vol 57, 4, **2005**, Pages 495–504

(117) Rejman, J.; Oberle, V.; Hoekstra, D. Biochem. J. **(2004**) 377 (159–169). .

(118) Pauletti, G.M.; Okumu, F.W.; Borchard, R.T. **1997**. Effect of size and charge on the passive diffusion of peptides across Caco-2 cell monolayers via the paracellular pathway. 14(2), pp. 164.

(119) Hirohara, S., Obata, M., Alitomo, H., Sharyo, K., Ando, T., Yano, S. and Tanihara, M. Bioconjug Chem. **2009,** 20:944-52

(120) Peng, S.; M; Sung, HW. J. Biomaterials, Vol 30, 9, **2009**, Pages 1797–1808.

(121) Ward, S.; Luk, S.; Madden, C. 2004. Applications of Raman microscopy: fast scanning chemical mapping of drug delivery systems.

(122) Rayan, G.; Guet, J.; Taulier, N.; Pincet, F.; Urbach, W., Sensors, **2010**. Recent Applications of Fluorescence Recovery after Photobleaching (FRAP) to Membrane Bio-Macromolecules. 10, pp. 5927.

(123) Cosgrave, L., Ph.D. Transfer Report - unpublished results.

(124) Cui, A., Peng, X., Fan, J., Chen, X., Wu, Y. and Guo, B., **2007**. Journal of Photochemistry and Photobiology A: Chemistry, 186, pp. 85-92.

(125) Lauer, B.A.; Mirrett, S., J Clin Microbiol. **1981**, 201–205.

Appendix 1

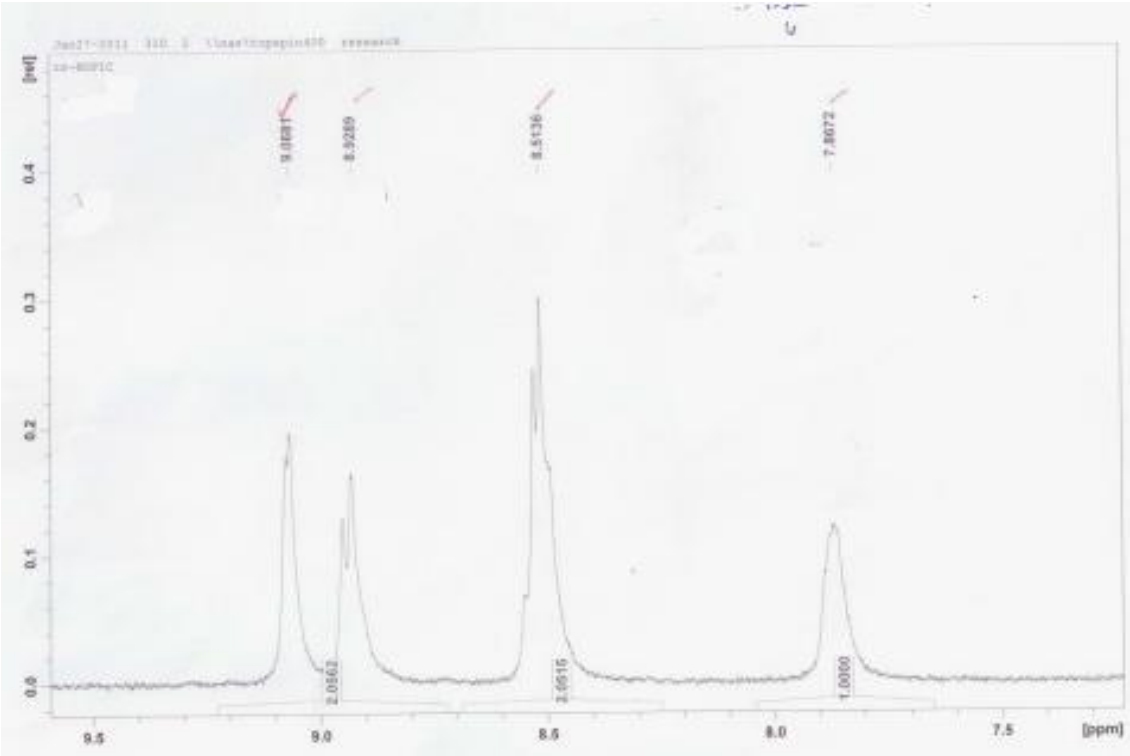

Figure A1: ^{1}H-NMR of [PicNO_2] ligand in DMSO-d_6

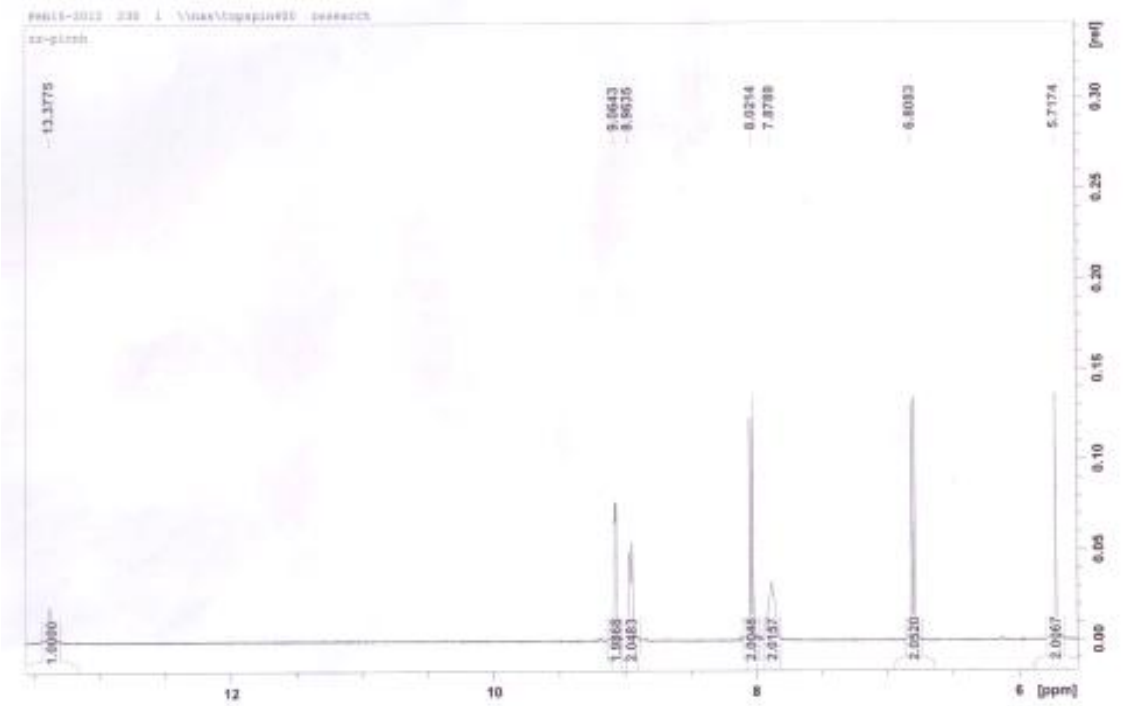

Figure A2: ^{1}H-NMR of [PicNH_2] ligand in DMSO-d_6

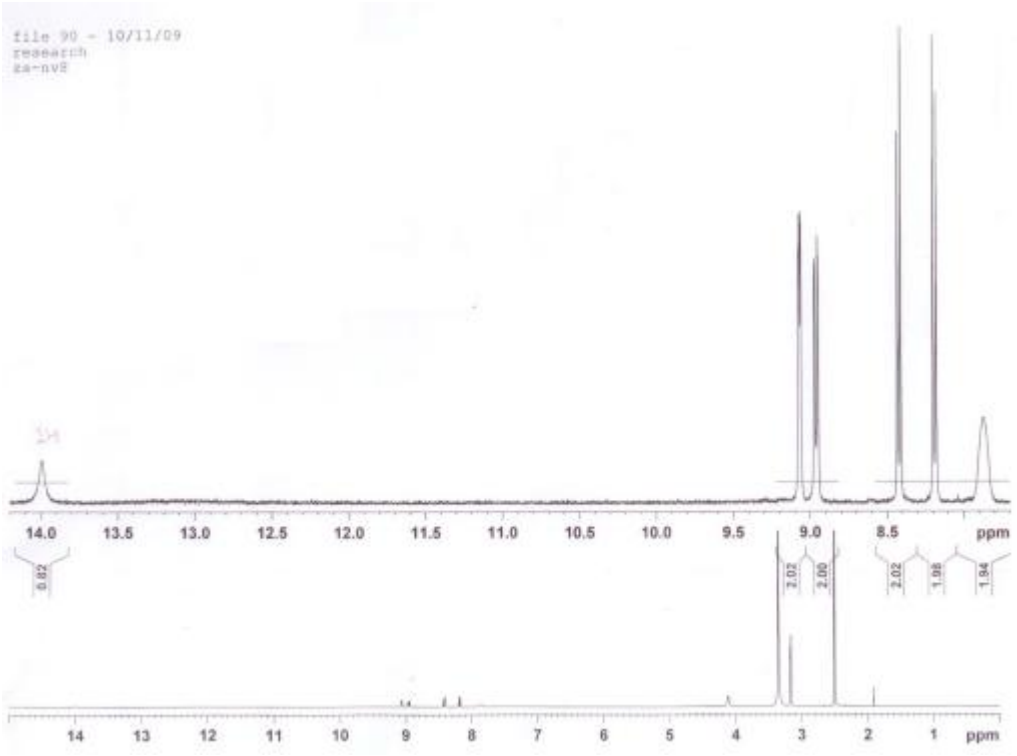

Figure A3: ^{1}H-NMR of [PicCOOH] ligand in DMSO-d_6

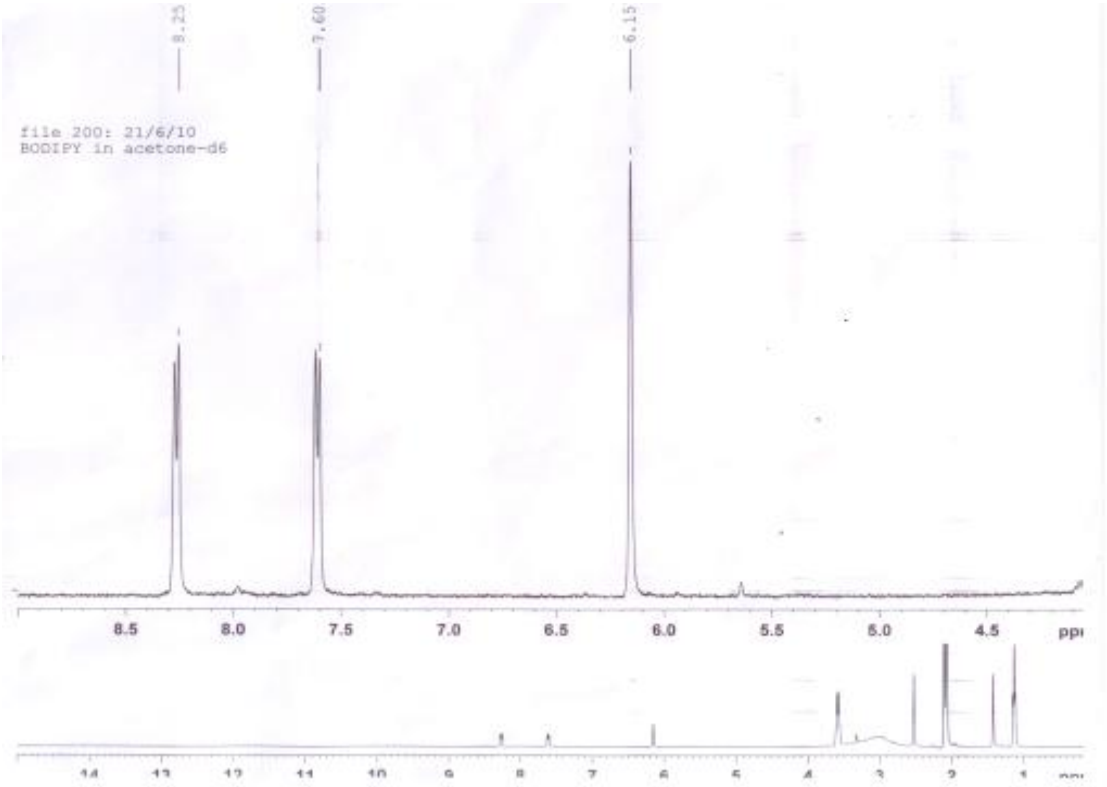

Figure A4: ^{1}H-NMR of [BODIPY] ligand in DMSO-d_6

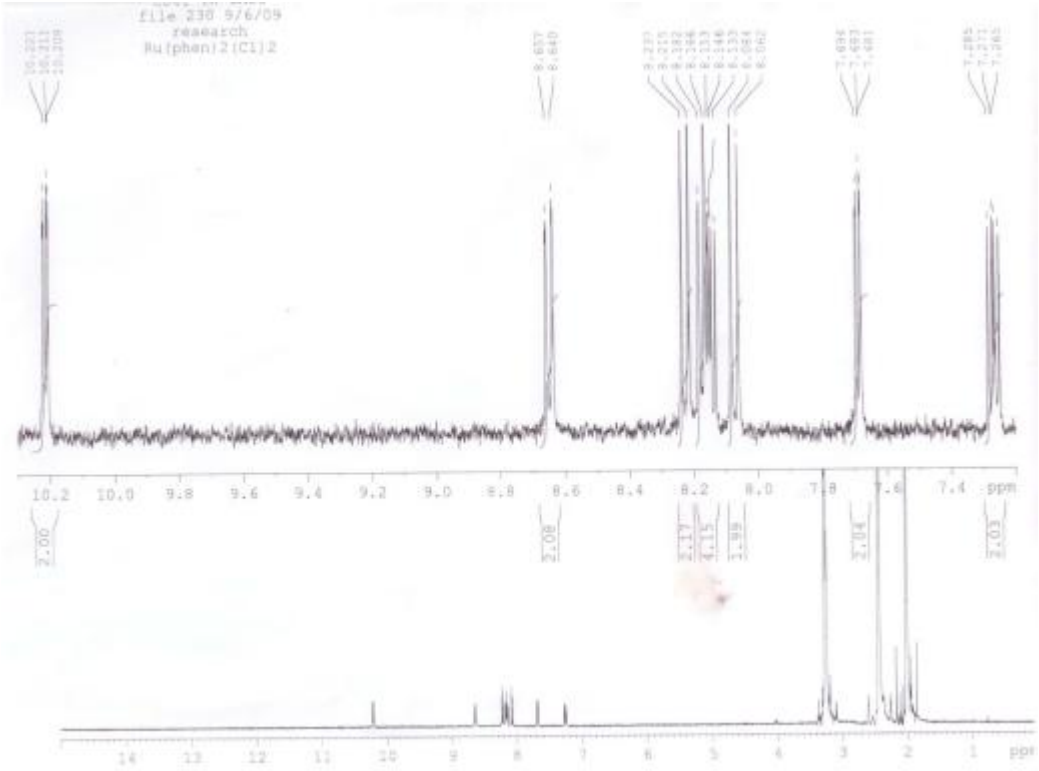

Figure A5: ^{1}H-NMR of $[Ru(phen)_2Cl_2]^{2+}$ ligand in DMSO-d_6

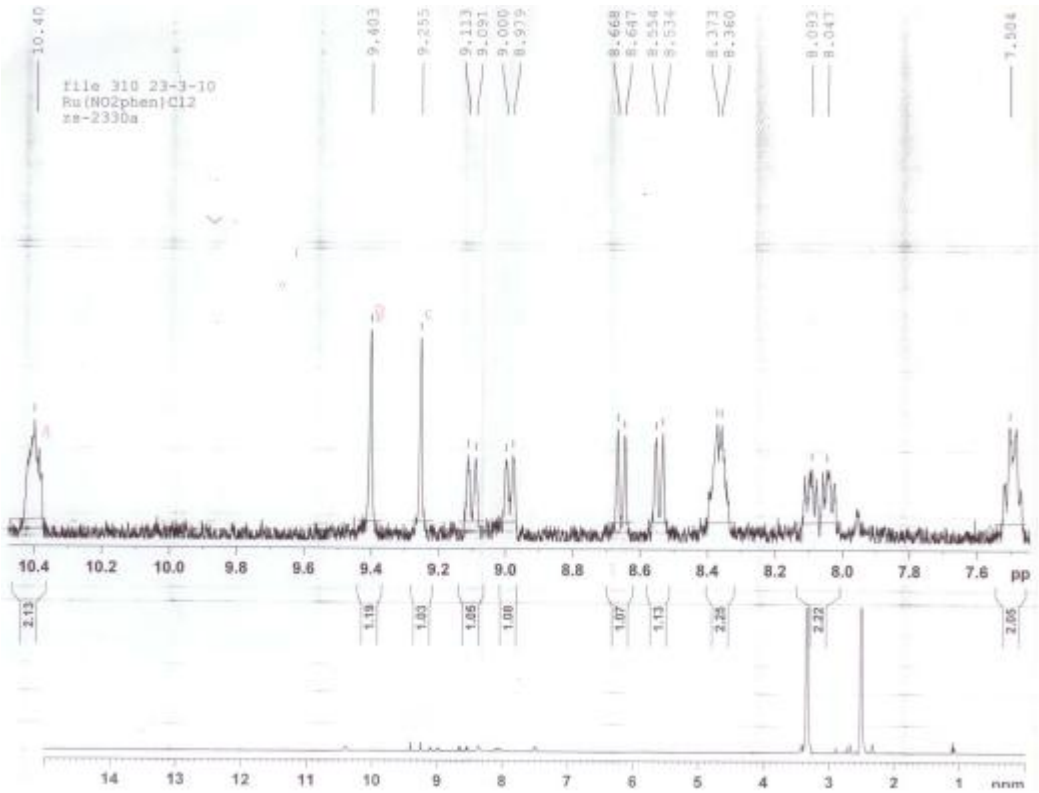

Figure A6: ^{1}H-NMR of $[Ru(NO_2phen)_2Cl_2]^{2+}$ ligand in DMSO-d_6

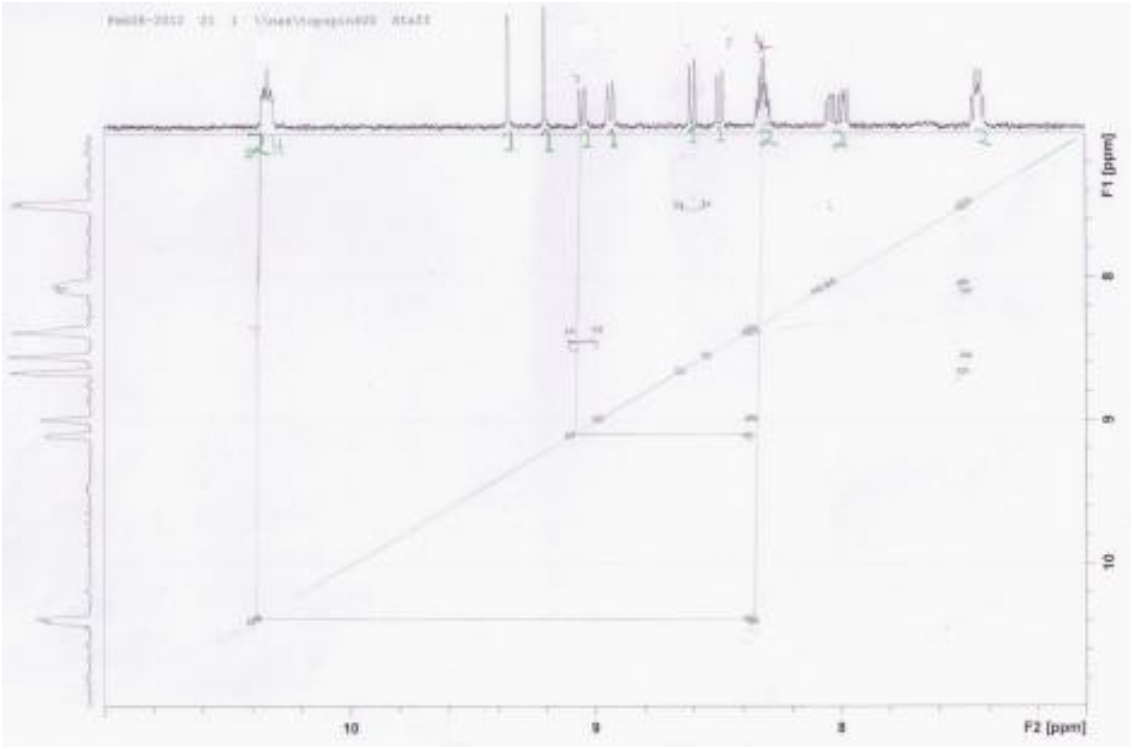

Figure A7: COSY 45 Spectrum of $[Ru(NO_2phen)_2Cl_2]^{2+}$ ligand in DMSO-d_6

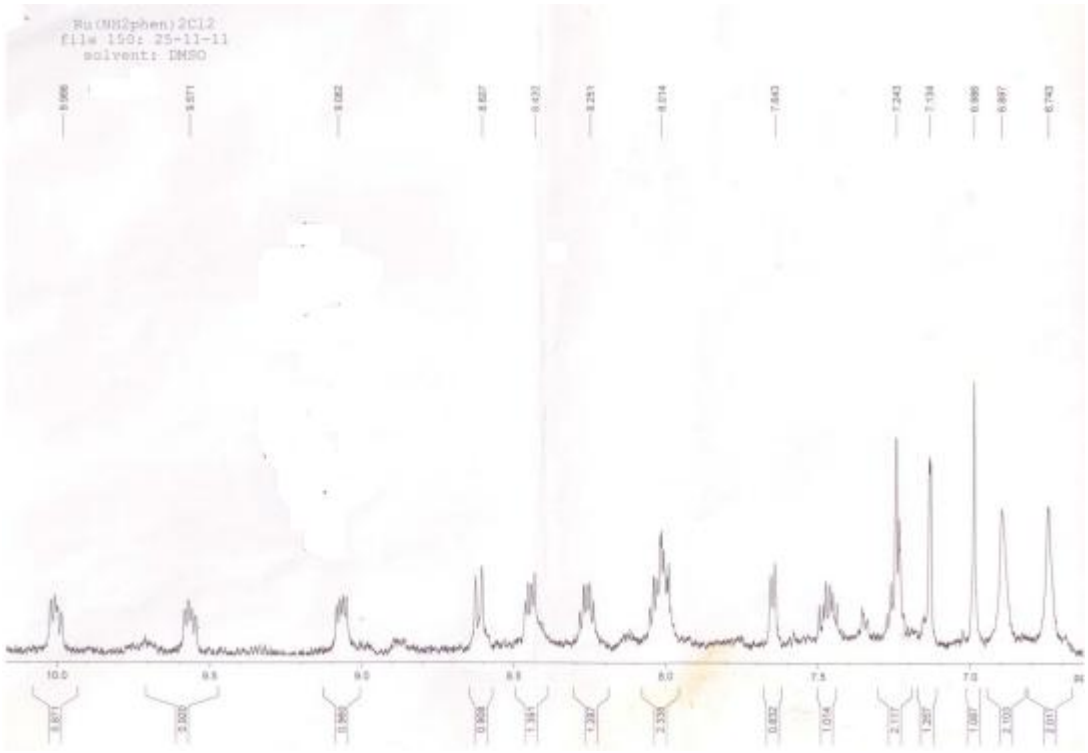

Figure A8: ^{1}H-NMR of $[Ru(NH_2phen)_2Cl_2]^{2+}$ ligand in DMSO-d_6

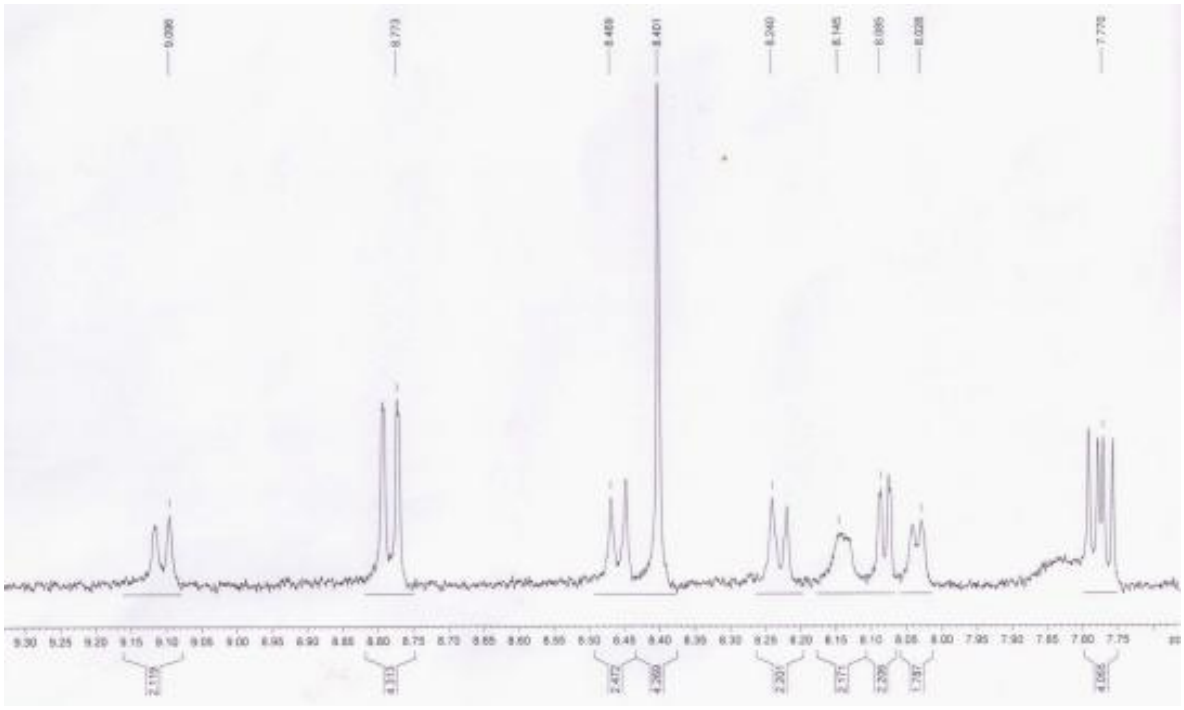

Figure A9: ^{1}H-NMR of $[Ru(phen)_2COOH]^{2+}$ ligand in MeOD

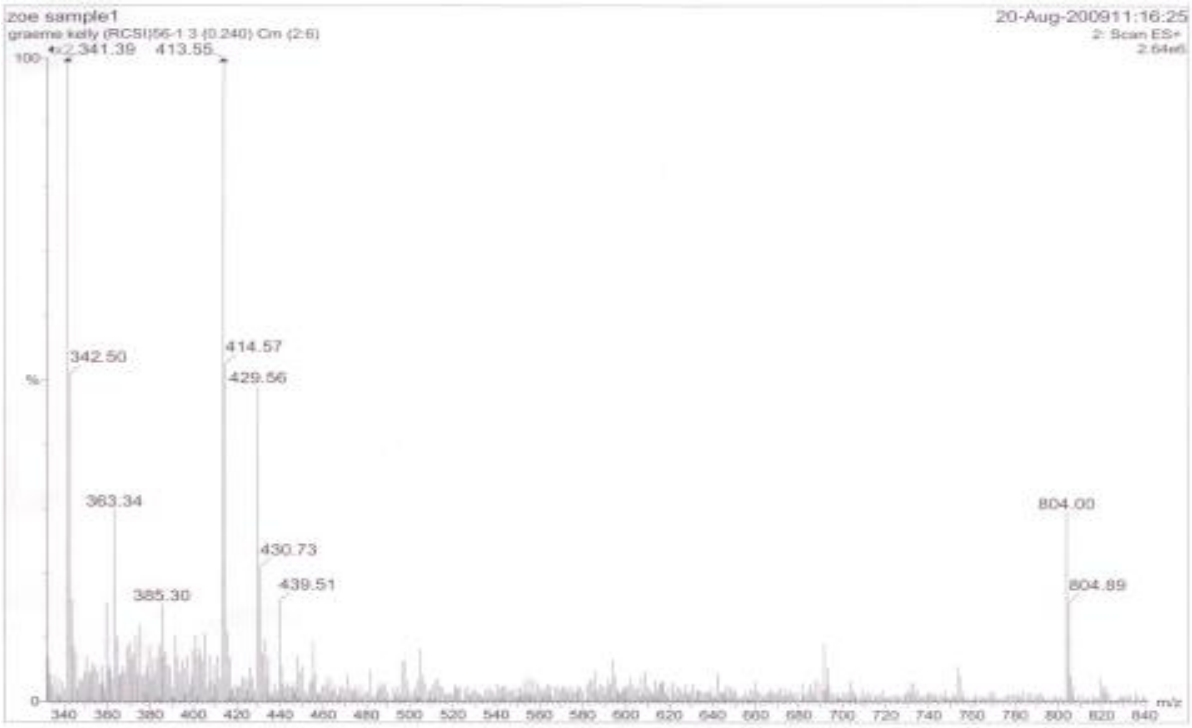

Figure A10: Mass Spectrum of $[Ru(phen)_2COOH]^{2+}$

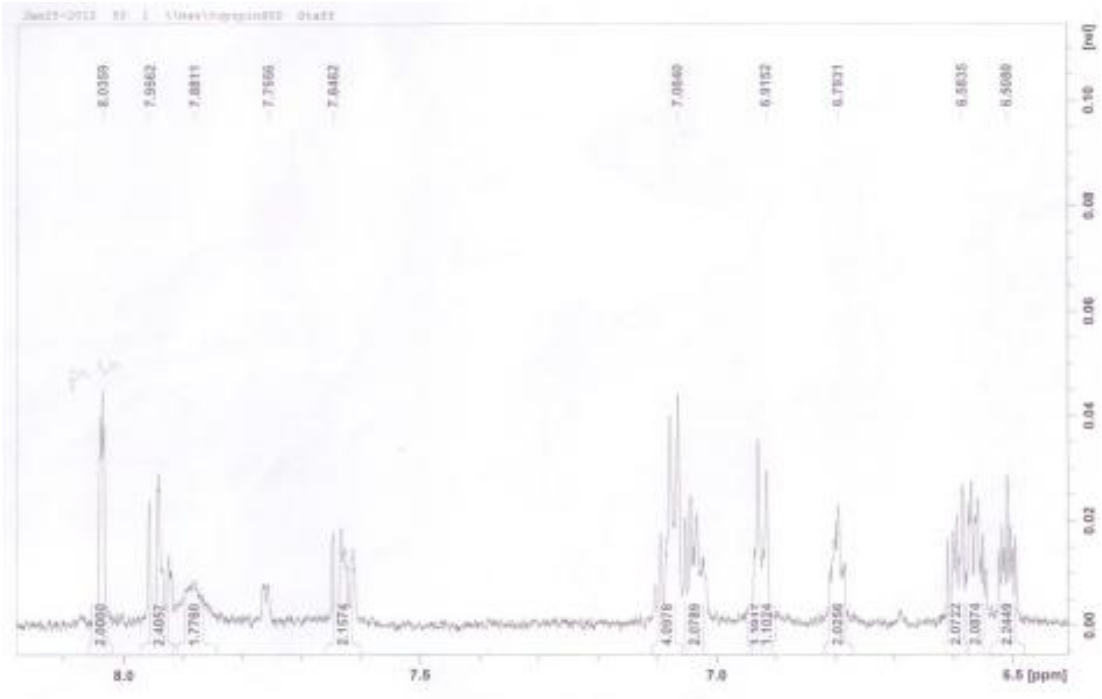

Figure A11: ^{1}H-NMR spectrum of $[Ru(NO_2phen)_2COOH]^{2+}$ in MeOD

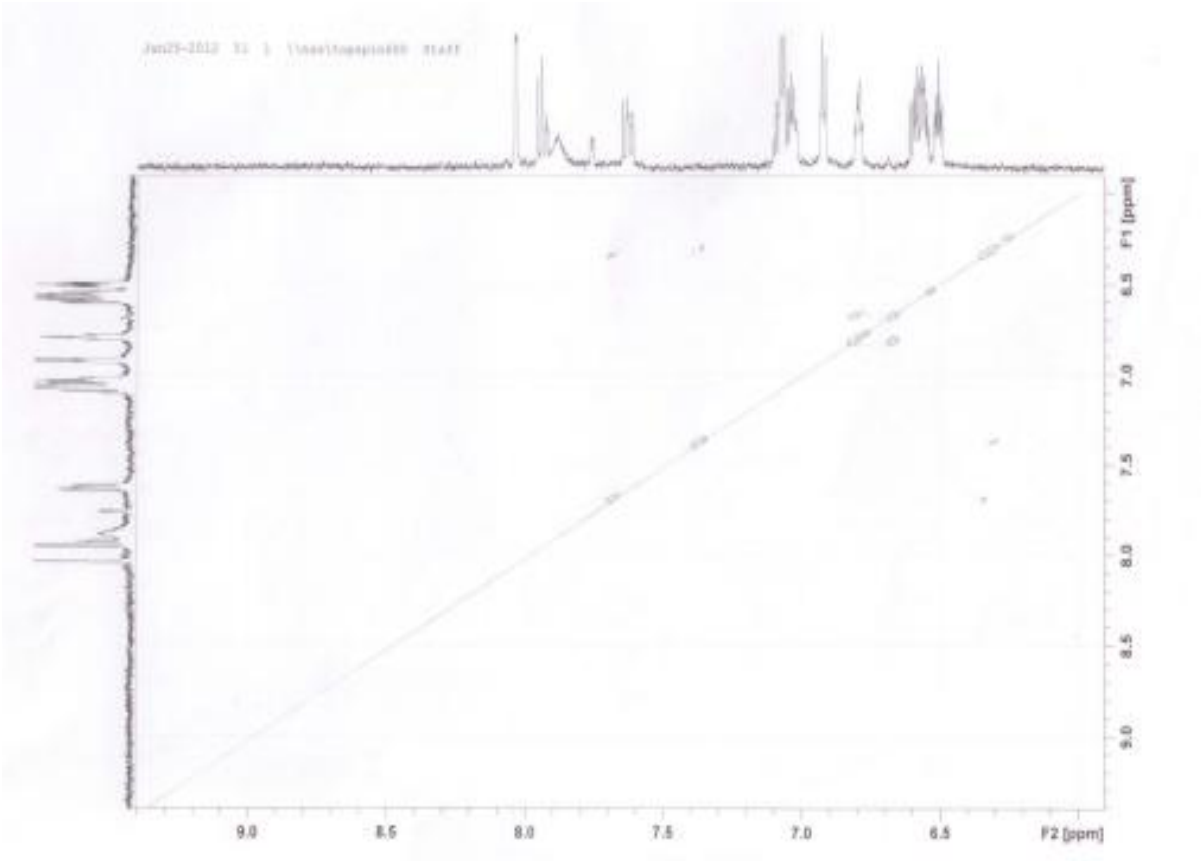

Figure A12: COSY 45 spectrum of $[Ru(NO_2phen)_2COOH]^{2+}$ in MeOD

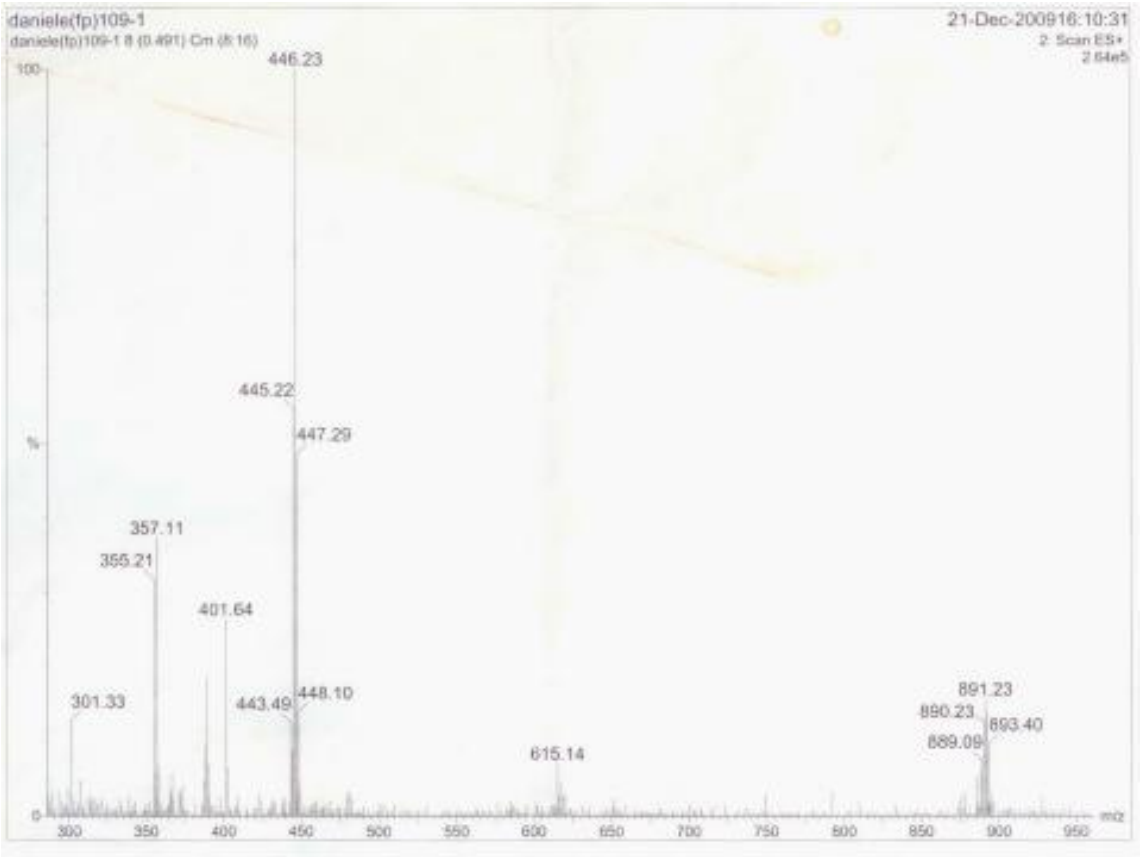

Figure A13: Mass Spectrum of $[Ru(NO_2phen)_2COOH]^{2+}$

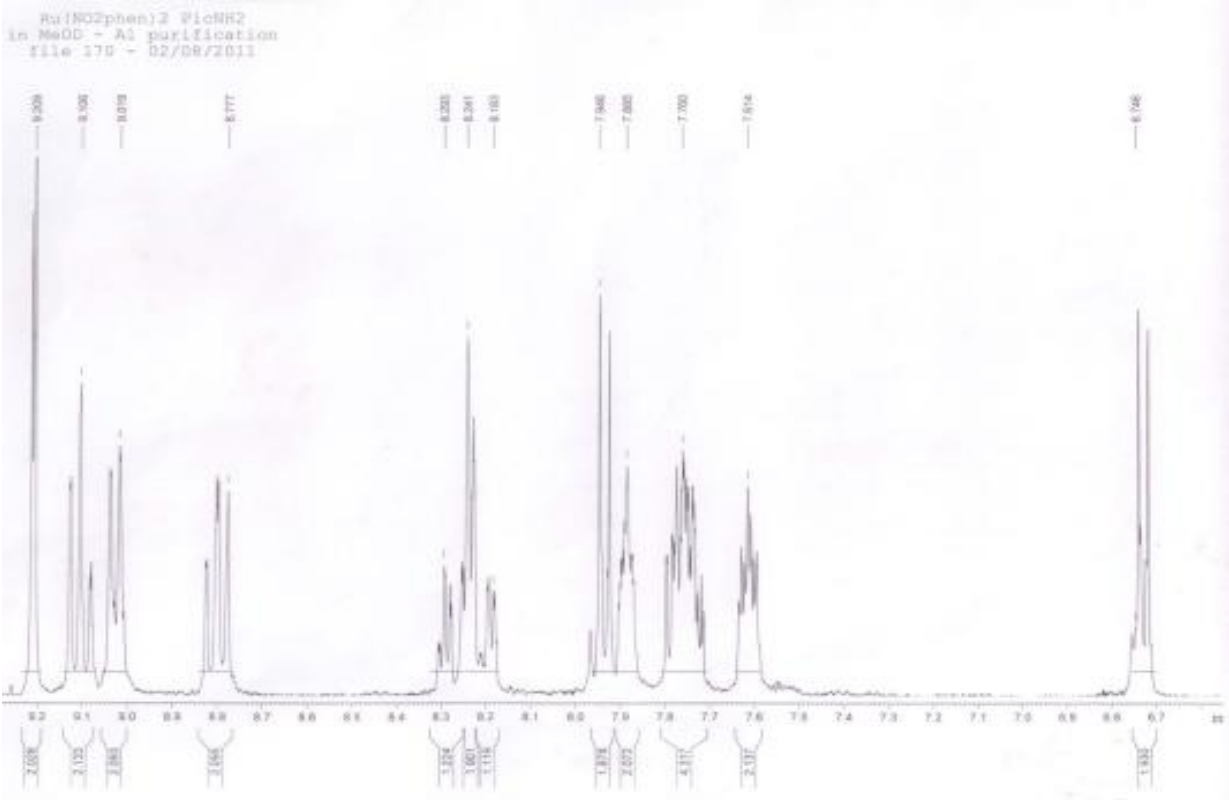

Figure A14: ^{1}H-NMR spectrum of $[Ru(NH_2phen)_2COOH]^{2+}$ in MeOD

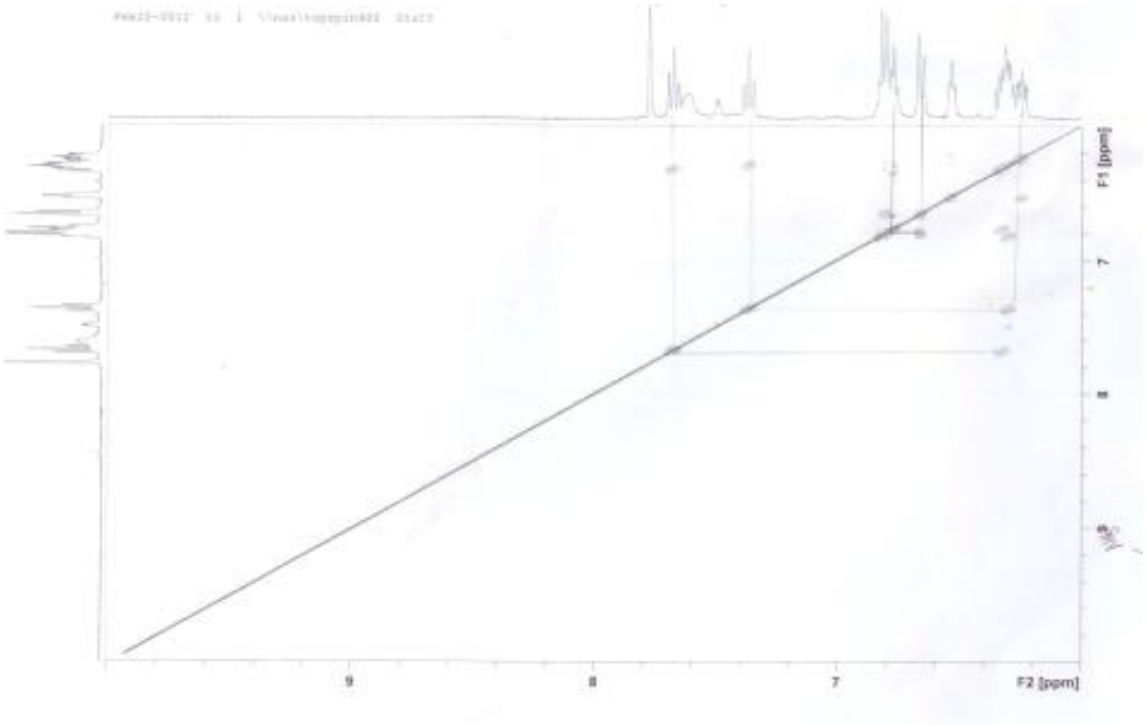

Figure A15: COSY 45 spectrum of $[Ru(NH_2phen)_2COOH]^{2+}$ in MeOD

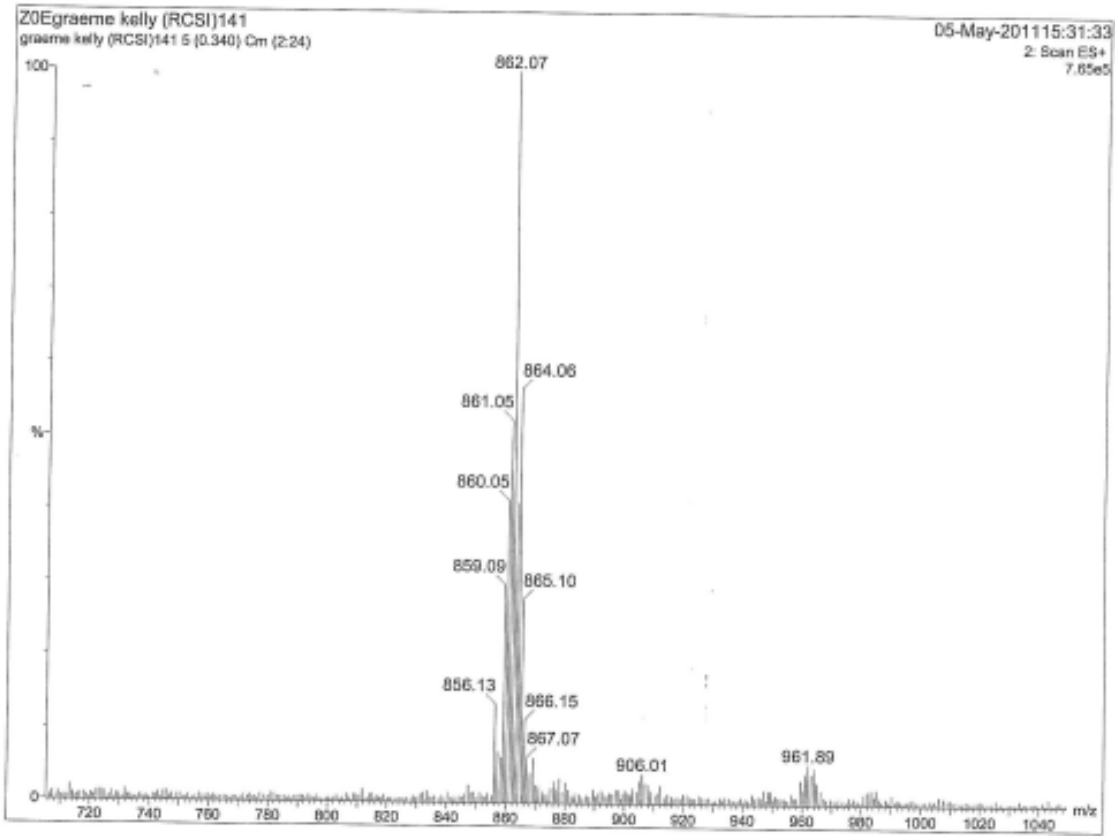

Figure A16: Mass Spectrum of $[Ru(NH_2phen)_2COOH]^{2+}$

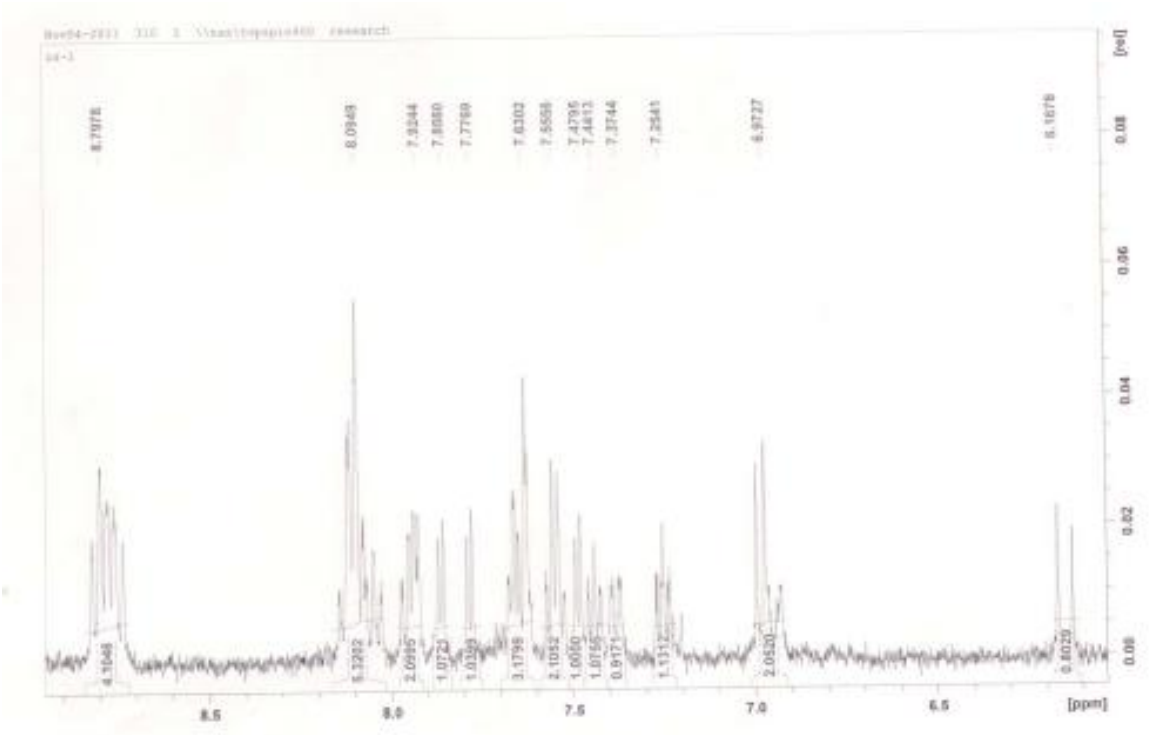

Figure A17: ^{1}H-NMR spectrum of $[Ru(bpy)_2htrz]^{+}$ in DMSO-d_6